Utilization of a frame store pnCCD for energy-dispersive Laue diffraction with white synchrotron radiation

DISSERTATION
zur Erlangung des Grades eines Doktors
der Naturwissenschaften

vorgelegt von
M. Sc. Sebastian Send

eingereicht bei der Naturwissenschaftlich-Technischen Fakultät
der Universität Siegen
Siegen 2013

Gutachter der Dissertation:
Prof. Dr. Ullrich Pietsch
Prof. Dr. Lothar Strüder

Datum der mündlichen Prüfung:
24. Juli 2013

Gedruckt auf alterungsbeständigem holz- und säurefreiem Papier.

Zusammenfassung

Die Verwendung hochbrillianter Synchrotronstrahlung, die von Speicherringen der dritten Generation bereitgestellt wird, erlaubt präzise Strukturanalysen von kristallinen Materialien mit Hilfe der Röntgenbeugung. Allerdings ist eine Vielzahl von Experimenten von Seiten der gegenwärtig verfügbaren Detektoren begrenzt. Die Möglichkeit, Beugungssignale der Probe gleichzeitig orts-, energie- und zeitaufgelöst nachweisen zu können, bieten erstmalig am Halbleiterlabor des Max-Planck-Institutes entwickelte pnCCD-Systeme mit Bildspeicherauslese. Das Funktionsprinzip eines pnCCDs basiert auf der Erzeugung von Elektron-Loch-Paaren innerhalb einer vollständig seitwärts verarmten Silizium-Schicht bei Röntgeneinfall.
Die vorliegende Arbeit beschreibt die allgemeinen Beschränkungen bei der Anwendung von pnCCDs für Beugungsexperimente mit weißer Synchrotronstrahlung. Dabei spielen sowohl die erreichbare Orts-, Energie- und Zeitauflösung einzelner Photonen im Spektroskopiemodus als auch das Verhalten des Detektors im Integrationsmodus eine wichtige Rolle. Die Energieauflösung des pnCCDs wird zunächst anhand fluoreszenzspektroskopischer Messungen im Energiebereich zwischen 6 keV und 20 keV untersucht. Die experimentelle Bestimmung der maximalen innerhalb eines Pixels speicherbaren Ladungsmenge, die den Dynamikbereich des Detektors festlegt, beruht auf Analysen des lokalen Zählratenverhaltens bei Beleuchtung eines einzelnen Pixels mit intensiver monochromatischer Röntgenstrahlung.
Im zweiten Teil der Arbeit wird das Potenzial von pnCCD-Systemen für Strukturanalysen im Rahmen von energiedispersiven Lauebeugungsexperimenten an tetragonalen Kristallen aus Hühnereiweiß-Lysozym demonstriert. Dabei ermöglicht die Auswertung simultan gemessener Reflexpositionen und -energien eine Berechnung der konventionellen Elementarzelle mittels einer einzigen Laue-Aufnahme. Dieses Ergebnis ist unabhängig von der Probenorientierung, ohne Einschränkungen auf polykristalline Materialien anwendbar und kann ohne zusätzliche Informationen über die Probe gewonnen werden. In diesem Sinne erlauben pnCCD-Systeme eine schnelle Charakterisierung von Polykristallen mit Hilfe der Weißstrahl-Lauebeugung. Die Bestimmung integraler Reflexintensitäten basiert auf einer statistischen Analyse von Pile-up-Ereignissen, bei denen sich die Signalamplituden verschiedener Photonen räumlich überlagern. Die dazu entwickelten Methoden verwenden, dass die Verteilungen detektierter Photonenzahlen der Poisson-Statistik genügen. Damit können Strukturfaktoramplituden aus den pnCCD-Datensätzen extrahiert und für eine Strukturverfeinerung auf atomarem Niveau verwendet werden.

Abstract

The use of highly brilliant synchrotron radiation provided by third-generation storage rings allows precise structure analyses of crystalline materials by means of X-ray diffraction. However, a variety of experiments is limited on the part of presently available detectors. The possibility to measure simultaneous position-, energy-, and time-resolved diffraction signals of the sample is offered for the first time by pnCCD systems developed at the Max-Planck-Institute Halbleiterlabor. The principle of a pnCCD is based on the electron-hole pair creation within a fully sideward depleted silicon layer by incident X-rays.
The present work describes the general limitations of pnCCDs used for diffraction experiments with white synchrotron radiation. In that respect, both the achievable position, energy, and time resolution of single photons in the X-ray spectroscopy mode and the detector response in the integration mode are of considerable importance. The energy resolution of the pnCCD is investigated in the energy range between 6 keV and 20 keV by means of X-ray fluorescence spectroscopy. The experimental determination of the maximum number of storable charges per pixel, which defines the dynamic range of the detector, relies on analyses of the count rate behavior in the case of single-pixel illumination with intense monochromatic X-rays.
In the second part of the work, the potential of pnCCD systems for structure analyses is demonstrated within the scope of energy-dispersive Laue diffraction experiments on tetragonal hen egg-white lysozyme crystals. The evaluation of the simultaneously measured spot positions and energies enables a calculation of the conventional unit cell from a single Laue pattern. This result is independent of the sample orientation, applicable to polycrystalline materials without restriction, and can be obtained without additional information about the sample. In this sense, pnCCD systems allow a fast characterization of polycrystals by means of white-beam Laue diffraction. The determination of integrated Bragg peak intensities is based on a statistical analysis of pile-up events generated by spatially overlapping charge clouds associated with different photons. The developed methods use the fact that the distribution of detected photon numbers is given by Poisson statistics. In this way, structure-factor amplitudes can be extracted from the pnCCD data sets and used for a structure refinement on an atomic level.

Contents

1 Introduction **1**

2 The pnCCD concept **5**

2.1 Fundamentals of X-ray detection 5

2.1.1 Interaction of X-rays with matter 5

2.1.2 Semiconductor radiation detectors 8

2.1.3 pn-junction 10

2.2 pnCCD and frame store pnCCD 12

2.2.1 Sideward depletion 12

2.2.2 Charge collection in a pnCCD 14

2.2.3 Frame store pnCCD 16

2.2.4 Charge transfer in a frame store pnCCD 17

2.2.5 Signal amplification and readout 19

2.2.6 Technical realization 22

2.3 4D X-ray detection using a frame store pnCCD 24

2.3.1 Measurements with a stationary sample 25

2.3.2 Quantum efficiency 26

2.3.3 Single events and split events 27

2.3.4 Position resolution and parallax effects 29

2.3.5 Energy resolution and noise 30

2.3.6 Time resolution 31

2.3.7 Pile-up events: The SPC limit 33

2.3.8 Photon statistics 34

3 Performance study of an eROSITA pnCCD **39**

3.1 X-ray fluorescence spectroscopy 40

3.1.1 XRF setup at the EDR beamline 40

3.1.2 Data acquisition and analysis 42

3.1.3 Gain and CTI correction factors 43

3.1.4 Signal stability 44

3.1.5 Linearity 45

3.1.6 Energy resolution 47

3.1.7 Effects at low gain settings 48

3.1.8 Characteristics at high count rates . . . 51
3.2 Single-pixel illumination with monochromatic X-rays . . . 52
3.2.1 Experimental conditions . . . 53
3.2.2 Count rate behavior . . . 55
3.2.3 Pixel saturation . . . 57
3.2.4 Charge handling capacity . . . 59
3.3 Measurements with an IμS . . . 60
3.3.1 The microfocus X-ray source IμS . . . 60
3.3.2 X-ray spectroscopy mode and X-ray imaging mode . . . 62
3.3.3 Dynamic range . . . 65

4 Application of pnCCDs in macromolecular crystallography 67
4.1 Energy-dispersive Laue diffraction . . . 68
4.1.1 Real lattice and reciprocal lattice . . . 68
4.1.2 Bragg condition and Laue equations . . . 70
4.1.3 Kinematical scattering theory . . . 72
4.2 Unit-cell determination from pnCCD data sets . . . 75
4.2.1 Cell extraction . . . 75
4.2.2 Delaunay reduction . . . 77
4.2.3 Gaussian reduction . . . 78
4.2.4 Unit-cell refinement and indexing . . . 79
4.3 Experimental conditions for EDLD on HEWL crystals . . . 81
4.3.1 EDLD setup at the EDR beamline . . . 81
4.3.2 Incident X-ray spectrum . . . 83
4.3.3 Absorber characteristics . . . 84
4.4 Analysis of a HEWL polycrystal . . . 86
4.4.1 HEWL single crystal . . . 88
4.4.2 HEWL double crystal . . . 91
4.5 Determination of integrated Laue spot intensities . . . 95
4.5.1 Cluster recombination . . . 95
4.5.2 Background subtraction . . . 97
4.5.3 Integration of single reflections . . . 99
4.5.4 Deconvolution of two overlapping harmonics . . . 102
4.5.5 Deconvolution of three overlapping harmonics . . . 106
4.5.6 Deconvolution of four overlapping harmonics . . . 109
4.5.7 Structure refinement . . . 112

5 Summary and Conclusions 119

Bibliography 121

Acknowledgements 131

1 Introduction

The use of highly brilliant synchrotron radiation provided by third-generation storage rings allows a variety of X-ray diffraction experiments for precise analyses of crystalline materials. In general, gaining structural information about a sample is based on the detection of its scattering signal and the interpretation of the recorded data in reciprocal-space coordinates. Particularly structure determination of organic materials relies on the collection of many Bragg peaks generated by the crystal within a large reciprocal-space volume ensuring a high resolution in real space. Since organic crystals suffer from radiation damage in many cases, two-dimensional area detectors are typically used for fast data collection. Therefore, as long as the sample is exposed to monochromatic X-rays, diffraction patterns need to be recorded for different orientations of the crystal in order to obtain the desired information. However, the sample rotation gives rise to experimental difficulties for data analyses if the crystal is not homogeneous as a result of polycrystallinity. In such situations, the accessible amount of information can be substantially enhanced by means of white-beam X-ray Laue diffraction techniques for which a rotation of the sample is not required. The disadvantage of these methods consists in the fact that on the part of presently established X-ray area detectors, the energies of individual Bragg peaks cannot be resolved with a sufficient accuracy. Consequently, with regard to unit-cell determination and indexing, *a priori* knowledge about the crystal has to be available in terms of an appropriate structure model.
From a conceptual point of view, an experimental possibility to quantitatively characterize organic crystals without the necessity of sample alignment and rotation is preferable. A new approach to achieve this consists in the use of pnCCD (pn-junction charge coupled device) systems for energy-dispersive Laue diffraction with white synchrotron radiation. In this thesis, the detection capabilities of a pnCCD, which enable analyses of polycrystalline materials by means of a single-shot exposure of the sample without any additional information, are investigated under real experimental conditions.
Modern X-ray diffraction experiments can be subdivided into two classes according to the choice of the incident X-ray beam:

- **Monochromatic mode**: The sample is illuminated with X-rays of fixed and user-defined energy E. Either characteristic radiation emitted by the anode material of an X-ray tube or highly brilliant X-rays generated by storage rings or free electron lasers are suitable. For that purpose, synchrotron radiation has to be monochromatized by selecting one specific energy out of the complete storage ring spectrum using precisely aligned monochromator crystals. The typical monochromacity of synchrotron radiation achieved for X-ray diffraction experiments is in the order of $\delta E/E \approx 10^{-4}$.

- **White-beam mode**: The sample is exposed to white X-rays with a continuous energy spectrum. Either bremsstrahlung delivered by an X-ray tube or white synchrotron radiation can be used. In the first case, the upper limit of the emitted spectrum is given by the applied high voltage for accelerating electrons within the X-ray tube. In the second case, the X-ray spectrum of a bending magnet deflecting relativistic electrons extends from the optical range up to hard X-ray energies of about 30 keV. Insertion devices in the form of multipole wigglers and undulators provide X-rays with energies above 100 keV. For particular applications, incident X-ray beams comprising narrow energy bands with widths of a few 100 eV are also required (pink-beam mode).

Nowadays, for both the monochromatic and the white-beam mode, different commercially available X-ray detector systems are used. If the energy of the diffraction signal is known and thus not of interest for the measurement process, a high-performance X-ray detector needs to be capable of counting as many photons as possible. Conventional point detectors, e.g. proportional counters and scintillation counters, deliver an intensity information at the observation point with a typical maximum count rate of about 10^5 cps (counts per second). By means of linear or curved series of many point detectors, X-rays can be resolved with one-dimensional position resolution. However, point detectors often show large dead times and a poor energy resolution of 20-40% which is why they are only suitable for applications with monochromatic X-rays. Special types of energy-dispersive point detectors consist of fully depleted pn-structures and allow the recording of a scattered X-ray spectrum at the detection point. An example of this is the Roentec X-Flash with an energy resolution below 2% which is sufficient for many white-beam X-ray diffraction experiments.
X-ray detectors formed by two-dimensional arrangements of individual sensitive units belong to the class of area detectors. Image plate systems and especially pixel detectors based on the concept of a charge coupled device (CCD) are widely used for X-ray structure analysis. Presently, the Pilatus detector is regarded as the most efficient area detector with a maximum count rate above 10^6 cps per pixel [1]. Despite the meanwhile excellent performance in the case of monochromatic applications, the energy resolution provided by CCDs is in the range of 10% and therefore still not sufficient to be exploited in the white-beam mode.
New developments in the field of X-ray area detectors are the pnCCD and the frame store pnCCD. In contrast to conventional point detectors and CCD area detectors, the pnCCD enables an efficient combination of two-dimensional position resolution, energy resolution, and time resolution of scattered X-rays. Under this condition, the experimentally accessible information about single photons becomes effectively four-dimensional. Table 1.1 summarizes the resolution capabilities of the mentioned detector systems and gives an overview in terms of overall resolution compared with the pnCCD.
Originally, the pnCCD was developed at the Max-Planck-Institute Halbleiterlabor (MPI-HLL) as a single-photon counting X-ray CCD for astrophysical applications. Within a cooperation between the MPI-HLL and PNSensor GmbH the detector modules were designed, fabricated, and tested with high technological effort. The spectroscopic performance of pnCCDs could

X-ray detector system	position resolution	energy resolution	time resolution	overall resolution
point detectors (proportional and scintillation counters)	—	—	—	0D
linear and curved point detectors (Braun, Inel)	1D	—	—	1D
energy-dispersive point detectors (Roentec X-Flash, Amptek)	—	x	—	1D
image plate systems (mar345)	2D	—	—	2D
CCD area detectors (Pilatus, Eiger, marCCD)	2D	—	x	3D
pnCCD and frame store pnCCD	2D	x	x	4D

Table 1.1: Resolution of the pnCCD in comparison with conventional X-ray detector systems.

successfully be demonstrated within the scope of the satellite mission XMM-Newton [2]. An advanced type of pnCCD with frame store operation was realized in 2004 [3] and will be used for the eROSITA satellite mission to be launched in 2014. Moreover, the flexibility of the pnCCD allowed to detect intense soft X-ray pulses generated by crystalline samples at the free electron lasers FLASH and LCLS [4]. For these purposes, the capability of the detector of both resolving single photons in the X-ray spectroscopy mode and counting photons in the X-ray imaging mode was exploited.

Within a collaboration between the University of Siegen, the MPI-HLL, and PNSensor GmbH the application field of X-ray diffraction experiments with white synchrotron radiation has been opened up. In a first test experiment, it could be shown that the simultaneous position and energy resolution of the pnCCD enables one-shot availability of structural information about the sample [5]. In 2007, the University of Siegen was equipped with one of the first routinely working frame store pnCCD modules comprising 256×256 pixels of 75×75 μm^2 quadratic size in the image area. This system was used to investigate inorganic crystals by means of energy-dispersive Laue diffraction techniques exploiting the 3D resolution of the pnCCD in the case of a stationary sample [6]. In another application, the 4D resolution served to detect thermally induced interdiffusion processes in Fe-Pt multilayers across the PtL absorption edges of the sample within a dynamic X-ray reflectivity experiment [7]. In the course of successive improvements of pnCCD performance, PNSensor GmbH provided the University of Siegen with a test module of the eROSITA pnCCD generation with 128×128 pixels in 2010 and an electronic upgrade to the final eROSITA system with 384×384 pixels in 2012.

The general aim of this work is a quantification of the 4D resolution of pnCCDs referred to the effective position, energy, and time resolution of single photons, with emphasis on their real performance parameters in energy-dispersive Laue diffraction experiments. Additionally, since the necessary steps for correct analyses of pnCCD-generated data sets are not fully understood

yet, a crucial part of this thesis concerns the related methods for unit-cell extraction, indexing, and in particular absolute intensity determination. The so-obtained resolution is evaluated in terms of the achievable accuracy of calculated unit-cell parameters and the results of a structure refinement. The work itself is structured as follows:
Chapter 2 gives a brief introduction into the fundamental concepts of X-ray detection and the principle of frame store pnCCD systems including considerations of various parameters which define the real 4D resolution and the limit of single-photon counting (SPC).
The response of an eROSITA type pnCCD module is investigated in chapter 3 based on a complete performance study of the eROSITA pnCCD test chip with 128×128 pixels. Due to the fact that the available eROSITA systems are electronically equivalent, the results of this study can be regarded as representative for both modules. The characterization summarizes the basic properties of eROSITA pnCCD systems used for SPC in the X-ray spectroscopy mode and photon integration in the X-ray imaging mode. It comprises a simulation of the quantum efficiency in the hard X-ray regime and a measurement of the energy resolution by means of fluorescence spectroscopy between 6 keV and 20 keV. The pnCCD response is discussed in detail in the case of low gain settings ensuring the highest possible dynamic range. Using the monochromatic 111 reflection of a Si(111) crystal with variable intensity, the charge handling capacity of an individual pixel is determined in the X-ray spectroscopy mode. Possibilities to increase the count rate capability are investigated in the X-ray imaging mode, based on a pnCCD operation with reduced back contact voltage, by exposing a single pixel with intense X-rays generated by the microfocus X-ray source IμS.
In chapter 4, the potential of the pnCCD is demonstrated by the example of energy-dispersive Laue diffraction experiments on hen egg-white lysozyme (HEWL) crystals. In this application, the quantitative interpretability of Laue spot positions and energies offers new possibilities for fast X-ray screening methods to test the sample for polycrystallinity. At this stage, the necessary algorithms to extract the unit cell of the crystal are presented in detail. Finally, the strong restriction of an SPC operation mode is motivated and quantified in terms of pile-up events occurring at high local count rates at the positions of individual Bragg peaks. Taking into account that the detected photon numbers follow Poisson distributions, it is shown how pile-up events can be statistically analyzed in order to obtain integrated Laue spot intensities. The presented method can also be applied to deconvolute spatially overlapping harmonics of the crystal. In this way, a set of experimental structure-factor amplitudes is extracted and used for a rigid-body refinement of the HEWL structure on an atomic level.
The results of this work, summarized in chapter 5, will be helpful to evaluate the pnCCD performance and its limiting parameters to be considered in real diffraction experiments with highly brilliant X-rays. Regarding the system response, especially as far as the occurrence of pile-up events and analyses of the dynamic range are concerned, optimized experimental conditions can be defined for particular applications. With respect to energy-dispersive Laue diffraction, the developed methods, which are required for quantitatively correct analyses of pnCCD-generated data, enable a routine operation of pnCCDs at experimental stations providing white synchrotron radiation.

2 The pnCCD concept

Crystalline materials can be analyzed by means of diffraction experiments. If the wavelength of the incident radiation is in the order of 1 Å, comparable with the lattice constants of the sample, the crystal gives rise to Bragg reflections. For precise structure analyses, highly brilliant synchrotron radiation with an X-ray energy of about 10 keV is typically used. In contrast to conventional techniques performed in the monochromatic mode, the pnCCD allows energy-dispersive Laue diffraction in the white-beam mode.
This chapter describes the concept and technical realization of a frame store pnCCD as a semiconductor radiation detector based on the principle of sideward depletion in high resistivity Si. In particular, it is shown how and under which constraints incident X-rays can be detected within a four-dimensional data volume. The achievable overall resolution with respect to position, energy, and time has to be considered as a general limiting parameter in the case of X-ray diffraction experiments with synchrotron radiation using pnCCDs.

2.1 Fundamentals of X-ray detection

The energy-dispersive proof of X-rays requires interactions with the atoms of the detector material resulting in the generation of charged particles. In semiconductor radiation detectors, these charged particles are electron-hole pairs. After separation of the electrons from the holes and charge collection, the electrons give rise to a measurable voltage signal with a height depending on the incident X-ray energy.

2.1.1 Interaction of X-rays with matter

The absorption of X-rays in matter is a statistical process. The average intensity I of an X-ray beam with energy E and primary intensity I_0 after traversing an absorbing layer of thickness x can be described by

$$I = I_0 e^{-\mu x}\,, \tag{2.1}$$

where μ, the energy-dependent linear absorption coefficient of the material, is proportional to the total absorption cross section σ according to [8]

$$\mu = \rho \frac{N_0}{A} \sigma \tag{2.2}$$

(ρ: density of the material, N_0: Avogadro number, A: atomic weight of the material). The inverse of μ defines the absorption length after which the intensity has decreased to $1/e$

of its initial value. For X-rays of *a priori* unknown energy to be measured by means of a semiconductor radiation detector, the following interaction processes of X-rays with matter need to be considered:

- **Photoelectric effect**: The energy E of the interacting X-ray photon is completely transferred to an atomic electron. In this case, the electron leaves the atom with the energy $E - B$, where B is the binding energy of the electron, and creates secondary charge carriers in subsequent ionization processes. The remaining excited atom then releases the energy $E - B$ in the course of the transition to its ground state by emitting characteristic fluorescence radiation. Normally, the fluorescence photon either undergoes further interactions with other atoms of the detector material or transfers its energy directly to the shell of the radiating atom (Auger effect) leading to Auger electrons with short range. In both cases, the secondary interactions contribute to the measurable signal, i.e. the energy of the incident photon is completely deposited within the detector volume. If the fluorescence photon leaves the material without any further interactions, the incident photon will be detected with a reduced energy giving rise to the so-called escape peak. The photoelectric cross section σ_{ph} is dominated by X-ray absorption within the K-shell of an atom and can be approximated by [9]

$$\sigma_{\mathrm{ph}} = \sqrt{32}\,\alpha^4 \frac{Z^5}{\epsilon^{7/2}}\,\sigma_{\mathrm{Th}}\,, \tag{2.3}$$

  where $\alpha = 1/137$ is the fine-structure constant, Z the atomic number of the absorbing material, $\epsilon = E/m_e c^2$ the incident photon energy in units of the electron's rest energy (m_e: electron mass, c: speed of light), and $\sigma_{\mathrm{Th}} = 8\pi r_e^2/3$ the Thomson cross section for elastic scattering of photons by free electrons (r_e: classical electron radius).

- **Compton effect**: The Compton effect describes the elastic scattering of X-ray photons by quasi-free electrons. In this process, the photon is scattered at the Compton angle θ with respect to the incident path direction and transfers a fraction of its initial energy to the electron. The energy E' of the scattered photon is given by

$$E' = \frac{E}{1 + \epsilon(1 - \cos\theta)}\ . \tag{2.4}$$

  In the case of Compton backscattering ($\theta = 180°$), the kinetic energy $E'_e = E - E'$ of the electron reaches a maximum value at

$$E'_e = E\,\frac{2\epsilon}{1 + 2\epsilon}\ , \tag{2.5}$$

  also denoted as the Compton edge. In general, the energy of a Compton electron may adopt any value between 0 and E'_e. As a result of secondary interactions with other atoms, for both the Compton electrons and the scattered photons, a continuous energy spectrum is measured within the detector.

The relativistic and quantum mechanical treatment of the Compton effect leads to the Klein-Nishina cross section σ_c per electron [10]

$$\sigma_c = 2\pi r_e^2 \left[\frac{1+\epsilon}{\epsilon^2} \left(\frac{2(1+\epsilon)}{1+2\epsilon} - \frac{1}{\epsilon} \ln(1+2\epsilon) \right) + \frac{1}{2\epsilon} \ln(1+2\epsilon) - \frac{1+3\epsilon}{(1+2\epsilon)^2} \right] \quad . \tag{2.6}$$

For small X-ray energies ($\epsilon \ll 1$), σ_c reaches the Thomson cross section according to [8]

$$\sigma_c = \sigma_{\mathrm{Th}}(1-2\epsilon) \quad . \tag{2.7}$$

In Compton scattering processes only a part of the photon energy is transferred to the electron, which is why the scattering cross section σ_{cs} and the corresponding absorption cross section σ_{ca} are usually defined by [11]

$$\sigma_{cs} = \frac{E'}{E}\,\sigma_c \quad , \quad \sigma_{ca} = \sigma_c - \sigma_{cs} \quad . \tag{2.8}$$

- **Coherent scattering**: Coherent scattering, also referred to as Rayleigh scattering, is an interaction process in which X-rays are elastically scattered by bound electrons. In this case, the atom itself remains unaffected, i.e. it is not ionized or excited. In the course of Rayleigh scattering, the electromagnetic field of the X-ray interacts with the electrons and induces an atomic dipole moment oscillating with the frequency of the incident wave. The radiation scattered by the atomic charge distribution can be considered as coherently emitted by multiple electrons leading to interference effects. The associated cross section and the angular distribution of Rayleigh-scattered X-rays depend on the atomic form factor of the material and are discussed in detail in [12]. Coherent scattering plays a minor role for materials with a low atomic number and is not of importance with respect to mechanisms resulting in X-ray absorption.

- **Pair production**: At high X-ray energies $E > 2m_e c^2 \approx 1\,\mathrm{MeV}$, corresponding to two electron rest masses, the generation of electron-positron pairs by incident photons within the Coulomb field of a nucleus becomes dominant. However, in the X-ray energy range of interest up to about 25 keV, this interaction is energetically not possible and will not be further considered at this point.

The total absorption cross section and the linear absorption coefficient in the hard X-ray regime are finally given by the contributions of photoelectric effect and Compton scattering:

$$\sigma = \sigma_{\mathrm{ph}} + Z\sigma_{\mathrm{ca}} \quad , \quad \mu = \mu_{\mathrm{ph}} + \mu_{\mathrm{ca}} \quad , \tag{2.9}$$

where $\mu_{\mathrm{ph}} = \rho N_0 \sigma_{\mathrm{ph}}/A$ and $\mu_{\mathrm{ca}} = Z\rho N_0 \sigma_{\mathrm{ca}}/A$. The additional factor Z takes into account that Compton absorption is caused by the Z electrons of an atom.
With regard to the pnCCD structure based on a fully sideward depleted Si bulk, the linear absorption coefficients of the various X-ray interactions in Si were calculated using the program

DABAX contained in the XOP software [13, 14]. The energy dependence of the obtained components is shown in figure 2.1 for the energy range between 1 keV and 100 keV.

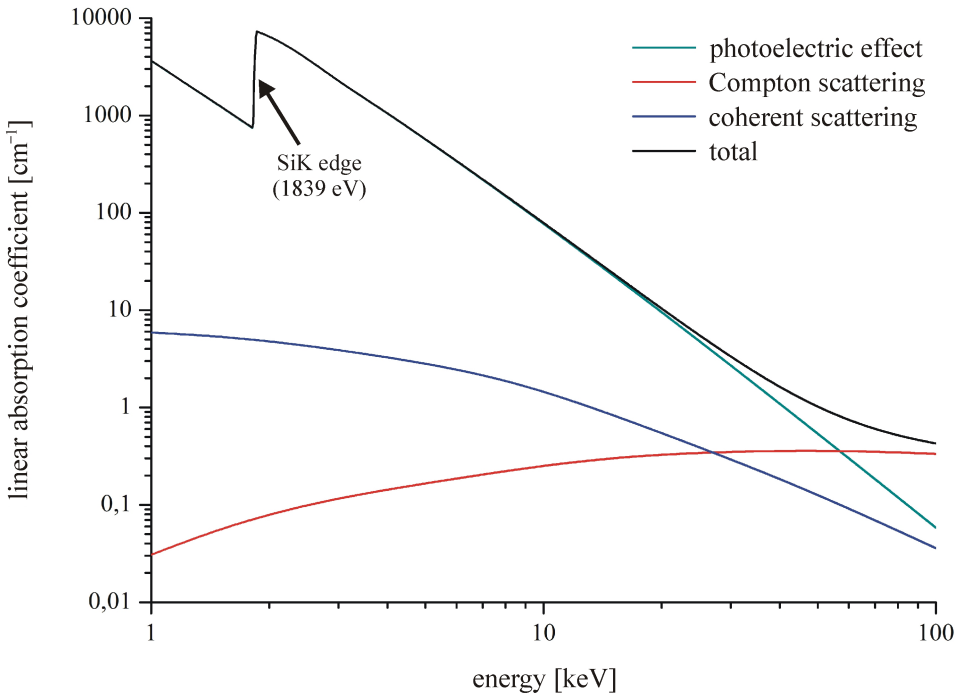

Figure 2.1: Calculated linear absorption coefficients of Si for different photon interactions in the X-ray regime between 1 keV and 100 keV.

In the case of X-ray energies below 25 keV, the photoelectric effect is the dominant interaction in Si. The strong decay of the linear absorption coefficient above the SiK absorption edge at 1839 eV entails limitations in detection capabilities of hard X-rays. At an energy of 55 keV, the probability of photoelectric effect equals the probability of Compton scattering. Towards 100 keV, the total absorption cross section of Si is mainly determined by Compton scattering.

2.1.2 Semiconductor radiation detectors

Among presently established detector systems the multidimensional resolution of X-rays with the best possible performance is achieved by means of semiconductor radiation detectors. The sensitive detector unit, in which the X-rays interact, consists of an intrinsic semiconductor material of high crystalline purity. Besides commonly used elements of the carbon group with four valence electrons like Si and Ge, special III-V and II-VI compounds like GaAs or CdTe have been tested [15, 16]. In the most basic realization of an X-ray detector, these materials are operated as conventional diodes with reverse-biasing.
In comparison to proportional counters and scintillation counters, semiconductor radiation detectors provide a larger ionization yield in the X-ray regime. Additionally, with respect to the significantly higher density of solids compared to gases, X-ray detectors based on

semiconductor structures can be fabricated in the form of compact systems with relatively small detector volumes. Proportional counters are gas detectors using the ionization of gas molecules by incident X-rays, where electron-ion pairs give rise to measurable voltage signals. For typical gases, the energy required to create an electron-ion pair is in the range of 30 eV [11]. In scintillation counters, the deposited X-ray energy leads to excitations of heavy atoms. Returning to the atomic ground state, electromagnetic radiation in the optical regime is emitted and recorded by means of photomultipliers. As standard materials for scintillators, crystalline solids (NaI(Tl), CsI(Tl)) and organic liquids have been used. In the case of CsI(Tl), light yields of 52 optical photons per keV deposited energy are obtained [8]. Due to their sensitivity at high incident energies, proportional counters and scintillation counters are also suitable detector systems for gamma spectroscopy.

The principle of solid-state X-ray detectors is based on the intrinsic band structure of a semiconductor. Under well-defined conditions, atomic electrons bound in the valence band can be transferred to the conduction band in which they are freely movable. This effect occurs if an electron adopts a certain amount of energy exceeding the energetic gap E_g between the valence band and the conduction band. The necessary gain in energy can be either thermally induced or caused by an X-ray interaction. The statistical probability of a transition to the conduction band by thermal excitation at a specific temperature T is proportional to $e^{-E_g/kT}$ (k: Boltzmann constant). The band gap between the valence band and the conduction band in Si amounts to 1.12 eV at room temperature ($T = 300\,\mathrm{K}$) and shows a monotonically rising behavior up to its maximum value of 1.17 eV in the limit $T \to 0\,\mathrm{K}$ [17]. Thermal excitation of electrons often leads to leakage currents which represent an unwanted contribution to the generated charge signal. For this reason, semiconductor radiation detectors are usually cooled down below room temperature in order to suppress thermal noise. Owing to the smaller band gap of 0.67 eV, Ge detectors have to be operated at lower temperatures.

In the case of an X-ray induced transition, the excitation of electrons is caused by secondary interaction processes, predominantly electron-electron collisions. In the course of X-ray absorption by photoelectric effect within the semiconductor, the photon transfers its complete energy to a single electron. The remaining kinetic energy of the liberated electron as well as the emitted fluorescence energy are then available for the excitation of other electrons. In general, a small part of the deposited energy is converted into lattice vibrations (phonons) and does not contribute to the measurable charge signal. Whenever an electron reaches the conduction band, it leaves a mobile hole with a single positive charge. The average energy w required to generate one electron-hole pair (exciton) in Si at room temperature is 3.65 eV and in the X-ray regime of interest approximately independent of the primary X-ray energy. As a consequence of the enhanced band gap, the electron-hole pair creation energy in Si also increases slightly towards low temperatures – $w = 3.73\,\mathrm{eV}$ was calculated for 5.9 keV X-rays at $T = 10\,\mathrm{K}$ [18]. Under normal conditions, CuK_α radiation with an energy of 8041 eV, absorbed by a Si layer, generates about 2200 electron-hole pairs within the detector volume. In order to avoid recombination of electrons and holes, the charges need to be separated from each other by means of an externally applied electric field. Favored by the high mobilities of electrons

in Si ($\mu_n > 3000\,\mathrm{cm}^2/\mathrm{Vs}$ for electrons in high-purity Si at $T < 200\,\mathrm{K}$ [19]), charge collection times in the order of 10 ns can be achieved for typical detector geometries and electric field strengths in the range of 1 kV/cm.

2.1.3 pn-junction

The success of a fast charge separation is of great importance for energy-dispersive X-ray spectroscopy using semiconductor radiation detectors. In a second step, the generated charges are collected at a well-defined position within the detector, where they give rise to a measurable voltage signal. Regarding the unique correlation between the number of deposited charges and the height of the amplified signal, the energy of the detected photon can be deduced. The easiest realization of an energy-dispersive X-ray detector is a pn-junction operated as a reverse-biased diode.

The conducting properties of a semiconductor can be controlled by the systematic insertion of defects, also referred to as doping. Si and Ge, which belong to the carbon group, are crystalline materials consisting of tetravalent atoms. If such crystals are doped with pentavalent elements of the nitrogen group (n-doping with donors, e.g. P, As), they form tetravalent bonds with Si or Ge atoms. The emerging surplus electrons are only weakly bound at an energy level of about 0.05 eV below the conduction band edge. These electrons can easily reach the conduction band by thermal excitation and become available for charge transport. Consequently, the crystal is called n-type. In contrast, the assembly of trivalent elements, which belong to the boron group (p-doping with acceptors, e.g. B, In), gives rise to incomplete Si bonds. In such cases, the defect atoms accept electrons from other Si atoms in order to complete the bonds. The energetic location of the remaining positively charged holes is about 0.05 eV above the valence band edge. Hence, the thermal excitation of these holes results in the release of freely mobile charge carriers in the valence band. The crystal, which is then able to drive a hole current, is called p-type.

The spatial contact of an n-type semiconductor and a p-type semiconductor creates a pn-junction. As a consequence of the concentration gradients of mobile charge carriers, electrons diffuse from the n-type region to the p-type region and holes from the p-type region to the n-type region. Within the barrier layer between the two semiconductors, the electrons and holes recombine and leave a characteristic zone which is depleted of free charge carriers. This depletion layer contains a positive space charge in the n-type region and a negative space charge in the p-type region. The evoked electric field between the two regions counteracts the diffusion current leading to an equilibrium state. The potential gradient V_{bi} ("built-in voltage") across the depletion layer at thermal equilibrium is given by [20]

$$V_{bi} = \frac{kT}{e} \ln \frac{N_\mathrm{A} N_\mathrm{D}}{n_i^2} \tag{2.10}$$

(N_A: concentration of acceptors in the p-type region, N_D: concentration of donors in the n-type region, n_i: intrinsic charge carrier concentration in Si, e: elementary charge).

The pn-junction shows the properties of a rectifier diode. An externally applied voltage V with the same polarity as V_{bi} widens the space-charge region. In this case, as no marked current flow can occur across the pn-junction, the diode is reverse-biased (figure 2.2).

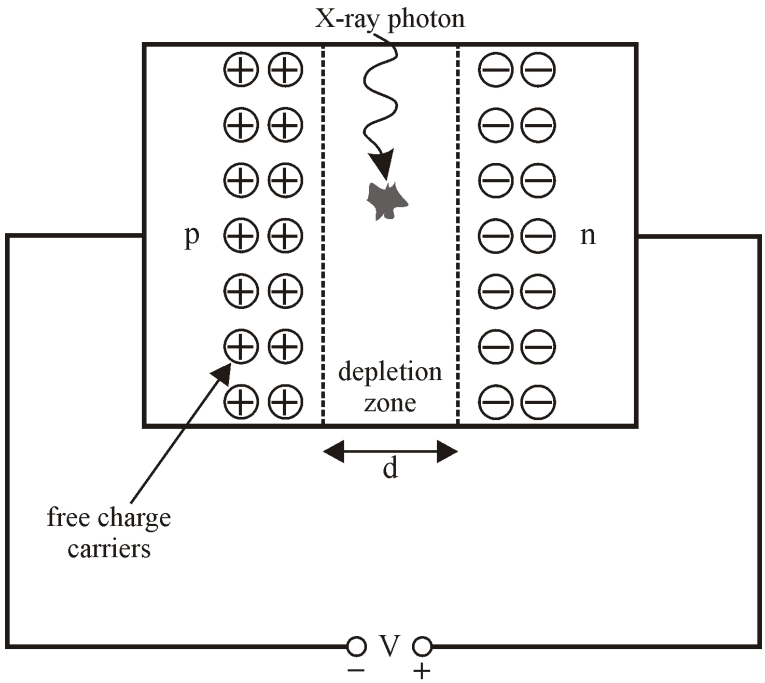

Figure 2.2: pn-junction with reverse-biasing. The electric fields associated with the built-in voltage V_{bi} and the externally applied voltage V are directed from the n-type region to the p-type region. The depletion zone serves as the sensitive volume of a semiconductor radiation detector. In this area, incident X-ray photons deposit signal charges whose numbers are proportional to the X-ray energy.

In semiconductor radiation detectors, the depletion layer serves as the sensitive volume for incident X-rays. With V_{bi} and V assumed to be positive, the width of the depletion layer can be controlled by the external voltage V according to [20]

$$d = \sqrt{\frac{2\varepsilon\varepsilon_0}{e}\,\frac{N_\mathrm{A}+N_\mathrm{D}}{N_\mathrm{A}N_\mathrm{D}}\,(V_{bi}+V)}\ , \tag{2.11}$$

where ε is the dielectric constant of Si and ε_0 the vacuum permittivity. If the external voltage is applied contrary to V_{bi} by reversing the polarity of V, the electric field within the depletion layer drops and a current flow across the pn-junction becomes possible. In this case, the diode is forward-biased.
Normally, energy-dispersive point detectors used for X-ray diffraction experiments in the white-beam mode (e.g. the Roentec X-Flash) are realized as diodes with reverse-biasing. Moreover, the pn-junction is the basic component of a pnCCD and its amplifying on-chip electronics formed by special arrangements of field effect transistors (FET).

2.2 pnCCD and frame store pnCCD

The pnCCD and the frame store pnCCD are special types of semiconductor radiation detectors for photon spectroscopy in an energy range reaching from the optical regime to the X-ray regime. They are characterized by high sensitivity, good radiation hardness, and low noise levels ensuring a multidimensional detection of single photons with high resolution.

2.2.1 Sideward depletion

The functionality of pnCCDs as well as of Si drift detectors (SDD) and active pixel sensors (APS), recently realized as depleted field effect transistors (DEPFET) [21], is based on the concept of sideward depletion proposed by Gatti and Rehak in 1983. The standard geometry consists of a weakly n-doped Si wafer (n^-) with a highly p-doped front and back side (p^+) (figure 2.3(a)-(c)). A small highly n-doped implantation (n^+) creates an ohmic contact to the Si bulk and serves as a readout node for the generated charge.

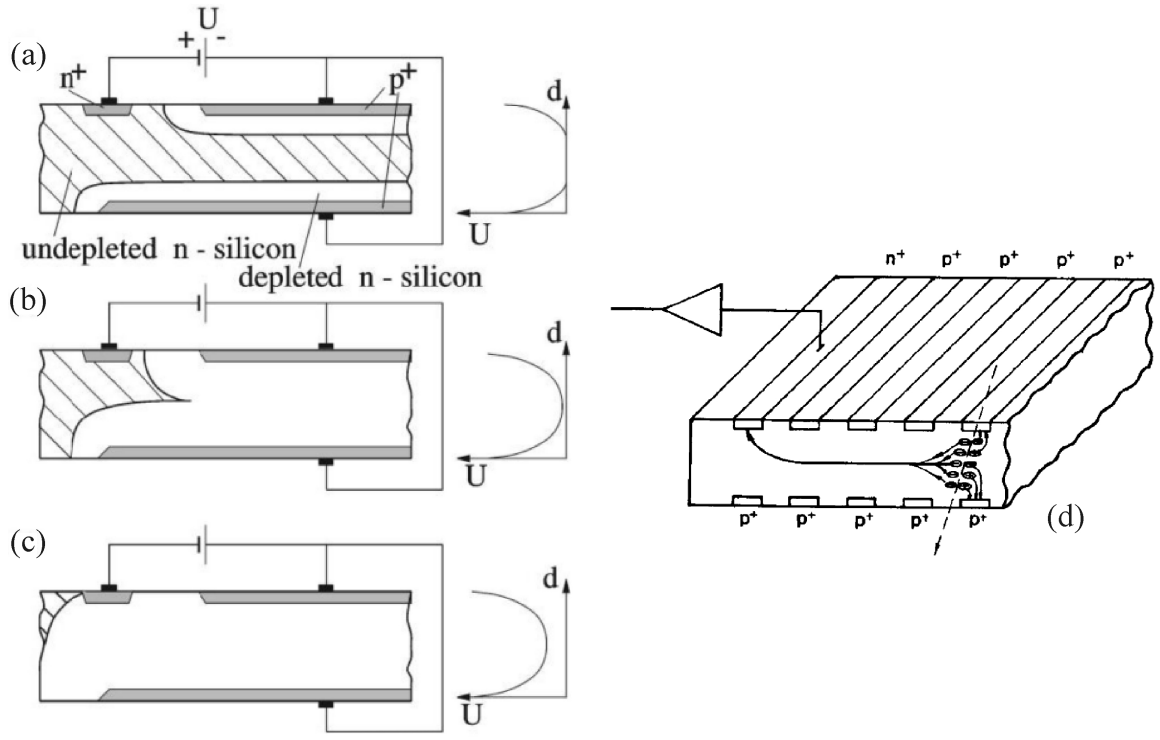

Figure 2.3: Principle of sideward depletion according to Gatti and Rehak [22]. The graphs show the qualitative shape of the storage potential for electrons depending on the depth in the Si bulk. (a) In the case of no applied reverse voltage, only the intrinsic depletion zones of two opposing pn-junctions have developed. (b) For enhanced reverse voltage, the depleted region within the bulk is extended starting from the pn-junctions on the wafer surfaces. (c) As a result of a sufficiently high reverse voltage, the region around the anode is also depleted (denoted as overdepletion). (d) Schematic view on a fully sideward depleted SDD [23].

The depletion of the Si bulk is achieved by means of an external reverse voltage keeping the p^+ implantations on the same negative electric potential and the n^+ contact on a higher potential. In this configuration, the system can approximately be considered as a composition of two opposing pn-junctions with reverse-biasing. Taking into account the high acceptor concentration within the p^+ implantations and the low donor concentration within the Si bulk, the vertical extension z of the depleted regions can be estimated by

$$z = \sqrt{\frac{2\varepsilon\varepsilon_0(V_{bi} + V)}{eN_\mathrm{D}}} \tag{2.12}$$

resulting from (2.11) in the limit $N_\mathrm{D} \ll N_\mathrm{A}$. Here, V is the externally induced potential drop across the pn-junctions. With increasing reverse voltage, the depletion regions propagating from the p^+ implantations are enlarged, thereby touching each other at a specific voltage. As only half of the device thickness has to be depleted from both sides, this voltage is about four times lower than the voltage required to completely deplete a diode of the same thickness. At a sufficiently high potential applied to the n^+ contact, the wafer is fully depleted. The configuration, in which the area around the n^+ contact has also been depleted, is denoted as overdepletion. For a pnp-structure of the above-described type, the electrostatic potential within the Si wafer shows a parabolic shape with a minimum for electrons in the middle of the wafer and maxima at the wafer surfaces. Under these conditions, X-ray generated electrons and holes can automatically be separated from each other. In this case, the electrons are stored in the middle of the wafer, whereas the holes disappear in their potential minimum within the p^+ implants. Applying different voltages to the p^+ implants shifts the potential minimum for electrons towards the surface with the higher potential.
In order to finally obtain a measurable voltage signal, the charges need to be transferred to the readout node. A simple possibility to achieve the charge transport is realized in an SDD (figure 2.3(d)): The unstructured p^+ implants on the wafer surface are replaced by a parallel p^+ strip pattern which enables the electric potential within the Si wafer to be superimposed by an appropriate horizontal drift field. This drift field is created by means of a voltage gradient applied to the p^+ strips in such a way that the n^+ contact has the highest potential, whereby the electrons can be moved continuously out of the detector volume towards the readout node. High-performance SDDs, optimized for energy resolution, are equipped with very small n^+ contacts to ensure a low anode capacitance which reduces the noise level of the detector. For such systems, typical voltage drops of about $3\,\mu$V per electron can be measured [24]. SDDs also allow a position determination of incident photons. For that purpose, the n^+ implantation is subdivided into many readout anodes. If the time of the X-ray interaction is known, the two-dimensional position of the recorded event can be deduced from a precise drift time measurement. The pnCCD principle is closely related to the SDD and represents an advancement of the described detector scheme. However, the charge transport mechanism in CCDs is fundamentally different. In contrast to SDDs, the electrons are drifted discretely to the readout node, i.e. in well-defined and externally clocked time intervals.

2.2.2 Charge collection in a pnCCD

The conceptual development of the pnCCD as a novel detector system for simultaneous position-, energy-, and time-resolved measurements in X-ray astronomy started in 1985. First reasonably working pnCCD devices equipped with an appropriate amplification and readout electronics could be provided in 1993 and were optimized for the satellite missions ABRIXAS and XMM-Newton [25, 26].
The principle of a pnCCD with back side illumination is shown schematically in figure 2.4. The sensitive volume consists of a double-sided polished Si substrate of high purity which is weakly n-doped with phosphorus of a concentration below $10^{12}/\mathrm{cm}^3$. A thin n-doped epitaxial layer with a donor concentration of $10^{14}/\mathrm{cm}^3$ creates an ohmic contact to the non-depleted high-resistivity Si bulk of 450 μm thickness. Within this layer, the potential minimum for electrons can be fixed in a depth of about 7 μm below the wafer surface. The desired pnp-structure is completed by means of p^+ boron implants with a typical doping concentration of $10^{18}/\mathrm{cm}^3$ at both wafer surfaces. The p^+ implants are realized as a homogeneous unstructured layer at the back side and as a parallel strip pattern at the front side of the wafer. The additional n^+ contact at the front side serves as the readout node and is kept at the highest electric potential.

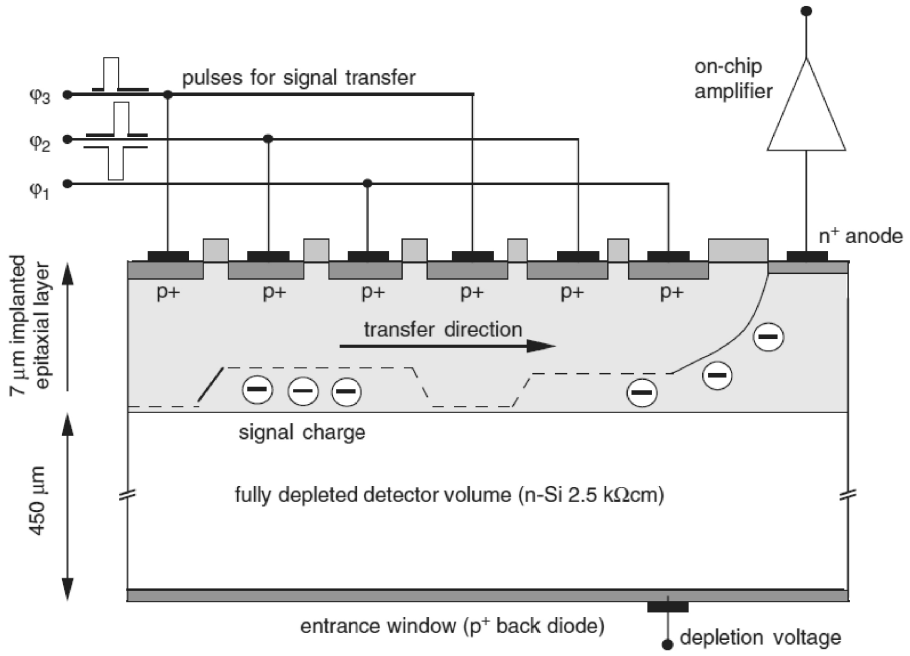

Figure 2.4: Cut through a fully sideward depleted pnCCD along one transfer channel [27]. X-rays enter the detector unit from the back side and create electron-hole pairs within the Si bulk. The electrons drift to the front side, which has a pixel structure, whereas the holes disappear in the p^+ implant at the back side. After being stored in potential minima and transferred to the readout anode, the electrons give rise to a measurable voltage signal.

The application of a negative voltage to the p^+ implants with respect to the n^+ contact enables a full sideward depletion of the Si bulk. If the depletion voltage at the wafer back side is further decreased, the potential minimum for electrons shifts from the center of the bulk towards the front side. In the X-ray spectroscopy mode, pnCCD systems are usually operated with a back contact voltage between $-200\,\mathrm{V}$ and $-250\,\mathrm{V}$. The p^+ strips at the front side form a characteristic register structure which allows a partition of the Si bulk into single image cells (pixels) in the storage depth of the electrons. For that purpose, one pixel is spatially defined by three adjacent registers under which the signal charge can be stored, optionally below one or two registers. Between the p^+ strips at the front side, the detector surface is covered by MOS (metal oxide semiconductor) structures [28] composed of a conducting Al layer and an insulating SiO_2 layer on top of an n-doped Si substrate. The MOS structure protects the detector material from humidity and chemical reactions with surrounding gases and is used to control the electric potential at the front side of the wafer. Moreover, crystal defects, which consist in free Si bonds induced by mechanical fabrications of the detector unit (cutting, polishing) at the wafer surface, can be saturated to a large extent.
Under the described conditions, the parallel arrangement of the register structure ensures that the potential shape in transfer direction is periodic with a repetition length given by the pixel size. After charge collection in the pixel structure for an externally fixed time interval, the electrons are shifted to the readout node along well-defined transfer channels perpendicular to the p^+ strips using a three-phase voltage sequence (figure 2.5(a)). The transfer channels consist of n-doped implants guiding the electrons to the terminating anodes (channel guides). In order to avoid a lateral drift of the charges, the channel guides are spatially separated from each other by additional p-doped implants (channel stops) (figure 2.5(b)). The negative space charges within these channel stops create a repulsive potential for the electrons. Thus, a confinement of the electrons in a lateral potential minimum within the channel guides can be achieved.

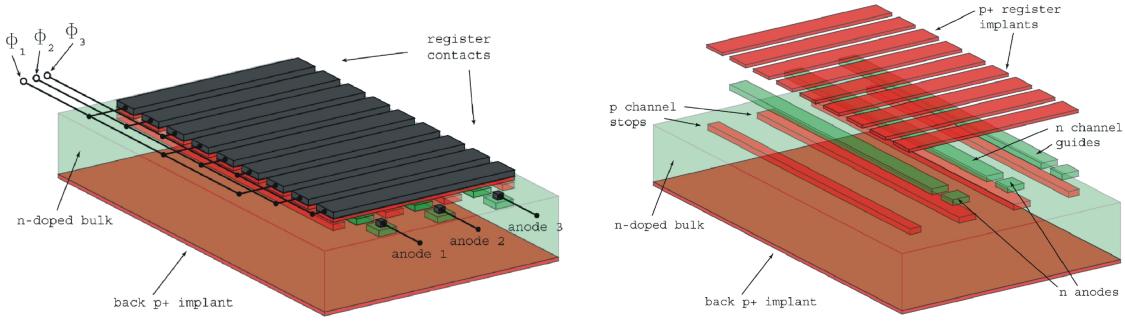

(a) (b)

Figure 2.5: Register and channel structure for signal-charge storage and transfer at the front side of a pnCCD [29]. (a) The transfer direction of the electrons is perpendicular to the p^+ implants. Each transfer channel is terminated by its own readout anode. (b) The channel structure in the transfer depth consists of n-doped channel guides and p-doped channel stops serving as potential barriers between different channels.

2.2.3 Frame store pnCCD

The pixel structure of a pnCCD combined with the charge-sensitive readout of generated electrons enables a simultaneous position and energy resolution of incident X-rays that were recorded during the exposure time of the detector. However, as a consequence of the charge transfer to the readout node, the position information in transfer direction cannot be maintained if an X-ray photon undergoes an interaction during the readout time to create an "out-of-time event". The readout of a single pnCCD line is typically performed within 28.8 μs resulting in an overall readout time of several milliseconds for a complete pnCCD frame. Accordingly, the spectroscopic performance of pnCCD devices is limited in the case of X-ray diffraction experiments in which the detector volume is continuously illuminated with X-rays. In order to substantially suppress out-of-time events, a novel pnCCD-based detector type was proposed in 2002 for the satellite mission ROSITA [30]. This system is denoted as frame store pnCCD and realizes the described charge collection and transport scheme in a two-step process. The total detector volume of a frame store pnCCD consists of an image area and an adjacent frame store area with the same number of pixels (figure 2.6).

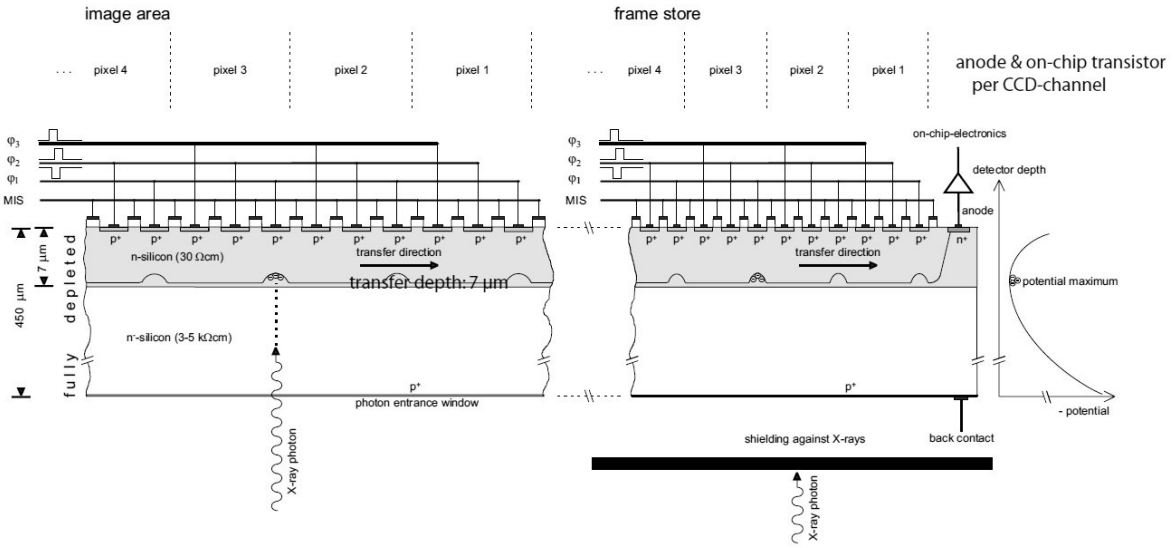

Figure 2.6: Functional principle of a frame store pnCCD [31]. The detector unit is subdivided into an image area, in which X-rays are accumulated, and a shielded frame store area with the same number of pixels.

The image area is sensitive to incident X-rays and corresponds to the pnCCD scheme depicted in figure 2.4 except for the fact that the readout anode is placed at the end of the frame store area. After the exposure time, the charge content collected within the image area is quickly transferred to the frame store area and read out subsequently. The extension of the detector unit by the frame store area offers the advantage that out-of-time events are excluded during the readout of the accumulated image. For that purpose, the frame store area needs to be shielded against X-rays by means of a rigid metallic plate. In this so-called frame store mode,

favored by the relatively short transfer time compared to the readout time, the probability of measuring out-of-time events is significantly reduced. The second advantage of the frame store pnCCD consists in the mutual independence of X-ray detection and signal readout: Whenever an accumulated image is read out in the frame store area, newly entering photons can be recorded in the image area. In that respect, the frame store pnCCD represents a permanently sensitive X-ray detector with the only constraint that out-of-time events are assigned with incorrect position coordinates in transfer direction. Alternatively, if the frame store area is not shielded, the system can also be operated in the so-called full frame mode. Although this mode provides a larger sensitive area, it is inconvenient for experiments with synchrotron radiation due to the unpractically long readout time being twice as long as in the case of frame store operation. The performance of the first routinely working and optimized frame store pnCCD systems is described in [32].
In order to reduce the chip dimensions, the pixels of the frame store area are usually downsized in transfer direction relative to the pixels of the image area. Therefore, the frame store pnCCD modules used in this work comprise quadratic pixels of $75\times75\,\mu\mathrm{m}^2$ size in the image area and rectangular pixels of $75\times51\,\mu\mathrm{m}^2$ size in the frame store area.

2.2.4 Charge transfer in a frame store pnCCD

The transfer of signal electrons from the image area to the frame store area and subsequently to the readout node is based on a three-phase clocking scheme of voltage pulses applied to the p^+ registers [24]. Initially, every third electrode has the same potential during the exposure time of the pnCCD. In this case, the register, below which the electrons are stored, must be supplied with a higher voltage relative to the other two registers of the same pixel. The discrete charge shift along the transfer channel is achieved by moving the generated potential well periodically from pixel to pixel (figure 2.7, upper part): In a first step, applying the same voltage (φ_2) to the neighboring register in transfer direction as to the storage register (φ_1) forces the electrons to distribute evenly over a larger potential well. Then, if φ_1 is set to the initially lower value of φ_2, the horizontal width of the potential well can be reduced to its original size used for charge collection. In the next step, the pixel content is shifted below the register with the voltage level φ_3 by means of the same procedure. In this way, the electrons are transferred by one pixel unit within six successive switching steps. The temporal length of the applied voltage pulses usually amounts to 300 ns with a mutual phase shift of 100 ns between the voltages of two adjacent registers. Under these conditions, the charge transfer across one pixel is performed within 600 ns which yields a total transfer time of $153.6\,\mu$s from the image area to the frame store area, presuming a pnCCD module with 256×256 pixels in both areas. The speed of the pixelwise charge transport from the frame store area to the readout node is limited by the readout time of a single pixel and can therefore not fall below $28.8\,\mu$s. Typical amplitudes of the applied voltage pulses, with an offset of 3 V...7 V between the highest and the lowest level, are in the range of -20 V...-15 V relative to the substrate contact and the MOS structure being kept at a potential of 0 V.

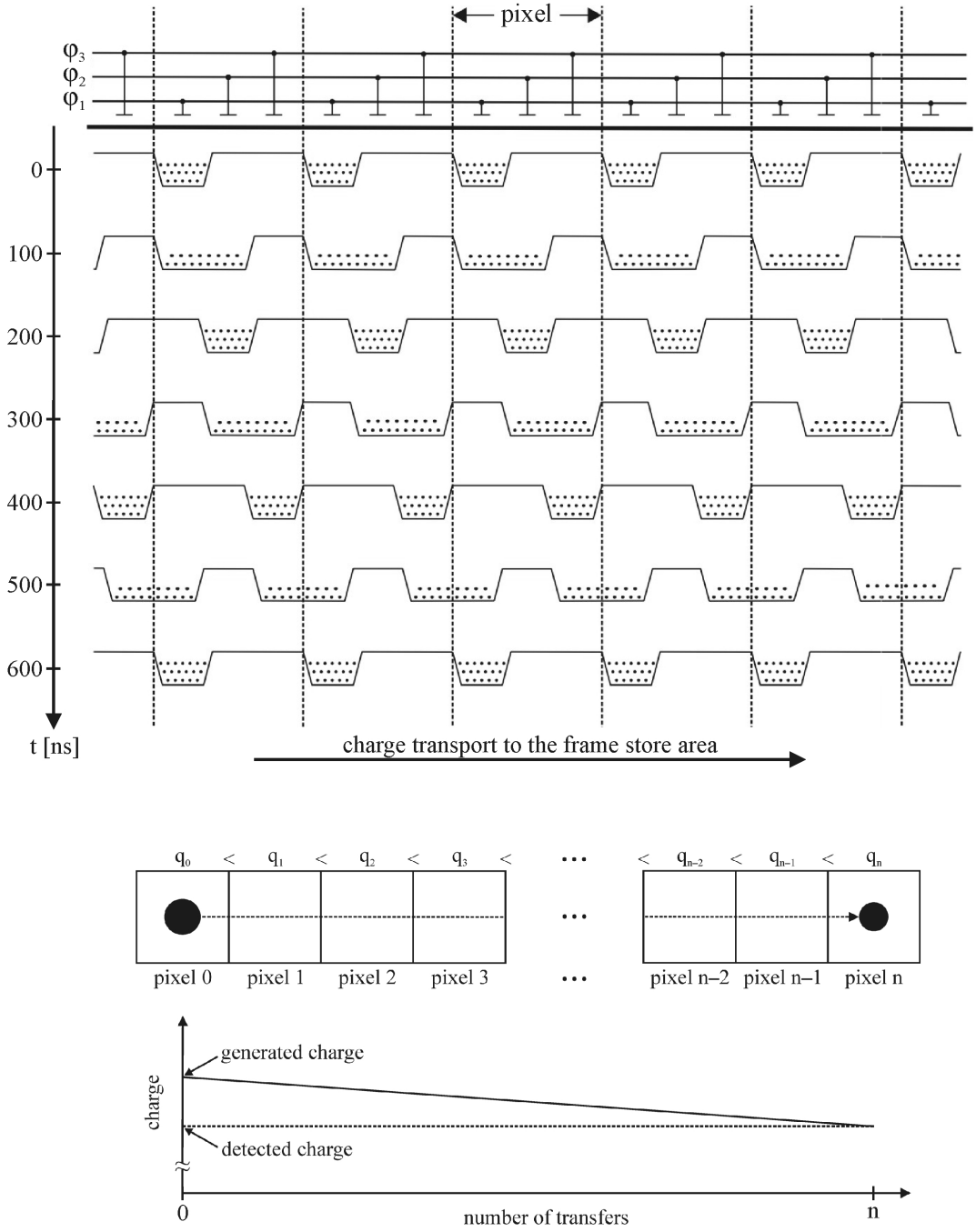

Figure 2.7: Upper part: Three-phase voltage sequence used to transport signal electrons from the image area to the frame store area. The charge transfer is performed within spatially and temporally varying potential wells. In the case of charge storage below one register, the electrons can be transferred by one pixel unit within 600 ns. In an alternative operation mode of the pnCCD, the charge is collected below two registers. Lower part: Charge loss within the pnCCD during transfer to the frame store area and to the readout node. The linear decay of the signal amplitude along the transfer channel is described by the CTE model.

In general, the number of electrons contained within the moving potential well decreases after each transfer step to the readout node (figure 2.7, lower part). The successive decay of the signal amplitude is caused by unavoidable, natural and technically conditioned crystal defects in the transfer depth within the bulk. These locally existing impurities (also denoted as traps), which provide energy levels within the Si band gap, are capable of capturing electrons and releasing them at a later point of time. Consequently, the released charges will be detected in other pixels that have a larger distance from the readout node. The characteristic time constants for electron capture into an empty trap and for emission out of an occupied trap strongly depend on the electron concentration and the detector temperature, respectively [33]. In a simple model, the charge transfer loss is different for every pnCCD channel and assumed to be constant for any pixelwise transfer in the considered channel. The average fraction of electrons being shifted from one pixel to another is described by the charge transfer efficiency

$$\mathrm{CTE} = \frac{q_{i+1}}{q_i} \ , \tag{2.13}$$

where q_i and q_{i+1} are the total charges located within the potential well moved from pixel i to pixel i+1. Its complement, the charge transfer inefficiency (CTI), gives the relative number of electrons which are captured by traps and fed to subsequent pixels,

$$\mathrm{CTI} = 1 - \mathrm{CTE} \ . \tag{2.14}$$

Typical CTI values of pnCCD systems, measured by means of monochromatic X-ray exposures of the detector, are in the order of 10^{-5}. In the case of a constant charge loss for every single transfer, the remaining charge q_n after n transfers of the initial charge q_0 amounts to

$$q_n = q_0 \, \mathrm{CTE}^n = q_0 \, (1 - \mathrm{CTI})^n \ , \tag{2.15}$$

which, in the limit $\mathrm{CTI} \ll 1$, can be approximated by

$$q_n \approx q_0 \, (1 - n \cdot \mathrm{CTI}) \ . \tag{2.16}$$

In that respect, the CTE is usually calculated from the slope of the linearly decaying signal amplitude in transfer direction, i.e. along the pnCCD rows [34].

2.2.5 Signal amplification and readout

For each pixel, the voltage signal generated by the electrons arriving at the anode is amplified in two steps before a parallel readout of the pnCCD channels takes place. In order to achieve the best possible energy resolution based on a low noise level, the first amplifier stage needs to be monolithically integrated on the pnCCD chip itself [35]. For that purpose, an n-channel junction field effect transistor (JFET), denoted as first FET, with its gate connected to the readout anode, is used (figure 2.8). The voltage induced at the gate of the first FET regulates the current between source and drain via a partial constriction of the n-channel, depending

on the potential difference between gate and drain. The resulting voltage drop at the source represents the electronic signal of the deposited charge within the pixel. Under the described conditions, the first FET is operated in source follower mode. An additional current source supplies the n-channel of the first FET with a constant current driven by the voltage applied to the first FET drain. Prior to the amplification of the charge signal contained in the subsequent pixel, the potential of the anode needs to get back to its original working point. In the first pnCCD systems, this reset was controlled by an additional JFET, denoted as reset FET, whose source is connected to the readout anode. However, it could be observed that the time constant of the obtained voltage decay was not low enough to ensure a full reset of the anode potential. Particularly for high count rates, at which many electrons are shifted to the anode, this incomplete reset led to charge avalanches at the first FET gate, constricting the transistor channel entirely and short-curcuiting the supply voltages of the first FET ("latch-up"). In modern realizations of the on-chip curcuit, currently used in eROSITA pnCCD systems, the complete reset to the working point is achieved by an n-channel MOSFET integrated instead of an n-channel JFET [36]. Hence, a sufficiently fast change of the reset FET gate potential (denoted as RFGA in figure 2.8) to a more positive value prevents the channel of the first FET from being entirely constricted, i.e. it remains conductive.

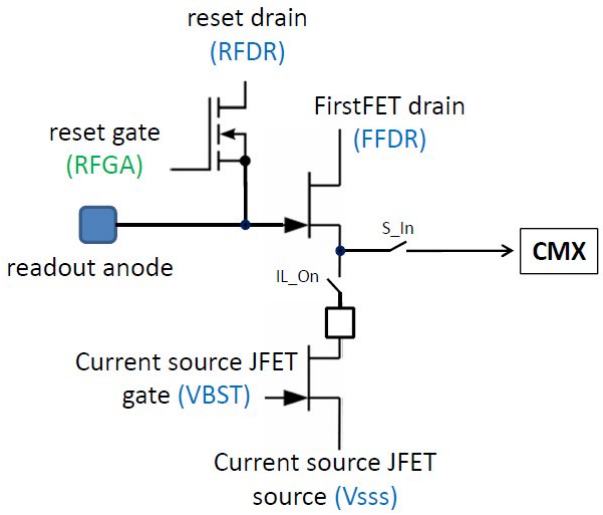

Figure 2.8: On-chip amplification curcuit of a pnCCD channel [37]. The charge signal collected at the readout anode is amplified by means of an on-chip transistor (first FET) and fed into the CAMEX for further processing. The reset FET serves to clear the anode charge before the electrons of the subsequent pixel arrive at the anode.

The second processing step of the voltage signal is performed within the charge-sensitive amplifier chip CAMEX (CMOS amplifier and multiplexer) which is connected to the first FET source by means of a wire bond. One CAMEX chip with a dimensioning of $6.3 \times 9.4\,\mathrm{mm}^2$ comprises 128 channels providing different sequential processing stages for the parallel readout of 128 pnCCD columns [38]. Figure 2.9 shows the structure of a single CAMEX channel.

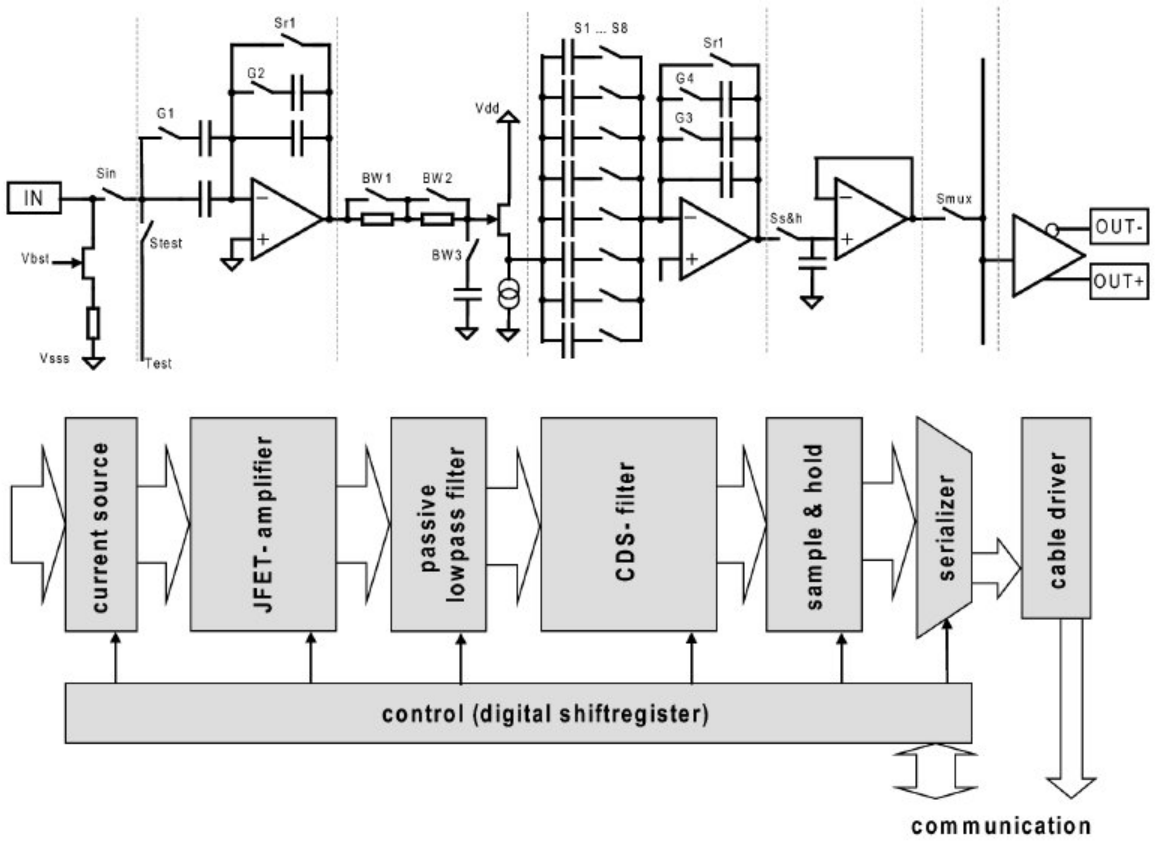

Figure 2.9: Schematic of a single CAMEX channel [31]. The voltage signal at the input is amplified by a second JFET, averaged within the CDS filter, and, after being stored on a sample & hold stage, multiplexed to either one or more output nodes. The serialized signals are finally digitized by an external ADC for data acquisition.

The input stage of the CAMEX channel consists of the connection to the first FET source and the JFET current source. In general, the maximum detectable X-ray energy per pixel can be selected externally by controlling two voltage amplifier stages. In this case, the absolute analog signal pulse height depends on the effective amplifier capacities defined by the configuration of different switches (denoted as G1,...,G4). The CDS-filter allows a low-noise determination of the detected charge based on the concept of multi-correlated double sampling (MCDS) [39]. At this stage, the voltage signal of the baseline, measured before the charges reach the anode (baseline sampling), is subtracted from the voltage signal obtained after amplification (signal sampling). The so-extracted difference signal is then proportional to the number of electrons arriving at the readout node. In total, the CDS-filter consists of eight capacitors that can be connected via the switches S1,...,S8 which enable MCDS to be at most 8-fold. Previous studies have shown that on the one hand, the readout structure creates the lowest possible noise in the case of 8-fold CDS. On the other hand, a smaller sampling number reduces the overall processing time of the CAMEX and can be suitable for high-speed applications [27].

In the subsequent steps, the analog difference signal is stored on a sample & hold stage and multiplexed to optionally one or more output nodes. As soon as the sample & hold capacitor is charged, the readout of the following pixel begins with a reset of the first amplifier. Finally, the processed signals are serialized and digitized for data acquisition on a PC by means of an analog-to-digital converter (ADC).

2.2.6 Technical realization

In 2007, PNSensor GmbH provided the University of Siegen with a fully functional frame store pnCCD system used for experiments with white synchrotron radiation. Figure 2.10(a) depicts the geometrical layout of the associated detector module comprising 256 columns and 512 rows, 256 of which belong to the image area and to the frame store area, respectively. With a quadratic pixel size of $75 \times 75\,\mu m^2$ in the image area, the sensitive region for incident X-rays covers an area of $19.2 \times 19.2\,mm^2$ in frame store mode. The accumulated images are read out by two CAMEX chips with 128 channels each.

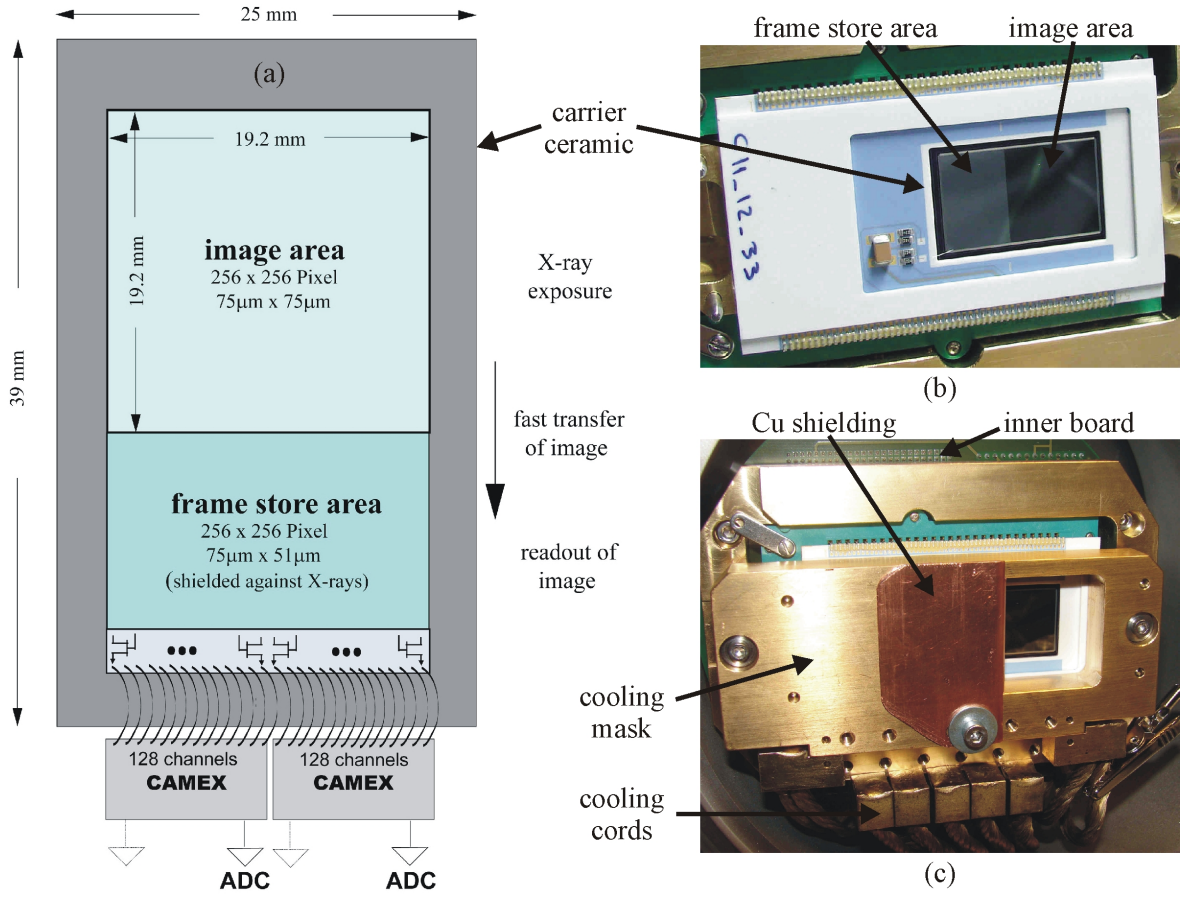

Figure 2.10: (a) Layout of a frame store pnCCD detector module with 256×512 pixels [40]. (b) pnCCD detector unit mounted on a carrier ceramic. (c) Rigid Cu plate on top of the cooling mask shielding the frame store area against incident X-rays.

In order to apply the required operation voltages to the pnCCD and the CAMEX, the detector unit itself is mounted on a ceramic substrate (figure 2.10(b)) equipped with the necessary electric contacts to the inner board. A cooling mask upon the detector module creates a connection to the external cooling system via cooling cords (figure 2.10(c)). The shielding of the frame store area against X-rays is achieved by means of a massive Cu plate placed on top of the cooling mask. Moreover, the voltage measured at an additional on-chip diode (not visible) serves as a permanent control of the detector temperature. The installation of the eROSITA pnCCD modules used since 2010 is technically identical to the mechanical conditions shown in figure 2.10(c). With regard to signal processing, the 128×128 pixel module is read out by one single CAMEX chip and the 384×384 pixel module by three CAMEX chips.

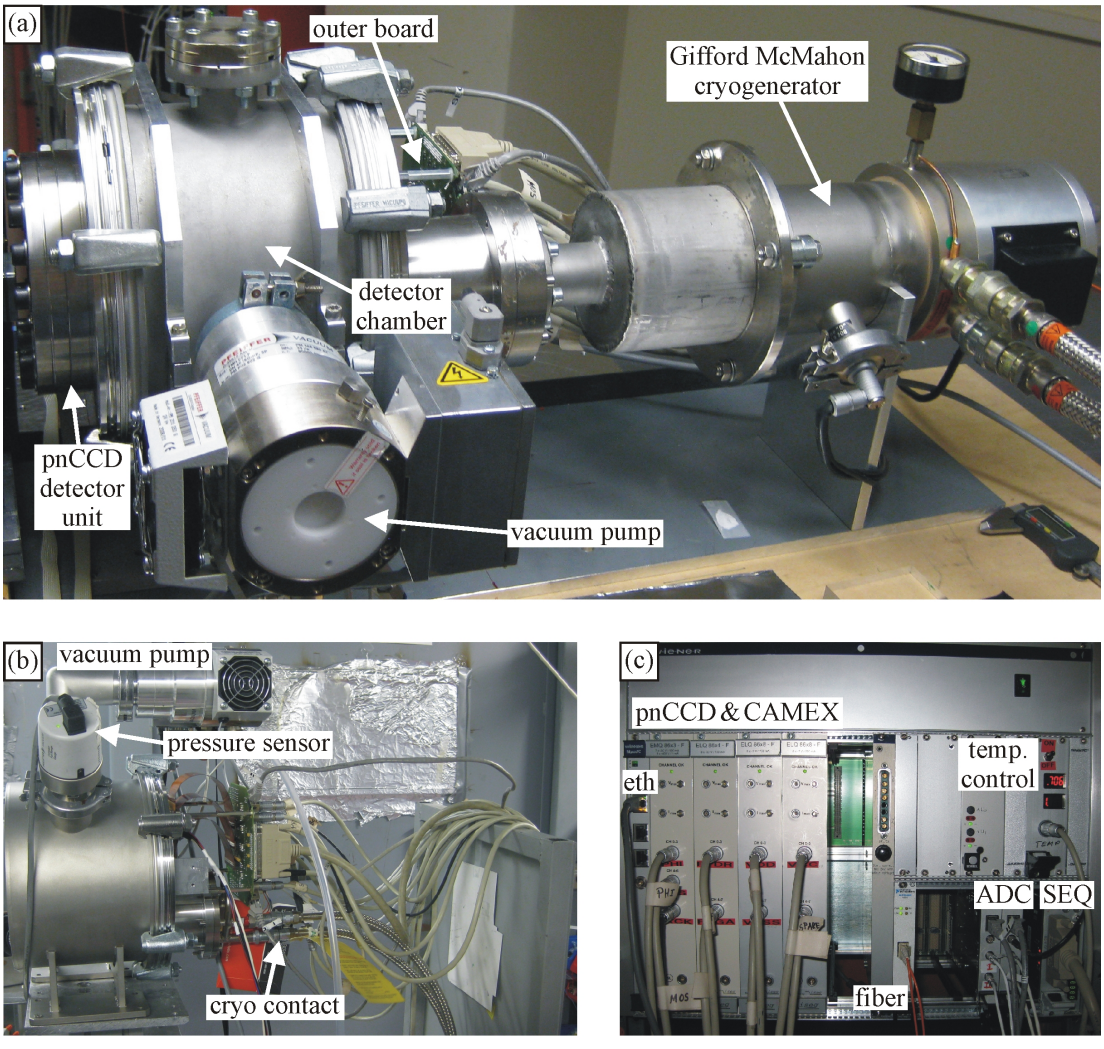

Figure 2.11: Technical realization of the pnCCD systems: Chamber housings with vacuum and cooling units (a) for the first system (256×256 pixels) and the eROSITA test module (128×128 pixels) and (b) for the new eROSITA detector (384×384 pixels). (c) Voltage supply and control units for the various detector components.

Good experimental conditions for a pnCCD operation with high performance based on a low thermal noise level require a cooling of the pnCCD module. For that purpose, the detector unit with shielded frame store area, including the inner board and the cooling units depicted in figure 2.10(c), is installed within a vacuum-sealed aluminum chamber (figure 2.11(a)). The housing window consists of a Kapton foil which creates a stable barrier between the air side and the vacuum side. Usually, the Kapton window needs to be coated with thin layers of aluminum or graphite to ensure light-tightness avoiding unwanted optical background signals during X-ray detection. In order to prevent freezing of the detector surface, the surrounding atmosphere is evacuated to a pressure below 10^{-6} mbar by means of a vacuum pump attached to the chamber. Additionally, a pressure sensor serves to permanently control the pressure inside the chamber. In the first realization of the pnCCD system, a liquid nitrogen (LN_2) cycle was used to cool the detector down to a temperature between $-60\,℃$ and $-100\,℃$ [41]. However, stable thermal conditions could not be achieved this way which is why cryogenerators, based on He cycles, were used for cooling in the following applications instead of LN_2. Recently, the chamber housing the new eROSITA pnCCD module with 384×384 pixels was technically optimized and reduced in size to a more compact form (figure 2.11(b)).
The operation voltages of the pnCCD and the CAMEX are applied via the outer board which is electrically connected to the inner board by means of flex leads. A WIENER crate with integrated voltage and control units for the various detector components supplies the outer board with the necessary voltage signals (figure 2.11(c)). The status of the crate can be externally monitored by means of an ethernet connection (eth) to a Linux-based PC. The same platform is used for data acquisition via an optical fiber link with a maximum data transfer rate of about 60 MB/s. For digitization of the analog detector signals, two ADC units were provided with 16-bit resolution for the 256×256 pixel module and 14-bit resolution for the eROSITA pnCCD systems. The timing signals required for charge transfer, signal processing, and digitization are generated by the sequencer (SEQ) which synchronizes the operation of pnCCD, CAMEX, and ADC on the basis of a well-defined timing scheme.

2.3 4D X-ray detection using a frame store pnCCD

In the SPC mode, each X-ray photon interacting inside the Si bulk of a frame store pnCCD can be considered as an individual hit within a four-dimensional data volume spanned by two spatial coordinates, an energy coordinate, and a time coordinate. If a photon with measured energy E is recorded at position (y, z) at time t, the event cannot be localized exactly at this particular point (y, z, E, t), but within a small four-dimensional volume surrounding it. The real size of this volume depends on the position resolutions in the horizontal and vertical directions (δy, δz), the energy resolution (δE), and the time resolution (δt) of the detector. Consequently, a natural smearing of the point (y, z, E, t) over a volume confined by points of the form $(y \pm \delta y, z \pm \delta z, E \pm \delta E, t \pm \delta t)$ arises which is given by the pnCCD performance. This section describes the effective limits of a 4D X-ray detection using a frame store pnCCD that need to be considered in X-ray diffraction experiments with white synchrotron radiation.

2.3.1 Measurements with a stationary sample

In the case of a stationary sample, whose structure and orientation relative to the incident X-ray beam does not change, the time resolution of the pnCCD is of minor interest. The integrated diffraction signal of the sample becomes manifest in a series of recorded pnCCD frames with an externally defined length. This image sequence can then be accumulated to extract absolute numbers of photons scattered into subvolumes $\delta y \delta z \delta E$ of the reduced three-dimensional data set. The associated intensity distribution $I(y, z, E)$ enables a decomposition of the integrated signal into many two-dimensional diffraction patterns recorded at various energies (image cut). Alternatively, if each pixel itself is considered as an energy-dispersive point detector, $I(y, z, E)$ contains the energy spectra measured within many individual pixels or pixel areas (spectrum cut). The different cuts through the three-dimensional pnCCD data volume are shown in figure 2.12 by the example of a stationary silver behenate powder sample illuminated with white synchrotron radiation.

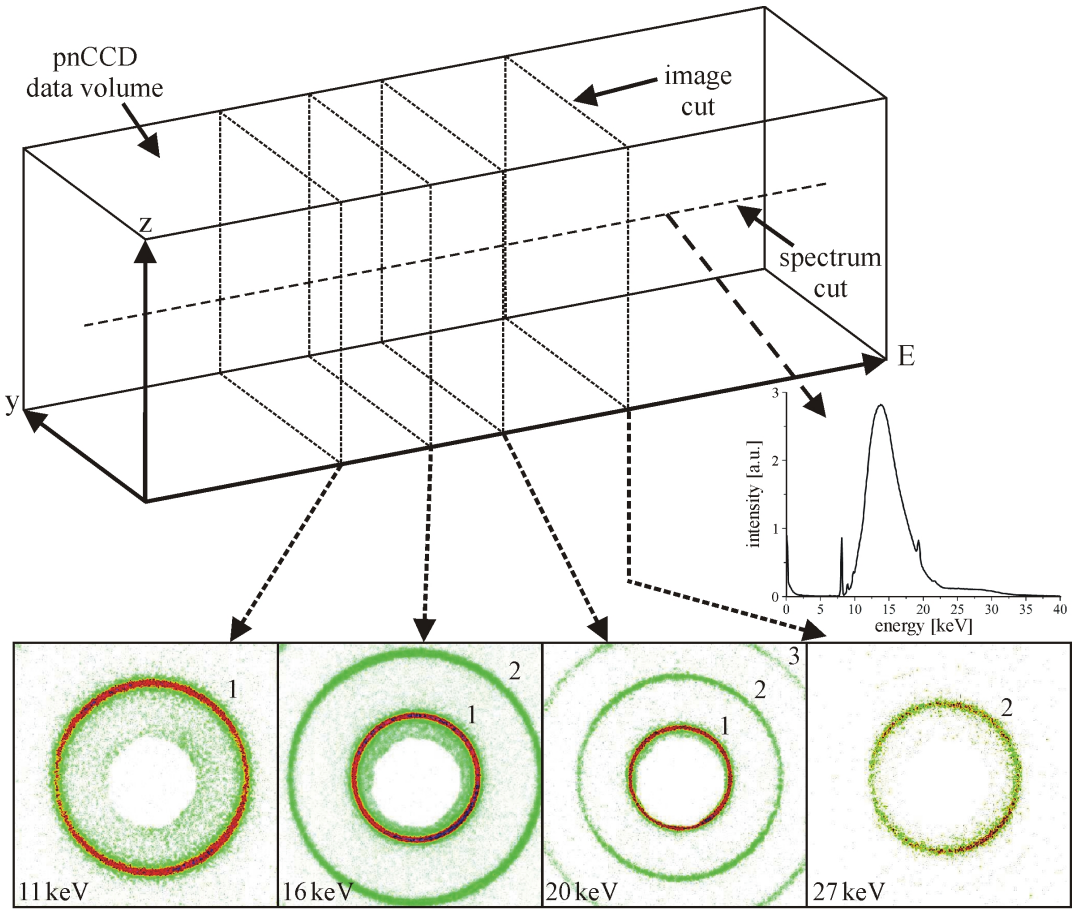

Figure 2.12: Image and spectrum cut through the three-dimensional pnCCD data volume of a silver behenate powder sample detected by the frame store pnCCD system with 256×256 pixels. The image cut delivers the diffraction rings of various energies and orders obtained in the course of a white-beam X-ray exposure of the sample.

2.3.2 Quantum efficiency

The sensitivity of a semiconductor radiation detector to incident X-rays is characterized by its quantum efficiency ε. Due to the statistical nature of X-ray absorption in matter, ε describes the probability that a photon traversing the detector system is absorbed within the sensitive area. In the X-ray regime, ε is strongly energy-dependent and limited by the finite detector thickness and the choice of the housing window. Under real experimental conditions, the path direction of an incident photon encloses an angle 2θ with the normal of the detector plane as a result of diffraction, as depicted in the framed part of figure 2.13. Hence, the photon can only produce a signal in the active layer if it is not already absorbed by the housing window.

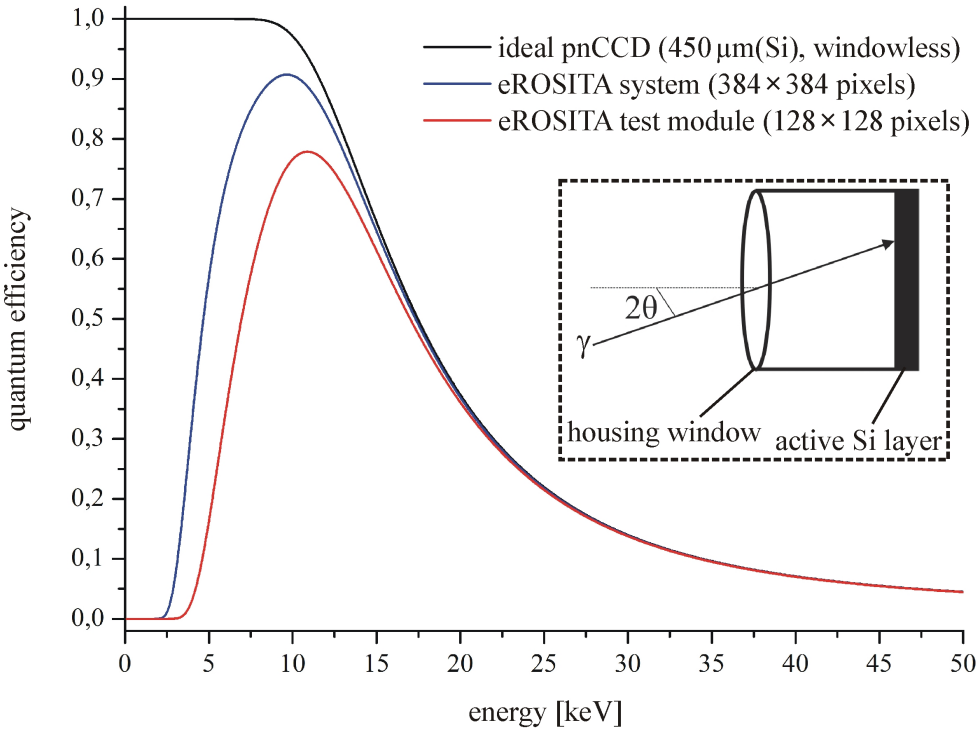

Figure 2.13: Calculated quantum efficiency of the eROSITA pnCCD systems compared to the quantum efficiency of an ideal pnCCD detector with 450 μm(Si) thickness in the case of normal incidence. The geometrical conditions for the simulation of X-rays entering the detector chamber are illustrated in the framed part.

Based on the discussions in [42], neglecting absorption in the evacuated detector environment, the quantum efficiency of the present pnCCD systems can be numerically simulated by

$$\varepsilon(E, 2\theta) = (1 - e^{-\mu_{\mathrm{Si}} d_{\mathrm{Si}}/\cos 2\theta})\, e^{-\mu_{\mathrm{w}} d_{\mathrm{w}}/\cos 2\theta} \quad . \tag{2.17}$$

Here, μ_{Si} denotes the total energy-dependent linear absorption coefficient of the Si layer shown in figure 2.1, d_{Si} its sensitive thickness, and $d_{\mathrm{Si}}/\cos 2\theta$ is the effective maximum path length of the photon within the detector module. The corresponding contribution of the housing

window (denoted with index w) is to be understood as a composition of all the materials with different absorption behavior contained in it. In a more accurate approach, dead layers resulting from metallization on the detector surface (Al, SiO_2) have to be taken into account as well [43]. However, such effects only play a role in the case of low energetic photons and are not further considered. The housing window of the chamber, which was used for the pnCCD system with 256×256 pixels and the eROSITA test module with 128×128 pixels, comprised a Kapton foil of 200 μm thickness with 10 μm graphite coating and a 20 μm(Al) foil of high purity (>99.999%). Accordingly, the exponent of the second term in (2.17) is given by

$$\mu_{\mathrm{w}} d_{\mathrm{w}} = \mu_{\mathrm{Ka}} d_{\mathrm{Ka}} + \mu_{\mathrm{Gr}} d_{\mathrm{Gr}} + \mu_{\mathrm{Al}} d_{\mathrm{Al}} \ , \tag{2.18}$$

where the contributions of Kapton and graphite are denoted with the indices Ka and Gr. The expected quantum efficiencies of the present detector systems were obtained by using the linear absorption coefficients of the housing window materials taken from [14]. The result of this calculation yielded the red curve of figure 2.13 compared to the theoretical quantum efficiency of an ideal (windowless) pnCCD with the same thickness of 450 μm assuming normal incidence ($2\theta = 0°$). In the soft X-ray regime below 8 keV, the ideal pnCCD is fully sensitive with a quantum efficiency of nearly 100%. For harder X-ray energies above 10 keV, the finite device thickness leads to an exponentially diminishing quantum efficiency curve and an effectively vanishing sensitivity above 50 keV. In contrast, the real pnCCD detector system exhibits a maximum quantum efficiency of about 78% at 11 keV. Due to the relatively thick housing window, photons with energies below 3.5 keV are already absorbed before they can reach the active layer. At hard X-ray energies above 25 keV, the quantum efficiency of the eROSITA system and the ideal pnCCD do not differ markedly, i.e. absorption effects within the housing window become negligible. In the case of the advanced eROSITA pnCCD system with 384×384 pixels, the probability of absorption by the housing window could be reduced by using a thinner Kapton foil of 125 μm thickness with 25 μm graphite coating. The simulated quantum efficiency of this system has the shape of the blue curve in figure 2.13 with the highest sensitivity above 90% between 9 keV and 10.5 keV. Taking into account imprecisions of various layer thicknesses and inhomogeneities of the housing window materials, the relative accuracy of the expected quantum efficiency values is below 2%. Alternative approaches for optimizing the routes to achieve light-tightness of the housing window are discussed in [44]. In general, but particularly for applications with white synchrotron radiation, the integrated diffraction signals of the sample have to be normalized to the energy- and angular-dependent quantum efficiency of the pnCCD in order to obtain real scattered intensities.

2.3.3 Single events and split events

Within the active layer of a pnCCD, X-rays absorbed by the detector material create charge clouds of electron-hole pairs. For typical photon energies in the X-ray regime between 5 keV and 25 keV, the generated charges are initially confined in volumes with radii below 1 μm. After separating the electrons from the holes by means of a high electric field, the charge

collection takes place in the pixel structure of the pnCCD. On the way to the potential minimum at the detector front side, the remaining electron cloud expands due to thermal diffusion and mutual electrostatic repulsion of the electrons. These effects show different dependencies on the electrons' drift time and were investigated in detail in [29]. The expanded charge distribution arriving in the pixel structure has roughly a Gaussian shape whose width is given by the number of generated charges, i.e. the X-ray energy, and the depth of the X-ray interaction within the Si bulk. Typical sizes of the collected charge clouds obtained in experiments with 17 keV X-rays are in the range of 10 μm [45]. Consequently, depending on the position of the X-ray interaction, the electrons are either stored within a single pixel (denoted as a single event) or distributed over adjacent pixels (charge splitting). In pnCCD detectors with 450 μm sensitive thickness and a pixel size of $75\times75\,\mu m^2$, a charge splitting over at most four pixels is possible. This situation occurs if the X-ray interaction takes place close to the corner of a pixel (quadruple event). In other cases of splitting, the electrons are shared between two pixels (double event) or three pixels (triple event). For concrete analyses of pnCCD data sets, split events are classified in terms of forward, backward, left, and right splittings referred to the transfer direction of the accumulated image. Figure 2.14 shows a simulated event distribution over a downsized pnCCD module with 16×16 pixels created by 16 photons of 13 keV energy.

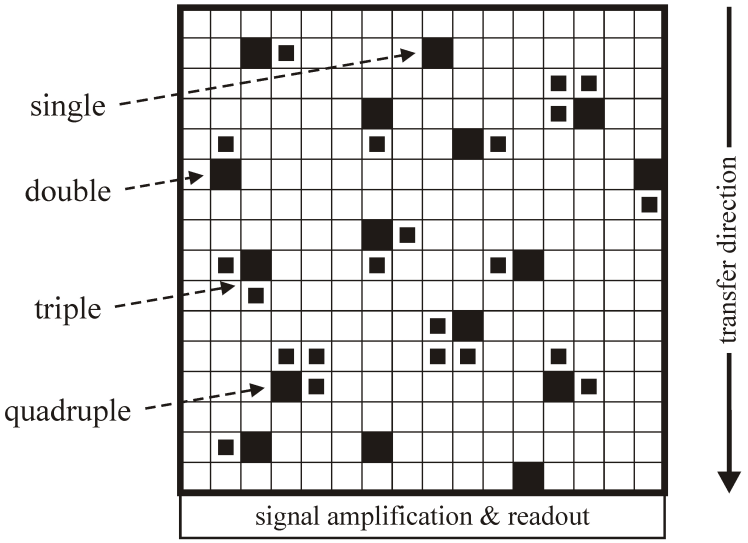

Figure 2.14: Spatial event distribution within the active pixel area of a pnCCD comprising 16×16 pixels. In the SPC mode, the pnCCD data pattern consists of single events and split events. The big squares indicate the pixels with the largest number of collected electrons.

In the case of low incident count rates avoiding multiple photon hits (pile-up events), the pnCCD data pattern is dominated by doubles accounting for about 50% of the total number of detected events. The frequencies of the remaining split events and single events exhibit

relatively strong variations with the X-ray energy [45]. The conventional treatment of pnCCD data sets relies on an appropriate event selection. To this end, besides singles and doubles, only triples showing "L"-type patterns with the largest amplitude at the corner of the event are accepted as single-photon hits. In the case of quadruples, it is necessary that the pattern shape is quadratic and that the largest and the lowest signals are measured along a diagonal of the square. With these restrictions, the number of possible event types comprises 13 patterns in total (singles and four patterns for each splitting type, respectively). All other kinds of events generated by one individual photon are of invalid type.

2.3.4 Position resolution and parallax effects

Based on the characteristic shapes of split event patterns, the spatial localization of recorded photons is possible with subpixel resolution [46]. At this stage, the fact that for quadruples, the interaction position has to be located close to the pixel corner, is exploited. Thus, the recombination of split events to individual photon hits enables a significantly more precise position determination in comparison to the pixel size. For that purpose, the photon hit is assigned with two center-of-mass coordinates of the obtained charge distribution and the sum of the collected charges providing the 2D position information and the energy information about the event, respectively. In a new approach, a unique relationship between the X-ray energy, the charge cloud radius, and the statistical occurrence of split events was used to spatially resolve triple and quadruple events with an accuracy of 2 μm [45].
The availability of subpixel resolution is effectively limited for X-ray diffraction experiments with white synchrotron radiation. In the most general situation, X-rays with different energies, e.g. diffracted by a crystal, enter the pnCCD at a well-defined incident angle referred to the normal of the detector plane resulting in parallax effects (figure 2.15).

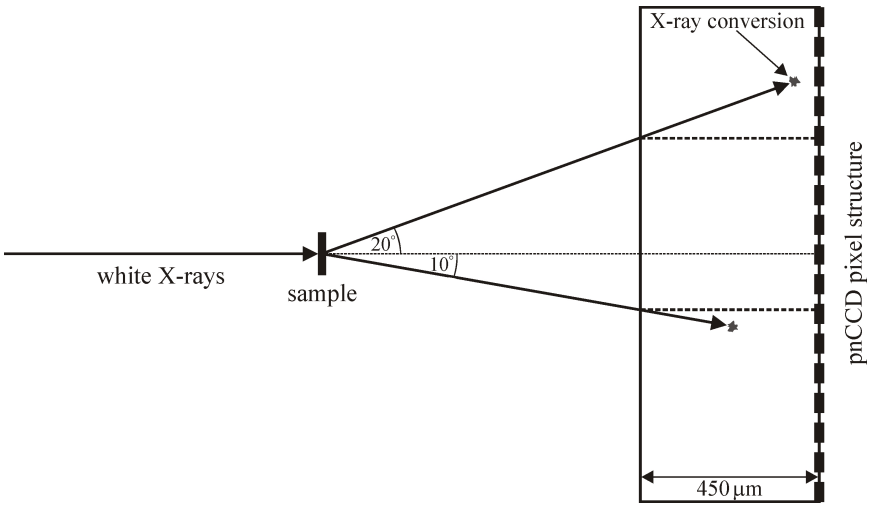

Figure 2.15: Parallax effects within the pnCCD in the case of a Laue diffraction experiment using white X-rays. The angles of the scattered X-rays' path directions relative to the detector normal lead to a spatial smearing of the detected diffraction signal.

Taking into account that X-rays are absorbed statistically along their path directions within the detector, the achievable position resolution of the measured diffraction signal is degraded. Especially for hard X-ray energies in the range of 20 keV, the electrons deposited within many absorption processes are distributed homogeneously along the X-ray track [47]. Consequently, high energetic Bragg peaks generated by a crystal are smeared over larger areas than low energetic reflections diffracted at the same angle. Typical incident angles of scattered photons within the energy-dispersive Laue diffraction experiments on HEWL crystals (chapter 4) cover a range between about 10° and 20°. Under these geometrical conditions, the expected spatial smearing of the signal in the pixel structure amounts to at most $450\,\mu\text{m} \cdot \tan 20° \approx 164\,\mu\text{m}$ corresponding roughly to two pixel widths. An extreme case, in which X-rays enter the pnCCD at an incident angle of 40°, is discussed in [47].

2.3.5 Energy resolution and noise

The energy resolution of a pnCCD is given by the standard deviation σ_E of the Gaussian distribution associated with the detected spectral peak of a monoenergetic X-ray line. Alternatively, the full width at half maximum (FWHM) of the photo peak can be used as a quality indicator of energy resolution. For semiconductor radiation detectors, the FWHM increases with the X-ray energy E according to [24]

$$\text{FWHM}(E) = 2.355w\sqrt{\frac{FE}{w} + \text{ENC}^2}\ , \tag{2.19}$$

where $F = 0.115$ is the Fano factor of Si, $w = 3.65\,\text{eV}$ the electron-hole pair creation energy, and $2\sqrt{2\ln 2} = 2.355$ the conversion factor between the standard deviation of a Gaussian and the FWHM. The equivalent noise charge (ENC) accounts for all the noise components of the detector leading to an additional broadening of the spectral peak. In particular, it includes different noise contributions of the on-chip electronics, the CAMEX, and the ADC (electronic noise) as well as thermally generated leakage current within the pixel structure (dark noise). Moreover, charge transfer losses in the storage depth of the electrons and virtual noise effects, caused by the selected event threshold, are contained in the ENC.
Low-noise X-ray detectors offer the best energy resolution with the smallest possible width of the photo peak at the considered energy. In the theoretical limit $\text{ENC} = 0$ of a noiseless detector, the standard deviation of the spectral Gaussian has the minimum value $\sigma_E = \sqrt{FEw}$. This minimum, denoted as the Fano limit, results from the statistical nature of electron-hole pair creation in Si. In general, the number $N = E/w$ of generated excitons needs to be understood as a statistical mean value of many absorption processes. Since in the course of individual X-ray interactions with the detector material small fractions of the X-ray energy are converted into lattice vibrations, the number of excitons fluctuates with the standard deviation $\sigma_N = \sigma_E/w = \sqrt{FE/w} = \sqrt{FN}$. In comparison to a Poisson distribution, which describes the statistical absorption of discrete photon numbers within a fixed time interval (chapter 2.3.8), the standard deviation is reduced by $\sqrt{F}$. If no phonons were generated within the detector volume, F would be zero. The fano factor is a material-specific property

which shows only a weak temperature dependence in the hard X-ray regime [18]. A formal justification of the Fano factor can be found in [11].
In the case of energy-dispersive X-ray detection using a pnCCD, the most accurate energy information is provided by single events as only the ENC of one indiviual pixel affects the generated charge signal. For split events, the charge integration over several pixels increases the effective noise level by approximately $\sqrt{n}$, where n is the number of pixels involved in the charge splitting [48]. In that respect, the qualification of a pnCCD system in terms of the measured energy resolution has to be exclusively referred to single events.

2.3.6 Time resolution

For pnCCD systems with frame store operation, the capability of a temporal resolution is given by the achieved cycle time. The cycle time arises from the sum of the integration time for X-rays entering the image area, the transfer time of the accumulated image to the frame store area, and the readout time of the image after the charge transfer. The effective exposure time, during which the pnCCD delivers a correct time information about X-rays, is understood as the sum of the externally defined integration time and the readout time. If the integration time is set to 0 ms, the exposure time and the readout time do not differ, i.e. a 4D resolution of X-rays entering the image area is possible during the readout time. The exposure time cannot be shorter than the readout time since the subsequent image can only be moved to the frame store area if the readout of the image is completed. Under these conditions, the time resolution of a frame store pnCCD is mainly determined by the relatively large readout time compared to the transfer time. In the standard operation mode, for which all the pnCCD rows are shifted within 153.6 μs to the frame store area and read out separately within 28.8 μs per row (full image mode), the cycle time of the pnCCD with 256×256 processed pixels amounts to $256 \cdot 28.8\,\mu\text{s} + 153.6\,\mu\text{s} \approx 7.5\,\text{ms}$. The resulting frame rate, given by the inverse of the cycle time, is about 133 Hz.
In general, the 4D detection of X-rays using a frame store pnCCD with the best possible overall resolution can be achieved in the full image mode. For particular types of events, namely out-of-time events generated during the image transfer and pile-up events discussed in chapter 2.3.7, the full 4D information about individual photons cannot be obtained. In the case of a vanishing additional integration time, the statistical probability of the occurrence of an out-of-time event can be expressed by the ratio between the transfer time and the readout time. In the above-described configuration of the 256×256 pixel module, this probability is $600\,\text{ns}/28.8\,\mu\text{s} \approx 2.1\%$. Regarding the technical realizations of the present pnCCD systems, out-of-time events cannot be experimentally separated from other events and thus give rise to an unwanted background signal within X-ray diffraction experiments.
For the eROSITA pnCCD systems, modified timing schemes were used providing a reasonable performance with cycle times of 5.1 ms for the 128×128 pixel module (frame rate 196 Hz) and 11.5 ms for the 384×384 pixel module (frame rate 87 Hz) in the full image mode. An alternative readout scheme, realized in other pnCCD systems, enables an operation of pnCCD

detectors with higher frame rates [49]. For that purpose, the frame store areas and the CAMEX chips are installed at opposing sides of the sensitive area. In this way, the image can be divided into two parts by transferring the signal charges along opposite directions. The pnCCD is then operated in the so-called split frame mode.

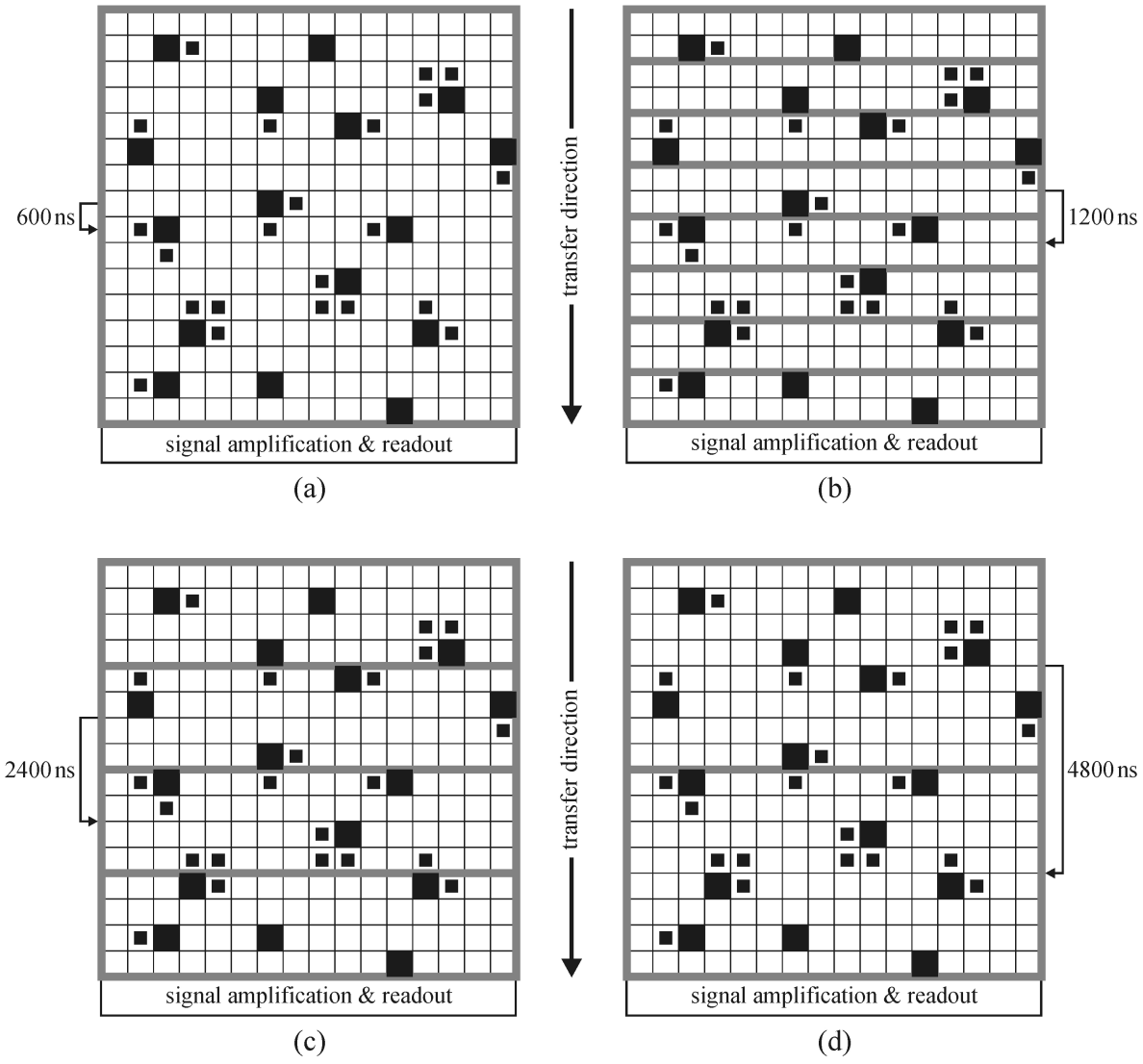

Figure 2.16: Principle of on-chip pixel binning used for an accelerated readout of the reduced pnCCD frame of figure 2.14. The durations for the shifts of integrated pixel blocks refer to the timing scheme of the 256×256 pixel module. (a) no binning (full image mode), (b) 2-fold binning, (c) 4-fold binning, (d) 8-fold binning.

An improved time resolution of X-rays, based on a significant reduction of the cycle time, can be realized by means of the timing mode [2] which uses the principle of on-chip pixel binning (figure 2.16): Instead of reading out all the pnCCD rows separately (figure 2.16(a)),

the number of processing steps is decreased by integrating the charge contents of several adjacent pixels in transfer direction. In the case of 2-fold pixel binning (figure 2.16(b)), two sequent rows are shifted to the anodes before the readout of the accumulated charge signals takes place in the CAMEX chips. The successive doubling of the number of integrated rows is then referred to as 4-fold binning (figure 2.16(c)), 8-fold binning (figure 2.16(d)), and so on. In each step in which the degree of binning is doubled, the readout time of the complete image decreases by a factor of two, whereas the transfer time remains unaffected.
For the eROSITA pnCCD test module with 128×128 pixels it was demonstrated that the timing mode enables a system operation at high frame rates above 1 kHz, i.e. with an effective time resolution in the submillisecond range, using at least 8-fold pixel binning [42]. The disadvantage of the timing mode becomes manifest in the spatial compression of the pnCCD image which results in a degraded position resolution in transfer direction. Moreover, in the course of an enhanced degree of binning, the 3D information about successively increasing numbers of individual events cannot be maintained. The timing mode is useful for dynamic analyses of integrated diffraction signals with *a priori* known or pre-measured position and energy. It also provides a suitable readout scheme for X-ray imaging techniques, where the precise position and energy information about single photons is not of interest.

2.3.7 Pile-up events: The SPC limit

The 4D detection of X-rays based on the SPC concept can only be guaranteed as long as the signal charges generated by different photons during one integration cycle of the pnCCD are not collected within the same pixel or within neighboring pixels. In such a case, the measured charge distribution corresponds to the signal of a multiple photon hit and does not provide the desired information about individual photons anymore. For spectroscopic applications with white synchrotron radiation, these so-called pile-up events represent the most important constraint with regard to multidimensional resolution of X-ray diffraction signals. From an experimental point of view, the occurrence of pile-up events is unavoidable, only its statistical probability can be minimized by means of a sufficiently low photon flux entering the pnCCD per unit area and unit time. According to the shape of the event pattern associated with a multiple photon hit, two different types of pile-up events are distinguished: If the charge clouds left by two (or more) photons overlap in such a way that an event, valid in terms of singles and charge splittings described in chapter 2.3.3, is created within the pixel structure, the obtained pattern was generated by event pile-up. All other cases, in which the detected charge distributions are characterized by event patterns of invalid types, result from pattern pile-up. Real signals observed in the course of pattern pile-up are not necessarily confined to small pixel areas, but can extend over large numbers of pixels, depending on the number of photons involved in the event. If the electrons spread over five (or more) adjacent pixels as a consequence of pattern pile-up, the recorded event is also denoted as a charge cluster.
Figure 2.17 shows a comparison between two random event pattern distributions generated within a pnCCD module comprising 16×16 pixels for different numbers of incident photons.

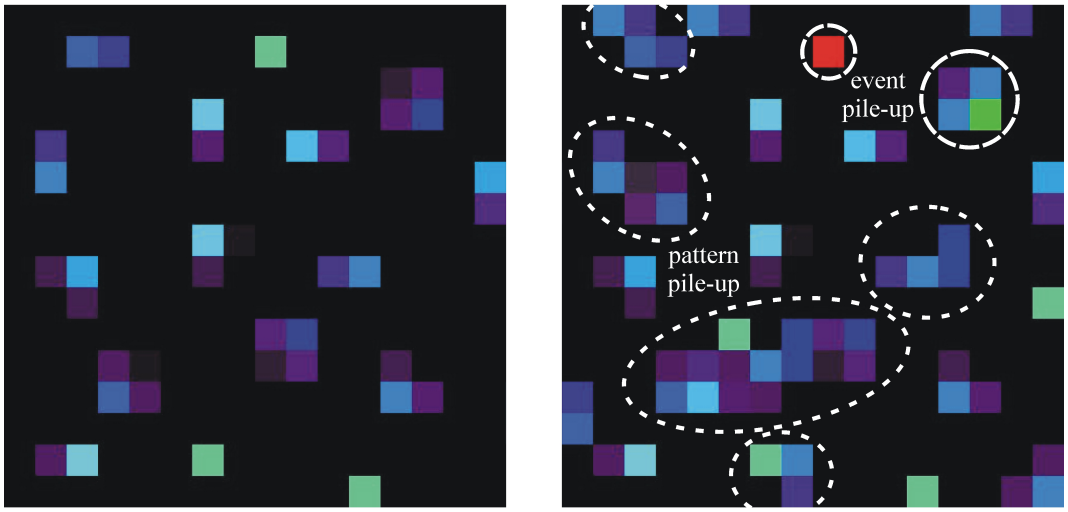

Figure 2.17: The SPC limit of the pnCCD. (a) Data pattern containing only valid and spatially separated event types in terms of SPC generated by single-photon hits of 13 keV energy. (b) Multiple photon hits giving rise to event pile-up and pattern pile-up in the case of enhanced count rate. The signals caused by event pile-up are a single event and a quadruple event with a total energy of 26 keV, respectively.

In the first case, which corresponds to the image depicted in figure 2.14, 16 photons of 13 keV energy were detected (figure 2.17(a)). Due to the fact that the events are spatially separated from each other, the position and energy of each individual photon can be experimentally determined based on the recombination of split events. In the second case, for which the number of photons was doubled, event pile-up and pattern pile-up significantly contribute to the event distribution (figure 2.17(b)). The condition of a sufficiently low count rate required for a safe SPC operation of the pnCCD is not fulfilled anymore. In contrast to the previous situation, only 13 of 32 detected photons can be identified with precise position and energy coordinates. As for events resulting from pattern pile-up the single-photon resolution is effectively lost, such event types are not further considered in conventional analyses of pnCCD data sets. However, in situations where pattern pile-up of photons with the same energy occurs, the integration of the spread charge signal normalized to the X-ray energy maintains the information about the number of photons generating the particular cluster.

2.3.8 Photon statistics

The real frequency of pile-up events, which contribute to a recorded pnCCD data set, depends on the incident photon flux. In general, the number of photons detected in an experiment, e.g. in an individual pixel or within a complete pnCCD frame, is randomly distributed due to the statistical nature of X-ray generation and X-ray absorption. In the most simple situation, a single pixel illuminated with a pencil beam of monochromatic X-rays can be considered.

The limited quantum efficiency of the pnCCD and the occurrence of out-of-time events imply that the number N_γ of photons recorded in this pixel during a fixed time interval falls below the number of incident photons. Denoting the total number of accumulated frames by N, the average count rate λ per frame within the exposed pixel is

$$\lambda = \frac{N_\gamma}{N} \ . \tag{2.20}$$

For sufficiently large values of N, the number of events detected independently from each other in a single experiment complies with a Poisson distribution, whereby the statistical probability P_k of finding find k photons in an individual measurement depends on λ according to [50]

$$P_k(\lambda) = \frac{\lambda^k}{k!} e^{-\lambda} \ , \ \ k = 0, 1, ... \ . \tag{2.21}$$

Due to the series expansion of the exponential function,

$$e^\lambda = \sum_{k=0}^{\infty} \frac{\lambda^k}{k!} \ , \tag{2.22}$$

the probability of measuring any number of photons in a single trial is

$$\sum_{k=0}^{\infty} P_k(\lambda) = \sum_{k=0}^{\infty} \frac{\lambda^k}{k!} e^{-\lambda} = e^\lambda e^{-\lambda} = 1 \tag{2.23}$$

ensuring the normalization of $P_k(\lambda)$. The variance σ^2 of the discrete probability distribution defined by (2.21) equals the mean value λ yielding the associated standard deviation

$$\sigma = \sqrt{\lambda} \ . \tag{2.24}$$

The Poisson distribution exhibits a strong asymmetry at low average count rates and becomes symmetric at large values of λ. In the limit $\lambda \to \infty$, $P_k(\lambda)$ approaches a Gaussian distribution with the mean value λ and the standard deviation $\sqrt{\lambda}$. Using (2.21) and (2.23), the probability $P_{\text{pile-up}}$ of detecting a pile-up event generated by at least two photons within the exposed pixel of the pnCCD is given by

$$P_{\text{pile-up}}(\lambda) = \sum_{k=2}^{\infty} P_k(\lambda) = \sum_{k=0}^{\infty} P_k(\lambda) - P_0(\lambda) - P_1(\lambda) = 1 - (1 + \lambda) e^{-\lambda} \tag{2.25}$$

The dependence of the pile-up probability on the mean value λ according to (2.25) is shown in figure 2.18 for a range of average count rates per pixel between $\lambda = 0.01$ and $\lambda = 100$. The strict requirement of a safe event separation, providing the capability of spectroscopic X-ray detection in the sense of SPC, can only be satisfied at low count rates $\lambda < 0.1$, in which case the pile-up probability is less than 0.5%. Above $\lambda = 0.1$, pile-up effects become increasingly pronounced expressed by a strong rise of $P_{\text{pile-up}}$. Towards higher count rates,

$P_{\text{pile-up}}$ converges to unity in the range of $\lambda > 10$. If a significant amount of pile-up events contributes to the recorded data pattern, the pnCCD effectively acts as an integrating X-ray detector. The pnCCD response at high average count rates $\lambda > 100$, for which in the X-ray spectroscopy mode the pixels' saturation limit is exceeded in the case of incident X-rays with an energy of about 11 keV, is discussed in detail in chapter 3.2.3.

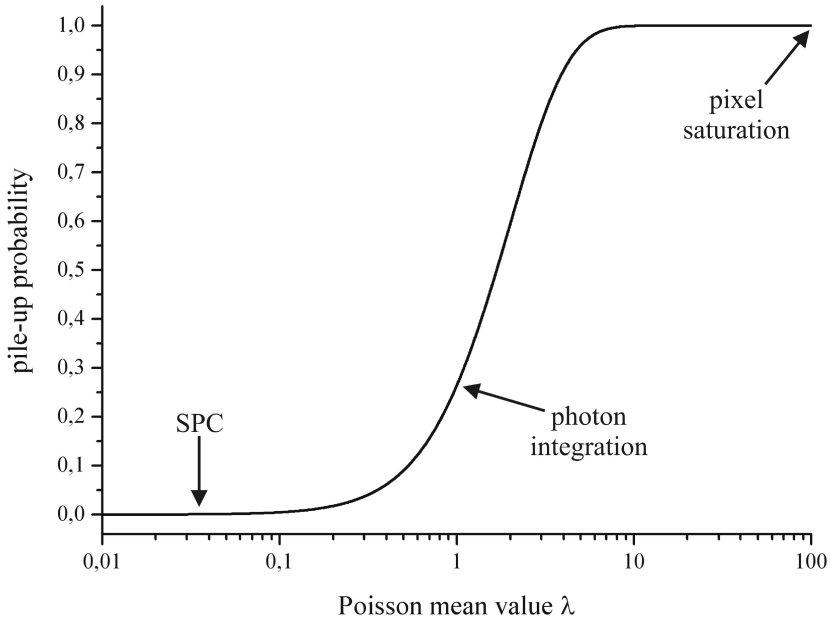

Figure 2.18: Pile-up probability as a function of the mean count rate λ within an individual pixel of the pnCCD exposed to monochromatic X-rays. Sufficiently low count rates ensure negligible pile-up probabilities, in which case the pnCCD can be used for X-ray spectroscopy in the SPC mode. At enhanced count rates, the signal amplitudes generated by different photons accumulate within the pixel structure. Then the pnCCD, operated in the integration mode for X-ray imaging, serves as a fast conventional CCD without energy resolution.

The statistical observations leading to the pile-up probability (2.25) are valid for the case of a single-pixel exposure to monoenergetic photons. In real white-beam X-ray diffraction experiments, complete energy spectra, including the diffraction signal of the sample as well as a white background continuum, are measured within individual pixels or small pixel areas. Under these circumstances, the integrated distribution of many statistically detected photons with different energies can be generalized based on the results for the monochromatic mode. In the easiest case, it can be assumed that one single pixel is illuminated with an X-ray beam containing photons with two different energies E_1 and E_2. The corresponding numbers of photons obtained in a single trial, k_1 and k_2, are determined by Poisson distributions $P_{k_1}(\lambda_1)$ and $P_{k_2}(\lambda_2)$ with the mean values λ_1 and λ_2. Since the signal charges deposited by distinct incident photons are generated independently from each other, the statistical probability of detecting k_1 photons with the energy E_1 and k_2 photons with the energy E_2 is $P_{k_1}(\lambda_1)P_{k_2}(\lambda_2)$.

Hence, pile-up occurs if k_1 and k_2 are combined in such a way that the total number $k_1 + k_2$ of recorded photons exceeds 1. The possible combinations of k_1 and k_2 to a pile-up event, together with their statistical probabilities following from (2.21), are summarized in table 2.1.

k_1	k_2	$P_{k_1}(\lambda_1)P_{k_2}(\lambda_2)$
0	≥ 2	$e^{-\lambda_1}(1-(1+\lambda_2)e^{-\lambda_2})$
1	≥ 1	$\lambda_1 e^{-\lambda_1}(1-e^{-\lambda_2})$
≥ 2	any	$1-(1+\lambda_1)e^{-\lambda_1}$

Table 2.1: Pile-up conditions for two distinct X-rays with the average count rates λ_1 and λ_2.

The total pile-up probability is given by the sum of the various probabilities $P_{k_1}(\lambda_1)P_{k_2}(\lambda_2)$ listed in the last column of table 2.1 yielding

$$P_{\text{pile-up}}(\lambda_1, \lambda_2) = 1 - (1 + \lambda_1 + \lambda_2)e^{-(\lambda_1+\lambda_2)} \quad . \tag{2.26}$$

This result reflects the reproductive property of two independent Poisson-distributed random variables, whereby the statistical probability of observing $k = k_1 + k_2$ photons within a single trial obeys a Poisson distribution with the mean value $\lambda_1 + \lambda_2$ [50],

$$P_k(\lambda_1, \lambda_2) = \frac{(\lambda_1 + \lambda_2)^k}{k!} e^{-(\lambda_1+\lambda_2)} \quad . \tag{2.27}$$

Consequently, considering the overall count rate Λ of the polychromatic signal detected within an individual pixel in the course of a white-beam experiment as a composition of many monochromatic signals with the energies E_1,...,E_n and the average count rates λ_1,...,λ_n,

$$\Lambda = \sum_{i=1}^{n} \lambda_i \quad , \tag{2.28}$$

the pile-up probability for this situation can be expressed by

$$P_{\text{pile-up}}(\Lambda) = 1 - (1 + \Lambda)e^{-\Lambda} \quad . \tag{2.29}$$

In real experimental situations, the total count rate

$$\Lambda = \lambda_s + \lambda_{bg} \tag{2.30}$$

consists of a dominant part λ_s including the integrated diffraction signal of the sample and a suppressed part λ_{bg} which quantifies the background level at the position of interest.
Particularly the pnCCD data sets obtained in energy-dispersive Laue diffraction experiments with white synchrotron radiation are characterized by significant contributions of event pile-up and pattern pile-up. In these cases, the spatial overlaps of photons with different energies give rise to pile-up signals which require an appropriate statistical interpretation. The described

formalism based on Poisson-distributed numbers of detected photons is used to determine integrated Laue spot intensities diffracted by a single crystal. The detailed algorithms needed for statistical analyses of the energy spectra measured at the positions of individual Bragg peaks are presented in chapter 4.5.

3 Performance study of an eROSITA pnCCD

The real performance of a pnCCD with respect to the capability of multidimensional X-ray detection depends on various parameters which limit the achievable position, energy, and time resolution as well as the dynamic range of the detector.

- **Position resolution**: The position resolution of single photons is determined by the pixel size, the charge collection time, and the electronic noise of the detector. Since the used frame store pnCCD systems solely contain quadratic pixels of $75\times75\,\mu\mathrm{m}^2$ size in the image area, the spatial resolutions in the horizontal and vertical directions do not differ. Hence, due to the common device thickness of $450\,\mu\mathrm{m}$, the achievable resolution in the subpixel regime is independent of the detector module.

- **Energy resolution**: The energy resolution depends on the ENC according to (2.19) and therefore in particular on the dark noise of the pnCCD. As the electronic components of the signal amplification and readout stages are effectively different for the frame store pnCCD with 256×256 pixels compared to the advanced eROSITA pnCCD, the energy resolution will not necessarily be the same for both systems.

- **Time resolution**: The time resolution is given by the frame rate and can be controlled by the user via the various timing schemes described in chapter 2.3.6. In this sense, the temporal accuracy of X-ray detection represents a flexible parameter adjusted on the basis of experimental aspects.

- **Dynamic range**: The dynamic range usable for X-ray imaging applications is limited by the maximum number of electrons that can be stored within an individual pixel. This characteristic quantity, also denoted as charge handling capacity (CHC), depends on the particular shape of the electric potentials applied for charge separation, storage, and transfer within the pnCCD. Moreover, the measurable CHC value is influenced by the effectivity of the reset mechanism used to clear the charge signal at the readout anode after on-chip amplification.

Regarding future applications of pnCCD systems for X-ray diffraction experiments with white synchrotron radiation, the performance of the eROSITA module comprising 128×128 pixels is investigated in this part. The analyses include measurements of the energy resolution by means of X-ray fluorescence spectroscopy and of the CHC in the course of a single-pixel exposure to intense monochromatic X-rays. The obtained results are representative for the advanced eROSITA pnCCD system with 384×384 pixels used for energy-dispersive Laue

diffraction (chapter 4.5.7). They show the effective limits that can be achieved for multi-dimensional X-ray detection in the SPC mode as well as for count rate capability in the integration mode under real experimental conditions. For each measurement discussed in this chapter, the pnCCD was operated in the full image mode with a frame rate of 196 Hz.

3.1 X-ray fluorescence spectroscopy

The interaction of X-rays with bound atomic electrons gives rise to the emission of X-ray fluorescence (XRF) signals which are characteristic of the illuminated material and allow a unique analysis of its chemical composition. If an X-ray photon liberates an electron from the K-shell of an atom by means of photoelectric effect, the excited atom passes into its ground state in the course of electronic transitions resulting in the emission of photons with discrete energies. In this case, the occupation of the free energy level in the K-shell by an electron from the L-shell (or a higher shell) of the atom is accompanied by element-specific K_α (K_β) radiation. Additionally, if a free energy level in the L-shell is filled with electrons from higher shells, the atom emits L_α, L_β, or L_γ radiation. Taking into account the fine structure of the available energy levels within the L- (and M-) shell, K_{α_1} (L_{α_1}) lines need to be distinguished from K_{α_2} (L_{α_2}) lines. The commonly used classification of K_β and L_β lines including various possible atomic transitions can be found in [51].
The relevant X-ray fluorescence lines of the investigated materials, together with their energies and relative intensities, are listed in table 3.1. Since the energy differences between the K_{α_1} and K_{α_2} lines (L_{α_1} and L_{α_2} lines in the case of Pb) as well as between the K_{β_1} and K_{β_3} lines (L_{β_1} and L_{β_2} lines in the case of Pb) are smaller than the Fano limit of Si at the considered energy, the corresponding photo peaks cannot be separated experimentally. In such situations, the energy of the effectively measurable XRF signal (e.g. denoted as $K_{\alpha_{1,2}}$ in table 3.1) results from the energies of the contributing fluorescence lines weighted by their associated relative intensities. In order to simplify the further notation, the $FeK_{\alpha_{1,2}}$ signal is abbreviated to FeK_α, the $FeK_{\beta_{1,3}}$ signal is abbreviated to FeK_β, and so on.

3.1.1 XRF setup at the EDR beamline

The experimental setup used for XRF spectroscopy at the energy-dispersive reflectometry (EDR) beamline at the storage ring BESSY II [52] is depicted in figure 3.1. A fluorescent material, illuminated with the white X-ray spectrum of a bending magnet, emits isotropically distributed XRF signals with discrete energies which are detected by the pnCCD at a distance of 500 mm from the sample. The incident beam size and intensity can be tuned by means of an aperture and a filter system containing absorbers of various thicknesses. A more detailed description of the beamline required for quantitative analyses of integrated diffraction signals is given in chapter 4.3. The samples consisted of thin metallic foils and plates with dominant contributions of Fe, Cu, Pb, Mo, and Sn, respectively. In another experiment, the RbK_α and RbK_β lines emitted by an RbOH-treated piece of pine wood served as XRF signals.

element	line	energy [eV]	intensity	measurable line	measurable energy [eV]
Fe	K_{α_1}	6403.8	100	$K_{\alpha_{1,2}}$	6400
	K_{α_2}	6390.8	50		
	$K_{\beta_{1,3}}$	7058.0	17	$K_{\beta_{1,3}}$	7058
Cu	K_{α_1}	8047.8	100	$K_{\alpha_{1,2}}$	8041
	K_{α_2}	8027.8	51		
	$K_{\beta_{1,3}}$	8905.3	17	$K_{\beta_{1,3}}$	8905
Pb	L_{α_1}	10551.5	100	$L_{\alpha_{1,2}}$	10541
	L_{α_2}	10449.5	11		
	L_{β_1}	12613.7	66	$L_{\beta_{1,2}}$	12616
	L_{β_2}	12622.6	25		
	L_{γ_1}	14764.4	14	L_{γ_1}	14764
Rb	K_{α_1}	13395.3	100	$K_{\alpha_{1,2}}$	13375
	K_{α_2}	13335.8	51		
	$K_{\beta_{1,3}}$	14961.3	17	$K_{\beta_{1,3}}$	14961
Mo	K_{α_1}	17479.3	100	$K_{\alpha_{1,2}}$	17443
	K_{α_2}	17374.3	52		
	K_{β_1}	19608.3	15	$K_{\beta_{1,3}}$	19602
	K_{β_3}	19590.3	8		
	K_{β_2}	19965.2	3	K_{β_2}	19965
Sn	K_{α_1}	25271.3	100	$K_{\alpha_{1,2}}$	25193
	K_{α_2}	25044.0	53		
	K_{β_1}	28486.0	17	$K_{\beta_{1,3}}$	28471
	K_{β_3}	28444.0	9		
	K_{β_2}	29109.3	5	K_{β_2}	29109

Table 3.1: X-ray fluorescence lines and associated measurable energies for various metallic samples investigated by means of XRF experiments. The data are taken from [51].

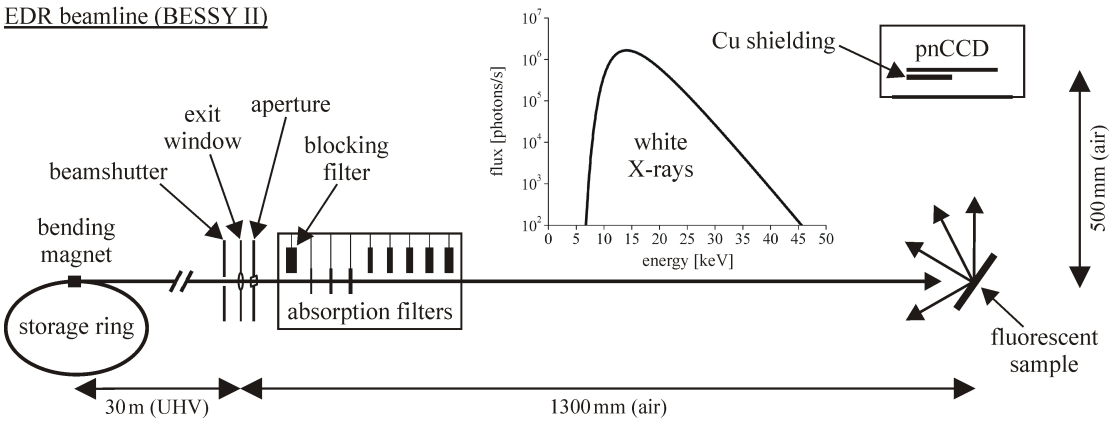

Figure 3.1: Experimental setup for XRF spectroscopy at the EDR beamline at BESSY II.

3.1.2 Data acquisition and analysis

The acquisition of pnCCD-generated data is controlled via a Linux-based platform equipped with Xonline [53]. The raw data sets consist of user-defined numbers of dark frames recorded in the absence of X-rays and signal frames including the XRF signal of the illuminated sample. The dark frames are needed in order to calculate the necessary noise, offset, and common mode corrections and to subtract them from the real photon events contained in the signal frames, as described in [34]. In the concrete case of XRF spectroscopy, 300 dark frames and 20000 signal frames were stored for each measurement corresponding to an overall exposure time of the sample of about 100 s. For further data treatment, a standardized software package provided by MPI-HLL [54] was used. This software accepts events with a signal amplitude above a selected threshold $n\sigma$, where σ is the mean dark noise of the pnCCD comprising all electronic and thermal noise contributions. Gain and CTI correction factors, which quantify the inhomogeneities between different pnCCD channels with regard to signal amplification and charge transfer, could be calculated by calibrating the detector with the most intense fluorescence line of the sample. Since the experiments were performed in an air environment, the XRF signals are accompanied by a white background continuum with the spectral shape of the primary synchrotron beam as a result of elastic scattering by air molecules. Hence, the amplitude distributions in the vicinity of the detected photo peak were fitted by a Gaussian with linear background taking into account single events and double events with a splitting parallel to the transfer direction. In the final step of data analysis, the pattern recombination to single-photon hits was carried out by assigning two center-of-mass coordinates and an integrated signal amplitude to individual split events. In this way, the peak position and the FWHM of the investigated fluorescence lines could be extracted for single events and separately for each type of split events. The 14-bit ADC generates digitized signal pulse heights on a scale of about 0...14300 adu (arbitrary digital units) with a maximum detectable X-ray energy per pixel depending on the selected gain. An overview of the different gain modes used for XRF experiments is given in table 3.2 including the measured mean noise, the peak position of CuK_α radiation, and the upper limit of the detectable energy range.

gain [adu/eV]	gain / max. gain	mean noise $\sigma[e^-]$	measured signal pulse height of CuK_α [adu]	max. detectable energy per pixel [keV]
2.56	1/1	8.2	—	5.6
1.28	1/2	8.2	10044	11.2
0.64	1/4	8.2	5019	22.4
0.16	1/16	9.3	1300	89.6
0.04	1/64	18.7	332	358.4
0.02	1/128	36.8	169	716.8
0.01	1/256	65.6	83	1433.6

Table 3.2: pnCCD gain modes and associated characteristics in the case of 8-fold CDS.

The listed values were obtained for various configurations of the switched capacitors G1,...,G4 in figure 2.9 and refer to a signal amplification with 8-fold CDS in the CAMEX. Using a reduced sampling number, the signal pulse height can be decreased by a factor of about $s/8$, where s is the number of taken samples. With respect to the discussed XRF experiments in the energy range between 6 keV and 25 keV, the highest available gain of 2.56 adu/eV is not suitable. Since the maximum detectable energy per pixel is below 6 keV for this gain mode, single events ensuring the best possible energy resolution exceed the bandwidth of the ADC already in the case of FeK_α radiation. In general, the spectroscopic performance of the pnCCD is limited by the dark noise which is usually understood as the root mean square (rms) of the corresponding ENC. For high gain modes, an ENC of about 8.2 e^- (rms) per pixel was observed being increased by nearly 50% in comparison to an ENC of 5.6 e^- (rms) measured for the 256×256 pixel module. The enhanced dark noise can be ascribed to the modified on-chip electronics implemented in the present eROSITA pnCCD systems. The typical contributions to the ENC are in the range of 3-5 e^- (rms) for the on-chip JFET and 0.5-1 e^- (rms) for the CAMEX. The significantly larger values of the mean noise at low gain modes result from the reduced signal-to-noise ratio dominated by the CAMEX contributions [42].

3.1.3 Gain and CTI correction factors

With regard to signal amplification and charge transfer, the inhomogeneities between the different pnCCD channels were analyzed in detail for the case of a calibration with CuK_α radiation emitted by an illuminated Cu foil. For that purpose, the incident intensity was tuned in such a way that the average count rate in the detection plane amounted to 116 cpf (counts per frame). Figure 3.2 shows the corresponding gain and CTI correction factors extracted by means of columnwise fits of the CuK_α photo peak, as described in [34, 54].

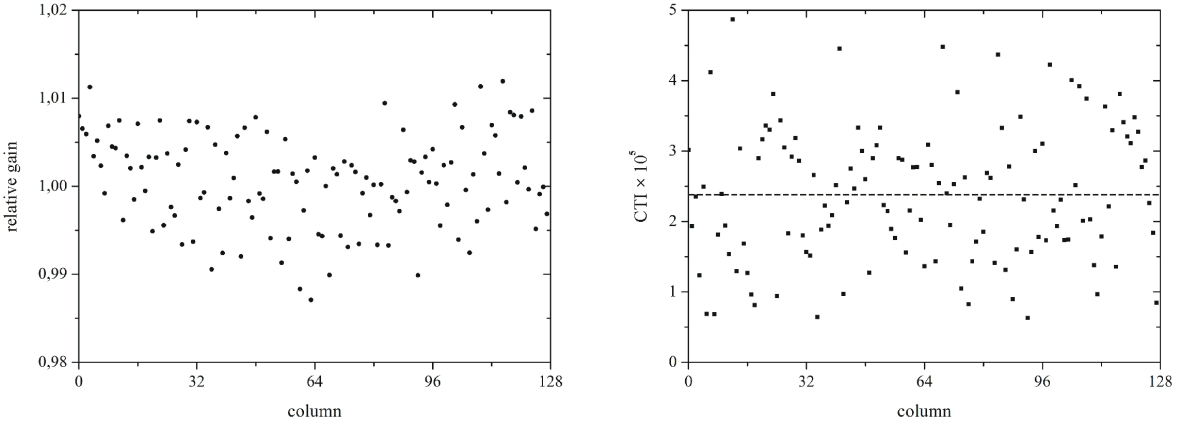

Figure 3.2: Gain and CTI correction factors calculated for the individual pnCCD channels.

The so-obtained values reveal that for the majority of the pnCCD channels, the gain correction factors applied to the recorded raw amplitudes are below 1% relative to the overall gain. In

this measurement, the charge loss during signal transfer is characterized by the mean CTI

$$\overline{\mathrm{CTI}} = (2.37 \pm 0.95) \cdot 10^{-5} \quad . \tag{3.1}$$

The effective influence of the CTI correction depends on the number of charge transfers according to (2.16). For the 128×128 pixel module, the maximum number of transfers is 256, whereby the expected relative correction falls below 1% for most of the channels. In the case of the eROSITA pnCCD system with 384×384 pixels (with at most 768 transfers), similar CTI values may lead to signal corrections above 2% for individual channels. Further studies of gain and CTI correction factors showed that the relative gain is independent of the count rate and the selected gain mode. In contrast, the CTI exhibits a successively decreasing behavior with enhanced count rate. This property results from the fact that the lattice defects in the transfer depth of the electrons can be saturated to a large extent if more signal charges are generated [55]. Hence, mean CTI values calculated at higher count rates of 333 cpf and 513 cpf amounted to $\overline{\mathrm{CTI}} = (1.95 \pm 0.74) \cdot 10^{-5}$ and $\overline{\mathrm{CTI}} = (1.67 \pm 0.57) \cdot 10^{-5}$.

3.1.4 Signal stability

The measured peak position of an XRF signal depends on the monochromacity of the line energy, the selected gain mode, and the event threshold used for data analysis. Moreover, the signal pulse height can be affected by instrumental constraints as well as by the specific experimental conditions which typically give rise to an unavoidable white background level. As far as the instrumental side itself is concerned, particularly in the case of the 256×256 pixel module, the incomplete reset of the anode charge signal after on-chip amplification became manifest in a remarkable instability of the peak position. Consequently, enhanced count rates resulted in unwanted shifts of the photo peaks towards larger signal amplitudes. In order to study the response of the eROSITA pnCCD system at increasing X-ray flux, the detector was exposed to CuK_α and CuK_β radiation with event densities varied in a similar range as in the experiment discussed in [41]. Figure 3.3 depicts the obtained pulse height spectra in the vicinity of the CuK lines, recorded with a gain setting of 0.16 adu/eV and integrated over the full sensitive area of the pnCCD including single events and split events.
Besides the XRF signals of the CuK_α and CuK_β photo peaks with signal amplitudes of 1300 adu and 1440 adu, the Si escape peaks of both lines are visible. In these cases, the ratios between the absolute intensities of the escape peaks and the associated photo peaks are approximately 1%. Towards higher count rates, the photo peak shapes become slightly asymmetric due to larger background contributions at low X-ray energies. In contrast to the behavior observed for the 256×256 pixel module, the peak positions measured by the eROSITA pnCCD show a significantly better stability with rising count rate. The variations of the signal pulse heights are below 2 adu within the recorded intensity range and therefore negligible for spectroscopic applications. The peak stability is based on the fast and complete reset of the detected voltage signal achieved by the integration of optimized on-chip electronics in comparison to detector systems of preceding pnCCD generations.

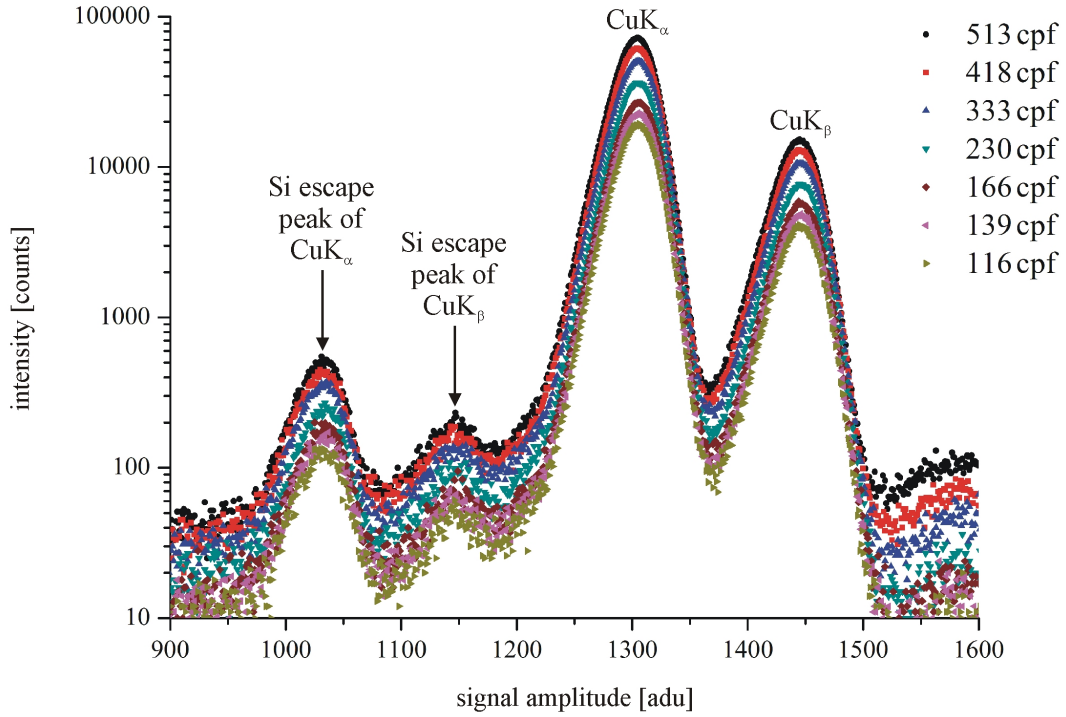

Figure 3.3: Measured pulse height spectra of a fluorescent Cu foil in the vicinity of the CuK$_\alpha$ and CuK$_\beta$ photo peaks. The XRF signals were recorded at different and gradually increased average count rates between 116 cpf and 513 cpf.

3.1.5 Linearity

The linear response is an essential property of an energy-dispersive X-ray detector regarding its spectroscopic performance in applications with white synchrotron radiation. In general, the linearity of the pnCCD can be experimentally verified by recording appropriate calibration curves which describe the dependence of the output signal on the X-ray energy over the energy range of interest. For that purpose, the eROSITA pnCCD module was illuminated with the various XRF lines listed in table 3.1 providing different average pulse heights in the hard X-ray regime. The required calibration measurements were performed for all the suitable gains of the pnCCD summarized in table 3.2 starting with a gain setting of 1.28 adu/eV (1/2 of the maximum gain). For the highest two gain modes (1/2 and 1/4 of the maximum gain), only those XRF lines with detectable energies could be used. The so-obtained calibration curves for the eROSITA pnCCD showed the desired linear behavior (figure 3.4). The slopes of the fitted lines correspond to the inverse gain values listed in the first column of table 3.2. In the case of low gain settings, at which the available amplitude range per keV energy is substantially limited, the energy resolution of the system cannot be maintained. Hence, at 1/128 of the maximum gain, the FeK lines and CuK lines overlap to single peaks (denoted as FeK$_{\alpha+\beta}$ and CuK$_{\alpha+\beta}$ in the lower left graph of figure 3.4), whereby the experimental separation of the K$_\alpha$ peaks from the K$_\beta$ peaks is no longer possible. Therefore, the remaining signals had

to be analyzed in terms of weighted energies taking into account the relative intensities of the involved fluorescence lines according to table 3.1. In the lowest gain mode (1/256 of the maximum gain), only the XRF signals of Rb, Mo, and Sn could be resolved properly. A more quantitative investigation of the degraded energy resolution at low gain settings is presented in chapter 3.1.7.

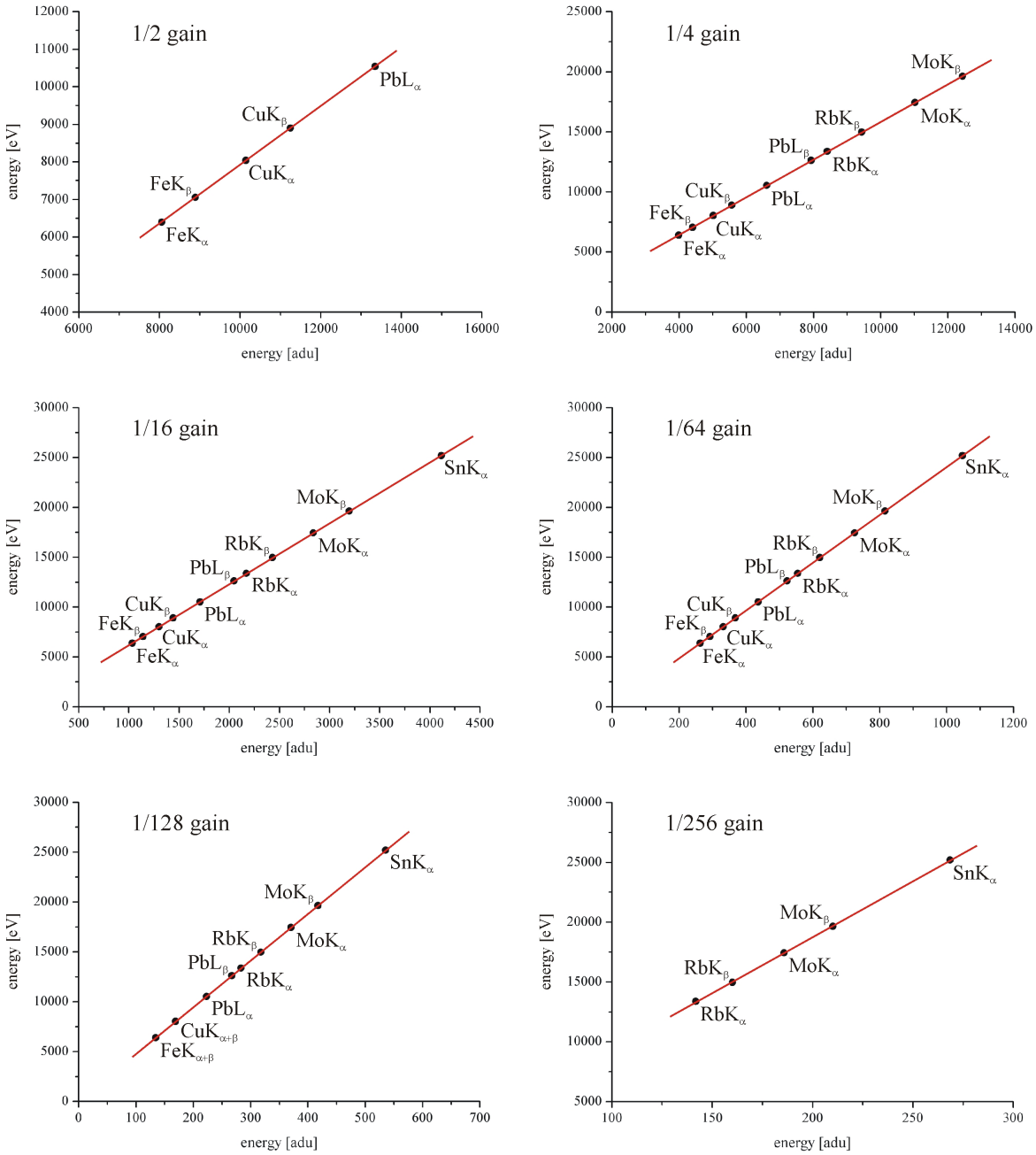

Figure 3.4: Measured signal pulse heights of different fluorescence energies for various gain modes of the eROSITA pnCCD. The red lines are the corresponding calibration curves obtained by means of linear fits through the data points.

3.1.6 Energy resolution

The real energy resolution of the pnCCD is given by the experimentally determined photo peak widths of the considered XRF lines. Since the FWHM of a measured signal depends on the dark noise affecting the pulse height in each pixel, the photo peaks need to be analyzed separately with regard to single events and split events. The minimum possible ENC, which effectively contributes to the generated charge signal, is guaranteed for single events. In that respect, the achievable energy resolution is quantified by the fitted FWHM of the associated photo peaks containing only single events. In contrast to measurements performed in the monochromatic mode, the present experimental conditions give rise to an enhancement of the FWHM as a consequence of the white background continuum that superimposes the photo peaks. Figure 3.5 shows the obtained FWHM of various XRF lines in the energy range between 6 keV and 20 keV for a gain setting of 1/16 and different event thresholds between 4σ and 8σ. For quantitative analyses of the FWHM, solely XRF signals with sufficient intensities and monochromacities were taken into account. The remaining XRF lines (in particular PbL_α, MoK_α, and SnK_α) exhibit natural spectral broadenings above 100 eV based on the overlapping components of the atomic fine structure. These photo peaks do not provide single Gaussian profiles required for a precise FWHM determination and were thus excluded from the analyses.

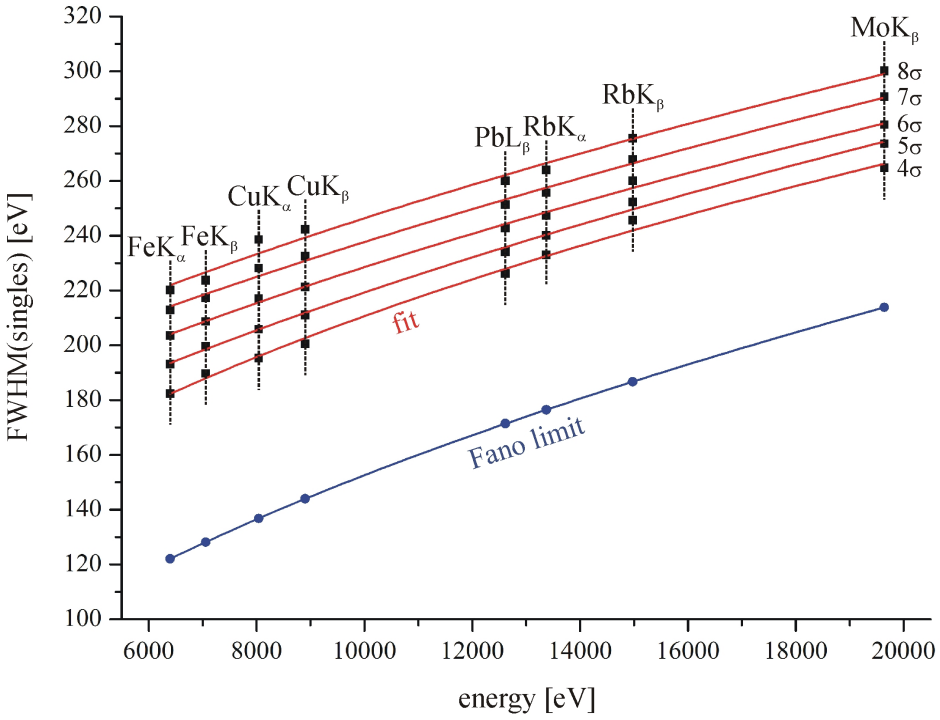

Figure 3.5: Energy resolution of the pnCCD for different fluorescence energies and selected event thresholds between 4σ and 8σ. The achievable resolution is defined by the FWHM of the individual photo peaks generated by single events. The red curves are least-squares fits of the data, the blue curve indicates the Fano limit of Si.

The energy dependence of the measured FWHM was fitted using power functions of the form

$$\mathrm{FWHM}(E) = 2.355w\Big(\frac{FE}{w} + c_1^2\Big)^{c_2} \tag{3.2}$$

with $F = 0.115$ and $w = 3.65\,\mathrm{eV}$, where c_1 and c_2 are fit parameters yielding the red curves in figure 3.5. At an event threshold of 6σ, the least-squares fit of the data is given by

$$c_1 = 13.0 \pm 2.4 \ , \ \ c_2 = 0.424 \pm 0.092 \ . \tag{3.3}$$

The calculated value of c_2 is in good agreement with the expected behavior (2.19) of a solid-state X-ray detector. Based on the direct use of (2.19), the energy resolution is limited by an effective ENC of 19.0 in this experiment. The significant exceedance of the dark noise charge ($\sigma = 9.3\,e^-$ (rms) for the selected gain mode) results from the experimental background and the chosen event threshold. In the latter case, the energy resolution is influenced by the event threshold in so far as it leads to a virtual noise component which becomes manifest in the incorrect interpretation of individual photon hits. Therefore, real double events with a high signal amplitude in one pixel and a low signal amplitude in the other pixel are recognized as single events if the lower amplitude falls below the threshold and is cut from the event. This effect causes a degraded energy resolution due to the fact that certain amounts of single events are assigned with incomplete energies. The successive broadening of the photo peaks with rising event threshold can be observed in figure 3.5. Further analyses show that the effective ENC increases from 15.7 to 21.3 for an enhancement of the threshold from 4σ to 8σ. Hence, under real experimental conditions of XRF spectroscopy with white X-rays, the Fano limit is exceeded in a range between 50 eV and 60 eV at an event threshold of 4σ. In this situation, the FWHM of the CuK_α single peak amounts to 195 eV translating into a standard deviation of about 83 eV and a relative energy resolution close to 1%.
The obtained result can be considered as the achievable limit of single-photon resolution in X-ray diffraction experiments with white synchrotron radiation using an eROSITA pnCCD system. For quasimonochromatic illumination, whereby a continuous background signal is suppressed, the pnCCD provides an improved energy resolution. With a gain setting of 1/2, MnK_α radiation ($E = 5898\,\mathrm{eV}$) emitted by a radioactive ^{55}Fe source could be resolved with about 150 eV (FWHM) at an event threshold of 4σ corresponding to an effective ENC of 10.9.

3.1.7 Effects at low gain settings

The choice of the gain mode, in which the pnCCD is operated, depends on experimental aspects. If the energy range of interest falls below the maximum detectable energy per pixel, listed in the last column of table 3.2, the highest suitable gain mode enables the best possible energy resolution of individual photons. As long as the count rate is sufficiently low to ensure a safe SPC operation in the X-ray spectroscopy mode, contributions of pile-up events are of minor interest. In contrast, the eROSITA pnCCD can be used as an integrating detector for X-ray imaging applications with a high dynamic range. Then, the event pattern distribution

is characterized by event pile-up and pattern pile-up signals containing many photons. In this case, the gain needs to be decreased and adapted in such a way that the integrated signal amplitudes associated with multi-photon hits are still measurable over a wide intensity range. Resulting from the enhanced dark noise at low gain settings, the energy resolution of the pnCCD is degraded owing to the reduced signal-to-noise ratio. The effect of a successively decreased gain on a typical pulse height spectrum is depicted in figure 3.6 by the example of the XRF signal emitted by a fluorescent Fe foil.

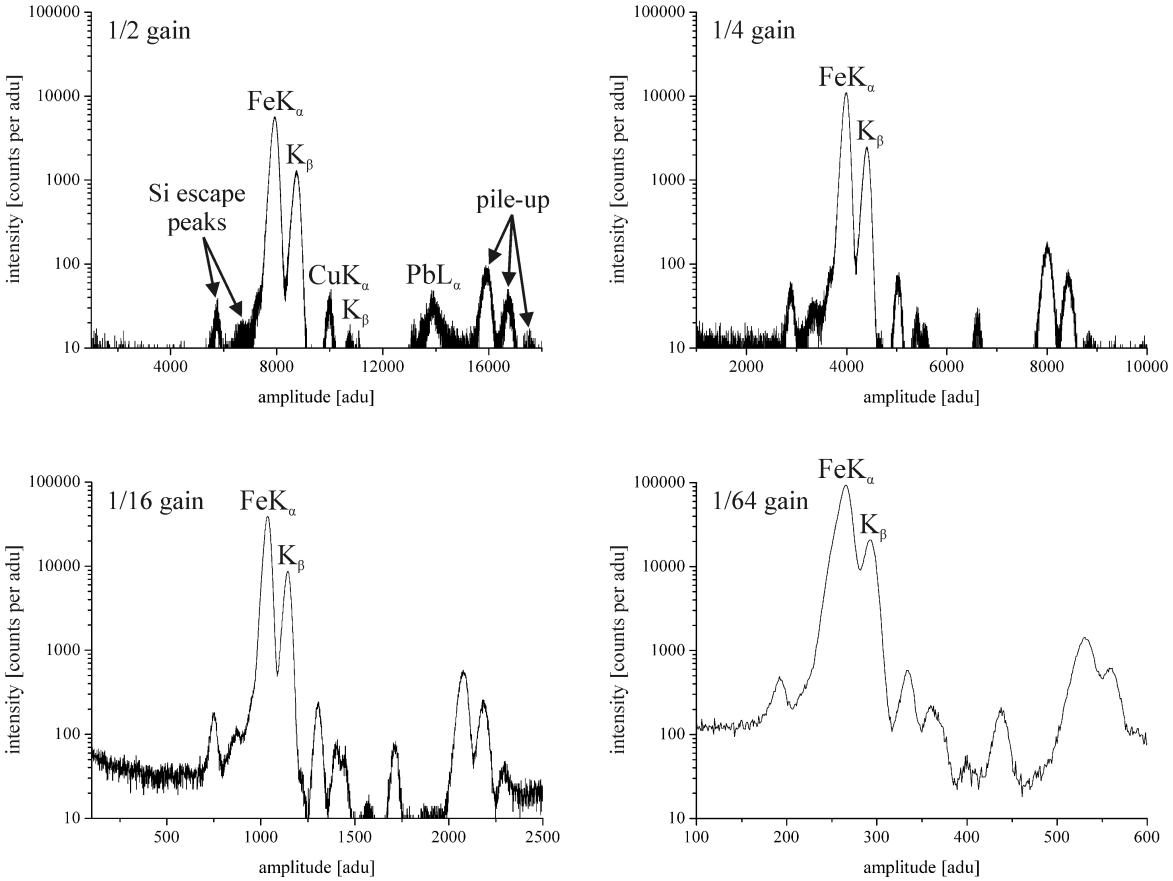

Figure 3.6: XRF spectra of an Fe foil recorded at different gain settings and at a count rate of 119 cpf. In the lowest gain mode (1/64 of the maximum gain), the FeK$_\alpha$ and FeK$_\beta$ lines overlap as a consequence of the degraded energy resolution of the pnCCD.

The measured XRF spectra are dominated by the FeK$_\alpha$ and FeK$_\beta$ photo peaks including the Si escape peaks and pile-up events. In the highest gain mode (1/2 of the maximum gain), all the signals with amplitudes exceeding the limited ADC range (0...14300 adu) belong to split events. The XRF signal is accompanied by suppressed contributions of CuK$_\alpha$ and CuK$_\beta$ radiation generated by the cooling mask covering the pnCCD module as well as a PbL$_\alpha$ line originating from the experimental setup. The PbL$_\beta$ signal overlaps with the first pile-up of two FeK$_\alpha$ photons and cannot be resolved properly. The second pile-up peak is created by

events which contain one FeK$_\alpha$ photon and one FeK$_\beta$ photon, the third pile-up peak arises from spatial overlaps of two FeK$_\beta$ photons.
In the highest gain modes selected (1/2, 1/4, and 1/16 of the maximum gain), the FeK$_\alpha$ and FeK$_\beta$ lines are well-separated from each other with a slowly increasing FWHM between 193 eV and 204 eV for the FeK$_\alpha$ line and between 197 eV and 209 eV for the FeK$_\beta$ line referred to single events at a threshold of 6σ. The successive enhancement of the photo peak heights results from the confinement of the XRF signals to smaller spectral ranges on the adu scale. In the lowest gain mode (1/64 of the maximum gain), the width of the accessible amplitude range is no longer sufficient to maintain the energy resolution achieved for higher gain modes. In this situation, the FeK$_\alpha$ and FeK$_\beta$ peaks, which are still separated but show a substantial overlap, can be resolved with a degraded FWHM of 302 eV and 254 eV, respectively. If the gain is further decreased to 1/128 of the maximum gain, the lines finally merge to one single peak, whereby the definition of an FWHM becomes meaningless. Figure 3.7 shows the results of analog analyses for a selected set of XRF lines with regard to the obtained resolution of the associated single peaks depending on the chosen gain.

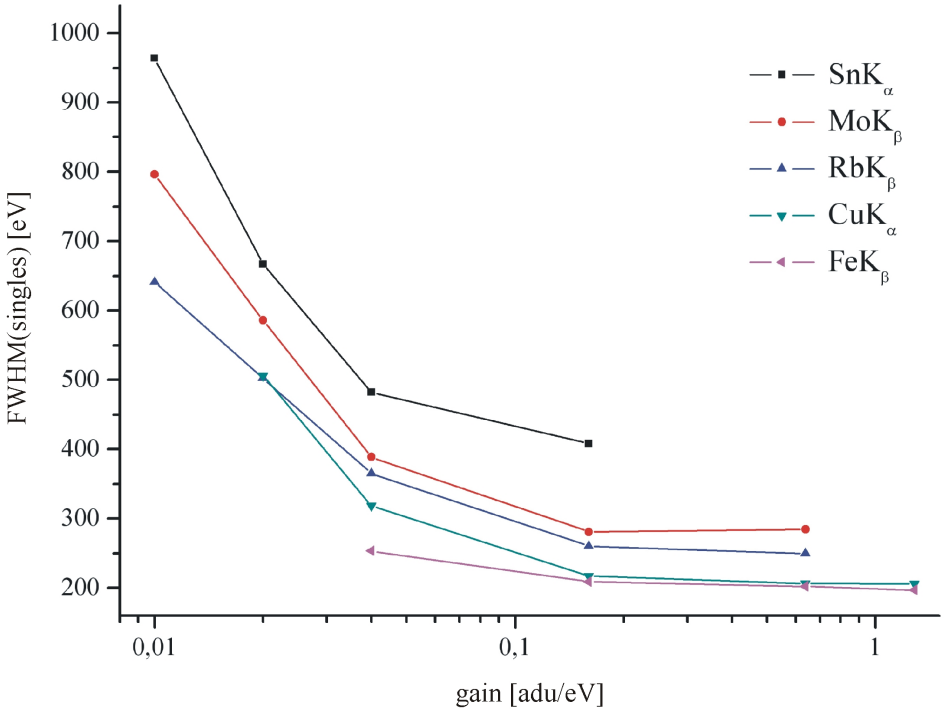

Figure 3.7: Effect of the gain setting on the energy resolution of the pnCCD for various selected XRF lines. The successive reduction of the gain gives rise to enhanced broadenings of the detected photo peaks.

Due to its insufficient monochromacity, the SnK$_\alpha$ line exhibits a significantly larger width already at the highest suitable gain mode in comparison to the remaining XRF signals. For a gain setting of 0.02 adu/eV (1/128 of the maximum gain), at which the Fe lines merge, the

CuK_α and CuK_β peaks are still separated with an FWHM of about 500 eV ascribed to the CuK_β line. The loss of energy resolution, based on the reduced signal-to-noise ratio at low gain settings, is quantitatively similar for the investigated photo peaks. In the lowest suitable gain mode required for a spectral separation of the individual XRF lines, the relative energy resolution amounts to approximately 2%. Operating the pnCCD in the integration mode for monochromatic X-rays, this accuracy allows to measure absolute numbers of photons with energies in the hard X-ray regime.

3.1.8 Characteristics at high count rates

For particular applications, the fast analysis of a metallic material with respect to its chemical composition is important. In general, such experiments rely on a detection of the XRF signals of the sample using high incident X-ray fluxes. For that purpose, the pnCCD response at different count rates was investigated in detail in the case of a fluorescent Cu foil (figure 3.8).

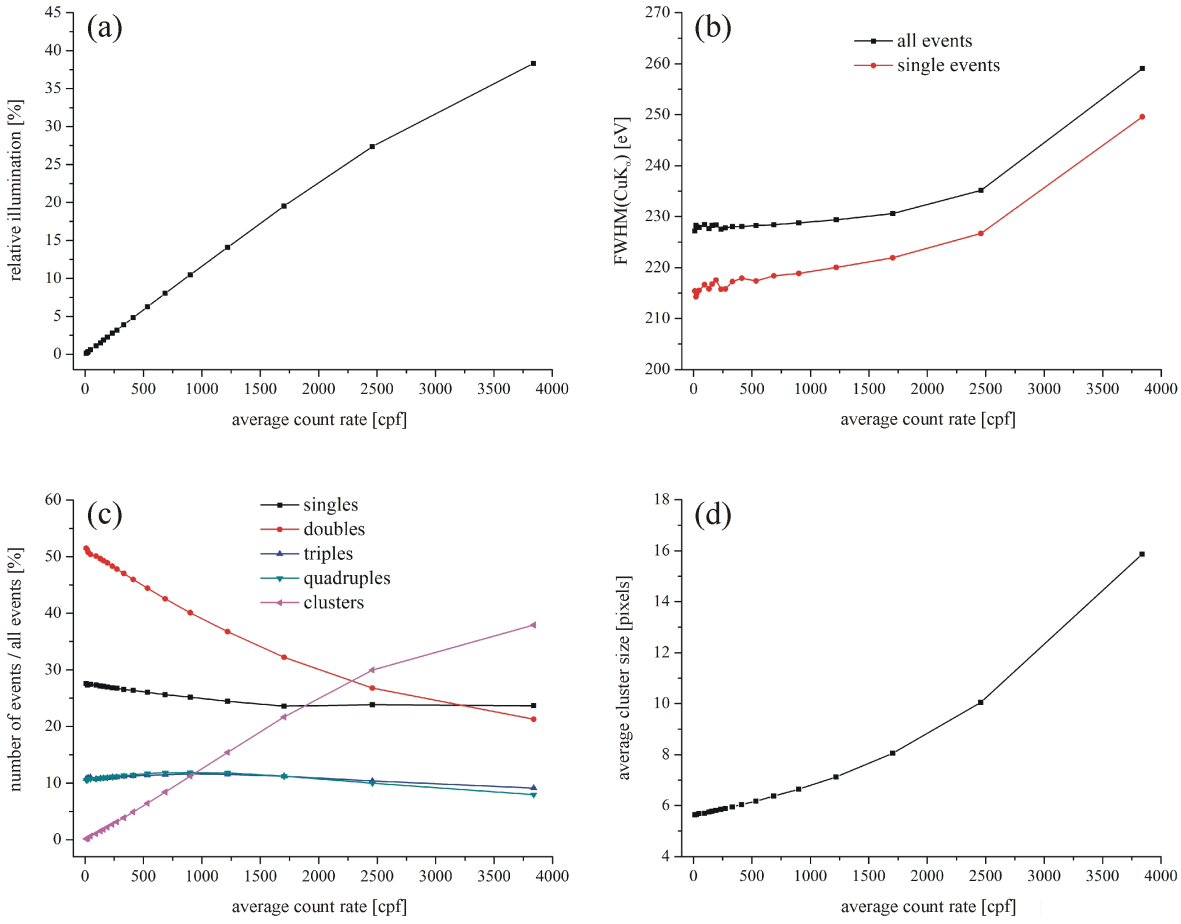

Figure 3.8: pnCCD response at high count rates. (a) Relative illumination of the pnCCD area. (b) FWHM of the CuK_α photo peak in terms of single events and all valid event patterns. (c) Frequencies of different event types. (d) Average cluster size.

The depicted results refer to a successively enhanced count rate up to a maximum value of about 3840 cpf which corresponds to an integral count rate of $7.5 \cdot 10^5$ cps distributed homogeneously over the complete sensitive area of the pnCCD. The concrete values assigned to the average count rate arise from the restriction that each pile-up signal is considered as one individual event, independent of the number of photons involved in it.
Based on the discussions in chapter 2.3.7 concerning the SPC limit of a pnCCD detector, the measured X-ray flux essentially influences the frequencies of event pile-up and pattern pile-up in the recorded data sets. The relative illumination of the pnCCD area, defined as the ratio between the total number of pixels containing a charge signal and the total number of processed pixels, shows a linearly rising behavior with increasing count rate up to 20% of the sensitive area at 1700 cpf (figure 3.8(a)). At the highest count rate used, about 38% of the pixels are filled with electrons generated by intense XRF signals, whereas a significant contribution to the enhanced number of detected photons results from the white background continuum. Consequently, a degraded energy resolution is observed in the case of the CuK_α photo peak evaluated in terms of single events and all valid event patterns (figure 3.8(b)). In this particular situation with a gain setting of 1/16 and a selected event threshold of 6σ, the broadening of the CuK_α line is about 30 eV at the highest count rate compared to the FWHM obtained at low count rates. As a result of pattern pile-up, the occurrence of charge clusters spreading over more than four connected pixels becomes increasingly pronounced towards larger X-ray fluxes (figure 3.8(c)). Hence, the cluster frequency exhibits a strong rise which scales with the relative illumination of the pixel area. At count rates above 2300 cpf, the pnCCD data pattern is dominated by cluster events at the expense of double events. Since the statistical probability of detecting high photon numbers within individual pattern pile-up events grows with enhanced count rate, the charge clusters extend over larger areas according to the curve shown in figure 3.8(d). At high incident X-ray fluxes, for which clusters are the most frequently recorded event types, the precise measurement of integrated XRF signals can no longer be performed in the white-beam mode. However, restricting the data analysis to valid event patterns associated with single-photon hits, the energy information about different XRF lines emitted by the sample is maintained.

3.2 Single-pixel illumination with monochromatic X-rays

The available dynamic range provided by eROSITA pnCCD systems is of particular interest for various kinds of X-ray diffraction experiments with synchrotron radiation. In contrast to XRF, real scattering signals are typically confined to small pixel areas depending on the intrinsic structure of the sample and the size of the primary X-ray beam. A special case consists in highly intense Bragg peaks generated by a single crystal which is exposed to white X-rays in the course of a Laue diffraction experiment. In this situation, many photons are scattered into single pixels giving rise to significant contributions of pile-up events to the recorded data pattern. As soon as the spectral distribution of X-rays at the position of a Laue spot including background signals is known, the absolute intensity of the reflection can be measured

at enhanced count rates. In the monochromatic mode, the number of electrons created within the illuminated pixel increases proportionally to the number of detected photons and to the incident X-ray flux. At sufficiently high count rates, the saturation limit of an individual pixel, which finally defines the dynamic range, is reached. In that respect, the performance of the eROSITA pnCCD was studied by exposing one single pixel to monochromatic X-rays of variable intensity and investigating the detector response at increasing count rates.

3.2.1 Experimental conditions

Figure 3.9 shows the experimental setup for single-pixel illumination with monochromatic X-rays at the EDR beamline at BESSY II: The 111 reflection of a cubic, high-purity Si(111) single crystal was excited by exposing the sample to white synchrotron radiation of variable intensity. The beam reflected from the crystal surface could be focussed down to the center of an individual pixel by guiding it through a pinhole of 15 μm diameter located at a distance of 100 mm from the pnCCD. Under the depicted geometrical conditions, using an indicent beam with a quadratic cross section of $100\times100\,\mu m^2$, the real Laue spot size in the detection plane amounted to approximately 20 μm. In order to avoid parallax effects, the pnCCD was mounted on a 2θ rotation stage and oriented in such a way that the diffracted beam entered the image area at normal incidence. The final centering on a single pixel could be achieved by means of stepping motors with a precision below 1 μm ensuring controlled movements of the detector in the horizontal and vertical directions. The count rate obtained in the illuminated pixel was gradually enhanced by decreasing the total thickness of the used absorption filters.

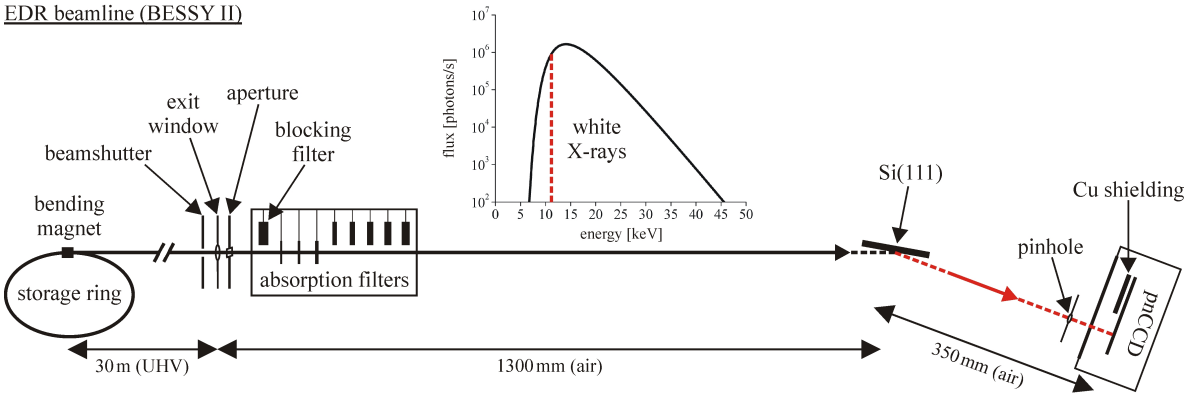

Figure 3.9: Experimental setup for single-pixel illumination with monochromatic X-rays at the EDR beamline at BESSY II. The incident white synchrotron beam is monochromatized by means of a Si(111) crystal and focussed on the center of a single pixel.

According to Bragg's law described in chapter 4.1.2, the Si(111) crystal selects a set of discrete energies out of the incident X-ray spectrum depending on its orientation relative to the primary beam direction. In general, the X-ray energies diffracted by the sample surface are

a consequence of elastic reflections from the parallel crystallographic (111), (222), (333), ... lattice planes. The energies $E_{hhh} = h \cdot E_{111}$, associated with Bragg peaks of different orders, are integer multiples of the energy E_{111} of the Si 111 reflection. In the setup of figure 3.9, the angle of incidence referred to the sample surface was chosen to be

$$\theta = (10.26 \pm 0.01)^\circ \tag{3.4}$$

translating into the spectrum of diffracted energies

$$E_{111} = (11.1 \pm 0.1)\,\mathrm{keV} \;\;,\;\; E_{222} = (22.2 \pm 0.2)\,\mathrm{keV} \;\;,\;\; E_{333} = (33.3 \pm 0.3)\,\mathrm{keV} \;\;,\;\; ... \tag{3.5}$$

incident on the exposed pixel. The discrete set (3.5) was calculated by converting (4.9) into the corresponding energy description and inserting the interplanar spacing distances

$$d_{hkl} = \frac{a}{\sqrt{h^2 + k^2 + l^2}} \tag{3.6}$$

of a cubic Si crystal with the lattice constant $a = 5.43\,\text{Å}$ at room temperature [56]. The real presence of the energy E_{111} was experimentally confirmed within a preliminary measurement of the air-scattered X-ray spectrum in the vicinity of the reflected beam by means of the Roentec X-Flash. The higher orders of the Si 111 reflection are not of further interest since the primary X-ray flux and the sensitivity of the pnCCD do not suffice to detect Bragg peaks at energies above 40 keV with reasonable statistics [6].
The expected integrated spot intensities I_{111}, I_{222}, and I_{333} of the various reflections in this experiment can be estimated from (4.17) taking into account the limited quantum efficiency of the eROSITA test module (figure 2.13, red curve) and the numbers of incident photons with the considered energies. The structure-factor amplitudes $|F_{111}| = 60.29$ and $|F_{333}| = 35.07$ of Si at room temperature were obtained using the ideal diamond structure of Si in the program StructFactor [57]. The non-zero value of the structure factor F_{222}, which belongs to the forbidden Si 222 reflection, arises from structural disturbances consisting in anharmonic thermal vibrations and an asymmetric valence charge density [58, 59]. Precise rocking curve measurements of the Si 222 reflection revealed that the associated structure-factor amplitude is about $|F_{222}| = 1.47$ at room temperature [60]. Under the above-described experimental conditions, the ratios of the absolute spot intensities satisfy the relations

$$\frac{I_{111}}{I_{222}} > 10^5 \quad , \quad \frac{I_{111}}{I_{333}} > 10^4 \quad . \tag{3.7}$$

Hence, the diffracted signal of the Si(111) crystal is strongly dominated by the 111 reflection. Apart from a suppressed background continuum, the reflected beam focussed on an individual pixel of the pnCCD can be considered as a monochromatic X-ray signal of high and tunable intensity in a good approximation. The spectral reduction of the incident white synchrotron beam to a single Laue spot with the energy $E_{111} = (11.1 \pm 0.1)\,\mathrm{keV}$ is indicated by the red dashed lines in figure 3.9.

3.2.2 Count rate behavior

In order to detect high photon fluxes giving rise to a saturation of the illuminated pixel in the described experiment, the pnCCD had to be operated in a sufficiently low gain mode. For that purpose, the signal processing in the CAMEX was performed at 1/256 of the maximum gain with 6-fold CDS. The exposed pixel, defined by the column index 64 and the row index 61, is located close to the center of the pnCCD module with 128×128 pixels in the image area. The recorded data sets comprised 6000 signal frames which were corrected for noise, offset, and common mode and analyzed with an event threshold of 8σ. For further data treatment, the accumulated events were integrated framewise over a 3×3 pixel area surrounding the exposed pixel without any applied gain and CTI corrections. This simplification is justified in high count rate experiments with hard X-rays since it has no effect on the precise determination of absolute intensities. The spectra of measured signal amplitudes, depicted exemplarily in figure 3.10 for the case of a low count rate, show characteristic distributions of pile-up events.

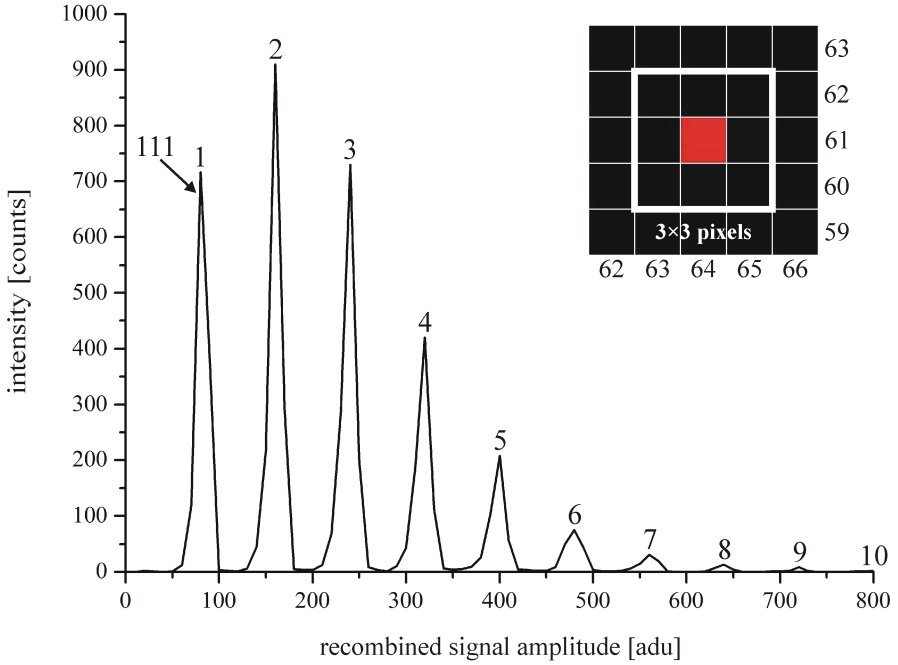

Figure 3.10: Pile-up spectrum of the Si 111 reflection recorded within a 3×3 pixel area around the illuminated pixel, as illustrated in the upper right part of the figure.

In the selected gain mode, the Si 111 reflection was detected with an average recombined signal amplitude of (80.6 ± 0.2) adu and a fitted FWHM of (1.4 ± 0.1) keV. The degraded relative energy resolution of about 13%, arising from the low gain setting and the abandonment of gain and CTI corrections, is sufficient for a spectral separation of the different pile-up signals. The integration of the individual pile-up peaks, generated by the photon numbers which are indicated at the top of the peaks in figure 3.10, provides a set of measured probabilities for the associated multi-photon events after normalization to the number of recorded frames.

Figure 3.11 shows the so-obtained pile-up distributions for various average count rates. The experimentally determined frequencies of detected photon numbers could be fitted by means of Poisson distributions with different mean values according to the red curves in figure 3.11.

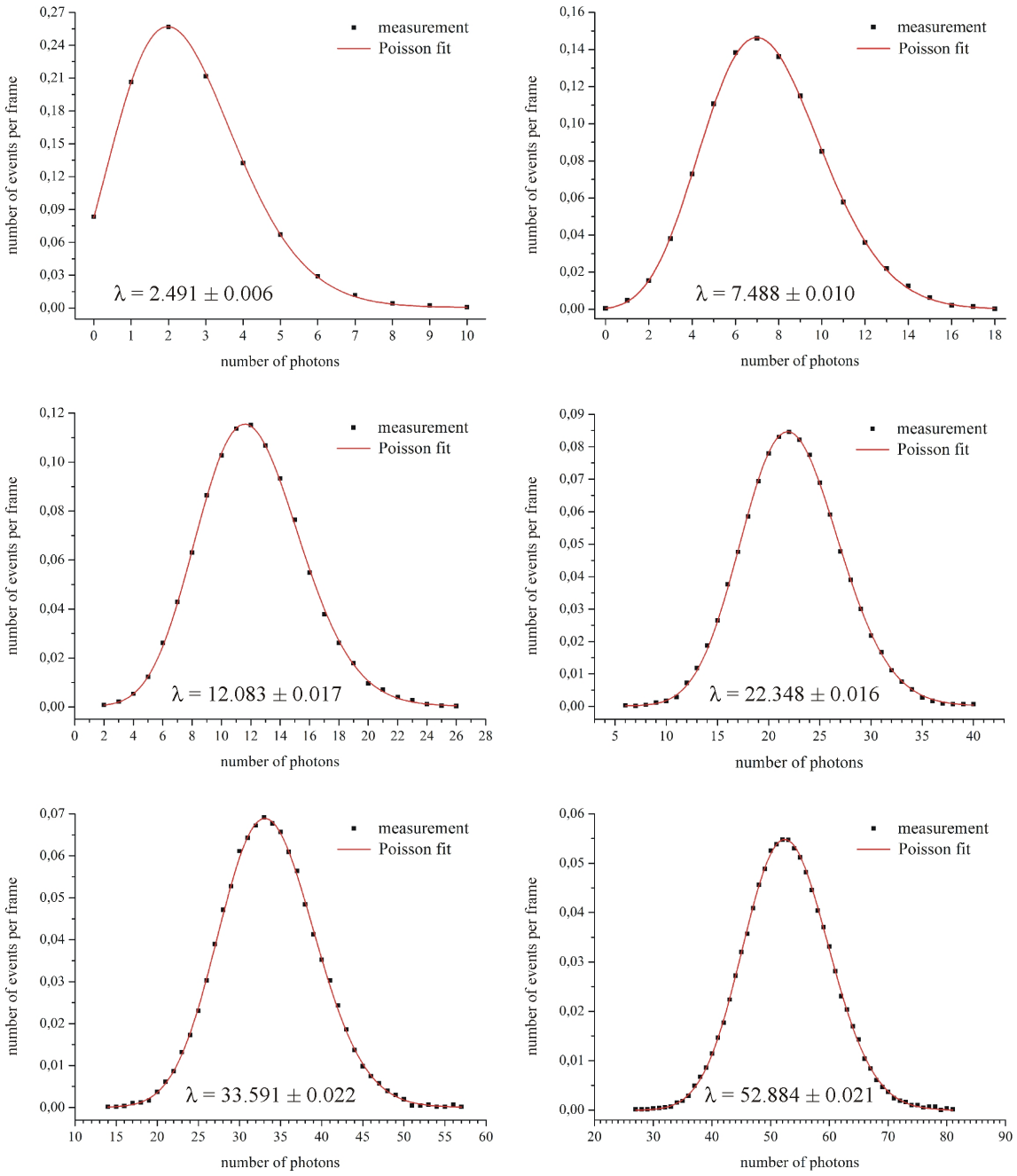

Figure 3.11: Statistical frequencies of photon numbers detected within the exposed pixel at successively enhanced primary X-ray fluxes. The measured curves were fitted using Poisson distributions with the ascribed mean values λ. The upper left plot resulted from the integrated pile-up spectrum of figure 3.10.

Consequently, the pile-up spectrum of figure 3.10 is characterized by the average count rate $\lambda = 2.491 \pm 0.006$ yielding the absolute intensity $I = N\lambda = 14946 \pm 36$ of the Si 111 reflection detected within the illuminated pixel, where $N = 6000$ denotes the number of accumulated signal frames. In this experiment, the measured spot intensity could be determined with a relative accuracy of 0.24%, whereas out-of-time events, giving rise to an intensity enhancement in the range of 2%, were not considered. Thus, taking into account the limited quantum efficiency $\varepsilon = 0.78 \pm 0.01$ of the pnCCD system at $E = 11.1\,\mathrm{keV}$, the real diffracted intensity associated with the Si 111 reflection finally amounts to $I_{111} = 19564 \pm 255$. This result was achieved by neglecting absorption effects in air along the path direction of the reflected beam. The obtained relative error of about 1.3% mainly arises from imprecisions of the simulated quantum efficiency curves discussed in chapter 2.3.2.
The analog measurements of the Si 111 reflection at enhanced count rates were based on a successive reduction of the absorber thickness, whereby the incident X-ray flux at the position of the crystal could be tuned to higher values. The corresponding statistical distributions of recorded photon numbers, calculated from the integrated and normalized pile-up spectra, are summarized in figure 3.11 together with the fitted Poisson curves. Towards increased count rates, the shape of the measured probability distributions becomes symmetric around the mean value reflecting the transition of a Poisson distribution into a Gaussian distribution. The relative accuracies of the extracted average count rates could be gradually improved up to 0.04% for the largest depicted count rate given by $\lambda = 52.884 \pm 0.021$. In general, the quality of the applied Poisson fits confirms that spectral overlaps of the assumed monochromatic signal with higher diffraction orders and air-scattered photons are negligible in this experiment. The first case has been expected in terms of the intensity ratios (3.7), the second case is a consequence of the spatial confinement to a small area of 3×3 pixels including less background contributions.
The formalism, which was used for absolute intensity determination, relies on a least-squares fit of the average count rate λ and represents the basis for measurements of integrated Laue spot intensities described in chapter 4.5. If several diffraction orders occur at the position of a particular Bragg peak, the Poisson-distributed numbers of photons lead to overlapping harmonics that can be deconvoluted by means of similar statistical methods. An alternative way to obtain the total intensity of a single reflection consists in the direct integration of the detected pile-up spectrum. In this sense, the measured spot intensity can be calculated by $I = \sum_j j I_j$, where I_j is the absolute intensity of the pile-up peak containing j photons.

3.2.3 Pixel saturation

For the intensity measurements discussed so far, the number of electrons collected within the illuminated pixel is still below its saturation limit. Under this condition, the diffraction signal of the Si 111 reflection, apart from out-of-time events, is restricted to the selected 3×3 pixel area enclosing the exposed pixel. A further stepwise enhancement of the incident X-ray flux results in the integrated charge distributions shown in figure 3.12.

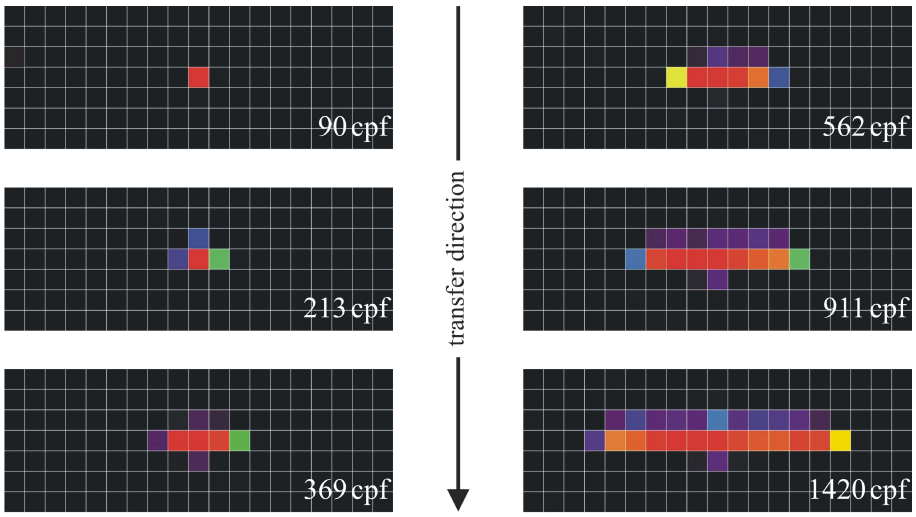

Figure 3.12: Integrated diffraction signal of the Si 111 reflection at increasing count rates between $\lambda = 90$ and $\lambda = 1420$ displayed within an area of 19×7 pixels. The charge distributions, referred to a linear color scale, are not normalized to each other.

If the saturation limit of the illuminated pixel is reached, any surplus charge spills over to an adjacent pixel perpendicular to the transfer direction. In this situation, the electrons collected in the completely filled pixel create a repulsive potential for newly generated charge clouds which arrive in the pixel structure. At the saturation limit, the closest accessible potential minimum for additional electrons is located within the neighboring pixels in row direction. The height of the potential well in this direction has a typical value between 2 V and 2.5 V defined by the p^+ channel stops. In contrast, the potential barrier in transfer direction is determined by the external voltages applied to the p^+ registers at the detector front side giving rise to an effective threshold of about 3.5 V in the storage depth of the electrons [42]. The spatial confinement of the signal charges in the transfer depth mainly results from a substantially higher potential well in the direction perpendicular to the pixel plane which is provided by the back contact voltage. Under the described conditions, the surplus electrons predominantly escape across the weakest potential barrier perpendicular to the transfer direction. Due to the experimental constraint that the reflected beam could not be focussed exactly on the center of the exposed pixel, a part of the signal is detected within the adjacent row in the opposite direction of the charge transfer.
The enhanced degree of charge spilling with increasing X-ray flux becomes manifest in the horizontal broadening of the integrated diffraction signals in figure 3.12: If the CHC of the illuminated pixel is exceeded (at a count rate of 213 cpf), pronounced amounts of charges are measured within the neighboring pixels. As soon as these pixels are also completely filled with electrons (at a count rate of 369 cpf), additional charges escape to the succeeding pixels perpendicular to the transfer direction. In this way, the saturation limit of 11 adjacent pixels was reached at the highest count rate of 1420 cpf.

3.2.4 Charge handling capacity

The maximum number of electrons that is effectively stored within an individual pixel under the operation conditions of the pnCCD can be deduced from the count-rate dependent charge spilling effects observed in figure 3.12. In order to determine the mean CHC of a single pixel, the detected charge distributions were quantitatively analyzed along the direction in which the charge spilling mainly occurred (assigned with the row index 61 according to figure 3.10). Figure 3.13 depicts the obtained column profiles of the average detected signal amplitudes per pixel and frame after conversion into equivalent photon numbers. For that purpose, the energy scale was appropriately calibrated by normalizing the integrated charge distributions to the signal pulse height of 80.6 adu associated with a single photon of 11.1 keV energy.

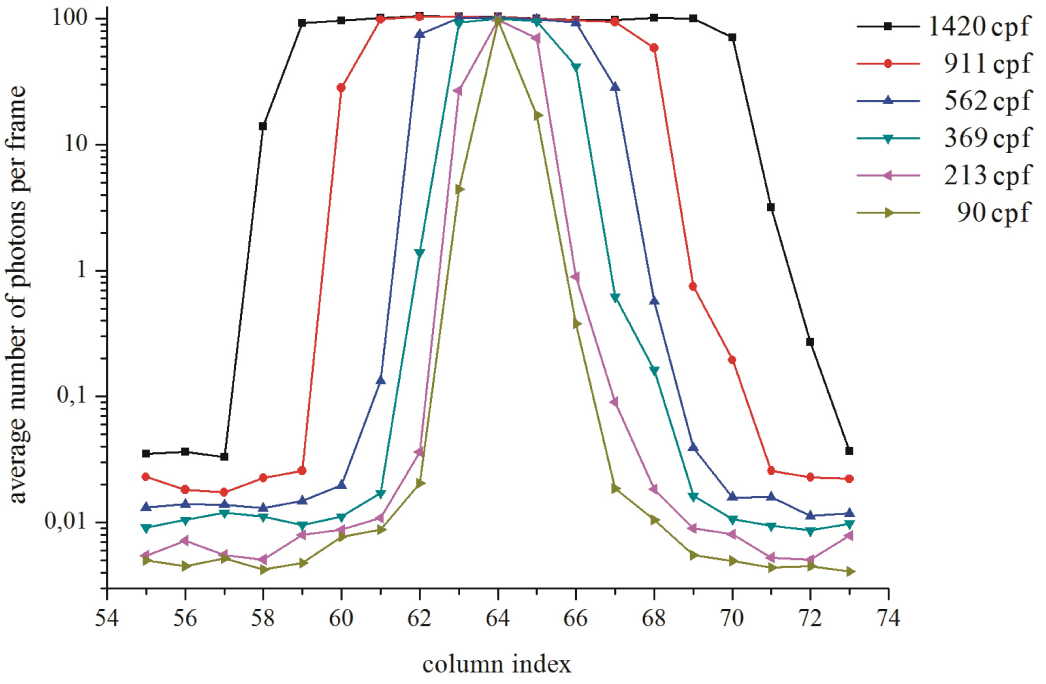

Figure 3.13: Column profiles of the integrated charge distributions of figure 3.12 along the charge spilling direction after translation into real photon numbers. The exposed pixel is assigned with the column index 64.

The successive saturation of an increasing number of pixels in the direction of charge spilling due to enhanced incident X-ray fluxes reflects the existence of a maximum possible signal amplitude per pixel which emerges as soon as the considered pixel is completely filled with electrons. In this case, the charge content of an already saturated pixel does not further increase as a consequence of higher overall count rates. Taking into account that no gain and CTI correction factors were applied to the recorded data, the maximum number of storable electrons per pixel shows slight fluctuations in the range of 2% around the mean CHC along the charge spilling direction. In the situation with a measured count rate of 1420 cpf, the CHC

can be intepreted as the number of photons detected in an individual pixel at the saturation limit. Under the present experimental conditions, assuming incident monochromatic X-rays of 11.1 keV energy, a mean photon number of approximately 100 is required to saturate a single pixel. Since each of these photons creates $11.1\,\mathrm{keV}/3.65\,\mathrm{eV} \approx 3000$ electron-hole pairs on average, the equivalent maximum number of collected electrons at the saturation limit of a pixel can be estimated by

$$\mathrm{CHC} = \frac{100 \cdot 11.1\,\mathrm{keV}}{3.65\,\mathrm{eV}} \approx 300000 \ . \tag{3.8}$$

The calculated mean CHC value corresponds to a total deposited energy of about 1.11 MeV and an integral count rate per pixel of nearly 20000 cps for this experiment. Favored by the optimized reset mechanism preventing latch-up of the first FET, the real measurable CHC of the eROSITA pnCCD is roughly a factor of two larger in comparison to the value obtained for the previously used pnCCD system [61]. Since the number of generated signal charges is proportional to the incident X-ray energy, higher count rates per pixel can be achieved for lower energetic photons. In that respect, the dynamic range of the pnCCD for optical applications improves by about four orders of magnitude. The measured average single-pixel CHC refers to an eROSITA pnCCD system which is operated in the X-ray spectroscopy mode ensuring the highest performance for multidimensional resolution of individual photons. Using the concept of on-chip pixel binning described in chapter 2.3.6, the detectable integral count rate per pixel can be enhanced by a factor of six in the case of 8-fold binning, whereas the CHC itself remains unaffected. Possibilities to increase the single-pixel CHC for experiments with high local count rates, leading to the X-ray imaging mode of the pnCCD, are discussed in chapter 3.3.2.

3.3 Measurements with an IμS

Further investigations of the pnCCD response at high count rates were accomplished using the microfocus X-ray source IμS developed by Incoatec GmbH. The IμS provides an intense monochromatic X-ray beam with a sufficient photon flux for single-pixel exposure giving rise to massive charge spilling effects. In this situation, the X-ray imaging mode of the pnCCD, which mainly relies on a reduced back side potential, was tested in the case of a significantly increased count rate compared to the previously described CHC measurements. The obtained results show achievements and limitations of a CHC enhancement and can be considered as a preliminary determination of the dynamic range provided by an eROSITA pnCCD system for X-ray imaging applications.

3.3.1 The microfocus X-ray source IμS

From a conceptual point of view, the IμS offers a variety of advantages in contrast to other laboratory X-ray sources used: In general, based on a precisely aligned optics system, a larger X-ray yield becomes available for experiments. Moreover, the X-ray tube itself is air-cooled,

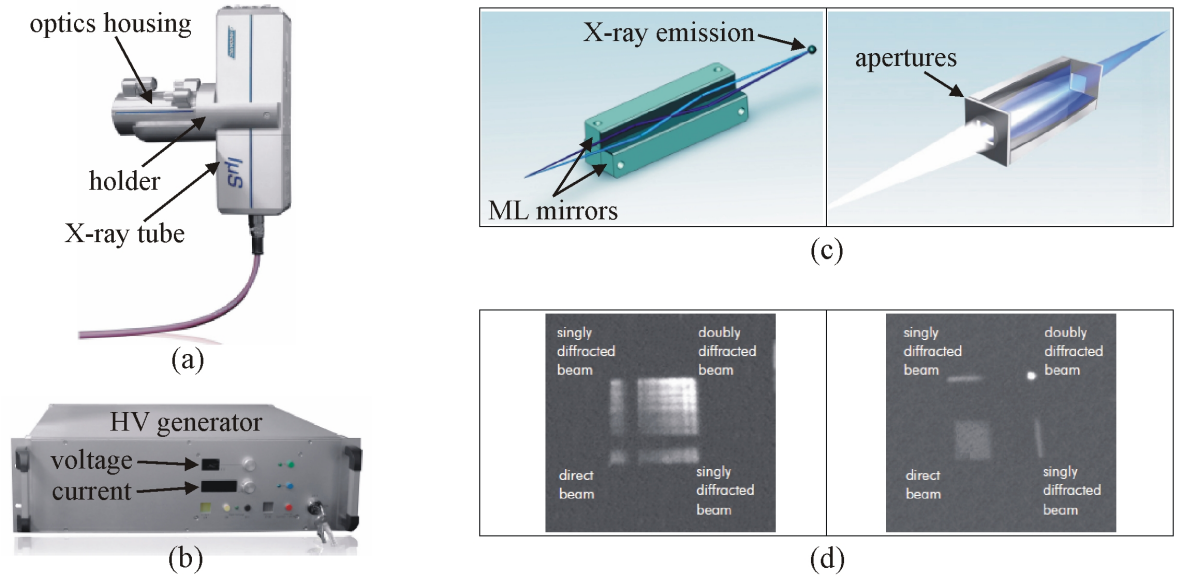

Figure 3.14: Principle of the microfocus X-ray source IμS [62]. (a) X-ray tube with attached optics housing. (b) High voltage generator and control units for IμS operation. (c) Focussing of the emitted X-rays by means of a Montel optics system using two multilayer mirrors (left) and apertures (right). (d) Beam profile directly behind the optics housing (left) and near the focal plane (right).

i.e. it requires no external water cycle for room temperature operation with a high beam stability. Finally, due to its compactness, the system is multi-directionally movable which enables a flexible mounting according to experimental aspects. Figure 3.14 shows the basic components of the IμS together with its characteristic beam profile.
The IμS consists of the X-ray tube equipped with a Cu anode, an attached housing for the focussing optics (figure 3.14(a)), and a high voltage generator (figure 3.14(b)). An additional vacuum pump (not depicted) keeps the IμS at a constant pressure below 5 mbar. Under usual conditions, the X-ray tube is operated with a high voltage of 45 kV and a current of 650 μA providing a power of nearly 30 W. Large monochromatic X-ray yields are achieved by means of a Montel optics system aligned in such a way that the most intense CuK$_\alpha$ component is filtered out. For that purpose, two curved multilayer mirrors with graded interplanar spacing distances are mounted perpendicular to each other (figure 3.14(c)). This arrangement, in connection with a suitably adjusted aperture system, creates a beam profile which comprises the direct (undiffracted) beam, two singly diffracted beams, and one doubly diffracted beam (figure 3.14(d)). The doubly diffracted beam converges in the focal plane with a focal spot diameter of 56 μm and a monochromatic X-ray flux of about $3 \cdot 10^8$ photons/s. In view of the measurements discussed below, the doubly diffracted beam was selected and focussed on a single pixel of the pnCCD. The current setup for CHC analyses in the case of the eROSITA pnCCD module with 384×384 pixels is depicted in figure 3.15. A similar geometry was used to study the performance of the eROSITA pnCCD test module with 128×128 pixels.

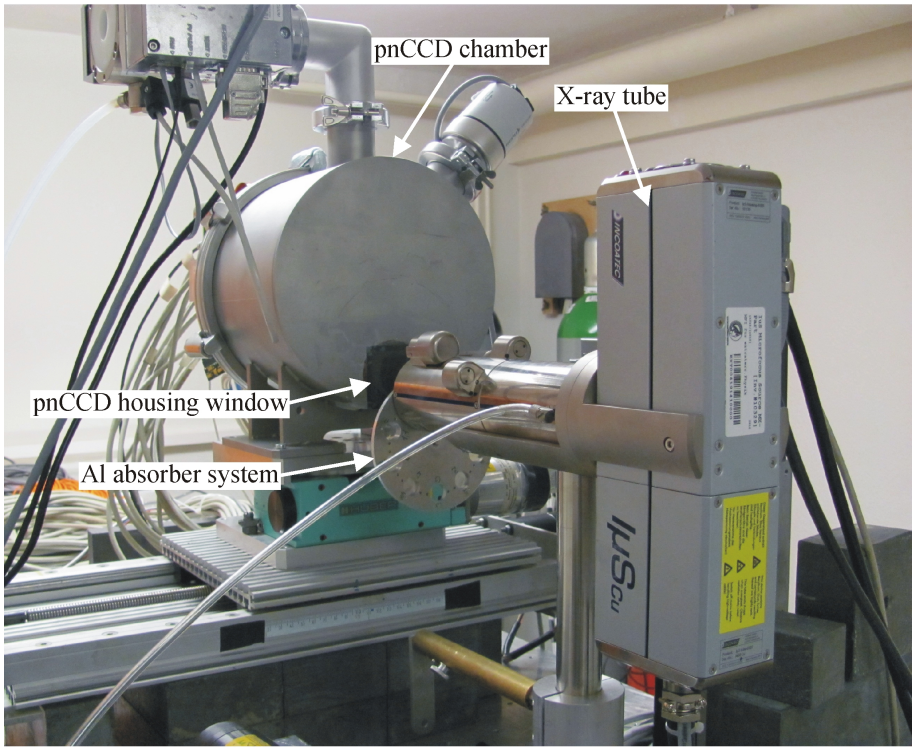

Figure 3.15: Experimental setup for CHC measurements with the pnCCD located in the focal plane of the IμS. The incident monochromatic X-ray flux is tuned by means of an absorber system containing Al filters of different thicknesses.

3.3.2 X-ray spectroscopy mode and X-ray imaging mode

Each individual data set discussed so far was recorded in the X-ray spectroscopy mode of the pnCCD. In this case, the detector is operated under standard conditions with an applied back contact voltage of $-230\,\mathrm{V}$ relative to the MOS structure being kept at a potential of $0\,\mathrm{V}$. The X-ray spectroscopy mode enables a four-dimensional detection of X-rays at low count rates with a sufficiently high gain setting. Moreover, based on a low gain selection with a degraded energy resolution, many photons per pixel can be integrated up to the saturation limit determined by the measured single-pixel CHC (3.8). For X-ray imaging applications, which rely on higher incident photon fluxes, the suppression of the occurring charge spilling effects is of interest in order to obtain precise information about the integrated intensities of diffraction signals. To this end, the count rate capability of individual pixels can be enhanced by means of a more negative voltage at the back side of the pnCCD. Previous studies have shown that under this condition, the potential minimum for electron storage is moved closer to the detector surface [63]. Prior to analyses of the CHC, the pnCCD response at a varying applied back contact voltage was investigated in the SPC mode. For that purpose, moving the pnCCD out of the intense doubly diffracted beam provided by the IμS, the air-scattered CuK_α signal was detected with a high gain setting of 1/4 using 8-fold CDS. The so-obtained

characteristics of the CuK$_\alpha$ photo peak in terms of the fitted pulse height and the FWHM restricted to single events are summarized in figure 3.16 for a back contact voltage between −190 V and −400 V, where a threshold of 6σ was selected for event extraction.

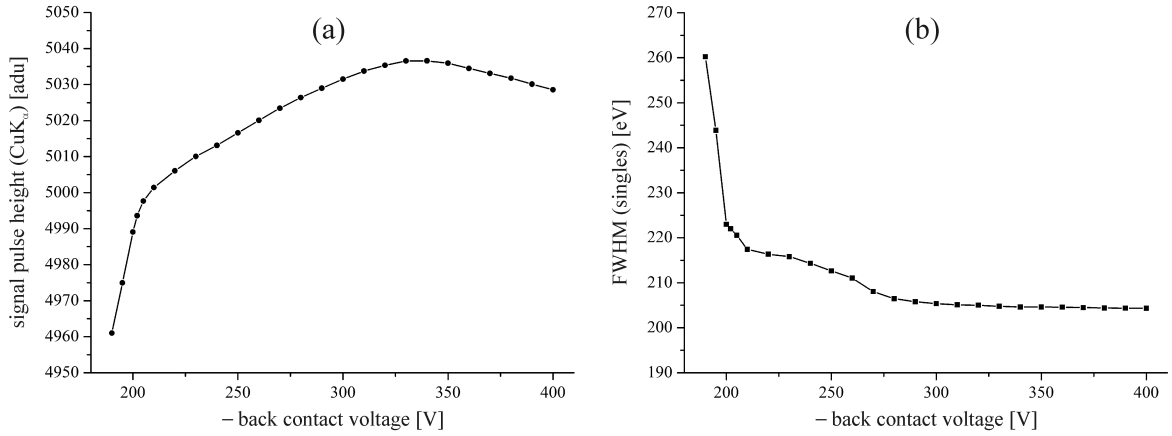

Figure 3.16: (a) Pulse height of CuK$_\alpha$ radiation and (b) FWHM of the corresponding CuK$_\alpha$ single peak for a variable potential at the pnCCD back side. The results refer to a direct fit of the photo peak with a Gaussian after gain and CTI corrections.

A more negative value of the potential at the back contact leads to a higher signal amplitude with a relative shift below 1% compared to the pulse height measured at standard operation conditions with a back contact voltage of −230 V (figure 3.16(a)). This behavior is caused by a change of the potential in the vicinity of the readout anode resulting in a higher detectable voltage drop, whereas the number of generated electrons remains unaffected. At the most positive back side potential of −190 V, the CuK$_\alpha$ photo peak does not show a Gaussian profile anymore, i.e. the achieved energy resolution is markedly degraded in this situation (figure 3.16(b)). Towards the most negative back contact voltage of −400 V, the width of the CuK$_\alpha$ single peak reaches a constant value of 205 eV (FWHM) which is slightly improved in relation to the width of 215 eV (FWHM) previously obtained for the used gain setting in the X-ray spectroscopy mode. The reduced FWHM can be explained by the fact that at enhanced back side potentials, the charge clouds approaching the pixel structure are confined to smaller radii. Hence, the event pattern distributions contain larger amounts of single events resolved with the lowest possible noise contribution. In this way, based on the applied calibration method taking into account single events and double events with a charge splitting parallel to the transfer direction, the energy resolution can be effectively improved.
Under the condition of a successively decreased back contact voltage, the X-ray imaging mode of the pnCCD was tested in the course of a high count rate experiment. For that purpose, the IμS was placed in such a way that the focal plane of the doubly diffracted beam and the detection plane coincided within the achievable experimental accuracy. Thus, the intense monochromatic X-ray beam could approximately be focussed on a single pixel close to the center of the pnCCD. The photon flux incident on the detector was tuned to a constant value

of $3.5 \cdot 10^6$ cps by means of appropriate high voltage and current settings for the IμS and a suitable choice of the damping Al filter. Considering the reduced sensitivity of the pnCCD with a quantum efficiency of 65% for CuK$_\alpha$ radiation according to figure 2.13, the average overall count rate amounted to about 11400 cpf in this experiment. In order to guarantee a sufficiently wide amplitude range for this count rate, the pnCCD was operated in the same gain mode (1/256 of the maximum gain combined with 6-fold CDS) as previously used for the analyses of the Si 111 reflection discussed in chapter 3.2. At this gain setting, one single photon contained in the doubly diffracted beam of the IμS generates a signal pulse height of about 60 adu. In the X-ray spectroscopy mode, the integral number of collected electrons associated with a count rate of 11400 cpf gives rise to massive charge spilling over an area of 48×3 pixels. Figure 3.17 shows the dependence of the detected integrated signal on the back side potential for selected values of the applied back contact voltage.

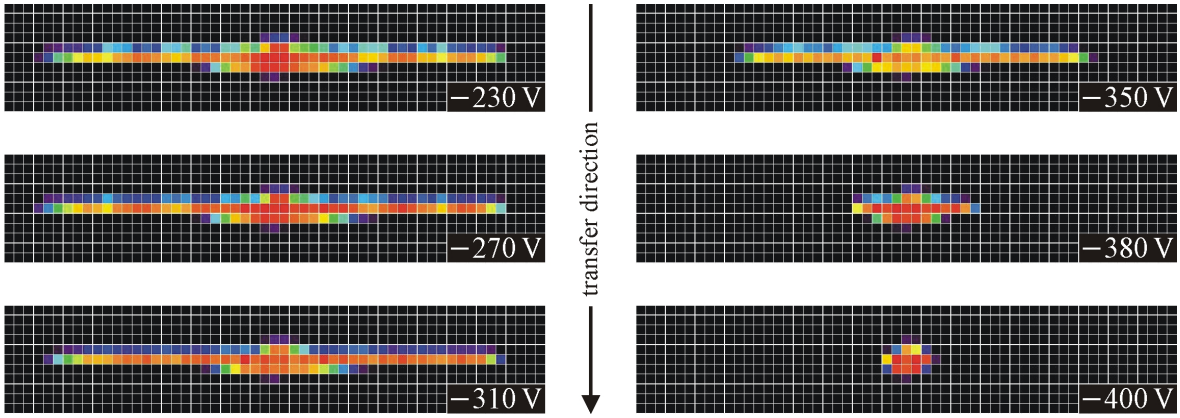

Figure 3.17: Integrated signal of the intense monochromatic X-ray beam provided by the IμS with an average count rate of 11400 cpf at different values of the back contact voltage. The displayed areas have a size of 55×11 pixels. The measured signals are again related to a linear color scale without normalization to each other.

As a consequence of the fact that the incident X-ray beam could not be focussed exactly on the center of an individual pixel, the obtained charge distributions exhibit a slight asymmetry along the transfer direction referred to the row in which the illuminated pixel is located. The stepwise reduction of the back side potential to more negative values creates a deeper potential well for the storage of electrons in each pixel, whereby the potential minimum is shifted in the direction of the detector surface. Under these circumstances, larger amounts of charges can be collected within the center pixel as well as in the neighboring pixels. Hence, a more negative back contact voltage constricts the integrated signal in the charge spilling direction. In that respect, the effect of the back side potential becomes more pronounced for applied values below −325 V. In the final configuration with a back contact voltage of −400 V, the horizontal extension of the charge distribution is reduced to a size of 5×3 pixels. In this case, the pnCCD is operated in the X-ray imaging mode characterized by the highest possible count rate capability of a pixel.

3.3.3 Dynamic range

In order to determine the maximum number of electrons that can be stored within a single pixel of the pnCCD in the X-ray imaging mode, the recorded data sets, comprising 300 dark frames and 5000 signal frames for each value of the applied back contact voltage, were analyzed in a more quantitative way. To this end, the gain and CTI factors extracted from the measurement of the CuK_α signal in the SPC mode leading to the graphs of figure 3.16, served to correct the raw amplitudes after noise, offset, and common mode subtraction. Moreover, due to the fact that only the information about the absolute numbers of detected electrons is relevant in this experiment, the calculated amplitudes were not recombined to individual multi-photon hits. The characteristics of the integrated charge distributions of figure 3.17, which indicate the pnCCD response in the X-ray imaging mode, are depicted in figure 3.18.

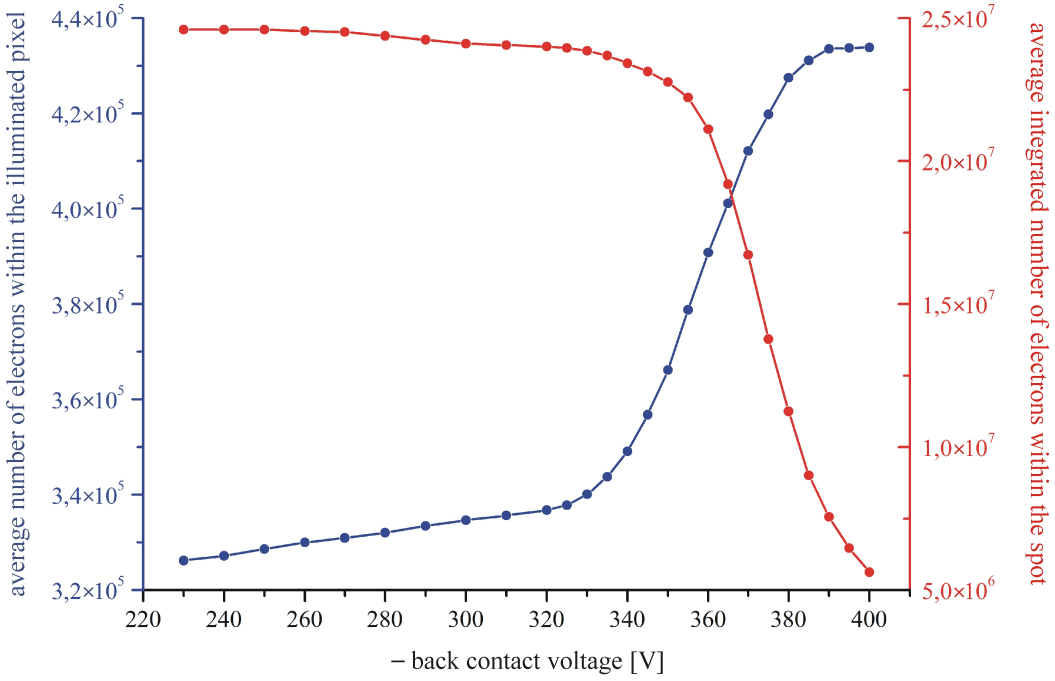

Figure 3.18: Effect of the pnCCD back contact voltage on the average CHC of the illuminated pixel (blue curve) and on the normalized integrated spot signal (red curve).

The average number of electrons stored within the illuminated pixel (figure 3.18, blue curve), reflecting the effective CHC in this measurement, scales with the inverse horizontal extension of the integrated charge signals in figure 3.17. In comparison to the result (3.8) obtained in the case of minor charge spilling at a back contact voltage of $-230\,\mathrm{V}$, the inset of the CHC is slightly increased to $\mathrm{CHC} \approx 325000$. The CHC enhancement can be classified into two separate regions with a linear rise above $-325\,\mathrm{V}$ and a stronger increase below $-325\,\mathrm{V}$, where a more pronounced effect of the back contact voltage on the integrated charge distribution is

observed. In the X-ray imaging mode, a constant value of

$$\mathrm{CHC} \approx 435000 \tag{3.9}$$

can be deduced at a back contact voltage of −400 V corresponding to a relative enhancement of 45% with respect to CHC ≈ 300000 in the X-ray spectroscopy mode. The relatively small increase of the CHC correlates with the measured shape of the total charge signal integrated over the complete spot area in which charge spilling occurred for a particular value of the back side potential (figure 3.18, red curve). In the voltage range above −325 V, the overall number of collected electrons shows a slowly decaying behavior with a relative decrease of about 3%. As soon as the stronger effect of the applied back contact voltage on the horizontal spread of the integrated charge distribution becomes manifest below −325 V, larger electron densities are generated in the vicinity of the illuminated pixel giving rise to a significant drop of the integrated spot signal. In this case, compared to the overall amplitude measured in the X-ray spectroscopy mode, the absolute number of detectable charges in the X-ray imaging mode is reduced to about 22% of its original value.
The successive decay of the integrated signal with a gradually lowered back side potential is caused by unwanted charge loss effects at the front side of the pnCCD. In the course of a decreasing back contact voltage, the potential well, in which the electrons are stored, is shifted in the direction of the detector surface. If the distance between the potential minimum and the surface becomes too small, some of the collected charges are pushed into the MOS gates located between the p^+ registers at the front side, where they disappear [36]. The so-absorbed electrons are no longer available for the transfer to the frame store area and therefore do not contribute to the measured signal. An optimized X-ray imaging mode of the pnCCD with a higher usable single-pixel CHC avoiding charge loss effects can be realized by applying a sufficiently negative voltage to the MOS gates in order to create a repulsive potential for the electrons at the detector surface and adapting the shape of the storage potential [36]. Under the above-discussed conditions, the achievable dynamic range in the full image mode with a frame rate of 196 Hz is limited by a maximum integral count rate of nearly 40000 cps per pixel for 8 keV X-rays. However, the information about absolute intensities can only be maintained in terms of the remaining integrated spot signal produced by those charges that do not disappear in the MOS gates.

4 Application of pnCCDs in macromolecular crystallography

X-ray structure analyses of crystalline materials are based on the precise detection of a large number of Bragg peaks generated by the sample. As a consequence of X-ray exposure, the crystal gives rise to Laue spots whenever the Bragg condition for the elastic reflection of X-rays from the lattice planes of the sample is fulfilled. In this case, a Bragg peak associated with a particular lattice plane can only be observed if the crystal is in the correct orientation referred to the primary beam direction. Conventional techniques to investigate crystalline structures of macromolecules rely on the illumination of the sample with monochromatic synchrotron radiation of high brilliance. Therefore, the crystal needs to be rotated in a well-defined way in order to collect a sufficient number of Laue spots in the monochromatic mode. Since the incident X-ray energy is known, the Laue patterns of the crystal can be recorded by means of area detectors without energy resolution. Nowadays, image plates and CCD detectors allow fully automated methods for fast structure analyses of protein crystals using high-performance goniometer systems for precise sample alignment and rotation [64].
From a conceptual point of view, the pnCCD offers new techniques to investigate crystalline materials by means of energy-dispersive Laue diffraction (EDLD) experiments which exploit the possibility to measure the Laue spot positions and energies simultaneously in the course of a white-beam exposure of the sample. Under this circumstance, the use of a continuous incident X-ray spectrum gives rise to enhanced spot densities within the detection plane providing a larger amount of accessible structural information about the crystal. Hence, if the number of collected reflections is sufficiently large, the pnCCD enables a direct determination of the crystallographic unit cell of the sample as well as a quantitative characterization of polycrystalline materials within single-shot experiments.
Presently, the routine use of a pnCCD for EDLD suffers from the generation of unhandily large raw data sets in the GB range and from time-consuming processing steps which are required to extract the desired structural information. For future applications, the eROSITA pnCCD system will be equipped with special multi-core processors, so-called graphics processing units (GPUs) [65]. GPUs perform a fast visualization of the accumulated data volume in near real-time favored by a significant gain of computational power compared to central processing units (CPUs). The applied algorithms are based on a particular software framework which realizes various processing graphs ensuring a fast treatment of the image-like pnCCD-generated data in a massively parallel fashion [66]. In the concrete case of an EDLD experiment, this framework is designated to analyze individual Bragg reflections in terms of their detected positions

and energies, to use the obtained information for unit-cell determination, and to extract the integrated intensities of the pre-indexed Laue spots.
In this part, the necessary steps to process pnCCD data sets being incurred in typical EDLD experiments with white synchrotron radiation, which allow complete analyses of recorded Laue patterns, are discussed. The presented methods include the required routines for unit-cell calculation and indexing as well as for the determination of absolute spot intensities based on an appropriate statistical treatment of pile-up events. Taking into account the achievable accuracies of the lattice constants and experimental structure-factor amplitudes, the possibilities to investigate polycrystals and macromolecular structures on an atomic level are demonstrated by the example of tetragonal hen egg-white lysozyme (HEWL) crystals. For that purpose, a user-defined model of the crystal can be refined against the obtained set of measured structure-factor amplitudes. The developed principles represent the basis for GPU-supported data analyses and can be applied to any kinds of EDLD experiments, provided that the local count rates at the Laue spot positions are sufficiently low to maintain the information about the diffracted energies and intensities.

4.1 Energy-dispersive Laue diffraction

The analysis of crystal structures by means of X-ray diffraction, regardless of whether the experiment is performed in the monochromatic mode or in the white-beam mode, relies on the evaluation of individual Bragg peaks in reciprocal-space coordinates. Since the real lattice and the reciprocal lattice of a crystalline material are uniquely related to each other, the unit cell of the sample results from the 3D information delivered by the pnCCD after conversion into the corresponding data volume in reciprocal space. In comparison to conventional techniques, EDLD offers the clear advantage that the Bragg condition is fulfilled for a significantly larger number of reflections independent of the crystal orientation relative to the incident X-ray beam. For this reason, the unit cell can be deduced from a single-shot exposure of the sample to white synchrotron radiation at fixed scattering geometry without any rotation steps applied to the crystal. The first EDLD experiment using a pnCCD was performed on an inorganic γ-$LiAlO_2$ single crystal in transmission geometry, whereby the expected tetragonal unit cell as well as the associated kinematical structure-factor amplitudes could be reproduced with a satisfactory precision [6].

4.1.1 Real lattice and reciprocal lattice

The real lattice of a three-dimensional crystal, to be experimentally determined by means of EDLD, is spanned by three translations $\vec{a}_1$, $\vec{a}_2$, and $\vec{a}_3$ ascribed to a characteristic group of atoms which forms the basis of the lattice. An ideal crystal is then generated by an infinite periodic arrangement of this basis in the directions of $\vec{a}_1$, $\vec{a}_2$, and $\vec{a}_3$. In that respect, two arbitrary lattice points of the crystal can be connected with each other by a translation vector

$$\vec{T} = u_1\vec{a}_1 + u_2\vec{a}_2 + u_3\vec{a}_3 \ , \tag{4.1}$$

where u_1, u_2, and u_3 are integers. Referred to the chosen set $\{\vec{a}_i\}$, provided that the origin of the corresponding lattice point is suitably defined, the position vector of a single atom j contained in the basis can be expressed by

$$\vec{r}_j = x_j\vec{a}_1 + y_j\vec{a}_2 + z_j\vec{a}_3 \tag{4.2}$$

with $0 \leq x_j, y_j, z_j \leq 1$. In general, the crystallographic unit cell of a lattice is not uniquely specified since the crystal can be spanned by many different sets $\{\vec{a}_i\}$ of translations. For the real description of a lattice, only primitive unit cells which enclose one single lattice point and thus comprise the common minimum volume

$$V = |\,\vec{a}_1 \cdot (\vec{a}_2 \times \vec{a}_3)\,| \tag{4.3}$$

are of interest. The conventional unit cell ascribed to a lattice structure is characterized by the shortest three non-coplanar translations $a_1 = |\vec{a}_1|$, $a_2 = |\vec{a}_2|$, and $a_3 = |\vec{a}_3|$ defining the lattice constants of the crystal. The cell angles enclosed by $\vec{a}_1$, $\vec{a}_2$, and $\vec{a}_3$ are usually denoted as $\alpha_1 = \angle(\vec{a}_2, \vec{a}_3)$, $\alpha_2 = \angle(\vec{a}_3, \vec{a}_1)$, and $\alpha_3 = \angle(\vec{a}_1, \vec{a}_2)$. In the case of a symmetrical basis, seven crystal systems are distinguished within 14 special lattice types, so-called Bravais lattices, according to their possible geometries. For general bases, the application of non-translative symmetry operations like reflections, rotations, and inversions to the atomic basis leads to 230 space groups which are listed in the International Tables for Crystallography [67]. A further classification of the symmetry associated with crystal structures consists in the distinction of 32 crystallographic point groups.
The primitive basis vectors $\vec{b}_1$, $\vec{b}_2$, and $\vec{b}_3$ spanning the reciprocal lattice of a crystal are uniquely related to the three primitive basis vectors $\vec{a}_1$, $\vec{a}_2$, and $\vec{a}_3$ of the real lattice via [56]

$$\vec{b}_1 = 2\pi\,\frac{\vec{a}_2 \times \vec{a}_3}{\vec{a}_1 \cdot (\vec{a}_2 \times \vec{a}_3)} \quad , \quad \vec{b}_2 = 2\pi\,\frac{\vec{a}_3 \times \vec{a}_1}{\vec{a}_1 \cdot (\vec{a}_2 \times \vec{a}_3)} \quad , \quad \vec{b}_3 = 2\pi\,\frac{\vec{a}_1 \times \vec{a}_2}{\vec{a}_1 \cdot (\vec{a}_2 \times \vec{a}_3)} \quad . \tag{4.4}$$

The reciprocal basis vectors (4.4) have the dimension of an inverse length and are orthogonal to two basis vectors of the real lattice in terms of

$$\vec{a}_i \cdot \vec{b}_j = 2\pi\delta_{ij} \tag{4.5}$$

with $\delta_{ij} = 1$ for $i = j$ and $\delta_{ij} = 0$ for $i \neq j$. Any reciprocal lattice point can be described by a linear combination of the reciprocal basis vectors,

$$\vec{G}_{hkl} = h\vec{b}_1 + k\vec{b}_2 + l\vec{b}_3 \ , \tag{4.6}$$

where h, k, and l are arbitrary integers. These so-called Miller indices, determined by the ratios of the inverse intersections between a crystallographic lattice plane and the real basis vectors, depend on the particular choice of $\vec{a}_1$, $\vec{a}_2$, and $\vec{a}_3$. The reciprocal lattice vector $\vec{G}_{hkl}$ is orthogonal to the considered real lattice plane (hkl). As soon as the reciprocal primitive

basis vectors $\vec{b}_1$, $\vec{b}_2$, and $\vec{b}_3$ have been extracted from the pnCCD data sets, the corresponding real primitive basis vectors can be calculated using the reverse transformation

$$\vec{a}_1 = 2\pi \frac{\vec{b}_2 \times \vec{b}_3}{\vec{b}_1 \cdot (\vec{b}_2 \times \vec{b}_3)} \quad , \quad \vec{a}_2 = 2\pi \frac{\vec{b}_3 \times \vec{b}_1}{\vec{b}_1 \cdot (\vec{b}_2 \times \vec{b}_3)} \quad , \quad \vec{a}_3 = 2\pi \frac{\vec{b}_1 \times \vec{b}_2}{\vec{b}_1 \cdot (\vec{b}_2 \times \vec{b}_3)} \quad . \tag{4.7}$$

The volume of the reciprocal unit cell spanned by the set $\{\vec{b}_j\}$,

$$| \vec{b}_1 \cdot (\vec{b}_2 \times \vec{b}_3) | = \frac{(2\pi)^3}{V} \quad , \tag{4.8}$$

is inversely proportional to the volume (4.3) of the real unit cell. In general, the reciprocal lattice of a crystal exhibits the same symmetry as the real lattice.
A special, highly symmetrical crystal system consists in the tetragonal lattice structure which is characterized by a rectangular unit cell ($\alpha_1 = \alpha_2 = \alpha_3 = 90°$) and two translations of equal magnitude ($|\vec{a}_1| = |\vec{a}_2| = a$, $|\vec{a}_3| = c \neq a$). In this case, the reciprocal crystal lattice also shows a tetragonal symmetry with the parameters $|\vec{b}_1| = |\vec{b}_2| = 2\pi/a$ and $|\vec{b}_3| = 2\pi/c$. In particular, the investigated HEWL crystals belong to the tetragonal space group $P4_32_12$ (No. 96 according to [67]) with the lattice constants $a = 79.1$ Å and $c = 37.9$ Å [68].

4.1.2 Bragg condition and Laue equations

The occurrence of Bragg peaks with discrete energies generated by an ideal crystal is based on elastic reflections of incident X-rays from the crystallographic lattice planes. In the course of X-ray diffraction, a periodic arrangement of identical lattice planes gives rise to constructive interference of X-rays in well-defined directions. If the path difference between two parallel X-ray beams reflected from adjacent lattice planes with the interplanar spacing distance d is an integer multiple of the incident wavelength λ, an intense Laue spot can be measured. With θ denoting the angle enclosed by the primary beam direction and the associated lattice plane according to figure 4.1(a), this requirement can be expressed by the Bragg condition

$$n\lambda = 2d \sin\theta \quad . \tag{4.9}$$

In (4.9), n is to be understood as the order of interference referred to the crystallographic lattice plane with the Miller indices h/n, k/n, and l/n [56]. Without loss of generality, n can be set to unity for all practical cases. The spacing distance is related to the magnitude G_{hkl} of the reciprocal lattice vector (4.6) via

$$d = \frac{2\pi}{G_{hkl}} \quad , \tag{4.10}$$

which, in the case of a tetragonal lattice, yields

$$d = \frac{a}{\sqrt{h^2 + k^2 + l^2 \frac{a^2}{c^2}}} \quad . \tag{4.11}$$

The explicit dependence on h, k, and l justifies the alternative notation d_{hkl} for the interplanar spacing distance that was already used in chapter 3.2.1 to calculate the discrete set of energies reflected from the surface of a cubic Si(111) crystal for the given orientation.

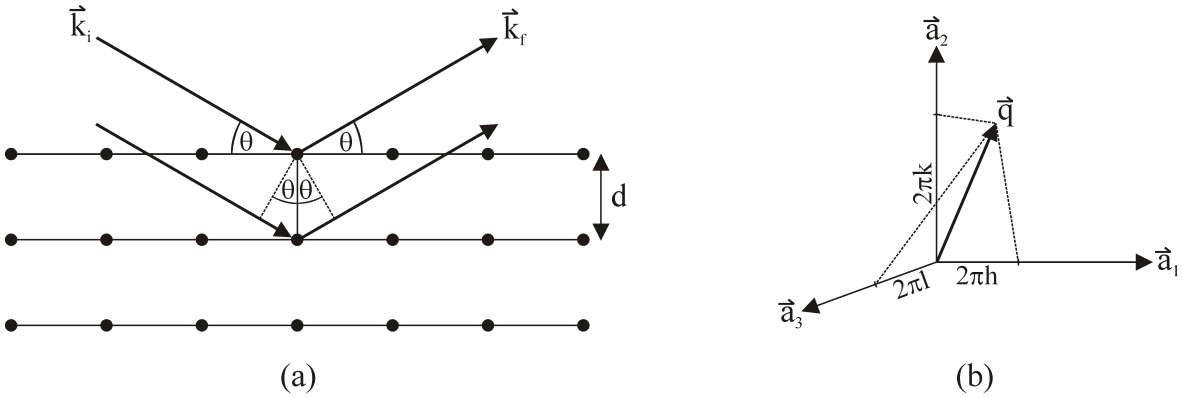

Figure 4.1: (a) Elastic reflection of X-rays from the lattice planes of a crystal according to the Bragg condition. The scattering angle between the directions of the incident beam and the diffracted beam amounts to 2θ. (b) Geometrical interpretation of the equivalent Laue equations.

In addition to (4.9), the diffraction of X-rays by crystalline materials can be described by means of an equivalent formalism based on reciprocal-space coordinates. For that purpose, an individual Bragg peak of energy E is characterized in terms of a scattering vector $\vec{q}$ defined by the difference between the scattered wave vector $\vec{k}_f$ and the incident wave vector $\vec{k}_i$,

$$\vec{q} = \vec{k}_f - \vec{k}_i \ . \tag{4.12}$$

Since the X-ray diffraction by crystals gives rise to elastic reflections of well-defined energies contained in the primary X-ray spectrum as soon as the Bragg condition is fulfilled, the magnitude of the involved wave vectors remains unaffected according to

$$k_i = k_f = \frac{2\pi}{\lambda} = \frac{E}{\hbar c} \ , \tag{4.13}$$

where $\lambda = 2\pi\hbar c/E$ with $\hbar = 6.582 \cdot 10^{-16}$ eVs (Planck constant) and $c = 2.998 \cdot 10^{8}$ m/s (speed of light). Thus, resulting from (4.9) and (4.10), the magnitude of the scattering vector satisfies

$$q = \frac{4\pi}{\lambda} \sin\theta = \frac{2E}{\hbar c} \sin\theta = \frac{2\pi}{d} = G_{hkl} \ . \tag{4.14}$$

Moreover, the scattering vector itself is oriented perpendicular to the reflecting lattice plane, whereby $\vec{q}$ has to be equal to a reciprocal lattice vector of the crystal,

$$\vec{q} = \vec{G}_{hkl} \ . \tag{4.15}$$

Using (4.6) and taking into account the orthogonality relation (4.5), the projection of the scattering vector onto the real basis vectors $\vec{a}_1$, $\vec{a}_2$, and $\vec{a}_3$ leads to

$$\vec{q}\cdot\vec{a}_1 = 2\pi h \quad , \quad \vec{q}\cdot\vec{a}_2 = 2\pi k \quad , \quad \vec{q}\cdot\vec{a}_3 = 2\pi l \quad . \tag{4.16}$$

The set (4.16) consists of the so-called Laue equations and represents an alternative description of X-ray diffraction by an ideal crystal. Hence, the elastic reflection from crystallographic lattice planes can only be possible if $\vec{q}$ is simultaneously located on three cones with the heights $2\pi h$, $2\pi k$, and $2\pi l$ around the directions of $\vec{a}_1$, $\vec{a}_2$, and $\vec{a}_3$ (figure 4.1(b)).
Regarding the conditions of an EDLD experiment, a crystal exposed to white synchrotron radiation selects sharp energies out of the incident X-ray spectrum whenever Bragg's law and the Laue equations are fulfilled giving rise to secondary X-ray beams which are distributed over the complete solid angle. In this situation, first-order Bragg peaks occur if the Miller indices h, k, and l associated with the set of diffracting lattice planes are coprime. However, depending on the crystal orientation and the spectral shape of the primary X-ray beam, reflections of higher orders can also be measured. In such cases, either the energy required to excite the corresponding first-order reflection is not contained within the incident spectrum, e.g. due to absorption effects along the beam path, or the reflection is forbidden for the present crystal structure and therefore of negligible intensity. An example of the latter situation is the non-detectable signal of the Si 222 reflection in the experiment discussed in chapter 3.2.1.
In general, if a first-order reflection hkl with the energy E is excited, Bragg peaks of higher orders n can be identified in terms of the Miller indices nh, nk, and nl and the energies nE as a consequence of (4.14)-(4.16). As the diffraction is caused by parallel lattice planes, different orders are reflected into the same direction resulting in a measurable set of discrete energies which are integer multiples of the first-order energy E.
Exploiting the 3D resolution of the pnCCD in EDLD experiments with white X-rays, the scattering vector ascribed to a detected Laue spot can be directly extracted since the combined position and energy information provides the direction and the magnitude of $\vec{q}$ at the same time. As soon as the unit cell of the investigated crystal spanned by the real basis vectors $\vec{a}_1$, $\vec{a}_2$, and $\vec{a}_3$ is known, the complete indexing of the recorded Laue pattern follows from (4.16) applied to every single Bragg reflection.

4.1.3 Kinematical scattering theory

For the experimental determination of crystallographic unit cells from pnCCD data sets, the evaluation of individual Laue spot positions and energies is adequate. In contrast, the gain of structural information about the sample on an atomic scale relies on analyses of the integrated intensities I_{hkl} coming along with the previously indexed set of identified reflections. In conventional applications of X-ray structure analysis performed in the monochromatic mode, the crystal itself needs to be rotated many times in order to collect a sufficiently large number of measured spot intensities. The obtained information is then converted into absolute structure-factor amplitudes by means of appropriate normalization procedures which

are required to create an electron-density map of the crystal and to refine the pre-defined atomic model against the observed data.
The structural deviation of real crystals from the perfectly periodic arrangement of identical unit cells becomes manifest in the presence of slightly disoriented mosaic blocks. For such kinds of systems, the elastic scattering of X-rays by electrons can be well-approximated by considering one single diffraction process inside the crystal. Within the scope of kinematical scattering theory, which is applicable to small, ideally imperfect crystals, multiple scattering effects are neglected. In this description, the integrated intensity I_{hkl} of a Bragg peak hkl is proportional to various angular- and energy-dependent factors according to

$$I_{hkl} \propto \varepsilon I_0 |F_{hkl}|^2 LPA \ . \tag{4.17}$$

Here, ε is the quantum efficiency of the pnCCD at the scattering angle 2θ and the energy E of the reflection given by (2.17), I_0 denotes the intensity of the incident white X-ray beam at this energy, and F_{hkl} is the kinematical structure factor [56]

$$F_{hkl} = \sum_j f_j e^{-i\vec{G}_{hkl}\vec{r}_j} = \sum_j f_j e^{-2\pi i(hx_j+ky_j+lz_j)} \tag{4.18}$$

with the atomic form factor f_j of the atom j defined by

$$f_j = \int_V n_j(\vec{r}-\vec{r}_j)\, e^{-i\vec{G}_{hkl}(\vec{r}-\vec{r}_j)}\, dV \ . \tag{4.19}$$

The contribution of this atom to the electron density at the position $\vec{r}$ within the crystal is incorporated by the term $n_j(\vec{r}-\vec{r}_j)$ in the atomic form factor. The Lorentz factor L in (4.17) takes into account that in real X-ray diffraction experiments, the Bragg condition cannot only be fulfilled by one specific wavelength λ and one single incident angle θ, but within narrow wavelength and angular bands enclosing these values. Previous studies have shown that the Lorentz factor depends on the method used to analyze the crystal, i.e. it is effectively different for measurements performed in the monochromatic mode and in the white-beam mode as well as for situations with a stationary sample and a rotating sample. In the present case of a spatially fixed crystal exposed to white X-rays, the Lorentz factor amounts to [69]

$$L = \frac{\lambda^2}{\sin^2\theta} \ . \tag{4.20}$$

Another influence on the integrated intensity arises from polarization effects associated with the nature of the incident radiation that are summarized in the polarization factor [70]

$$P = \tfrac{1}{2}(1+\cos^2 2\theta) - \tfrac{1}{2}\tau\cos 2\rho \sin^2 2\theta \ . \tag{4.21}$$

The first term in (4.21), which represents the contribution of an unpolarized X-ray beam, also has to be applied to diffraction data collected in experiments with X-rays generated by a

conventional X-ray tube. The second term in (4.21) describes the attenuation of the scattered intensity due to the polarization of synchrotron radiation, where

$$\tau = \frac{I_{\parallel} - I_{\perp}}{I_{\parallel} + I_{\perp}} \tag{4.22}$$

is the degree of polarization given by the ratio of the components with a polarization direction parallel ($I_{\parallel}$) and perpendicular ($I_{\perp}$) to the plane of the electron orbit in a storage ring. For bending magnet radiation, the component $I_{\perp}$ vanishes in the orbital plane [71], i.e. $\tau \approx 1$ holds if the cross section of the primary synchrotron beam is sufficiently small. The angle

$$\rho = \arctan \frac{z}{y} \tag{4.23}$$

denotes the position of the Bragg peak in the detection plane measured from the horizontal axis. The notation in (4.23) refers to a coordinate system which is defined in such a way that the incident beam direction corresponds to the x-axis, whereas y and z are the horizontal and vertical directions of the pnCCD plane. For typical geometries of EDLD experiments on HEWL crystals, the applied polarization factors have values in the range $0.9 < P < 1$.
The last factor A in (4.17) takes into account absorption effects within the sample and its surroundings consisting of a thin-walled glass capillary. Since HEWL crystals contain organic macromolecules of solely light elements, the absorption of hard X-rays with relevant energies above 9 keV inside the sample environment was neglected for further corrections of integrated Laue spot intensities assuming $A \approx 1$.
In macromolecular crystallography, various parameters are used to characterize the quality of diffraction data [72]. The achieved true resolution, defined as the minimum distance between two objects in a crystal that can be imaged within the obtained electron-density map, is often approximated by the nominal resolution

$$d_{\min} = \frac{\lambda}{2 \sin \theta_{\max}} = \frac{2\pi}{q_{\max}} \ . \tag{4.24}$$

The first expression in (4.24) corresponds to Bragg's law (4.9) and refers to data collection at a fixed wavelength λ, where $2\theta_{\max}$ is to be understood as the maximum detected scattering angle limited by experimental constraints. The more general second expression, resulting from (4.14), can be applied to Laue diffraction data recorded in the white-beam mode by means of the pnCCD, where the scattering angle and the wavelength are varying measurands.
Another quality indicator describes the discrepancy between the observed structure-factor amplitudes $\{|F_{\mathrm{obs}}|\}$ and the ones calculated from the atomic model $\{|F_{\mathrm{calc}}|\}$. The goodness of the structure refinement is quantified in terms of the crystallographic R-factor

$$R = \frac{\sum_{hkl} ||F_{\mathrm{obs}}| - |F_{\mathrm{calc}}||}{\sum_{hkl} |F_{\mathrm{obs}}|} \ , \tag{4.25}$$

where $\{|F_{\mathrm{obs}}|\}$ and $\{|F_{\mathrm{calc}}|\}$ need to be on the same scale.

4.2 Unit-cell determination from pnCCD data sets

In order to deduce the conventional unit cell of the investigated crystal from the recorded Laue pattern, a suitable processing sequence has to be applied to the pnCCD-generated data sets. In a first step, the simultaneous position and energy information about individual Bragg reflections is exploited to determine the reciprocal lattice of the crystal in the externally defined coordinate system. Subsequently, the primitive unit cells contained in this data volume are reduced to the associated unit cells with the shortest three non-coplanar translations by means of crystallographic standard methods and fitted to the remaining spot distribution in the course of a least-squares refinement. In the final step, after conversion from reciprocal-space to real-space coordinates, the reduced unit cells are refined in such a way that the Laue pattern is indexed with the highest accuracy. The so-obtained unit cell with the best matching real lattice parameters can be used for a structure refinement based on the knowledge of experimental structure-factor amplitudes.

4.2.1 Cell extraction

The 3D information delivered by the pnCCD in the case of a stationary sample consists in the energy resolution of individual Bragg peaks and their spatial resolution yielding two position coordinates in the detection plane for each collected reflection. In general, the event distribution needs to be analyzed within small pixel areas enclosing the identified Laue spots in terms of both the image and the spectum cut according to figure 2.12. For that purpose, quadratic regions are selected around the centers of the reflections whose effective sizes depend on the cross section of the primary X-ray beam, the diffracted energy, and the scattering angle. Taking into account the parallax effects discussed in chapter 2.3.4, spot areas with an extension of 5×5 pixels seem to be convenient in the case of EDLD experiments on HEWL crystals with a beam size of $100\times100\,\mu\mathrm{m}^2$.
The Laue spot energies can then be extracted by analyzing the spectral peaks detected in these pixel areas in calibrated units and fitting them by suitable Gaussians. For cell extraction, the considerations are restricted to the dominant Bragg peaks with the highest integrated intensities including only single-photon hits in the sense of SPC. The applied Gaussian fit provides the spot energy $E \pm \delta E$, where the error δE is estimated by the calculated standard deviation σ_E which has a value in the range of $0.01E$ according to the results of chapter 3.1.6. In contrast, the position information about individual Laue spots can be obtained from the image cut in the vicinity of the fitted energy by assigning two center-of-mass coordinates to the amplitude distribution measured in the selected pixel area. This method allows to assign horizontal and vertical coordinates in the form $y \pm \delta y$ and $z \pm \delta z$ to the investigated reflection. Owing to energy- and angular-dependent parallax errors, the achieved accuracies δy and δz are in the range of the pixel width.
For unit-cell computations, the origin of the experimental coordinate system was defined as the interaction point of the white synchrotron beam, incident along the positive x-direction, with the HEWL crystal. Laue patterns of the sample were recorded in the y-z-plane at the

distance $x \pm \delta x$ from the crystal, where y and z describe the horizontal and vertical pixel directions. In this coordinate system, the incident and reflected wave vectors are given by

$$\vec{k}_i = \frac{E}{\hbar c}\,\vec{e}_x \tag{4.26}$$

$$\vec{k}_f = \frac{E}{\hbar c}\begin{pmatrix} x/s \\ y/s \\ z/s \end{pmatrix} \tag{4.27}$$

with

$$s = \sqrt{x^2 + y^2 + z^2} \tag{4.28}$$

denoting the distance between the crystal and the position at which the Laue spot with the spatial coordinates x, y, and z was detected. Hence, inserting (4.26) and (4.27) into (4.12), the scattering vector $\vec{q}$ of the considered reflection can be obtained from

$$\hbar c\vec{q} = \hbar c \begin{pmatrix} q_x \\ q_y \\ q_z \end{pmatrix} = \frac{E}{s}\begin{pmatrix} x-s \\ y \\ z \end{pmatrix} \quad . \tag{4.29}$$

In the above-defined coordinate system, q_x is negative. Taking into account the experimental errors δx, δy, and δz of the position measurement and δE of the energy determination, the corresponding components δq_x, δq_y, and δq_z of the vector $\delta\vec{q}$, which represents the limited reciprocal-space resolution of individual Bragg peaks, result from

$$\hbar c\delta q_x = \sqrt{\left(\frac{x-s}{s}\delta E\right)^2 + \frac{E^2}{s^6}\Big\{\big[(y^2+z^2)\delta x\big]^2 + (xy\delta y)^2 + (xz\delta z)^2\Big\}} \tag{4.30}$$

$$\hbar c\delta q_y = \sqrt{\left(\frac{y}{s}\delta E\right)^2 + \frac{E^2}{s^6}\Big\{(xy\delta x)^2 + \big[(x^2+z^2)\delta y\big]^2 + (yz\delta z)^2\Big\}} \tag{4.31}$$

$$\hbar c\delta q_z = \sqrt{\left(\frac{z}{s}\delta E\right)^2 + \frac{E^2}{s^6}\Big\{(xz\delta x)^2 + (yz\delta y)^2 + \big[(x^2+y^2)\delta z\big]^2\Big\}} \quad . \tag{4.32}$$

Via (4.29)-(4.32), the accessible 3D information about the complete number of reflections collected within the Laue pattern of the crystal is translated into a set $\{\vec{q}_i \pm \delta\vec{q}_i\}$ that spans small reciprocal-space volumes around the set $\{\vec{q}_i\}$ of measured reciprocal lattice points. As soon as the shortest three basis vectors $\vec{b}_1$, $\vec{b}_2$, and $\vec{b}_3$ of this dot-like distribution are known, the real unit cell of the crystal can be calculated using (4.7). Previous investigations have shown that to this end, many triples of three distinct reciprocal lattice points $\vec{q}_i$ need to be analyzed by means of suitable routines for cell reduction and indexing. Crystallographic reduction procedures are essential to find the conventional unit cell with the shortest non-coplanar translations since in general, an arbitrary choice of three reciprocal lattice vectors out of the set $\{\vec{q}_i\}$ does not have this property. The applied methods leading to the correct unit cell of the crystal comprise two reduction steps, known as Delaunay reduction (chapter 4.2.2)

and Gaussian reduction (chapter 4.2.3), followed by an appropriate least-squares refinement of the reduced basis (chapter 4.2.4). In order to successfully extract the conventional unit cell associated with the present crystal structure, already the initially selected set of three reciprocal lattice vectors needs to span a primitive unit cell of the measured lattice. In the last step of unit-cell determination, it is required that the refined basis yields the most precise indexing of the recorded Laue pattern.

4.2.2 Delaunay reduction

The starting point of the reduction method developed by Delaunay [73] is any set $\{\vec{b}_1, \vec{b}_2, \vec{b}_3\}$ of primitive basis vectors completed to the quadruple $\{\vec{b}_1, \vec{b}_2, \vec{b}_3, \vec{b}_4\}$ by adding the vector

$$\vec{b}_4 = -\vec{b}_1 - \vec{b}_2 - \vec{b}_3 \ . \tag{4.33}$$

The six scalar products of two distinct vectors belonging to this quadruple are denoted by

$$h_{ij} = \vec{b}_i \cdot \vec{b}_j \quad (i \neq j) \ . \tag{4.34}$$

As long as the set $\{h_{ij}\}$ contains a positive value, the Delaunay algorithm transforms the quadruple $\{\vec{b}_1, \vec{b}_2, \vec{b}_3, \vec{b}_4\}$ to a reduced cell described by the sorted quadruple $\{\vec{b}_{1d}, \vec{b}_{2d}, \vec{b}_{3d}, \vec{b}_{4d}\}$ with $b_{1d} \leq b_{2d} \leq b_{3d} \leq b_{4d}$. The iterative procedure starts by changing the sign of one of those two vectors giving rise to $h_{ij} > 0$, leaving the other vector unchanged, and adding the vector, whose sign was changed, to the remaining two vectors of the initial quadruple. In the special case of $h_{12} > 0$ (figure 4.2), this transformation is expressed by

$$\vec{b}_1 \ \rightarrow \ -\vec{b}_1 \tag{4.35}$$
$$\vec{b}_2 \ \rightarrow \ \vec{b}_2 \tag{4.36}$$
$$\vec{b}_3 \ \rightarrow \ \vec{b}_3 + \vec{b}_1 \tag{4.37}$$
$$\vec{b}_4 \ \rightarrow \ \vec{b}_4 + \vec{b}_1 \ . \tag{4.38}$$

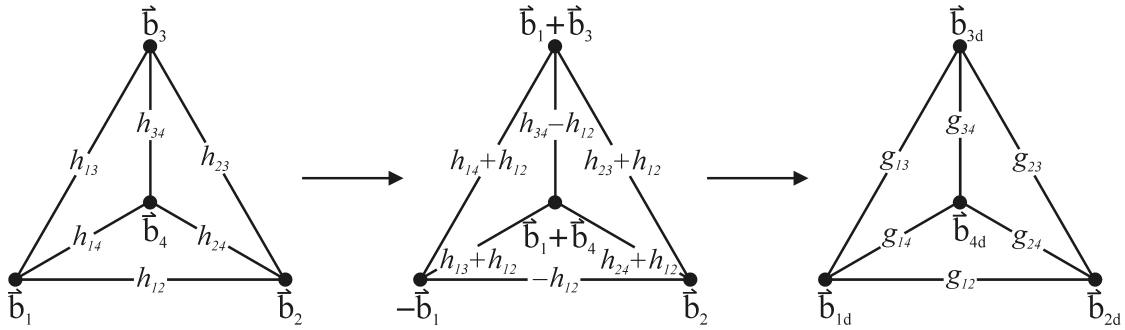

Figure 4.2: Series of single steps in the Delaunay reduction, provided that h_{12} has a positive value. The iterative method stops as soon as the six scalar products g_{ij} $(i \neq j)$ are all negative or zero.

After each single step, the sum of the four vectors included in the obtained quadruple vanishes, whereby a constant cell volume is ensured in the course of the Delaunay reduction. Moreover, the negative sum of the scalar products h_{ij} decreases by h_{12} in each step. In the final situation, in which the algorithm converges, the six scalar products

$$g_{ij} = \vec{b}_{id} \cdot \vec{b}_{jd} \quad (i \neq j) \tag{4.39}$$

related to the reduced quadruple $\{\vec{b}_{1d}, \vec{b}_{2d}, \vec{b}_{3d}, \vec{b}_{4d}\}$ are all negative or zero. If the scalar products g_{ij} are all negative, the Delaunay reduction leads to a unique tri-obtuse cell spanned by the vectors $\vec{b}_{1d}$, $\vec{b}_{2d}$, and $\vec{b}_{3d}$. A discussion of ambiguities arising in the case of $g_{ij} = 0$ for a particular pair of vectors $(\vec{b}_{id}, \vec{b}_{jd})$ can be found in [74] together with an alternative reduction which shows a faster convergence. However, situations with $g_{ij} = 0$ are not further considered since they do not occur for analyses of pnCCD data based on floating-point numbers.

4.2.3 Gaussian reduction

The Delaunay-reduced cell is not necessarily the one with the shortest three non-coplanar translations, i.e. in order to obtain the conventional unit cell of the present crystal structure, another transformation needs to be applied. For that purpose, the reciprocal-space result $\{\vec{b}_{1d}, \vec{b}_{2d}, \vec{b}_{3d}\}$ of the Delaunay reduction is translated into the corresponding tri-acute unit cell $\{\vec{a}_{1d}, \vec{a}_{2d}, \vec{a}_{3d}\}$ in real-space coordinates by means of (4.7). Additionally, the signs of these vectors are defined in such a way that they span a right-handed basis of the real lattice. This unit cell can then be converted into a so-called Minkowski-reduced basis characterized by the three primitive unit-cell vectors with the smallest possible magnitudes [75]. The computation of the conventional unit cell of the lattice is carried out using a three-dimensional realization of an algorithm developed by Gauss [76] which performs successive reduction steps within the $\vec{a}_{1d}$-$\vec{a}_{2d}$-, the $\vec{a}_{1d}$-$\vec{a}_{3d}$-, and the $\vec{a}_{2d}$-$\vec{a}_{3d}$-plane.
Figure 4.3 illustrates the principle of the implemented iterative procedure for the case of a two-dimensional quadratic lattice. The conventional unit cell with the shortest two translations is given by the Minkowski-reduced basis vectors $\vec{a}_{1m}$ and $\vec{a}_{2m}$ which are orthogonal to each other and of the same length. Another (arbitrarily defined) primitive unit cell of the lattice is spanned by the selected acute-angled basis $\{\vec{a}'_1, \vec{a}'_2\}$ with $a'_1 < a'_2$ (figure 4.3(a)). In this situation, the first basis vector $\vec{a}_{2m}$ of the quadratic lattice can be found by subtracting a particular integer multiple n_1 of the vector $\vec{a}'_1$ from $\vec{a}'_2$ according to the transformation

$$\vec{a}'_2 \;\rightarrow\; \vec{a}_{2m} = \vec{a}'_2 - n_1 \vec{a}'_1 \;. \tag{4.40}$$

In (4.40), n_1 results from the requirement that the magnitude a_{2m} of the Minkowski-reduced vector $\vec{a}_{2m}$ is minimized and has a value of 3 (or 4) for the depicted example. As soon as $\vec{a}_{2m}$ is determined, the second basis vector $\vec{a}_{1m}$ can be calculated by the transformation

$$\vec{a}'_1 \;\rightarrow\; \vec{a}_{1m} = \vec{a}'_1 - n_2 \vec{a}_{2m} \;, \tag{4.41}$$

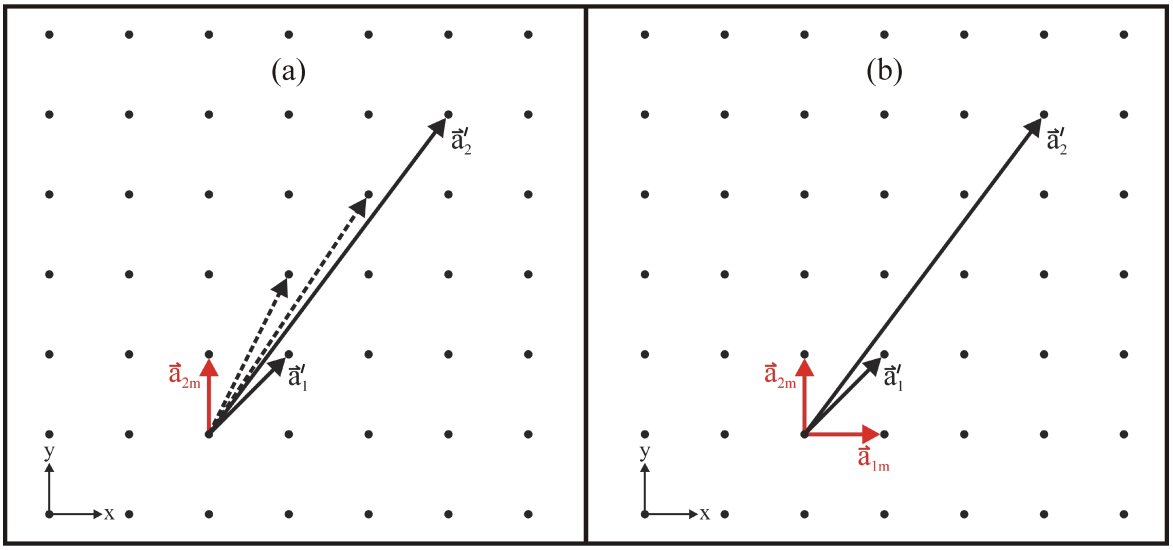

Figure 4.3: Gaussian reduction in the case of a two-dimensional quadratic lattice. The stepwise reduction of the initial basis vectors (a) $\vec{a}'_2$ and (b) $\vec{a}'_1$ leads to the conventional unit cell of the lattice spanned by the shortest possible translations $\vec{a}_{1m}$ and $\vec{a}_{2m}$.

where a suitable integer multiple n_2 of the previously obtained basis vector $\vec{a}_{2m}$ is subtracted from $\vec{a}'_1$. The corresponding minimization of the magnitude a_{1m} is guaranteed by $n_2 = 1$ in the example of figure 4.3(b).
In other cases, for which the initial vectors $\vec{a}'_1$ and $\vec{a}'_2$ span an obtuse-angled basis of the lattice, the Gaussian reduction can be performed in a similar way by adding $n_1\vec{a}'_1$ to $\vec{a}'_2$ in (4.40) and $n_2\vec{a}_{2m}$ to $\vec{a}'_1$ in (4.41), where n_1 and n_2 are assumed to be positive integers. Hence, this iterative procedure is equivalent to applying (4.40) and (4.41) for the minimization of the magnitudes a_{1m} and a_{2m} under the condition that n_1 and n_2 are negative integers. Situations with obtuse-angled bases arise if the sign of one of the vectors $\vec{a}'_1$ and $\vec{a}'_2$ in figure 4.3 is changed or if $n_1 = 4$ steps are used for the first reduction of $\vec{a}'_2$ in figure 4.3(a) which also yields the desired rectangular unit cell of the quadratic lattice.
In general, the subsequent reduction of the real-space Delaunay cell $\{\vec{a}_{1d}, \vec{a}_{2d}, \vec{a}_{3d}\}$ to the Minkowski-reduced basis $\{\vec{a}_{1m}, \vec{a}_{2m}, \vec{a}_{3m}\}$ requires at most one single transformation step in a two-dimensional subspace, whereby, in agreement with the discussions in [74], at least one of the integers n_1 and n_2 is zero. In order to finally extract the three-dimensional conventional unit cell with the shortest translations, the Gaussian algorithm needs to be repeatedly applied within the $\vec{a}_{1d}$-$\vec{a}_{2d}$-, the $\vec{a}_{1d}$-$\vec{a}_{3d}$-, and the $\vec{a}_{2d}$-$\vec{a}_{3d}$-plane.

4.2.4 Unit-cell refinement and indexing

The Minkowski-reduced cell $\{\vec{a}_{1m}, \vec{a}_{2m}, \vec{a}_{3m}\}$ is obtained from a selected triple contained in the set $\{\vec{q}_i \pm \delta\vec{q}_i\}$ of reciprocal lattice vectors associated with the detected Bragg reflections of the crystal. For that purpose, a triple of vectors suitable for unit-cell determination has to

be primitive and, prior to crystallographic reduction, capable of indexing a particular number of Laue spots using (4.16) with an externally specified accuracy. The degree of pre-indexing is typically defined by the condition that about 50% of the Laue pattern can be initially indexed. To this end, the absolute deviations of the calculated Miller indices ascribed to an individual Bragg peak i from integers may amount to at most 0.25 within the reciprocal-space resolution $\delta\vec{q}_i$. In the final step of data processing, the Minkowski-reduced basis is refined by means of a least-squares method including the complete set of collected Laue spots, whereby in the course of reduction and refinement, the fraction of indexed reflections successively increases to a value in the range of 90%. Technically, the conventional unit cell $\{\vec{a}_1, \vec{a}_2, \vec{a}_3\}$ can be calculated by adding a suitable set $\{\delta\vec{a}_{1m}, \delta\vec{a}_{2m}, \delta\vec{a}_{3m}\}$ of vectors with sufficiently small magnitudes $\delta a_{jm} \ll a_{jm}$ $(j = 1, 2, 3)$ to the Minkowski-reduced cell (figure 4.4) according to

$$\vec{a}_1 = \vec{a}_{1m} + \delta\vec{a}_{1m} \quad , \quad \vec{a}_2 = \vec{a}_{2m} + \delta\vec{a}_{2m} \quad , \quad \vec{a}_3 = \vec{a}_{3m} + \delta\vec{a}_{3m} \quad . \tag{4.42}$$

These basis vectors of the crystal lattice yield the Miller indices

$$h_i = \frac{\vec{q}_i \cdot \vec{a}_1}{2\pi} \quad , \quad k_i = \frac{\vec{q}_i \cdot \vec{a}_2}{2\pi} \quad , \quad l_i = \frac{\vec{q}_i \cdot \vec{a}_3}{2\pi} \tag{4.43}$$

of spot i with the errors

$$\delta h_i = \frac{|\delta\vec{q}_i \cdot \vec{a}_1|}{2\pi} \quad , \quad \delta k_i = \frac{|\delta\vec{q}_i \cdot \vec{a}_2|}{2\pi} \quad , \quad \delta l_i = \frac{|\delta\vec{q}_i \cdot \vec{a}_3|}{2\pi} \quad . \tag{4.44}$$

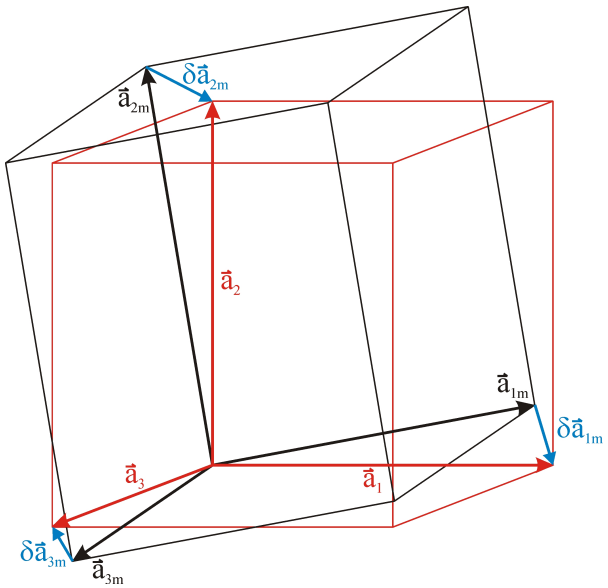

Figure 4.4: Principle of unit-cell refinement. The Minkowski-reduced basis $\{\vec{a}_{1m}, \vec{a}_{2m}, \vec{a}_{3m}\}$ is corrected by the set $\{\delta\vec{a}_{1m}, \delta\vec{a}_{2m}, \delta\vec{a}_{3m}\}$ resulting after a least-squares refinement of the unit cell. The so-obtained basis vectors $\vec{a}_1$, $\vec{a}_2$, and $\vec{a}_3$ provide an indexing of the Laue pattern with the highest possible accuracy.

The refinement of the nine parameters in total contained in the set $\{\delta\vec{a}_{1m}, \delta\vec{a}_{2m}, \delta\vec{a}_{3m}\}$ is carried out under the condition that the deviations of the Miller indices from integer values become as small as possible. Using (4.42)-(4.44), the function

$$\chi^2 = \sum_i \left\{ \frac{(h_i - \widetilde{h}_i)^2}{\delta h_i^2} + \frac{(k_i - \widetilde{k}_i)^2}{\delta k_i^2} + \frac{(l_i - \widetilde{l}_i)^2}{\delta l_i^2} \right\} \tag{4.45}$$

to be minimized in the sense of the applied least-squares method comprises each collected Laue spot, where $\widetilde{h}_i$, $\widetilde{k}_i$, and $\widetilde{l}_i$ denote the neighboring integer numbers of the Miller indices h_i, k_i, and l_i of spot i defined by (4.43). In this way, the set $\{\delta\vec{a}_{1m}, \delta\vec{a}_{2m}, \delta\vec{a}_{3m}\}$ is fitted to the recorded Laue pattern with associated standard deviations given by the 9×9 covariance matrix [77] calculated from (4.45). The conventional unit cell obtained after crystallographic reduction and least-squares refinement can be expressed in terms of (4.42) completed by the set $\{\delta\vec{a}_1, \delta\vec{a}_2, \delta\vec{a}_3\}$ which quantifies the statistical errors of the lattice vectors $\vec{a}_1$, $\vec{a}_2$, and $\vec{a}_3$. The basis $\{\vec{a}_1 \pm \delta\vec{a}_1, \vec{a}_2 \pm \delta\vec{a}_2, \vec{a}_3 \pm \delta\vec{a}_3\}$ finally serves to index the identified Bragg reflections whose Miller indices are rounded to the neighboring integers. Preliminary analyses of various Laue patterns have shown that the best matching unit cell typically provides an indexing of about 90% of the spots with reduced absolute deviations of at most 0.15 from integer values. This cell results from a repeated application of the described reduction and refinement steps to the selected triple of reciprocal lattice points. In general, depending on the initially defined requirements for indexing, different choices of measured scattering vectors may lead to the same conventional unit cell within the experimentally relevant limits.

4.3 Experimental conditions for EDLD on HEWL crystals

Analyses of crystalline materials based on the determination of structure-factor amplitudes according to (4.17) require precise knowledge of the primary X-ray spectrum incident on the sample. For that purpose, the white synchrotron beam available at the EDR beamline at the storage ring BESSY II, which served as a probe of the investigated HEWL crystals, was measured and simulated under the present experimental conditions including absorption effects along the air path of the beam and within the attenuating absorption filters.

4.3.1 EDLD setup at the EDR beamline

The highly brilliant synchrotron beam used for EDLD and XRF experiments at the EDR beamline corresponds to the white bending magnet radiation spectrum emitted by radially accelerated relativistic electrons. At the storage ring BESSY II, operated by the Helmholtz-Zentrum Berlin (HZB), electrons of 1.7186(6) GeV energy are deflected within a homogeneous magnetic field of 1.29932(12) T strength [71] giving rise to a bending radius of about 4.4 m. The generated electromagnetic spectrum ranges continuously from the infrared to the hard X-ray regime with a critical energy of 2.5 keV, where the overall spectral flux is proportional to the number of circulating charges. Usually, the electrons are confined in a spatial structure of

discrete bunches providing the highest emitted intensity in the multi-bunch hybrid mode with storage ring currents between 150 mA and 300 mA. As a consequence of collisions between the electrons and remnant gas molecules within the evacuated storage ring, the current decreases with time and is therefore enhanced to its original value by means of external charge injection after several hours of operation.
At the EDR beamline, the white X-ray component of the synchrotron beam, after traversing a distance of about 30 m from the source point to the experimental hutch, can be used for particular applications. In order to reduce absorption, an ultra-high vacuum with a pressure below 10^{-8} mbar is generated along the beam path and stabilized by a 50 μm(Be) layer and two Kapton foils of 125 μm thickness each [78]. One of these Kapton foils defines the exit window of the synchrotron beam whose presence in the hutch can be controlled via a switched beamshutter. The EDLD experiments themselves were performed in an air environment with the crystal localized at a typical distance in the range of 1 m behind the exit slit. Hence, the real X-ray spectrum at the position of the sample depends on the effective path length of the synchrotron beam in air and is shifted towards higher X-ray energies with increasing distance from the exit window. The beam size and the photon flux incident on the sample can be tuned by means of an aperture system, which provides a rectangular beam cross section, and a set of attenuating absorption filters with different thicknesses. Figure 4.5 shows the geometrical conditions of the experimental setup used for white-beam X-ray exposure of HEWL crystals at the EDR beamline including the pnCCD and the mounting of the sample.

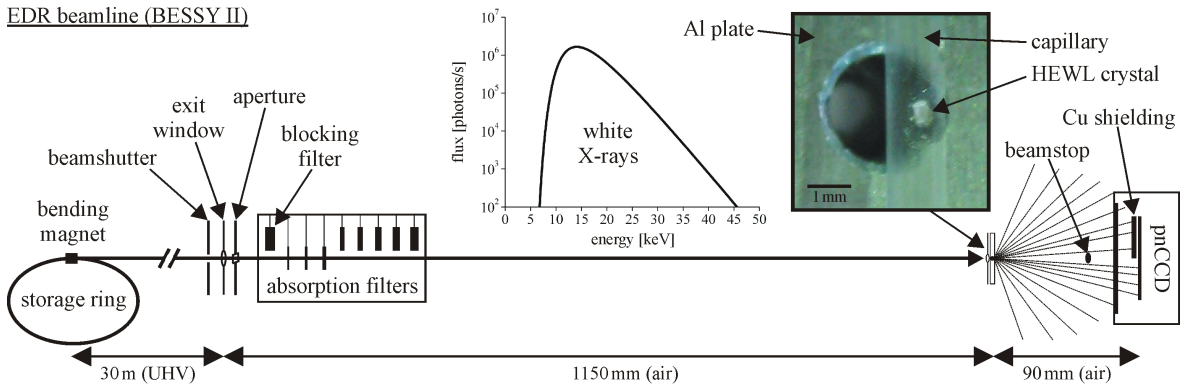

Figure 4.5: Experimental setup for EDLD on HEWL crystals with white synchrotron radiation at the EDR beamline at BESSY II. The sample is kept in a thin-walled glass capillary mounted on top of an Al plate. The Bragg reflections of the crystal with different scattering angles and energies are recorded by means of the pnCCD at a distance of 90 mm behind the sample. The detector chamber is fixed on motorized stages which enable controlled horizontal and vertical translations of the pnCCD within the y-z-plane (not depicted). A Pb beamstop of 1 mm diameter serves to protect the pnCCD from the undiffracted part of the primary beam and to reduce the background level on the detector caused by air-scattered photons.

4.3.2 Incident X-ray spectrum

The X-ray spectrum of the primary white synchrotron beam at the EDR beamline is defined by the energy of the electrons circulating within the storage ring, the deflecting magnetic field strength, and the ring current. In the multi-bunch hybrid mode, the integral X-ray flux of the incident beam behind the exit window is above 10^{11} photons per second and thus not directly measurable with any existing X-ray detector. For this reason, a particular amount of the storage ring operation time at BESSY II is allocated to the Physikalisch-Technische Bundesanstalt (PTB) for calibration purposes at low ring currents in the order of 100 nA. One of these PTB shifts was used to measure the spectrum of the synchrotron beam at EDR by means of the energy-dispersive point detector Roentec X-Flash positioned at a distance of 378 mm from the exit slit. In this experiment, the sensitive area of the Roentec X-Flash was oriented in such a way that the primary synchrotron beam with a quadratic size of $100\times100\,\mu m^2$ entered the detector unit at normal incidence. In order to extract real spectral intensities from this measurement, the recorded signals had to be divided by the quantum efficiency of the Roentec X-Flash which was calculated on the basis of (2.17) with $2\theta = 0°$ taking into account the present device thickness of $450\,\mu$m(Si) and the composition of the entrance window ($8\,\mu$m(Be) + 30 nm(Al)). The so-obtained X-ray spectrum, detected during a total exposure time of 300 s at a mean storage ring current of 76.4 nA, corresponds to the black dotted distribution in figure 4.6.

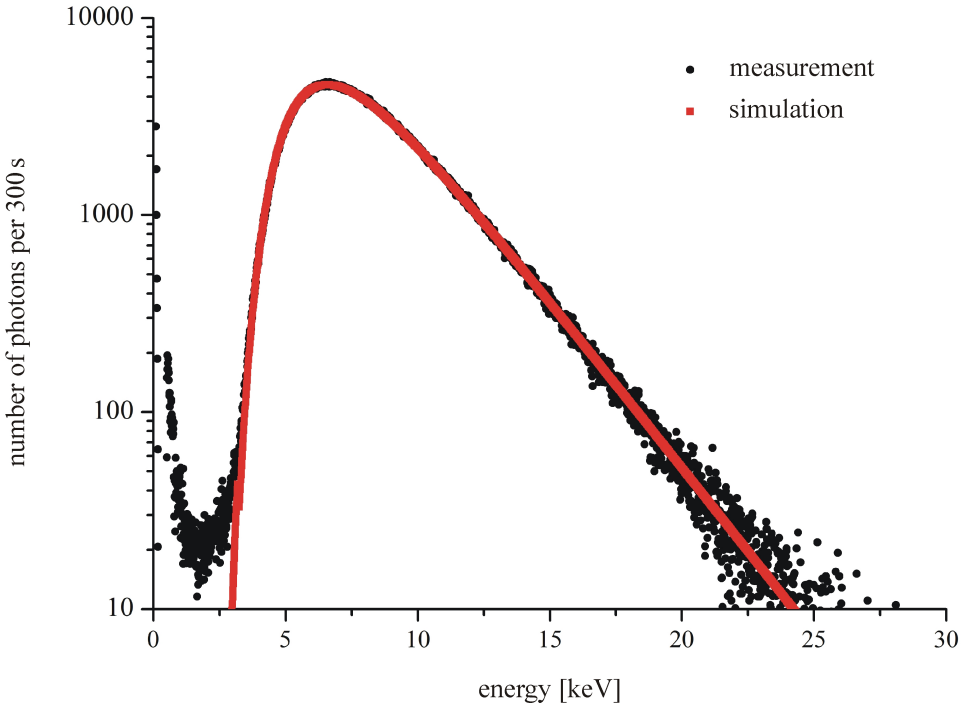

Figure 4.6: Measured and simulated energy spectrum of the incident white synchrotron beam at the EDR beamline usable for EDLD experiments on HEWL crystals.

The normalized intensity distribution exhibits a spectral maximum at 6.5 keV which is shifted towards higher X-ray energies in the case of increasing beam path lengths through the air environment between the exit slit and the sample. Low energetic signals created within the Roentec X-Flash consist in a pronounced dark noise peak at an energy of about 100 eV and a continuous background resulting from interactions of the X-ray beam with the surrounding atmosphere. Above its maximum, the recorded spectrum is characterized by an exponential decay up to the highest detectable X-ray energies in the range of 25 keV. The bending magnet radiation spectrum was simulated using the afore-mentioned parameters of the storage ring BESSY II in the program BM provided by XOP [14]. Moreover, absorption effects within the beamline windows ($250\,\mu$m(Kapton) + $50\,\mu$m(Be)) were considered according to (2.1) yielding the spectral intensity $I_{00}(E)$ of the primary beam behind the exit slit. The remaining photon flux $I_0(E)$ after traversing an additional air path length x_{air} is then given by

$$I_0(E) = I_{00}(E)e^{-\mu_{\mathrm{air}}x_{\mathrm{air}}} \tag{4.46}$$

with μ_{air} denoting the energy-dependent linear absorption coefficient of the air environment at room temperature. The simulated spectrum $I_0(E)$, represented by the red curve in figure 4.6, is in good agreement with the measured intensity distribution in the relevant energy range.

4.3.3 Absorber characteristics

In many X-ray diffraction experiments with pnCCD systems, the incident X-ray flux needs to be attenuated in order to ensure a safe SPC operation by restricting the count rate in the pnCCD plane to a value at which the capability of a 3D X-ray detection is maintained in terms of a sufficiently low pile-up probability (2.29). At the EDR beamline, the primary beam intensity can be controlled by eight absorption filters that mainly consist of Al layers with different thicknesses. For that purpose, the first five absorbers (referred to as filters 1-5) are realized as stacks of identical plates of the same material. Filter 1 contains one single layer, whereas filters 2, 3, 4, and 5 are composed of 2, 4, 8, and 16 layers, respectively, i.e. in each step to the next filter, the thickness is doubled [78]. Under this condition, filters 1-5 can effectively be combined to an absorber comprising any number of layers between 1 and 16. The remaining filters 6-8, which contain thicker plates of different materials, were not used for EDLD experiments on HEWL crystals and are therefore not of further interest.
Precise analyses of the first three absorption filters could be performed by measuring the primary beam spectrum after being attenuated by one of these filters. To this end, the Roentec X-Flash was used in the same setup as in the previous experiment described in chapter 4.3.2 which allowed to detect the incident X-ray spectrum in the absence of additional absorbers. Since the average count rate at a particular energy decreases exponentially with enhanced filter thickness, the exposure time of the Roentec X-Flash was extended to 900 s in the cases of the first two filters and to 3600 s in the case of the third filter. The shape of the white synchrotron beam recorded behind filter 1 corresponds to the black dotted distribution in figure 4.7(a). The obtained spectrum shows a characteristic irregularity in the vicinity of the FeK absorption

edge at 7112 eV which is marked by a dashed box in figure 4.7(a) and magnified for the energy range between 6 keV and 8 keV in figure 4.7(b). The observed behavior indicates the presence of impurities within the used Al absorbers arising from natural ferric contaminations. These impurities typically consist in remnants of iron oxide (Fe_2O_3) that is filtered out in the course of Al extraction from bauxite [79]. The black dotted intensity distributions in figures 4.7(c) and (d) represent the accordingly measured spectra of the primary beam after penetration through the individual filters 2 and 3, respectively.

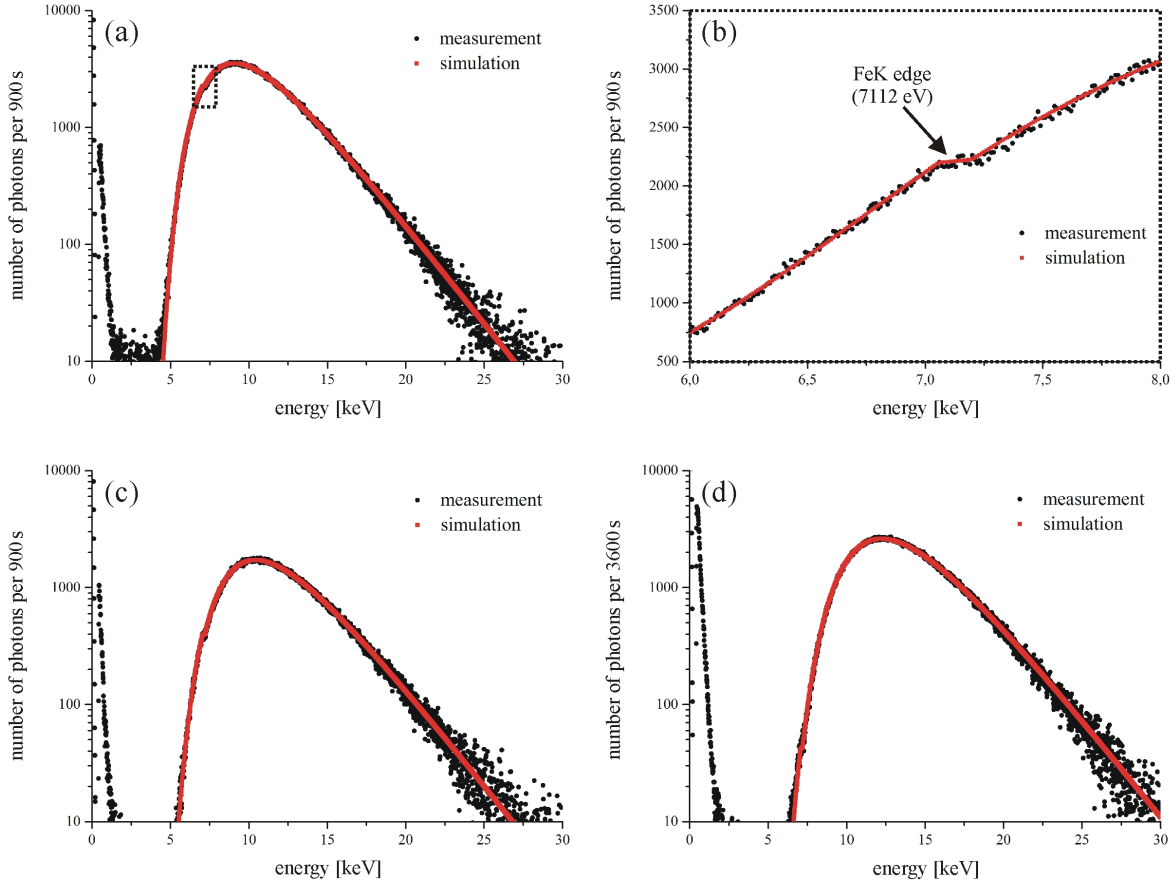

Figure 4.7: Measured and fitted energy spectra of the primary white synchrotron beam behind (a) filter 1, (c) filter 2, and (d) filter 3. The intensity distributions were recorded at storage ring currents of 76.3 nA, 76.0 nA, and 74.8 nA. (b) Spectral irregularity at the FeK absorption edge caused by Fe contaminations within the absorbers.

In analogy to (4.46), the spectra $I_0(E)$ at the position of the Roentec X-Flash were simulated and fitted to the data based on the expression

$$I_0(E) = I_{00}(E) e^{-\mu_{\mathrm{air}} x_{\mathrm{air}}} e^{-\mu_{\mathrm{Al}} x_{\mathrm{Al}}} e^{-\mu_{\mathrm{Fe}} x_{\mathrm{Fe}}} \quad , \tag{4.47}$$

where $x = x_{\mathrm{Al}} + x_{\mathrm{Fe}}$ denotes the total thickness of the inserted filter regarded as a series of an

absorber	x_{Al} [μm]	x_{Fe} [μm]	x_{Fe}/x [%]
filter 1	90.30 ± 0.12	0.262 ± 0.019	0.29 ± 0.03
filter 2	178.40 ± 0.25	0.653 ± 0.024	0.36 ± 0.02
filter 3	363.30 ± 0.94	1.196 ± 0.058	0.33 ± 0.02

Table 4.1: Composition of the first three absorption filters at the EDR beamline.

Al layer (thickness x_{Al}) and an Fe layer (thickness x_{Fe}). Besides the known air path length x_{air} and energy-dependent linear absorption coefficients μ_{air}, μ_{Al}, and μ_{Fe} taken from [14], the effective thicknesses x_{Al} and x_{Fe} were considered as fit parameters obtained from the least-squares fit of the simulated spectrum to the measured intensity distribution. The results of this method, which are summarized in table 4.1 including the calculated errors, yielded the red curves in figures 4.7(a), (c), and (d). The last column of table 4.1 quantifies the filters' impurities reflected in an average Fe contamination of about 0.33%.

4.4 Analysis of a HEWL polycrystal

The HEWL samples investigated in the course of EDLD experiments with white synchrotron radiation using pnCCDs were grown according to the method described in [80], whereby large tetragonal crystals with a maximum size of about $500\times500\times200\,\mu\mathrm{m}^3$ could be obtained. For data collection, these crystals were mounted in a thin-walled glass capillary, as illustrated in figure 4.5, and kept at room temperature.

Prior to conventional X-ray structure analysis based on the measurement of integrated Laue spot intensities and related structure-factor amplitudes in the sense of (4.17), the recorded Laue pattern needs to be indexed with respect to the pre-determined unit cell of the crystal. For that purpose, the crystalline quality of the sample, being typically quantified by means of fast screening techniques [81], is of particular interest. In certain cases, imperfections of the crystallized materials are induced by non-optimized growth conditions which become manifest in deviations from the ideal single-crystalline lattice structure. Hence, depending on the degree of polycrystallinity, various unit cells may contribute to the Laue pattern of a crystal entailing complications associated with the indexing of individual Bragg peaks.

In order to characterize the grown HEWL samples in terms of crystalline quality, the sample environment, including the capillary and the Al plate used for spatial fixing, was attached to a motorized stage providing horizontal and vertical translations of the crystal referred to the incident beam direction. Under these conditions, the homogeneity of the HEWL crystals could be analyzed by moving the sample in the y- and z-directions perpendicular to the primary beam axis and detecting the Laue pattern of the sample obtained from a single-shot exposure of the crystal for each scan position [82]. In conformity with the selected beam cross section of $100\times100\,\mu\mathrm{m}^2$, the two-dimensional scan across the sample surface was carried out using horizontal and vertical step sizes of $100\,\mu$m within the 3×3 quadratic grid shown in

figure 4.8. The Laue patterns of the HEWL crystal generated for different sample positions (enumerated as 1-9 according to figure 4.8) were recorded at the distance $x = (90 \pm 1)\,\mathrm{mm}$ behind the sample by means of the 256×256 pixel module, where the pnCCD center was located at the horizontal and vertical positions $y = 11.1\,\mathrm{mm}$ and $z = -9.6\,\mathrm{mm}$. In this setup, the Bragg reflections of the crystal could be collected with the maximum reciprocal scattering length $q_{\mathrm{max}} = 2.3\,\mathrm{\AA}^{-1}$ translating into the nominal resolution $d_{\mathrm{min}} = 2.7\,\mathrm{\AA}$.

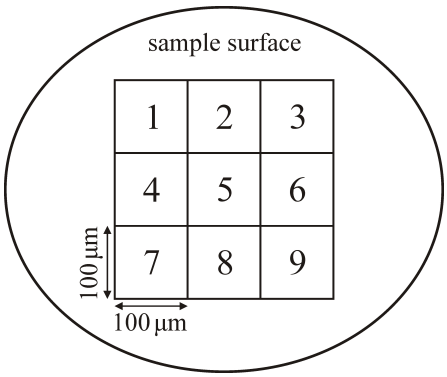

Figure 4.8: Scanned area on the surface of a HEWL sample. Laue patterns of the crystal were recorded for different scan positions 1-9 along a 3×3 grid with 100 μm step size.

For each grid point, the pnCCD data sets comprised 500 dark frames and 50000 signal frames corresponding to an overall single-shot exposure time of 376 s with the pnCCD operated in the frame store mode at a readout frequency of 133 Hz. In comparison to the eROSITA pnCCD module with 128×128 pixels, the available gains of this pnCCD system are different from the values listed in the first column of table 3.2. In the present experiment, the signal amplification in the two CAMEX chips was performed with 8-fold CDS yielding a pulse height of about 3000 adu for CuK_α radiation and a maximum detectable energy per pixel below 44 keV for the selected medium gain of 0.37 adu/eV. After noise, offset, and common mode corrections of the signal frames, the recombination to individual photon hits was carried out at an event threshold of 6σ with the mean dark noise $\sigma = 5.8\,e^-$ (rms). In order to extract gain and CTI correction factors for the accumulated raw data sets, the CuK_α line generated by the cooling mask served as a calibration signal for the pnCCD channels. At an average count rate of about 400 events per frame, measured within the active pnCCD area using filters 1 and 4 at a storage ring current of 220 mA, including the Bragg reflections of the crystal and a white background continuum, the charge transfer losses were described by a mean CTI of $3.7 \cdot 10^{-5}$. Applying the calculated gain and CTI correction factors to the data, the CuK_α single peak could be resolved with an FWHM of 175 eV. Since the information about absolute Laue spot intensities is not of interest for quantifying the polycrystallinity of the illuminated HEWL sample in this experiment, only valid event patterns in the sense of SPC were considered for further analyses and recombined in the conventional way by assigning two center-of-mass coordinates and an integrated energy to each detected event.

4.4.1 HEWL single crystal

The Laue pattern of the HEWL crystal obtained by single-shot exposures of the sample at scan positions 1-3 is depicted in figure 4.9, where the collected Bragg peaks with a sufficiently high intensity in relation to the background level are marked as black squares. For reasons of clarity, the continuous background signal spreading over the complete pnCCD image with a size of 256×256 pixels was suppressed. The spatial positions assigned to individual Laue spots correspond to the two-dimensional center-of-mass coordinates resulting from pixelwise evaluations of the event distributions after integration over quadratic areas of 3×3 pixels around the reflections. For simplicity, the so-extracted spot positions were rounded to integer values given by the associated pixel coordinates in the detector array. Taking into account the

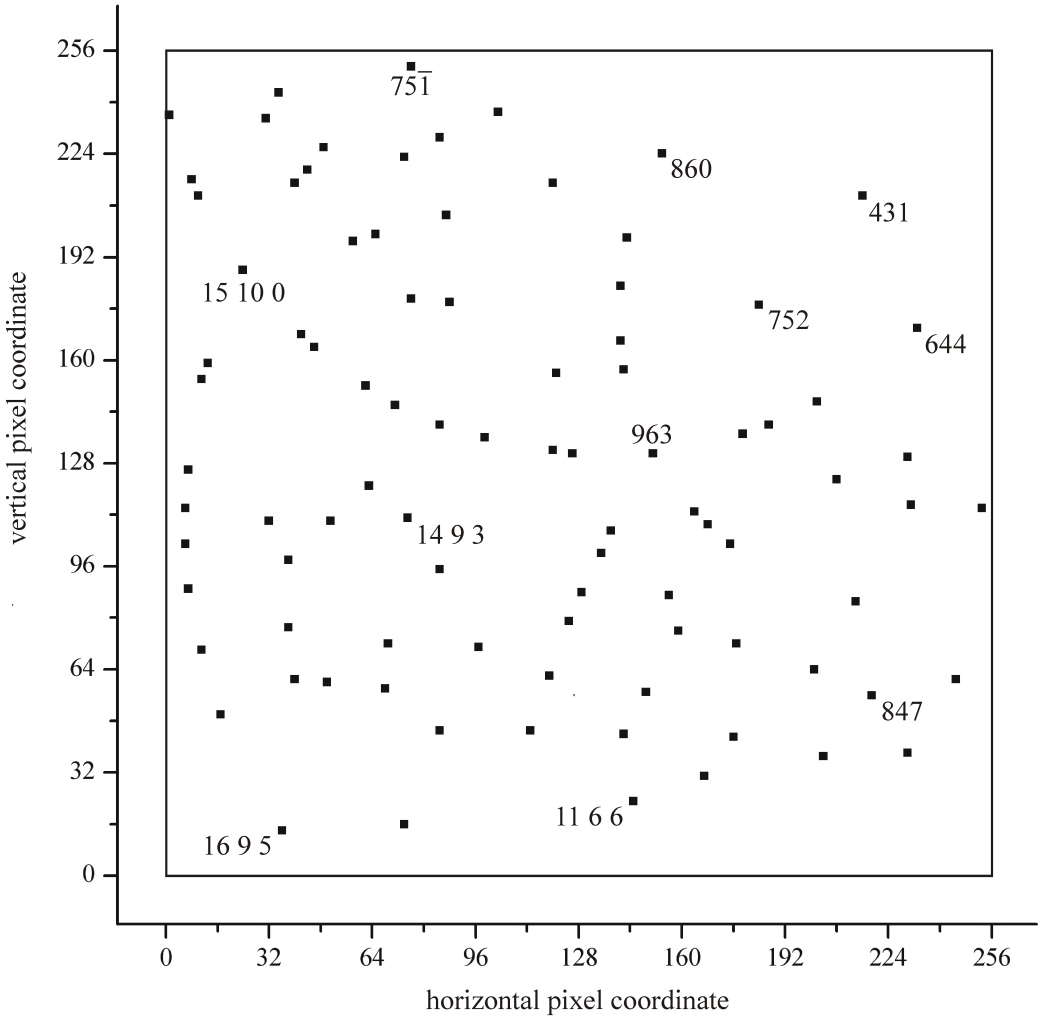

Figure 4.9: Laue pattern of the HEWL crystal measured for the scan positions 1-3 by means of a single-shot exposure of the sample, respectively. A few of 90 identified Bragg peaks are indexed referred to the experimentally determined unit cell (4.48).

used primary beam size of $100\times100\,\mu\mathrm{m}^2$ as well as parallax effects discussed in chapter 2.3.4, the accuracy of horizontal and vertical position determination within the detection plane is typically in the range of the pixel width, i.e. $\delta y \approx \delta z \approx 75\,\mu\mathrm{m}$.
The energies of the identified reflections were deduced from the spectra of recombined events measured within the selected pixel areas enclosing the spots. Apart from white background signals generated by air-scattered photons, the detected intensity distributions exhibit sharp peaks at those energies, for which the Bragg condition is fulfilled and that are contained in the primary beam spectrum. These peaks were fitted by means of Gauss functions with a parabolic background level yielding the dominant energy $E \pm \delta E$ of each Laue spot, where the error δE corresponds to the standard deviation of the Gaussian. In this experiment, the collected reflections were located in an energy range extending from 9 keV to 25 keV and resolved with the relative accuracy $\delta E/E \approx 1\%$. In order to calculate the conventional unit cell of the HEWL crystal in the externally defined coordinate system, the simultaneous two-dimensional position and energy information, expressed in terms of the triple (y, z, E), was used to determine the scattering vector $\vec{q}$ of each single reflection by means of (4.29). The so-obtained spatial distribution of reciprocal lattice points, resulting from the energy resolution of the recorded Laue pattern, is included within a cuboid confined by the intervals $-0.3\,\text{Å}^{-1} \le q_x \le 0\,\text{Å}^{-1}$, $0\,\text{Å}^{-1} \le q_y \le 2\,\text{Å}^{-1}$, and $-1.5\,\text{Å}^{-1} \le q_z \le 0\,\text{Å}^{-1}$ (figure 4.10).

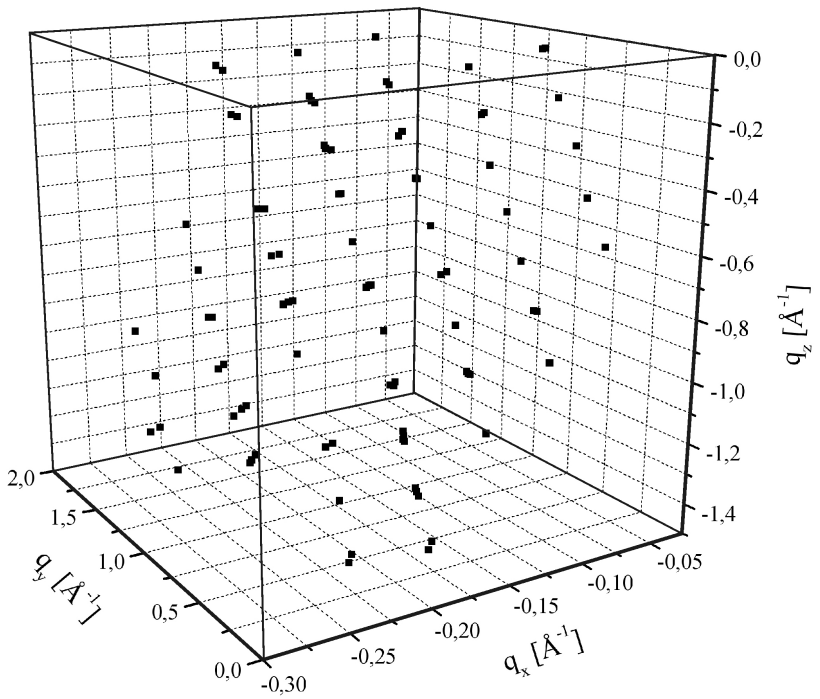

Figure 4.10: Laue pattern of the HEWL crystal after energy resolution and conversion into reciprocal-space coordinates. The observed 3D distribution spans the reciprocal lattice of a HEWL single crystal.

As a consequence of the above-mentioned experimental errors concerning position and energy determination of individual Bragg peaks, the components q_x, q_y, and q_z of the scattering vectors could be resolved with absolute accuracies below $0.03\,\text{Å}^{-1}$ on the basis of (4.30)-(4.32). Using the formalism described in chapter 4.2, the set $\{\vec{q}_i \pm \delta\vec{q}_i\}$ of 90 measured reciprocal lattice points then served to extract the real conventional unit cell of the HEWL single crystal. In the defined coordinate system, the calculated basis vectors are given by

$$\vec{a}_1 = \begin{pmatrix} -51.51 \pm 2.68 \\ 58.69 \pm 1.65 \\ -17.23 \pm 1.38 \end{pmatrix} \text{Å} \;\; , \;\; \vec{a}_2 = \begin{pmatrix} 59.15 \pm 1.79 \\ 49.98 \pm 1.09 \\ -10.25 \pm 1.03 \end{pmatrix} \text{Å} \;\; , \;\; \vec{a}_3 = \begin{pmatrix} 4.25 \pm 1.02 \\ -9.35 \pm 1.15 \\ -36.69 \pm 1.04 \end{pmatrix} \text{Å} \quad (4.48)$$

with the lattice constants

$$a_1 = (79.96 \pm 1.95)\,\text{Å} \;\; , \;\; a_2 = (78.11 \pm 1.54)\,\text{Å} \;\; , \;\; a_3 = (38.10 \pm 1.06)\,\text{Å} \quad (4.49)$$

and the cell angles

$$\alpha_1 = (86.91 \pm 3.95)^\circ \;\; , \;\; \alpha_2 = (92.54 \pm 3.74)^\circ \;\; , \;\; \alpha_3 = (89.42 \pm 3.06)^\circ \;\; . \quad (4.50)$$

The unit-cell parameters of the illuminated HEWL crystal could be determined with relative accuracies $\delta a_i/a_i$ between 2.0% and 2.8% for the magnitudes of the basis vectors and $\delta\alpha_i/\alpha_i$ between 3.4% and 4.5% for their enclosed angles. Considering the obtained errors, the results are in agreement with the expected lattice structure of tetragonal HEWL characterized by $\alpha_1 = \alpha_2 = \alpha_3 = 90^\circ$ and the lattice constants $a_1 = a_2 = 79.1$ Å, $a_3 = 37.9$ Å.
In comparison to a previous EDLD experiment on an inorganic tetragonal γ-$LiAlO_2$ crystal using the same pnCCD system presented in [6], where the lattice constants were reproduced with accuracies between 0.2% and 0.5%, the achieved resolution of the HEWL unit cell is significantly degraded. This observation can be traceable to the fact that for the method applied for unit-cell calculation, the corresponding relative errors $\delta a_i/a_i$ depend linearly on the lattice constants themselves. Since in the case of a tetragonal crystal system the real and reciprocal cell parameters are related to each other via

$$a_i = \frac{2\pi}{b_i} \;\; , \quad (4.51)$$

the relative error $\delta a_i/a_i$ can be expressed by

$$\frac{\delta a_i}{a_i} = \frac{\delta b_i}{b_i} = \frac{a_i}{2\pi}\delta b_i \;\; . \quad (4.52)$$

The errors δb_i result from the resolutions δq_x, δq_y, and δq_z of the scattering vector $\vec{q}$ in the different reciprocal-space directions given by (4.30)-(4.32). Owing to the comparable errors associated with the position and energy measurement of individual Laue spots in both experiments, the relative accuracy of the real lattice a_i constant is mainly proportional to a_i.

Hence, taking into account the ratios

$$\frac{a_{1,\mathrm{HEWL}}}{a_{1,\gamma\text{-}\mathrm{LiAlO_2}}} = \frac{a_{2,\mathrm{HEWL}}}{a_{2,\gamma\text{-}\mathrm{LiAlO_2}}} \approx 15 \quad , \quad \frac{a_{3,\mathrm{HEWL}}}{a_{3,\gamma\text{-}\mathrm{LiAlO_2}}} \approx 6 \tag{4.53}$$

between the lattice parameters of the tetragonal unit cells of HEWL and γ-$LiAlO_2$, the marked loss of real-space resolution can be quantitatively explained.
Combined with the set $\{\vec{q}_i \pm \delta\vec{q}_i\}$ of measured scattering vectors, the extracted basis (4.48) spanning the real lattice of the HEWL single crystal served to completely index the recorded Laue pattern using the Laue equations (4.16). The so-obtained Miller indices $\{h_i k_i l_i\}$ showed absolute deviations below 0.1 from integer numbers for this data set and could therefore be rounded directly to the neighboring integers. The results of these calculations, exemplarily illustrated in figure 4.9 including the Miller indices of a few selected reflections, indicate that the dominant Bragg peaks belong to various diffraction orders. In the depicted case, most of the collected Laue spots are of first order, such as 431, $75\bar{1}$, or 847, for which h_i, k_i, and l_i are coprime. The 644 and 860 reflections can be identified as the second orders of 322 and 430, where, based on the discussions in chapter 4.1.2, the corresponding first orders occur at the halves of the second-order energies. In these situations, the integrated diffraction signals of the first-order Bragg peaks are suppressed as a result of too low incident X-ray fluxes at the required energies caused by the afore-described absorption effects at the EDR beamline. Higher diffraction orders, that are explicitly marked in figure 4.9, consist in the 963 and the 15 10 0 reflections representing the third order of 321 and the fifth order or 320, respectively. Particular cases, in which several diffraction orders contribute to the energy spectrum detected at the positions of individual Laue spots in terms of overlapping harmonics, are investigated in detail in chapters 4.5.4-4.5.6.

4.4.2 HEWL double crystal

In contrast to the previously obtained Laue pattern of the HEWL crystal being generated by one single unit cell A with the basis vectors (4.48), the diffraction signal recorded for the scan positions 4-9 exhibits a higher complexity (figure 4.11). In addition to the already indexed reflections ascribed to cell A (again marked as black squares according to figure 4.9), a second set of Bragg peaks, marked as red circles in figure 4.11, can be observed in this situation. These spots result from the simultaneous presence of another HEWL unit cell A' giving rise to a double-crystalline structure at the corresponding sample positions. The different orientation of cell A' with respect to cell A becomes manifest in the occurrence of split reflections which could be spatially separated from each other for the majority of the Laue spots. For clarity, a selected number of equivalent Bragg peaks, characterized by the same Miller indices referred to the distinct crystallographic basis vectors spanning cells A and A', respectively, is encircled in figure 4.11.
In order to extract the desired structural information from the recorded diffraction pattern, the identified reflections were analyzed in an analog way by fitting the Laue spot positions and energies and converting the obtained coordinates including their errors into the associated

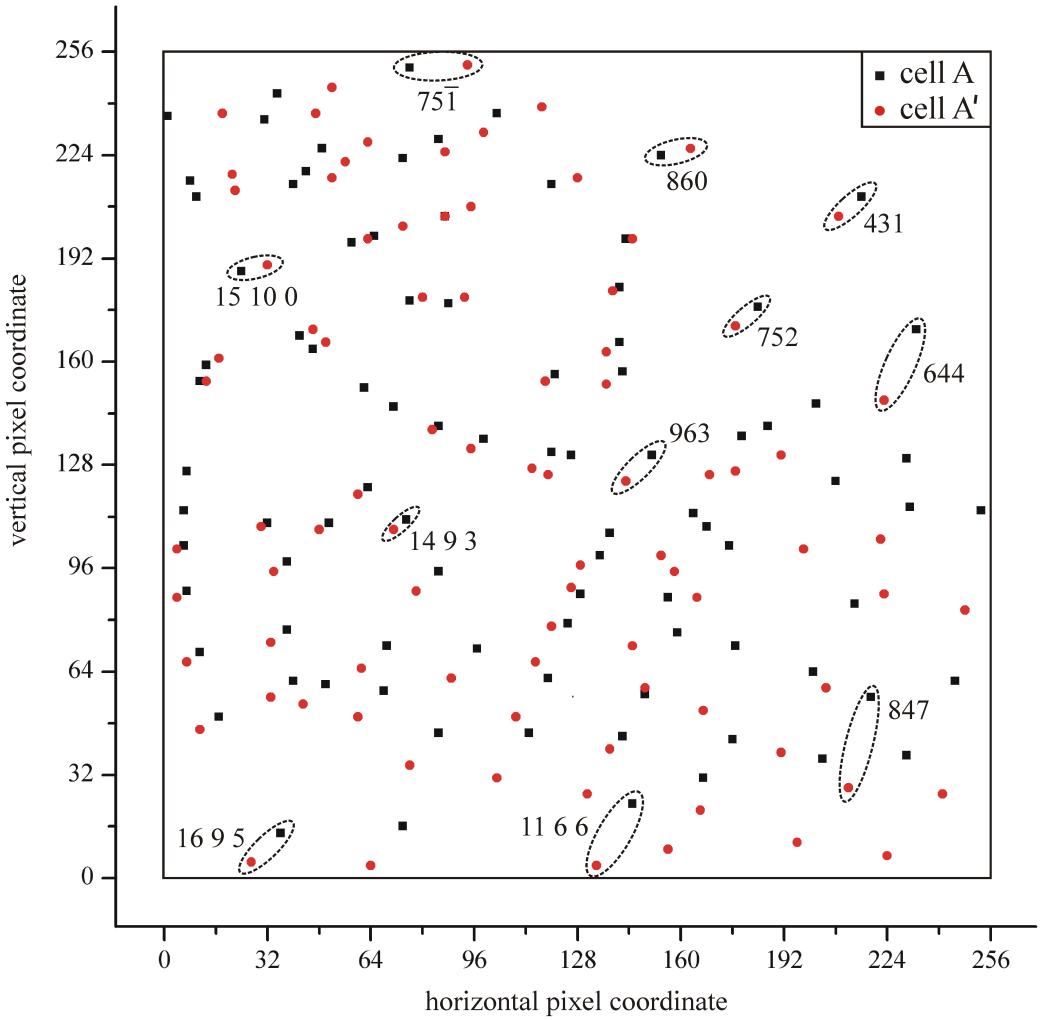

Figure 4.11: Diffraction signal of the HEWL crystal measured for the sample positions 4-9. The black spots coincide with the Laue pattern of figure 4.9, whereas the red spots were generated by another HEWL unit cell A'. Equivalent split reflections with the same Miller indices related to cells A and A' are encircled.

reciprocal-space volume. Further quantitative investigations revealed that for single pairs of split reflections, the maximum energy shift is in the range of 1 keV translating into a change of the scattering angle below 1°. The calculated set $\{\vec{q}_i \pm \delta\vec{q}_i\}$ of reciprocal lattice points, after separating the contributions of cells A and A' in accordance with the Laue pattern shown in figure 4.11, yielded the distribution of figure 4.12. In this case, the present double-crystalline structure, which is reflected in two reciprocal lattices with a visible tilt relative to each other, could be confirmed.

For the determination of the real basis vectors spanning the different lattices, the described method comprising cell extraction, crystallographic reduction, and unit-cell refinement was applied to the complete set of reciprocal lattice points taking into account that the number

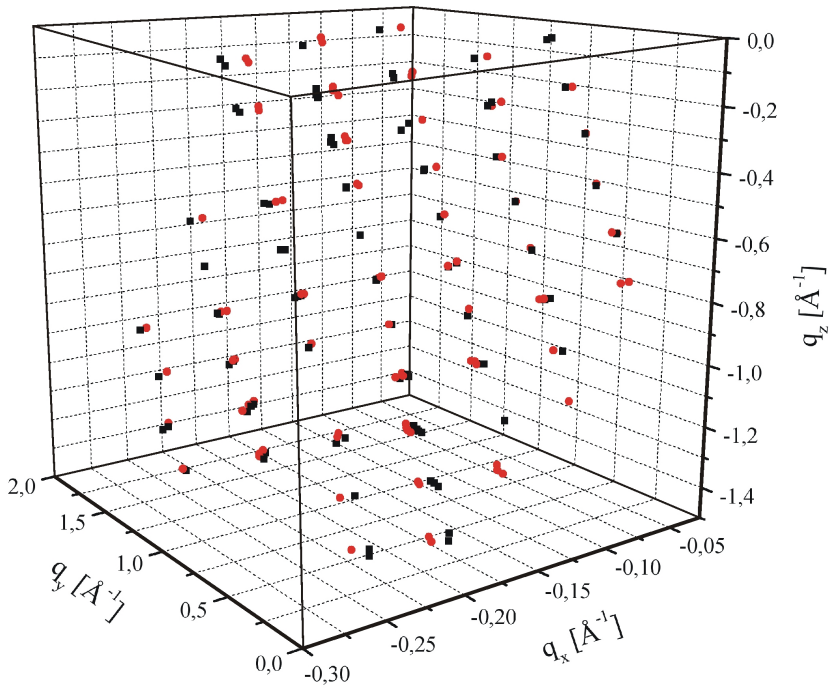

Figure 4.12: Measured 3D distribution of reciprocal lattice points obtained after position and energy resolution of the individual reflections collected within the Laue pattern of figure 4.11. The HEWL sample shows a polycrystalline structure which becomes manifest in two distinct unit cells with a slight tilt relative to each other.

of reflections indexed with a reasonable accuracy is effectively reduced. In this way, the unit cell A given by (4.48) could be reproduced providing the Miller indices of the black spots in figure 4.11. However, in the course of indexing, particular pairs of split reflections with approximately the same positions and energies were characterized by similar (floating-point) values of h, k, and l with respect to cell A. In such situations, one of these spots, for which the Miller indices referred to the basis (4.48) showed a smaller absolute deviation from the neighboring integer numbers in comparison to the other spot, was indexed with a higher accuracy and thus ascribed to the first HEWL unit cell A. All other reflections, that could not be indexed with the required accuracy (marked as red circles in figures 4.11 and 4.12), belong to the second HEWL unit cell A'.

In the final step of data treatment, the basis vectors of cell A' were calculated by using the previously applied procedure for the remaining set of reciprocal lattice points excluding the already identified spots of cell A. The so-obtained basis vectors $\vec{a}'_1$, $\vec{a}'_2$, and $\vec{a}'_3$ spanning the conventional unit cell A' in the externally defined coordinate system are given by

$$\vec{a}'_1 = \begin{pmatrix} -49.16 \pm 2.56 \\ 59.08 \pm 1.64 \\ -17.05 \pm 1.37 \end{pmatrix} \text{Å} \quad , \quad \vec{a}'_2 = \begin{pmatrix} 58.72 \pm 1.78 \\ 50.02 \pm 1.09 \\ -11.20 \pm 1.13 \end{pmatrix} \text{Å} \quad , \quad \vec{a}'_3 = \begin{pmatrix} 3.86 \pm 0.93 \\ -9.40 \pm 1.16 \\ -36.98 \pm 1.05 \end{pmatrix} \text{Å} \quad (4.54)$$

yielding the lattice constants

$$a_1' = (78.73 \pm 1.92)\,\text{Å} \;\;,\;\; a_2' = (77.95 \pm 1.54)\,\text{Å} \;\;,\;\; a_3' = (38.35 \pm 1.07)\,\text{Å} \tag{4.55}$$

and the cell angles

$$\alpha_1' = (86.73 \pm 3.94)^\circ \;\;,\;\; \alpha_2' = (92.18 \pm 3.73)^\circ \;\;,\;\; \alpha_3' = (87.58 \pm 3.00)^\circ \;\;. \tag{4.56}$$

Within the error limits, this result for the crystallographic unit cell A' is also consistent with the expected tetragonal structure of HEWL. Since the same method was applied for lattice-basis determination, the parameters of cell A' could be extracted with the same relative accuracy as in the case of cell A. The calculated lattice constants of cell A and cell A' show deviations in the range of 1% from each other, which can be caused by distance effects within this experiment that were not considered for data evaluation. If the polycrystallinity of the illuminated HEWL sample consists in a domain structure with two grains located behind each other along the primary beam direction, the distances of the cells A and A' from the detection plane are effectively different. The indexing of the remaining spots was carried out with respect to the determined basis (4.54) of cell A' and, after rounding the Miller indices to the neighboring integer values, coincided with the indexing obtained for the single-crystalline contribution of cell A to the Laue pattern of figure 4.11 within the identified split pairs. The orientation of cell A' relative to cell A can be described by three tilt angles φ_i between the basis vectors $\vec{a}_i$ and $\vec{a}_i'$ given by

$$\varphi_1 = (1.39 \pm 0.05)^\circ \;\;,\;\; \varphi_2 = (0.80 \pm 0.04)^\circ \;\;,\;\; \varphi_3 = (0.44 \pm 0.02)^\circ \;\;. \tag{4.57}$$

In terms of the calculated unit cells (4.48) and (4.54) the structure of the HEWL sample comprising single- and double-crystalline parts was quantitatively characterized. The origin of the observed polycrystallinity, which is induced either during the crystallization process or by thermal effects leading to instabilities of the HEWL crystal at room temperature, could not be uniquely clarified. Though the results for the unit cells A and A' are in agreement with the expected HEWL structure, a tetragonal lattice cannot be distinguished from an orthorhombic lattice with similar unit-cell parameters by the applied method owing to the limited position and energy resolution of the pnCCD. In this sense, the computed structure might also indicate the presence of two different, closely related Bravais lattices within the sample. In order to overcome this experimental limitation, a sufficient number of reflections needs to be recorded with the objectives of structure refinement on an atomic level and space-group determination based on the measurement of absolute Laue spot intensities.
In general, the developed method for unit-cell extraction exploiting the simultaneous position and energy resolution of individual Bragg peaks provided by the pnCCD is also applicable in the case of higher degrees of polycrystallinity. The clear advantage of EDLD experiments with white synchrotron radiation consists in the availability of structural information within single-shot exposures of the crystal, whereby no alignment and rotation steps are necessary. Since

the results are independent of the sample orientation and achievable by means of a model-free data evaluation, the pnCCD offers new possibilities for fast X-ray screening techniques with regard to analyses of crystalline quality without *a priori* knowledge about the sample in a simplified experimental setup.

4.5 Determination of integrated Laue spot intensities

The refinement of an externally defined structure model of the crystal against the collected data is based on the measurement of structure-factor amplitudes $\{|F_{hkl}|\}$ given by (4.17) in terms of absolute Laue spot intensities $\{I_{hkl}\}$ associated with the detected reflections $\{hkl\}$. In the case of EDLD experiments with white synchrotron radiation, the event distributions at the Bragg peak positions comprise the diffraction signals of the crystal accompanied by a continuous background. As the Laue spot of the sample become apparent in the form of intense local X-ray fluxes incident on a few pixels of the pnCCD, the corresponding data pattern is generated with a high pile-up probability (2.29). In order to finally obtain real diffracted intensities, various steps are required to analyze the recorded spectra including a consideration of invalid event types (chapter 4.5.1), an appropriate separation of background signals (chapter 4.5.2), and a statistical interpretation of pile-up events (chapters 4.5.3-4.5.6) using the count rate behavior of detected photon numbers (chapter 2.3.8).

4.5.1 Cluster recombination

The occurrence of enhanced count rates gives rise to significant contributions of pile-up events to the recorded pnCCD data sets, whereby the condition of a safe SPC operation, relying on the spatial separation of different charge clouds, can no longer be fulfilled. As discussed and exemplarily illustrated in chapter 2.3.7, multi-photon hits result in event pile-up and pattern pile-up characterized by invalid event patterns in the sense of SPC. Since the simultaneous position and energy resolution of single photons cannot be maintained in these situations, charge clusters are usually rejected for further data analyses. However, due to the fact that pattern pile-up events contain substantial information about the integrated intensity of a Bragg peak, a suitable treatment of charge clusters is essential.
Within the scope of a previous EDLD experiment on an inorganic γ-$LiAlO_2$ crystal it was already demonstrated that by taking pattern pile-up into account, a reasonable agreement between calculated and measured structure-factor amplitudes can be achieved [6]. Various event distributions at the position of the most intense 105 reflection, obtained in different signal frames of this measurement, are shown in figure 4.13 together with the number of photons which generated the detected event patterns. In particular cases, monochromatic X-rays diffracted by the crystal create single-photon hits which are spatially separated from each other (figure 4.13(a)) and hence accepted as valid events by conventional methods for pnCCD data analysis. In contrast, pattern pile-up leads to the formation of charge clusters covering large connected pixel areas whose sizes depend on the cross section of the incident

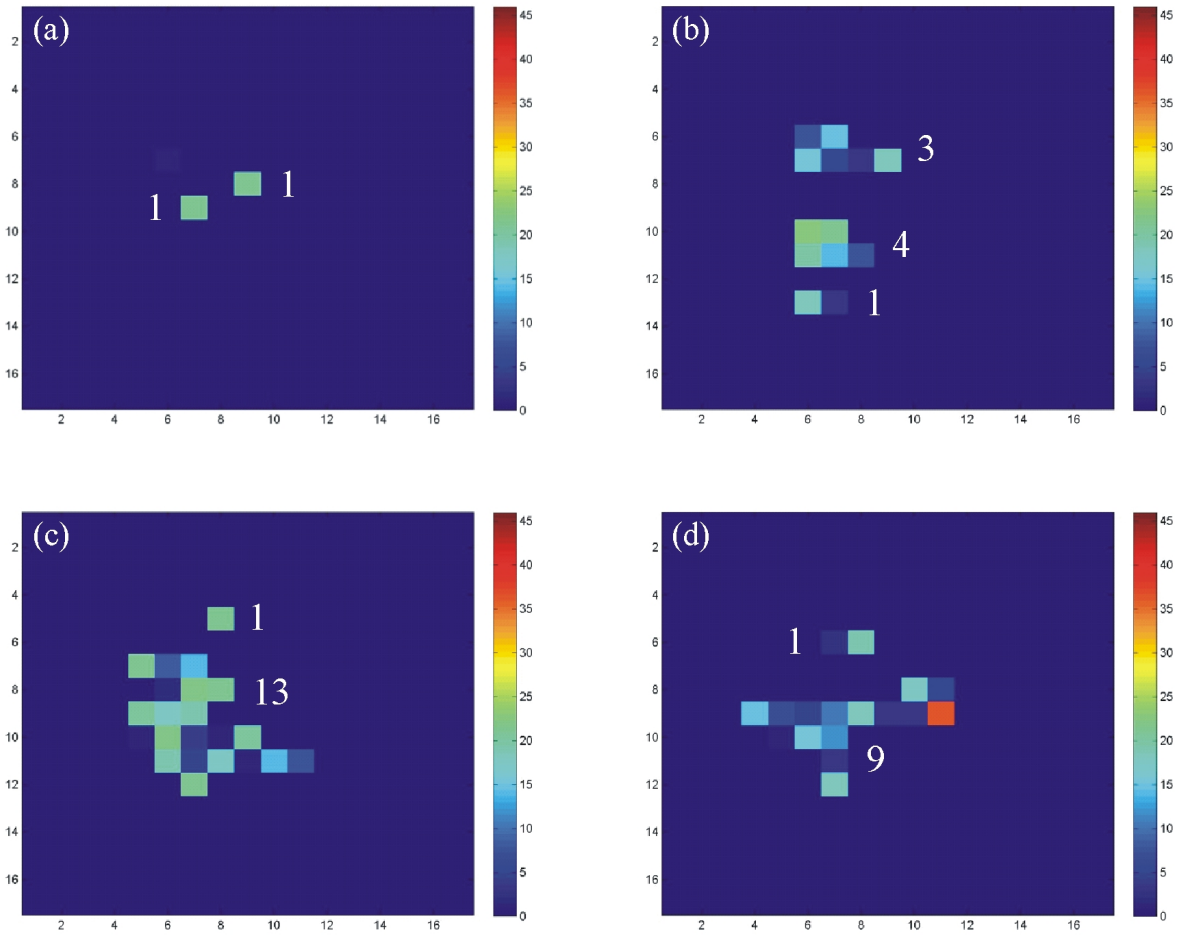

Figure 4.13: Charge clusters within the 105 reflection of γ-$LiAlO_2$ ($E = 21.29\,\mathrm{keV}$) in a linear color scale of calibrated energies (in keV). In all the depicted cases, the integrated signal amplitudes of individual pattern pile-up events are integer multiples of the spot energy, indicated by the white numbers of photons that generated the observed clusters. The red pixel in (d) contains the signal of two piled photons.

beam and the involved photon number (figures 4.13(b)-(d)). Since a quadratic primary beam size of $100\times100\,\mu\mathrm{m}^2$ was used for the EDLD experiments on HEWL crystals, the spatial extension of pattern pile-up events could be confined to a 3×3 pixel area, whereas for the measurements on γ-$LiAlO_2$ with $500\times500\,\mu\mathrm{m}^2$ beam size, spot areas of about 7×7 pixels had to be considered. In order to include the contributions of multi-photon hits to the Bragg peak intensities for further data treatment, the recombination of charge clusters is carried out by assigning two center-of-mass coordinates and integrated signal amplitudes to the individual events. In the course of absolute intensity determination, situations in which charge clusters are generated by X-rays of different energies, consisting either in overlapping harmonics or pile-up signals with the background continuum, can then be analyzed statistically based on the Poisson distributions of detected photon numbers.

4.5.2 Background subtraction

The spectral separation of the background continuum caused by air-scattered X-rays from the Bragg peaks of the crystal relies on its direct measurement in the surroundings of well-defined spot regions. For that purpose, accounting for energy- and angular-dependent parallax effects within the pnCCD, the spectrum at the position of a Laue spot is extracted from a 5×5 pixel area whose center coincides with the spatial intensity maximum of the reflection after rounding the fitted pixel coordinates to integer values. The effective contribution of the background signal to this intensity distribution can be quantitatively determined by evaluating the X-ray spectrum recorded in the immediate vicinity of the spot region (figure 4.14). In a most basic approach, the neighboring areas of the Bragg peaks with sizes of 5×5 pixels included in the framed parts of figure 4.14 were used to obtain average background spectra, provided that the selected regions do not overlap with other spot areas.

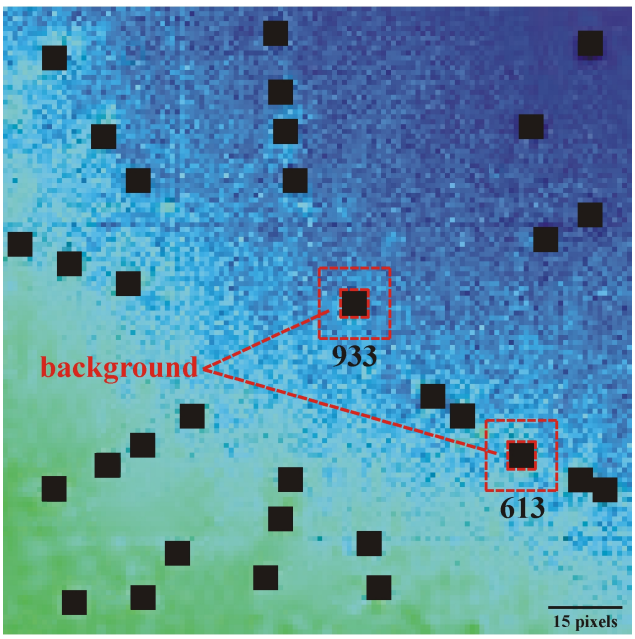

Figure 4.14: Section of the Laue pattern of figure 4.15 (image size 128×128 pixels). The spot areas comprise regions with a defined size of 5×5 pixels (black squares), whereas the white background continuum is measured around the spots (red frames).

In general, the background levels superimposing the diffraction signals of the crystal depend on the incident beam cross section and intensity, the presence of any additional scattering materials within the setup, and the distance of the considered spot position from the primary beam axis. Under the conditions of the performed EDLD experiments on HEWL crystals, using a circular Pb beamstop of 1 mm diameter to shield the white synchrotron beam behind the sample, the background signals could be suppressed to average count rates $\lambda_{bg} < 0.05$ resulting in a negligible maximum pile-up probability in the range of 0.1%. Therefore, the

background continuum is measured in terms of SPC for each individual Laue spot without significant contributions of pile-up events to the energy spectra recorded within the selected background areas. In that respect, statistical methods for the determination of integrated Bragg peak intensities can be restricted to analyses of single-photon hits and pile-up signals which contain a particular number of photons diffracted by the crystal and at most one photon scattered from air molecules.
The count rate behavior associated with reflections of various orders was investigated for the case of EDLD on a HEWL single crystal using filters 1, 2, and 3 to attenuate the incident X-ray flux in the experimental setup of figure 4.5. The Laue pattern was recorded by means of the pnCCD module with 256×256 pixels around the primary beam axis within four single-shot exposures of the sample yielding a diffraction image of 512×512 pixels (figure 4.15).

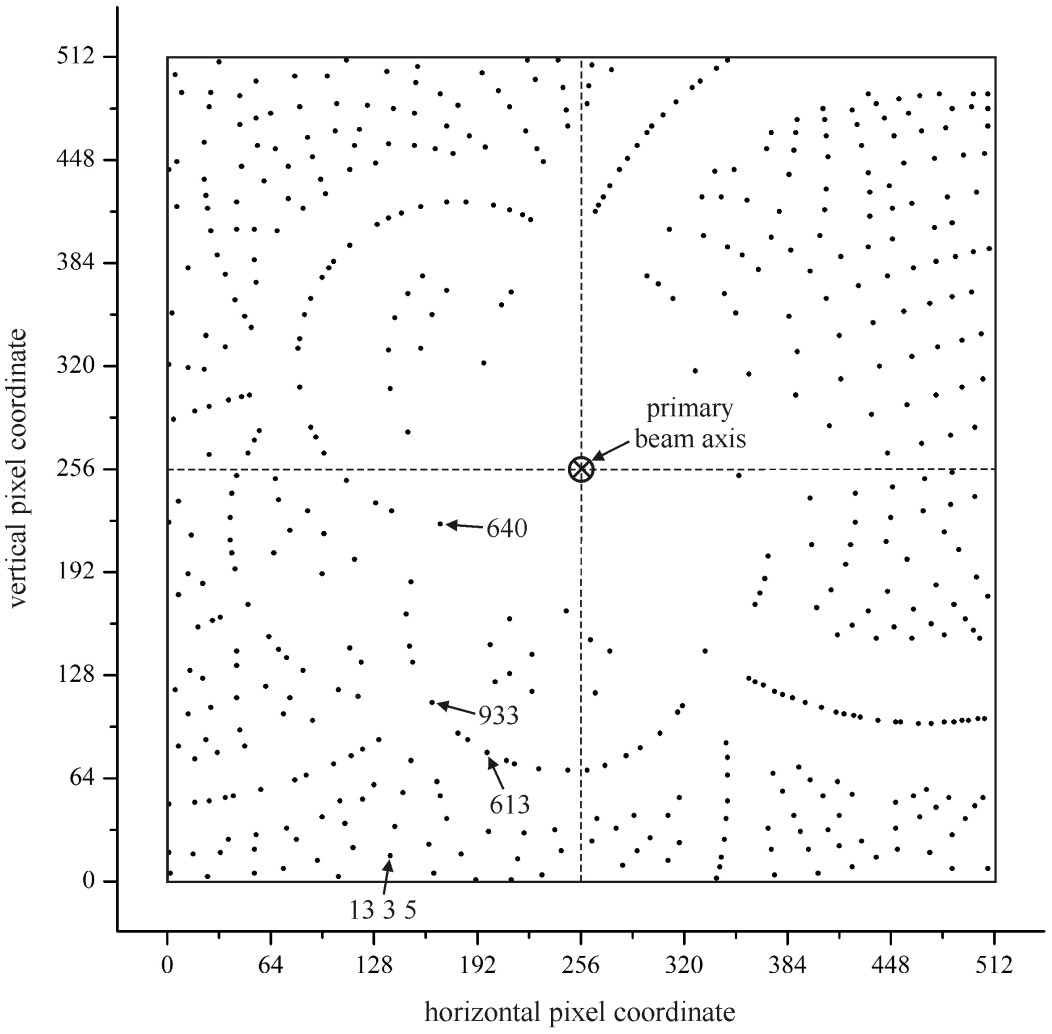

Figure 4.15: Laue pattern of a HEWL single crystal measured around the primary beam axis. Due to the presence of the beamstop, no Laue spots could be detected in the center of the image. Reflections with different count rate behavior are indexed.

In order to assign Miller indices to the collected Bragg peaks, their positions and dominant energies were resolved and used for unit-cell calculation and indexing according to the method described in chapter 4.2. In this way, the tetragonal unit cell spanned by the real basis vectors

$$\vec{a}_1 = \begin{pmatrix} 60.13 \pm 1.83 \\ 51.09 \pm 1.68 \\ 3.23 \pm 1.03 \end{pmatrix} \text{Å} \;\; , \;\; \vec{a}_2 = \begin{pmatrix} -41.36 \pm 2.16 \\ 56.41 \pm 1.57 \\ -36.52 \pm 1.23 \end{pmatrix} \text{Å} \;\; , \;\; \vec{a}_3 = \begin{pmatrix} -14.18 \pm 1.42 \\ 12.41 \pm 1.16 \\ 33.73 \pm 1.65 \end{pmatrix} \text{Å} \tag{4.58}$$

with the lattice constants

$$a_1 = (78.97 \pm 1.77)\,\text{Å} \;\; , \;\; a_2 = (78.91 \pm 1.70)\,\text{Å} \;\; , \;\; a_3 = (38.64 \pm 1.09)\,\text{Å} \tag{4.59}$$

and the cell angles

$$\alpha_1 = (88.97 \pm 3.64)^\circ \;\; , \;\; \alpha_2 = (92.06 \pm 3.83)^\circ \;\; , \;\; \alpha_3 = (87.45 \pm 3.11)^\circ \;\; . \tag{4.60}$$

was obtained for this measurement. The 13 3 5, 613, 640, and 933 reflections which exhibit a characteristic count rate behavior in terms of single Bragg peaks and overlapping harmonics, in the following analyzed for absolute intensity determination, are marked in figure 4.15.

4.5.3 Integration of single reflections

In the most simple case, only one single reflection is recorded within the selected 5×5 pixel area covering a particular Laue spot. Under this condition, an intense monochromatic X-ray beam of diffracted photons can be measured with the mean count rate λ superimposed by a white background spectrum with the mean count rate λ_{bg}. Since the intensity of the background signal is sufficiently low in this experiment, the occurring multi-photon hits contain at least one photon associated with the considered Bragg peak of the crystal. This situation can be observed in the energy spectrum detected at the position of the 13 3 5 reflection with the fitted energy $E = (14.50 \pm 0.13)\,\text{keV}$ (figure 4.16, black curve), where second-order contributions of the 26 6 10 reflection are neglected due to the weak incident X-ray flux at its energy of 29.00 keV. The corresponding background distribution (figure 4.16, red curve), measured in the vicinity of the spot region, becomes manifest in a continuum of air-scattered photons which shows the shape of the primary beam spectrum accompanied by CuK radiation originating from the detector surroundings. The average background signal comprises $N_\gamma = 4320$ photons accumulated within $N = 100000$ signal frames of this measurement and is thus characterized by the effective count rate $\lambda_{\text{bg}} = 0.04320$ according to (2.20).
In order to interpret the pile-up spectrum of the 13 3 5 reflection in an appropriate way, the numbers of diffracted photons giving rise to the recorded signals in particular energy ranges are encircled in figure 4.16. Below 25 keV, the 13 3 5 single peak with the extracted spot energy can be identified on top of the background continuum. Above 25 keV, the spectrum is dominated by pile-up contributions of larger reflected photon numbers which result in the expected peaks at integer multiples of the Bragg peak energy. These pile-up events are

also superimposed by a respective background distribution containing pile-up signals of one air-scattered photon and the assigned (reduced) number of diffracted photons.

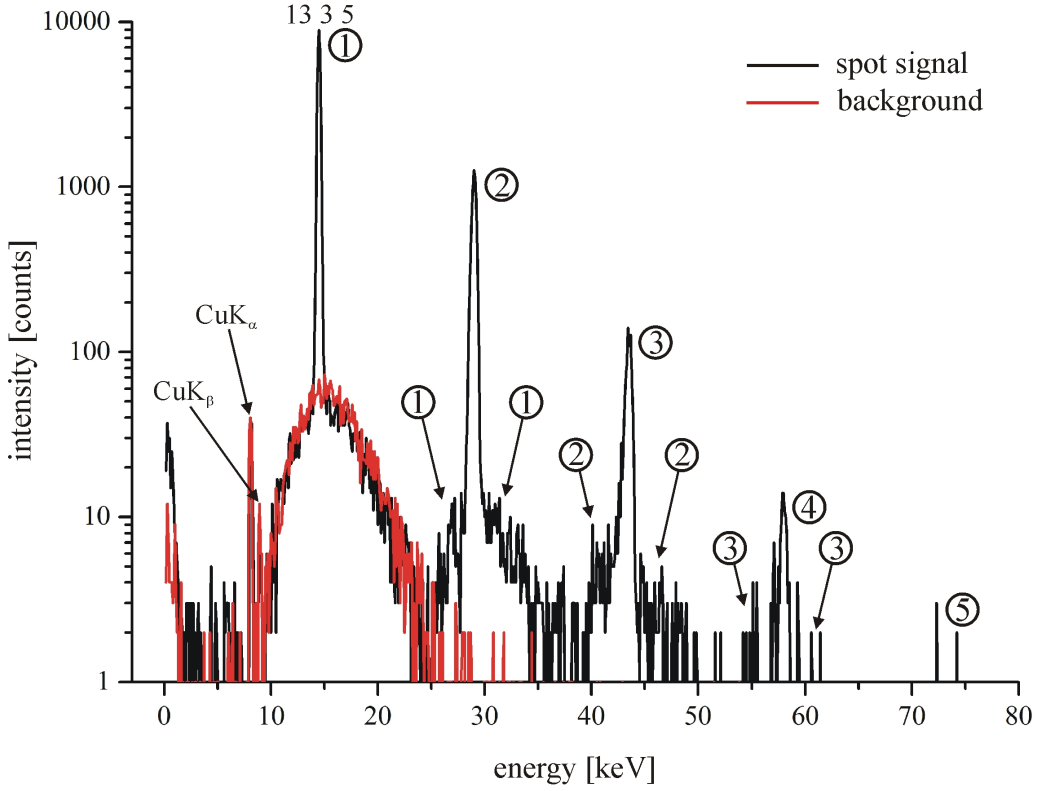

Figure 4.16: Energy spectrum measured at the position of the 13 3 5 reflection (black curve) and continuous background signal in the vicinity of the spot region (red curve).

In a first step of intensity determination, the dominant spectral peaks were fitted by means of Gaussian functions and, after background subtraction, integrated to the intensities N_1 of the 13 3 5 single peak at 14.50 keV, N_2 of the first pile-up peak at 29.00 keV, and so on. The obtained values N_1,...,N_5 could then be used to calculate a set of corrected photon numbers

$$N'_k = N_k + \Delta N_k = N_k(1 + \lambda_{\mathrm{bg}}) \tag{4.61}$$

taking into account the number ΔN_k of observed pile-up events including k diffracted photons and one air-scattered photon. The correction factor in (4.61) results from the ratio

$$\frac{\Delta N_k}{N_k} = \frac{NP_k(\lambda)P_1(\lambda_{\mathrm{bg}})}{NP_k(\lambda)P_0(\lambda_{\mathrm{bg}})} = \frac{\lambda_{\mathrm{bg}}e^{-\lambda_{\mathrm{bg}}}}{e^{-\lambda_{\mathrm{bg}}}} = \lambda_{\mathrm{bg}} \ , \tag{4.62}$$

where N denotes the number of accumulated signal frames and $P_k(\lambda)P_{k_{\mathrm{bg}}}(\lambda_{\mathrm{bg}})$ is the statistical probability of detecting k diffracted photons and k_{bg} background photons ($k_{\mathrm{bg}} = 0, 1$) within the spot area at the same time. The normalization of the so-corrected intensity values to the

number of signal frames provides a set of experimental probabilities

$$P_{k,\mathrm{exp}} = \frac{N'_k}{N} \tag{4.63}$$

associated with the individual events containing $k = 0,...,5$ photons diffracted by the crystal. In this case, the intensity N'_0 describes the number of images in which no diffracted photon was measured within the spot area of the 13 3 5 reflection, comprising empty frames as well as background signals generated by one single photon. According to the count rate statistics discussed in chapter 2.3.8, the set $\{P_{k,\mathrm{exp}}\}$ represents a one-dimensional Poisson distribution with statistical probabilities defined by (2.21) and listed in the last column of table 4.2.

measured signal [keV]	number of detected photons with the energy 14.50 keV	statistical probability
0	0	$e^{-\lambda}$
14.50	1	$\lambda e^{-\lambda}$
29.00	2	$\frac{1}{2}\lambda^2 e^{-\lambda}$
43.50	3	$\frac{1}{6}\lambda^3 e^{-\lambda}$
58.00	4	$\frac{1}{24}\lambda^4 e^{-\lambda}$
72.50	5	$\frac{1}{120}\lambda^5 e^{-\lambda}$

Table 4.2: Statistical pile-up peak probabilities of detecting $k = 0,...,5$ diffracted photons in the case of the single reflection 13 3 5.

In the final step of intensity analysis, the experimental pile-up peak probabilities $\{P_{k,\mathrm{exp}}\}$ were fitted by means of a Poisson distribution using a least-squares method in analogy to the procedure applied in chapter 3.2.2. The fit result (figure 4.17) yielded the average count rate

$$\lambda = 0.45745 \pm 0.00393 \tag{4.64}$$

and the integrated intensity

$$I_{13\ 3\ 5} = N\lambda = 45745 \pm 393 \tag{4.65}$$

of the 13 3 5 Bragg peak which corresponds to a signal-to-background ratio of about 10:1. It shows that in the situation of a single reflection, the determination of absolute Laue spot intensities is possible with a relative accuracy in the range of 1%. Additionally, the expected Poisson distribution of detected photon numbers could be confirmed for significantly lower count rates in comparison to the high-flux experiments described in chapter 3.2.2.
The developed technique can be generalized for cases of overlapping harmonics as long as the background level is sufficiently low to ensure a negligible pile-up probability of measuring two (or more) air-scattered photons at the same position during the exposure time of the pnCCD.

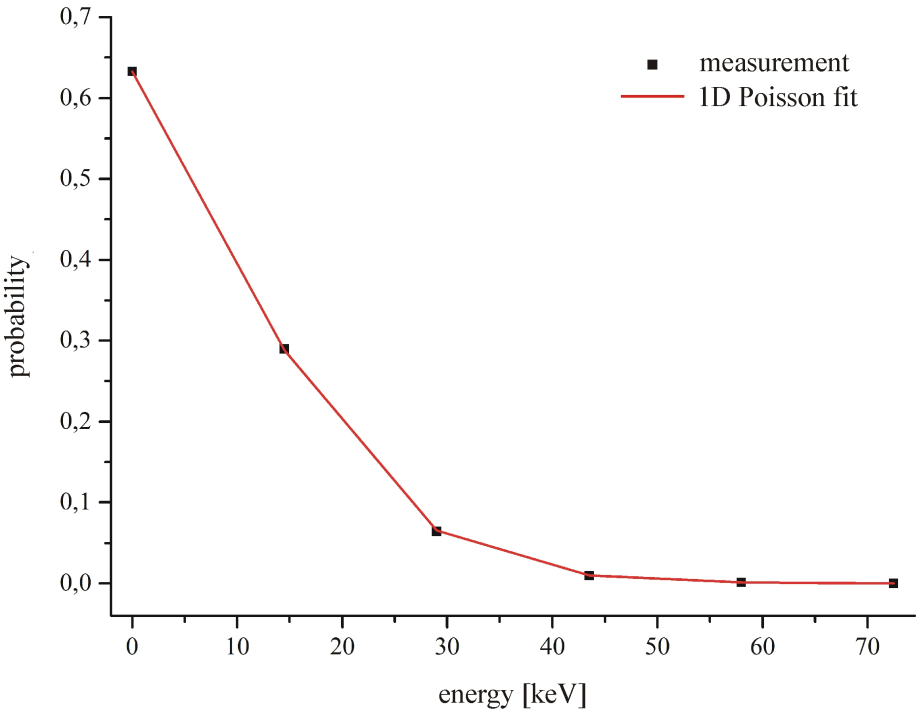

Figure 4.17: 1D Poisson distribution fitted to the integrated and normalized pile-up spectrum of the 13 3 5 reflection depicted in figure 4.16.

4.5.4 Deconvolution of two overlapping harmonics

The problem of intensity analysis in EDLD experiments using white synchrotron radiation exhibits a higher degree of complexity if Bragg peaks of different orders are simultaneously present within the selected spot areas. As discussed in chapter 4.1.2, the Bragg condition can be fulfilled by a set of several discrete X-ray energies reflected from the crystal, provided that these energies are contained in the primary beam spectrum at the sample position with sufficient intensity. In general, the real experimental situation can be described in such a way that the scattering signal of the crystal in a particular direction defined by Bragg's law consists of diffracted energies $E_1,...,E_n$ with average count rates $\lambda_1,...,\lambda_n$ superimposed by the background count rate λ_{bg}. In this case, the detectable energies $E_1,...,E_n$, which belong to reflections of various orders, are integer multiples of the energy assigned to the first-order Bragg peak with coprime Miller indices hkl. Depending on the count rates $\lambda_1,...,\lambda_n$, the occurrence of spatially overlapping harmonics may lead to pile-up events including diffracted X-rays with different energies and at most one air-scattered photon.

A two-dimensional example of this situation arises in the energy spectrum recorded at the position of the 613 reflection (figure 4.18). The measured intensity distribution is dominated by the 613 single peak with the fitted energy $E_1 = (10.75 \pm 0.11)\,\mathrm{keV}$ superimposed by the second-order reflection 12 2 6 with the energy $E_2 = (21.50 \pm 0.18)\,\mathrm{keV}$ and a white background spectrum with the average count rate $\lambda_{bg} = 0.03127$. The third-order Bragg peak 18 3 9 with

the expected energy $E_3 = (32.25 \pm 0.23)\,\mathrm{keV}$ could not be observed due to the low incident X-ray flux at this energy.

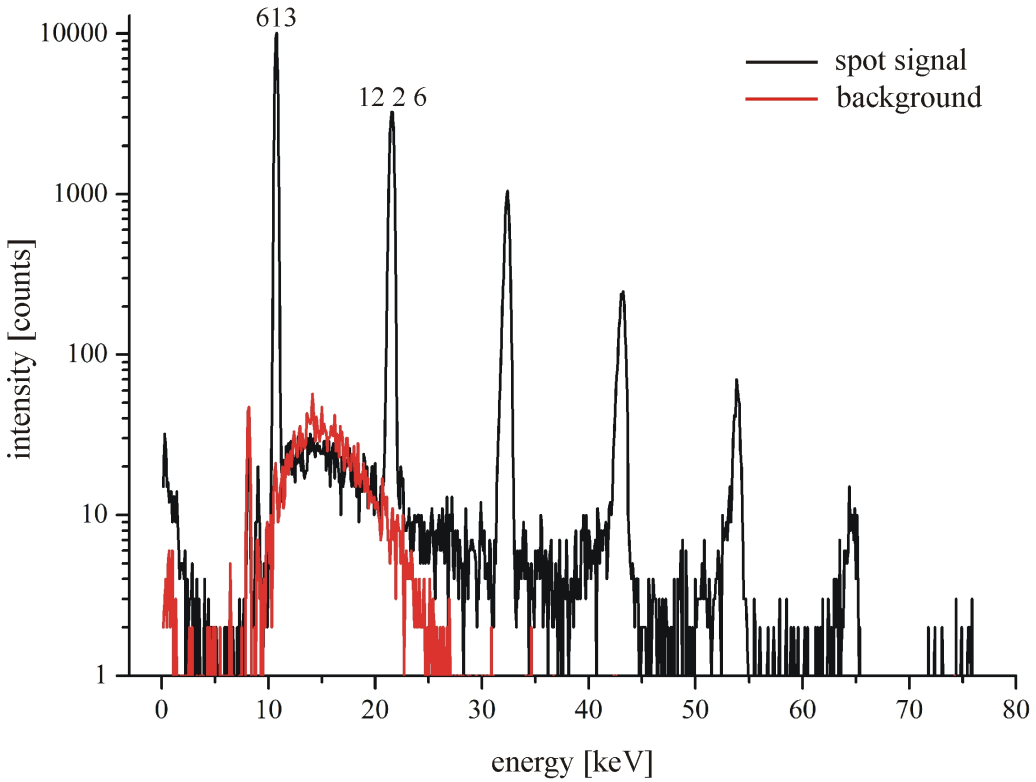

Figure 4.18: Energy spectrum detected at the position of the 613 reflection (black curve) and associated background signal (red curve). The pile-up peaks are generated by the overlapping harmonics 613 and 12 2 6 with different energies.

The recorded spectrum contains multi-photon hits resulting from overlaps of the determined Laue spot energies E_1 and E_2, whose peak positions are integer multiples of the first-order energy E_1, and suppressed contributions of pile-up signals including one air-scattered photon. In particular, the second peak assigned to the 12 2 6 reflection comprises both single-photon events with the energy $E_2 = 2E_1$ and pile-up events of two photons with the energy E_1 of the 613 reflection. Accordingly, the third spectral peak with the energy $E_3 = 3E_1$ is generated by overlaps of both three photons of energy E_1 and two photons with the energies E_1 and E_2. Further considerations show that the number of statistically possible combinations of E_1 and E_2 to the higher pile-up peak energies $4E_1$ and $5E_1$ increases to three, whereas the creation of the energies $6E_1$ and $7E_1$ is enabled by four different combinations of E_1 and E_2. The total probability of detecting an event with one of these energies in the selected spot area depends on the average count rates λ_1 and λ_2 of the 613 and the 12 2 6 Bragg peaks. Based on the condition that the numbers k_1 and k_2 of recorded photons with the energies E_1 and E_2 are Poisson-distributed with the independent mean values λ_1 and λ_2, this statistical probability

can be expressed in terms of λ_1 and λ_2 taking into account the various overlaps of photons with these energies. The combinations to be considered, giving rise to the pile-up spectrum of figure 4.18, are summarized in table 4.3 together with their statistical probabilities defined by products of the form $P_{k_1}(\lambda_1)P_{k_2}(\lambda_2)$ using (2.21).

measured	numbers of detected photons with the energies		statistical
signal [keV]	10.75 keV	21.50 keV	probability
0	0	0	$\left(e^{-\lambda_1}\right)\left(e^{-\lambda_2}\right)$
10.75	1	0	$\left(\lambda_1 e^{-\lambda_1}\right)\left(e^{-\lambda_2}\right)$
21.50	2	0	$\left(\frac{1}{2}\lambda_1^2 e^{-\lambda_1}\right)\left(e^{-\lambda_2}\right)$
21.50	0	1	$\left(e^{-\lambda_1}\right)\left(\lambda_2 e^{-\lambda_2}\right)$
32.25	3	0	$\left(\frac{1}{6}\lambda_1^3 e^{-\lambda_1}\right)\left(e^{-\lambda_2}\right)$
32.25	1	1	$\left(\lambda_1 e^{-\lambda_1}\right)\left(\lambda_2 e^{-\lambda_2}\right)$
43.00	4	0	$\left(\frac{1}{24}\lambda_1^4 e^{-\lambda_1}\right)\left(e^{-\lambda_2}\right)$
43.00	2	1	$\left(\frac{1}{2}\lambda_1^2 e^{-\lambda_1}\right)\left(\lambda_2 e^{-\lambda_2}\right)$
43.00	0	2	$\left(e^{-\lambda_1}\right)\left(\frac{1}{2}\lambda_2^2 e^{-\lambda_2}\right)$
53.75	5	0	$\left(\frac{1}{120}\lambda_1^5 e^{-\lambda_1}\right)\left(e^{-\lambda_2}\right)$
53.75	3	1	$\left(\frac{1}{6}\lambda_1^3 e^{-\lambda_1}\right)\left(\lambda_2 e^{-\lambda_2}\right)$
53.75	1	2	$\left(\lambda_1 e^{-\lambda_1}\right)\left(\frac{1}{2}\lambda_2^2 e^{-\lambda_2}\right)$
64.50	6	0	$\left(\frac{1}{720}\lambda_1^6 e^{-\lambda_1}\right)\left(e^{-\lambda_2}\right)$
64.50	4	1	$\left(\frac{1}{24}\lambda_1^4 e^{-\lambda_1}\right)\left(\lambda_2 e^{-\lambda_2}\right)$
64.50	2	2	$\left(\frac{1}{2}\lambda_1^2 e^{-\lambda_1}\right)\left(\frac{1}{2}\lambda_2^2 e^{-\lambda_2}\right)$
64.50	0	3	$\left(e^{-\lambda_1}\right)\left(\frac{1}{6}\lambda_2^3 e^{-\lambda_2}\right)$
75.25	7	0	$\left(\frac{1}{5040}\lambda_1^7 e^{-\lambda_1}\right)\left(e^{-\lambda_2}\right)$
75.25	5	1	$\left(\frac{1}{120}\lambda_1^5 e^{-\lambda_1}\right)\left(\lambda_2 e^{-\lambda_2}\right)$
75.25	3	2	$\left(\frac{1}{6}\lambda_1^3 e^{-\lambda_1}\right)\left(\frac{1}{2}\lambda_2^2 e^{-\lambda_2}\right)$
75.25	1	3	$\left(\lambda_1 e^{-\lambda_1}\right)\left(\frac{1}{6}\lambda_2^3 e^{-\lambda_2}\right)$

Table 4.3: Statistical pile-up peak probabilities for the overlapping harmonics 613 and 12 2 6.

Hence, the total probability of measuring an event with the energy $E_3 = 3E_1 = 32.25\,\text{keV}$ arising from overlaps of the listed numbers of photons with the energies $E_1 = 10.75\,\text{keV}$ and $E_2 = 2E_1 = 21.50\,\text{keV}$ in the absence of background contributions is

$$\begin{aligned} P_{32.25\,\text{keV}} &= P_3(\lambda_1)P_0(\lambda_2) + P_1(\lambda_1)P_1(\lambda_2) \\ &= \left(\tfrac{1}{6}\lambda_1^3 e^{-\lambda_1}\right)\left(e^{-\lambda_2}\right) + \left(\lambda_1 e^{-\lambda_1}\right)\left(\lambda_2 e^{-\lambda_2}\right) \\ &= \left(\tfrac{1}{6}\lambda_1^3 + \lambda_1\lambda_2\right) e^{-(\lambda_1+\lambda_2)} \ . \end{aligned} \tag{4.66}$$

Analog analyses of the remaining spectral pile-up peaks with the energies nE_1 including the case of no detected photon ($n=0$) provide the set

$$\begin{aligned}
P_{0\,\mathrm{keV}}(\lambda_1,\lambda_2) &= e^{-(\lambda_1+\lambda_2)} \\
P_{10.75\,\mathrm{keV}}(\lambda_1,\lambda_2) &= \lambda_1\, e^{-(\lambda_1+\lambda_2)} \\
P_{21.50\,\mathrm{keV}}(\lambda_1,\lambda_2) &= \left(\tfrac{1}{2}\lambda_1^2+\lambda_2\right) e^{-(\lambda_1+\lambda_2)} \\
P_{32.25\,\mathrm{keV}}(\lambda_1,\lambda_2) &= \left(\tfrac{1}{6}\lambda_1^3+\lambda_1\lambda_2\right) e^{-(\lambda_1+\lambda_2)} \\
P_{43.00\,\mathrm{keV}}(\lambda_1,\lambda_2) &= \left(\tfrac{1}{24}\lambda_1^4+\tfrac{1}{2}\lambda_1^2\lambda_2+\tfrac{1}{2}\lambda_2^2\right) e^{-(\lambda_1+\lambda_2)} \\
P_{53.75\,\mathrm{keV}}(\lambda_1,\lambda_2) &= \left(\tfrac{1}{120}\lambda_1^5+\tfrac{1}{6}\lambda_1^3\lambda_2+\tfrac{1}{2}\lambda_1\lambda_2^2\right) e^{-(\lambda_1+\lambda_2)} \\
P_{64.50\,\mathrm{keV}}(\lambda_1,\lambda_2) &= \left(\tfrac{1}{720}\lambda_1^6+\tfrac{1}{24}\lambda_1^4\lambda_2+\tfrac{1}{4}\lambda_1^2\lambda_2^2+\tfrac{1}{6}\lambda_2^3\right) e^{-(\lambda_1+\lambda_2)} \\
P_{75.25\,\mathrm{keV}}(\lambda_1,\lambda_2) &= \left(\tfrac{1}{5040}\lambda_1^7+\tfrac{1}{120}\lambda_1^5\lambda_2+\tfrac{1}{12}\lambda_1^3\lambda_2^2+\tfrac{1}{6}\lambda_1\lambda_2^3\right) e^{-(\lambda_1+\lambda_2)}
\end{aligned} \tag{4.67}$$

of statistical probabilities associated with the identified pile-up signals. The individual peaks in figure 4.18 were background-corrected, integrated, and normalized in the way described in chapter 4.5.3. The so-extracted experimental probabilities could then be fitted with the computed set (4.67) by means of a least-squares method yielding a two-dimensional Poisson fit of the recorded pile-up spectrum (figure 4.19).

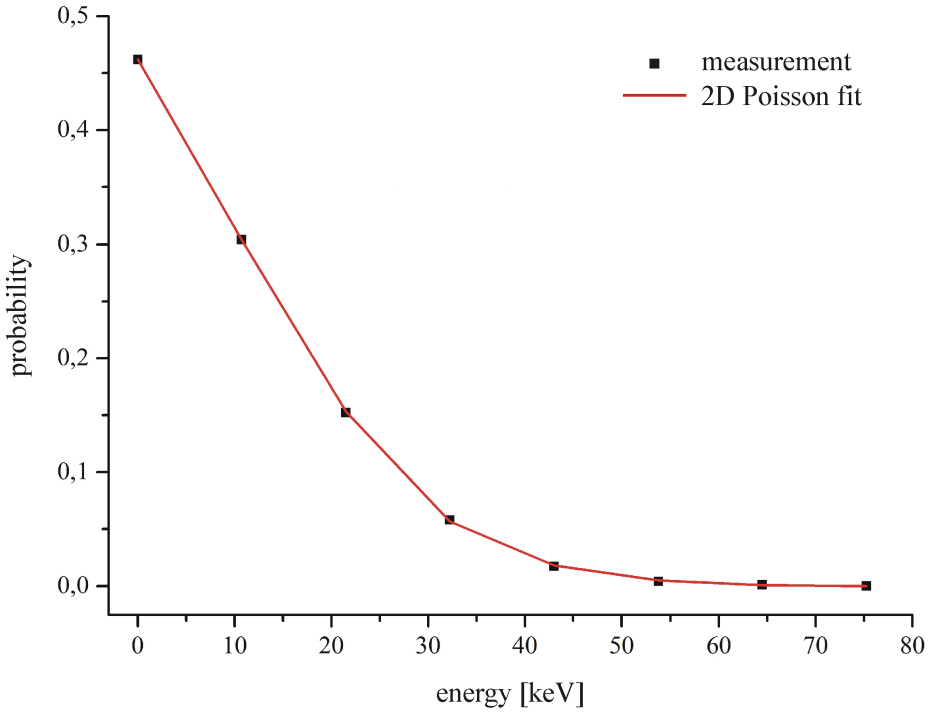

Figure 4.19: 2D Poisson fit of the experimental pile-up peak probabilities calculated from the integrated and normalized energy spectrum of figure 4.18 caused by the spatial overlap of the 613 and 12 2 6 reflections.

The obtained curve enables a statistical deconvolution of the simultaneously present 613 and 12 2 6 Bragg peaks in terms of the average count rates

$$\lambda_1 = 0.65721 \pm 0.00534 \ , \ \lambda_2 = 0.11514 \pm 0.00122 \tag{4.68}$$

and the corresponding integrated spot intensities

$$I_{613} = 65721 \pm 534 \ , \ I_{12\,2\,6} = 11514 \pm 122 \ . \tag{4.69}$$

This result shows that also in the case of two spatially overlapping diffraction orders, an absolute intensity determination can be achieved with a relative accuracy in the range of 1%.

4.5.5 Deconvolution of three overlapping harmonics

The developed method for quantitative analyses of superimposed harmonics can be directly generalized for more complicated situations in which Laue spots generated by the crystal comprise three (or more) diffracted energies. An instructive example of such a case consists in the signal detected at the position of the dominant 640 Bragg peak (figure 4.20).

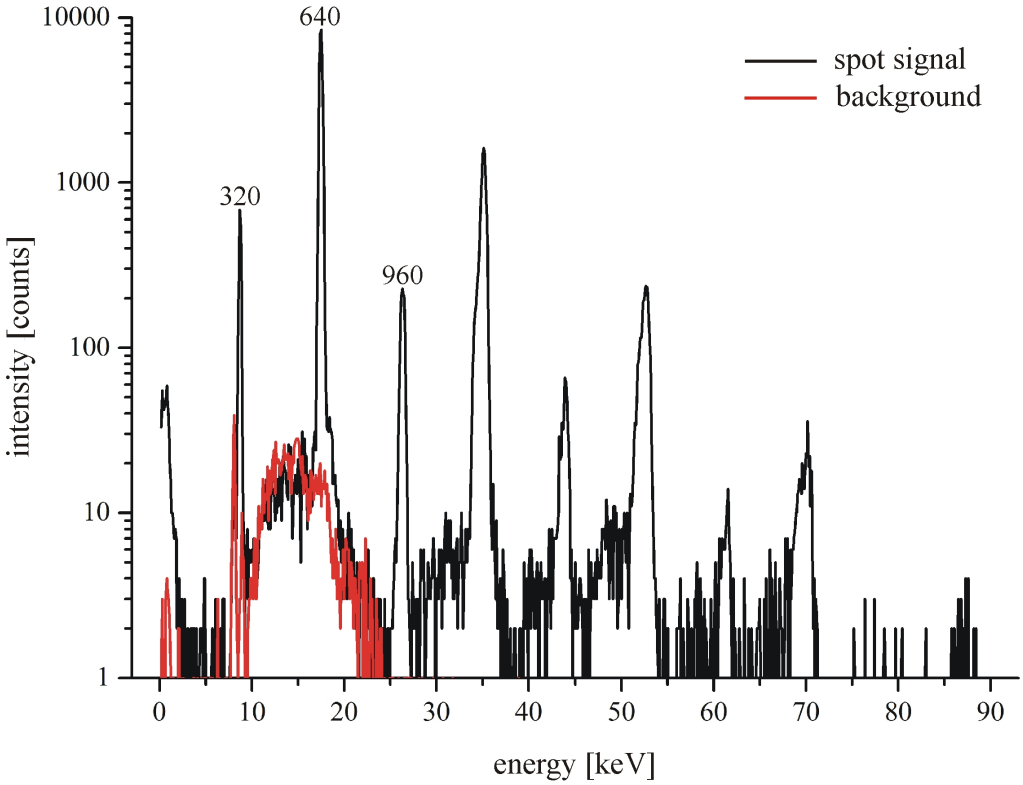

Figure 4.20: Energy spectrum measured within the selected spot area of the 640 reflection (black curve) and accompanying background signal (red curve).

The pile-up spectrum includes contributions of the 320, 640, and 960 reflections with the fitted energies $E_1 = (8.74 \pm 0.11)\,\mathrm{keV}$, $E_2 = (17.48 \pm 0.16)\,\mathrm{keV}$, and $E_3 = (26.22 \pm 0.23)\,\mathrm{keV}$ on top of a background continuum with the average count rate $\lambda_{\mathrm{bg}} = 0.01771$. Since 320 represents a first-order reflection, the observed pile-up peaks occur at integer multiples of E_1 extending up to the maximum energy $10E_1 = 87.40\,\mathrm{keV}$. The statistical probabilities of individual pile-up signals, determined by the mean count rates λ_1, λ_2, and λ_3 at which the 320, 640, and 960 Bragg peaks were recorded, result from spatial overlaps of particular photon numbers with the energies E_1, E_2, and E_3. The associated multi-photon hits leading to the various pile-up combinations to the identified spectral peak energies are listed in table 4.4.

measured signal [keV]	possible pile-up combinations of detected photons with the energies 8.74 keV | 17.48 keV | 26.22 keV
0	0|0|0
8.74	1|0|0
17.48	2|0|0, 0|1|0
26.22	3|0|0, 1|1|0, 0|0|1
34.96	4|0|0, 2|1|0, 1|0|1, 0|2|0
43.70	5|0|0, 3|1|0, 2|0|1, 1|2|0, 0|1|1
52.44	6|0|0, 4|1|0, 3|0|1, 2|2|0, 1|1|1, 0|3|0, 0|0|2
61.18	7|0|0, 5|1|0, 4|0|1, 3|2|0, 2|1|1, 1|3|0, 1|0|2, 0|2|1
69.92	8|0|0, 6|1|0, 5|0|1, 4|2|0, 3|1|1, 2|3|0, 2|0|2, 1|2|1, 0|4|0, 0|1|2
78.66	9|0|0, 7|1|0, 6|0|1, 5|2|0, 4|1|1, 3|3|0, 3|0|2, 2|2|1, 1|4|0, 1|1|2, 0|3|1, 0|0|3
87.40	10|0|0, 8|1|0, 7|0|1, 6|2|0, 5|1|1, 4|3|0, 4|0|2, 3|2|1, 2|4|0, 2|1|2, 1|3|1, 1|0|3, 0|5|0, 0|2|2

Table 4.4: Pile-up combinations in the case of the overlapping harmonics 320, 640, and 960. The notation $n_1|n_2|n_3$ indicates a pile-up event containing n_1 photons with the energy E_1, n_2 photons with the energy E_2, and n_3 photons with the energy E_3.

Taking into account the different contributions to the pile-up spectrum, the total probability of detecting an event with the energy $E_3 = 26.22\,\mathrm{keV}$, generated either by a single photon of this energy or by an appropriate overlap of photons with the energies E_1 and E_2, amounts to

$$\begin{aligned} P_{26.22\,\mathrm{keV}} &= P_3(\lambda_1)P_0(\lambda_2)P_0(\lambda_3) + P_1(\lambda_1)P_1(\lambda_2)P_0(\lambda_3) + P_0(\lambda_1)P_0(\lambda_2)P_1(\lambda_3) \\ &= \left(\tfrac{1}{6}\lambda_1^3 e^{-\lambda_1} e^{-\lambda_2} e^{-\lambda_3}\right) + \left(\lambda_1 e^{-\lambda_1}\lambda_2 e^{-\lambda_2} e^{-\lambda_3}\right) + \left(e^{-\lambda_1} e^{-\lambda_2}\lambda_3 e^{-\lambda_3}\right) \\ &= \left(\tfrac{1}{6}\lambda_1^3 + \lambda_1\lambda_2 + \lambda_3\right) e^{-(\lambda_1+\lambda_2+\lambda_3)} \ . \end{aligned} \tag{4.70}$$

The corresponding consideration of the pile-up combinations to the remaining spectral peaks with the energies nE_1 ($n = 0,...,10$) yields the set $\{P_{nE_1}(\lambda_1, \lambda_2, \lambda_3)\}$ of statistical probabilities of the pile-up signals excluding air-scattered X-rays. The background-corrected intensities, which resulted after integrating the pile-up spectrum of figure 4.20, were again normalized to the number of accumulated signal frames. The so-obtained, experimentally determined probabilities associated with the recorded pile-up peaks could then be fitted with the set $\{P_{nE_1}(\lambda_1, \lambda_2, \lambda_3)\}$ predicted by Poisson statistics using a least-squares method with the three fit parameters λ_1, λ_2, and λ_3.

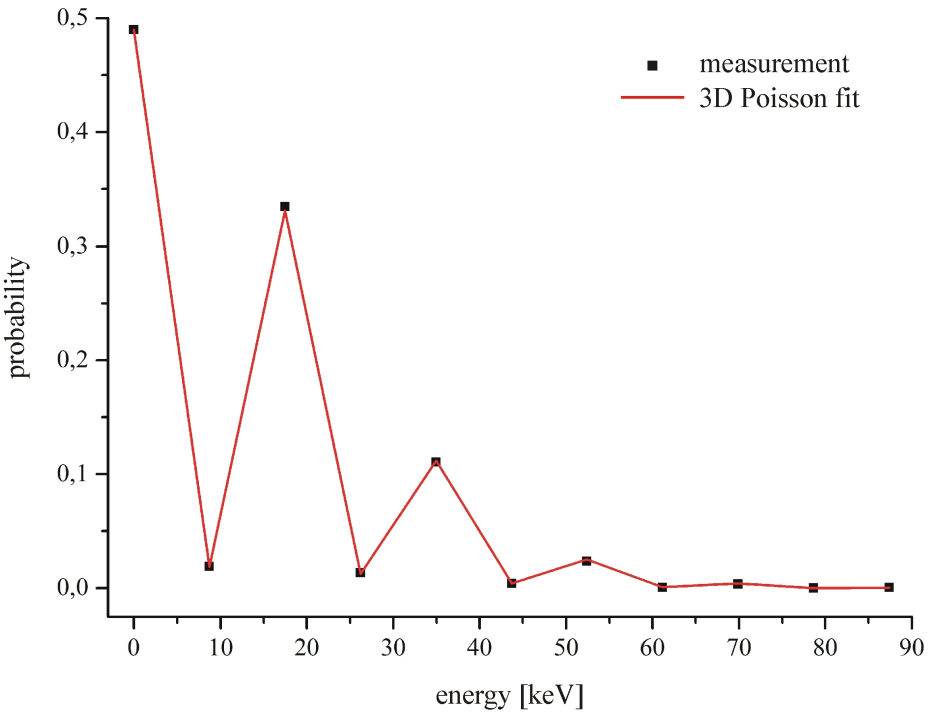

Figure 4.21: 3D Poisson fit of the experimental pile-up peak probabilities calculated from the integrated and normalized energy spectrum of figure 4.20 caused by the spatial overlap of the 320, 640, and 960 reflections.

The applied fit, depicted in figure 4.21, is described by the Poisson mean values

$$\lambda_1 = 0.03803 \pm 0.00048 \ , \ \lambda_2 = 0.67614 \pm 0.00526 \ , \ \lambda_3 = 0 \tag{4.71}$$

leading to the integrated intensities

$$I_{320} = 3803 \pm 48 \ , \ I_{640} = 67614 \pm 526 \ , \ I_{960} = 0 \ . \tag{4.72}$$

According to (4.72), the pile-up spectrum of figure 4.20 is strongly dominated by the 640 Bragg peak, whereas the 960 reflection exhibits a vanishing diffraction signal. This result could be confirmed within an independent analysis of another HEWL crystal at room temperature

which was performed in the monochromatic mode at the MX beamline 14.2 at BESSY II [83] with a gradually rotated sample [84]. As a consequence of $I_{960} = 0$, the spectral peak with the energy $E_3 = 26.22\,\text{keV}$ was solely generated by pile-up events of two photons with the energies $E_1 = 8.74\,\text{keV}$ and $E_2 = 17.48\,\text{keV}$ since overlaps of three photons with the energy E_1 are statistically negligible for the obtained count rate λ_1.

4.5.6 Deconvolution of four overlapping harmonics

The analyses of pile-up spectra detected at the positions of individual Laue spots require an increasingly extensive algorithm for deconvolution of superimposed harmonics, the more diffraction orders, resulting in a larger number of possible pile-up combinations, are involved. In the Laue pattern of figure 4.15, the most complicated situation arises at the position of the 933 reflection. The spectrum measured within the selected spot region comprises the four overlapping harmonics 622, 933, 12 4 4, and 15 5 5 with the energies $E_1 = (10.00 \pm 0.11)\,\text{keV}$, $E_2 = (15.00 \pm 0.13)\,\text{keV}$, $E_3 = (20.00 \pm 0.16)\,\text{keV}$, and $E_4 = (25.00 \pm 0.19)\,\text{keV}$ accompanied by a background signal with the average count rate $\lambda_{\text{bg}} = 0.02642$ (figure 4.22).

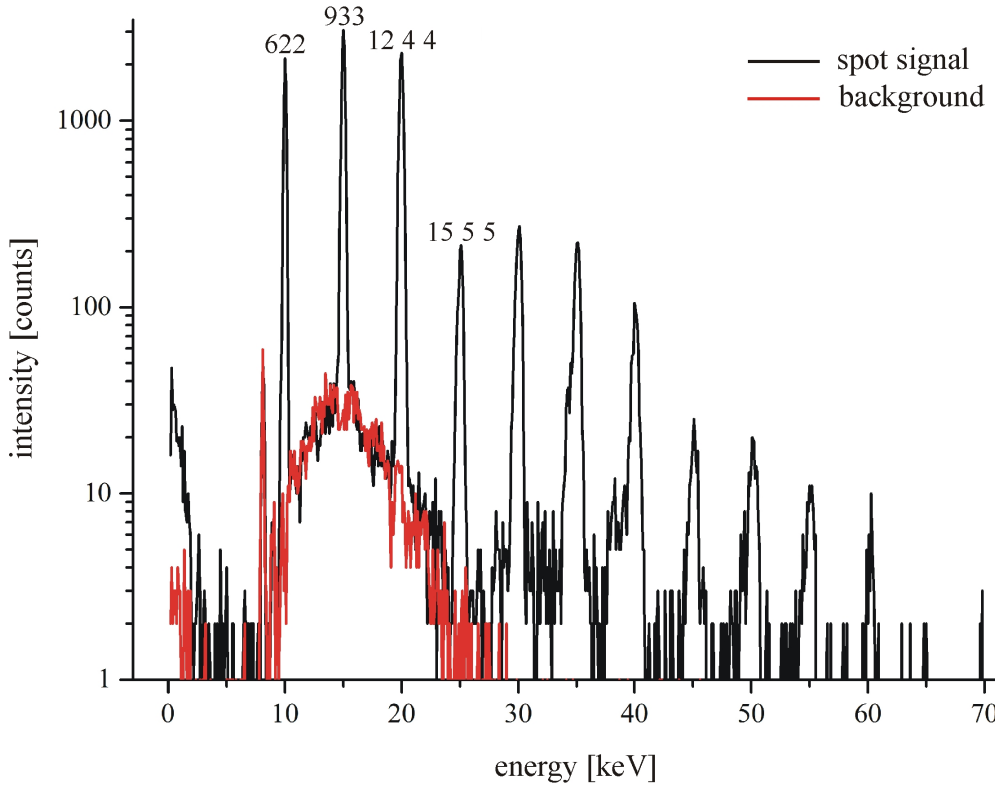

Figure 4.22: Energy spectrum recorded at the position of the 933 reflection (black curve) and corresponding background signal (red curve).

The identified Bragg peaks represent higher diffraction orders of the 311 reflection that could not be excited under the experimental conditions as the required energy $E_0 = 5.00\,\text{keV}$ is not

contained in the white X-ray spectrum incident on the crystal due to absorption effects within the used filters. Nevertheless, the energies associated with the pronounced spectral peaks are integer multiples of the first-order energy E_0 giving rise to measurable pile-up signals up to $14E_0 = 70.00\,\mathrm{keV}$. In principle, each pile-up peak includes contributions of particular numbers of photons with the energies E_1,...,E_4 defined by the average count rates λ_1,...,λ_4 of the 622, 933, 12 4 4, and 15 5 5 reflections. Following the method applied in the previous chapters, the statistical probabilities of the various pile-up signals were calculated in terms of the possible combinations of photon numbers creating the observed pile-up energies listed in table 4.5.

measured signal [keV]	possible pile-up combinations of detected photons with the energies 10.00 keV | 15.00 keV | 20.00 keV | 25.00 keV
0	0|0|0|0
10.00	1|0|0|0
15.00	0|1|0|0
20.00	2|0|0|0, 0|0|1|0
25.00	1|1|0|0, 0|0|0|1
30.00	3|0|0|0, 1|0|1|0, 0|2|0|0
35.00	2|1|0|0, 1|0|0|1, 0|1|1|0
40.00	4|0|0|0, 2|0|1|0, 1|2|0|0, 0|1|0|1, 0|0|2|0
45.00	3|1|0|0, 2|0|0|1, 1|1|1|0, 0|3|0|0, 0|0|1|1
50.00	5|0|0|0, 3|0|1|0, 2|2|0|0, 1|0|2|0, 0|2|1|0, 0|1|1|1, 0|0|0|2
55.00	4|1|0|0, 3|0|0|1, 2|1|1|0, 1|3|0|0, 1|0|1|1, 0|2|0|1, 0|1|2|0
60.00	6|0|0|0, 4|0|1|0, 3|2|0|0, 2|1|0|1, 2|0|2|0, 1|2|1|0, 1|0|0|2, 0|4|0|0, 0|1|1|1, 0|0|3|0
65.00	5|1|0|0, 4|0|0|1, 3|1|1|0, 2|3|0|0, 2|0|1|1, 1|2|0|1, 1|1|2|0, 0|3|1|0, 0|1|0|2, 0|0|2|1
70.00	7|0|0|0, 5|0|1|0, 4|2|0|0, 3|1|0|1, 3|0|2|0, 2|2|1|0, 2|0|0|2, 1|4|0|0, 1|1|1|1, 1|0|3|0, 0|2|2|0, 0|0|1|2

Table 4.5: Pile-up combinations for the overlapping harmonics 622, 933, 12 4 4, and 15 5 5. In analogy to the notation used in table 4.4, $n_1|n_2|n_3|n_4$ indicates a pile-up event containing n_1,...,n_4 photons with the energies E_1,...,E_4.

Thus, based on Poisson distributions of the involved numbers of photons with the energies E_1,...,E_4, the total probability of a pile-up event with the energy $9E_0 = 45.00\,\mathrm{keV}$ is given by

$$P_{45.00\,\mathrm{keV}} = \left(\tfrac{1}{6}\lambda_1^3\lambda_2 + \tfrac{1}{2}\lambda_1^2\lambda_4 + \lambda_1\lambda_2\lambda_3 + \tfrac{1}{6}\lambda_2^3 + \lambda_3\lambda_4\right) e^{-(\lambda_1+\lambda_2+\lambda_3+\lambda_4)} \quad . \tag{4.73}$$

The integrated, background-corrected, and normalized pile-up peak intensities extracted from the energy spectrum of figure 4.22 yielded the required set of experimental probabilities for the corresponding pile-up signals which could finally be fitted with the set $\{P_{nE_0}(\lambda_1, \lambda_2, \lambda_3, \lambda_4)\}$ of statistical probabilities for the occurrence of events with the energies nE_0 $(n = 0,2,3,...,14)$.

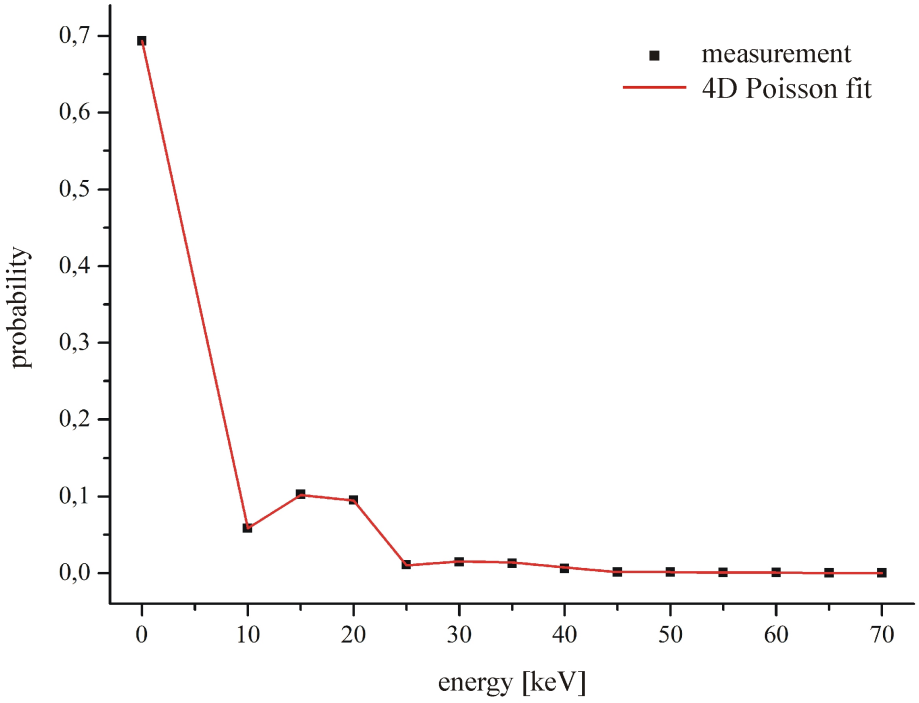

Figure 4.23: 4D Poisson fit of the experimental pile-up peak probabilities calculated from the integrated and normalized energy spectrum of figure 4.22 caused by the spatial overlap of the 622, 933, 12 4 4, and 15 5 5 reflections.

The result of the applied least-squares method including the four fit parameters $\lambda_1,...,\lambda_4$ is shown in figure 4.23. In this case, the statistical deconvolution of the recorded pile-up spectrum was achieved by means of the average count rates

$$\begin{aligned} \lambda_1 &= 0.08427 \pm 0.00096 \quad , \quad \lambda_2 = 0.14723 \pm 0.00135 \quad , \\ \lambda_3 &= 0.13250 \pm 0.00149 \quad , \quad \lambda_4 = 0.00184 \pm 0.00065 \end{aligned} \tag{4.74}$$

translating into the absolute intensities

$$\begin{aligned} I_{622} &= 8427 \pm 96 \quad , \quad I_{933} = 14723 \pm 135 \quad , \\ I_{12\,4\,4} &= 13250 \pm 149 \quad , \quad I_{15\,5\,5} = 184 \pm 65 \quad . \end{aligned} \tag{4.75}$$

The obtained values (4.75) reveal that the effective contribution of the 15 5 5 Bragg peak to the energy spectrum of figure 4.22 is strongly suppressed compared to the influence of the 622, 933, and 12 4 4 reflections. Moreover, the weak integrated signal $I_{15\,5\,5}$ could be determined

with a degraded relative error of about 35% in contrast to the intensities of the remaining diffraction orders being resolved with accuracies in the range of 1%. Therefore, with respect to X-ray structure analyses on an atomic level, the set $\{hkl\}$ of collected and deconvoluted Bragg peaks needs to be restricted to reflections which were detected with sufficient statistics and precision required for a reliable calculation of structure-factor amplitudes.

4.5.7 Structure refinement

As soon as the set $\{I_{hkl}\}$ of integrated Laue spot intensities is extracted from the recorded Laue pattern using the methods described in chapters 4.5.1-4.5.6, the associated set $\{|F_{hkl}|\}$ of observed structure-factor amplitudes can be obtained from (4.17),

$$|F_{hkl}|^2 \propto \frac{I_{hkl}}{\varepsilon I_0 LP} \ . \tag{4.76}$$

The proportionality constant in (4.76) is a scale factor taken into account for normalizing the modeled structure-factor amplitudes to the collected data prior to structure refinement. The relative accuracy of $|F_{hkl}|^2$ depends on the experimental conditions and the instrumental resolution of the pnCCD and can be estimated by

$$\frac{\delta|F_{hkl}|^2}{|F_{hkl}|^2} = \sqrt{\left(\frac{\delta I_{hkl}}{I_{hkl}}\right)^2 + \left(\frac{\delta I_0}{I_0}\right)^2 + \left(\frac{\delta\varepsilon}{\varepsilon}\right)^2 + \left(\frac{\delta L}{L}\right)^2 + \left(\frac{\delta P}{P}\right)^2} \ . \tag{4.77}$$

According to the discussions in chapter 4.5.6, the error $\delta I_{hkl}/I_{hkl}$ is in the range of 1% for Bragg peaks with sufficiently intense diffraction signals. The accuracy $\delta I_0/I_0$ of the primary X-ray flux at the measured spot energy, which originates from the fit results of table 4.1 and imprecisions of the linear absorption coefficients μ_{Al}, μ_{Fe}, and μ_{air} as well as of the beam path length in air, amounts to about 2%. The errors $\delta\varepsilon/\varepsilon$ of the quantum efficiency (2.17), $\delta L/L$ of the Lorentz factor (4.20), and $\delta P/P$ of the polarization factor (4.21) are given by the energy and angular resolution of the pnCCD. Quantitative analyses of the quantum efficiency curves $\varepsilon(E, 2\theta)$ at scattering angles 2θ below 25° have shown that the experimental accuracy $\delta\varepsilon/\varepsilon$ varies between 1% and 2% in the energy range $E = 10...20\,\mathrm{keV}$. The relative error $\delta L/L$ is

$$\frac{\delta L}{L} = 2\sqrt{\left(\frac{\delta E}{E}\right)^2 + \left(\frac{\delta\theta}{\tan\theta}\right)^2} \tag{4.78}$$

using (4.20) with $\delta\lambda/\lambda = \delta E/E \approx 1\%$ and

$$\delta\theta = \frac{x^2}{2s^2}\sqrt{\frac{y^2+z^2}{x^2}\left(\frac{\delta x}{x}\right)^2 + \frac{y^2}{y^2+z^2}\left(\frac{\delta y}{x}\right)^2 + \frac{z^2}{y^2+z^2}\left(\frac{\delta z}{x}\right)^2} \tag{4.79}$$

resulting from

$$2\theta = \arctan\frac{\sqrt{y^2+z^2}}{x} \ . \tag{4.80}$$

Under real experimental conditions of EDLD on HEWL crystals with the considered position errors δx, δy, and δz, the angular resolution $\delta\theta$ is in the range of 0.1° giving rise to $\delta L/L \approx 4\%$. The error δP can be expressed by

$$\delta P = \sqrt{\Big(2\sin 2\theta\cos 2\theta\big(1+\cos 2\rho\big)\delta\theta\Big)^2 + \Big(\sin^2 2\theta\sin 2\rho\,\delta\rho\Big)^2}\ , \tag{4.81}$$

where

$$\delta\rho = \sqrt{\Big(\frac{z}{y^2+z^2}\delta y\Big)^2 + \Big(\frac{y}{y^2+z^2}\delta z\Big)^2} \tag{4.82}$$

as a consequence of (4.23). The angular resolution $\delta\rho$ within the detection plane is below 0.2° yielding $\delta P/P < 1\%$ and the achievable relative accuracy

$$\frac{\delta|F_{hkl}|^2}{|F_{hkl}|^2} \approx 5\%\ . \tag{4.83}$$

The potential of the pnCCD for structure analyses based on the measurement of absolute Laue spot intensities was investigated in the course of an EDLD experiment on a tetragonal HEWL single crystal using the eROSITA pnCCD with 384×384 pixels. In comparison to the other pnCCD systems with smaller chip sizes, the obvious advantage of this detector module is the larger sensitive area which allows for an enhanced number of recordable reflections per image. In the setup of figure 4.5 with an air path length of 1470 mm between the exit slit and the sample position, various Laue patterns of the HEWL crystal were detected at the distance $x = 95$ mm behind the sample. The capillary was mounted on a one-axis goniometer providing a rotation of the crystal around the vertical z-axis. In this experiment, caused by the increased cycle time of the pnCCD in frame store mode (11.5 ms, frame rate 87 Hz), the incident X-ray flux had to be attenuated by the insertion of filter 4. The signal processing in the CAMEX chips was performed in a medium gain mode with 8-fold CDS characterized by an amplification of 0.20 adu/eV and a mean dark noise of about $8\,e^-$ (rms). For calibration purposes, gain and CTI correction factors were determined by means of an XRF measurement in which fluorescence radiation of a thin Cu foil served as a reference signal. In this case, the CuK_α single peak could be detected with a pulse height of about 1600 adu and resolved with an FWHM in the range of 200 eV at an event threshold of 6σ.
The data collection was carried out for different positions of the pnCCD and three orientations $\phi = -45^\circ, 0^\circ, 45^\circ$ of the HEWL sample relative to the z-axis, where $\phi = 0^\circ$ denotes its original orientation. Under the geometrical conditions of this experiment, the Bragg peaks of the crystal could be recorded with the nominal resolution $d_{\min} = 1.5$ Å ($q_{\max} = 4.2\,\text{Å}^{-1}$). The raw data sets consisted of 300 dark frames and 100000 signal frames for each detector position and sample orientation corresponding to an exposure time of 1150 s, respectively. Applying the pre-calculated gain and CTI calibration factors to the data, the accumulated event patterns were recombined to single- and multi-photon hits including charge clusters. Figure 4.24 shows the measured diffraction patterns of the sample comprising 2774 identified Laue spots in total.

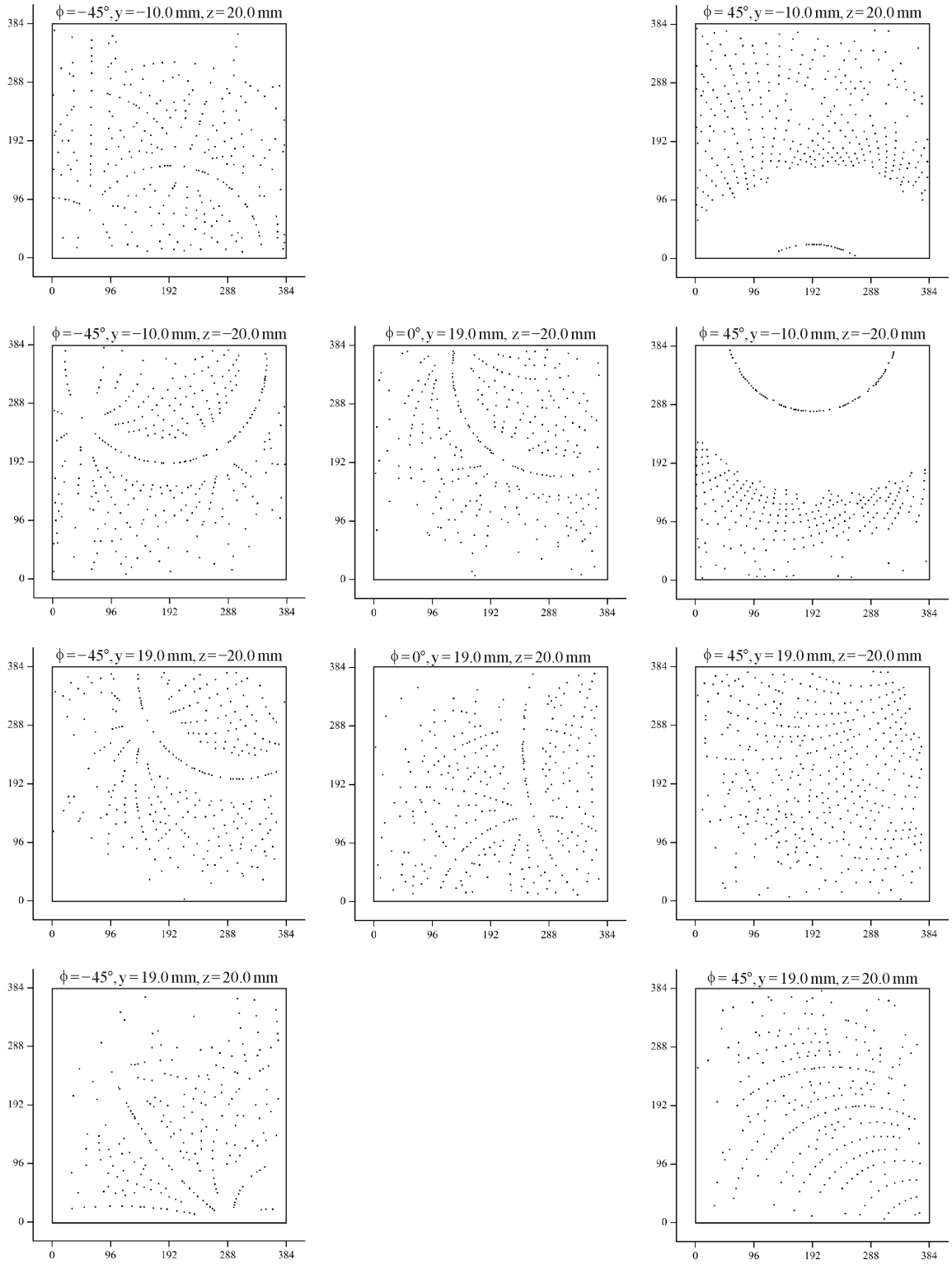

Figure 4.24: Laue patterns of a HEWL single crystal used for structure refinement. Images with a size of 384×384 pixels were recorded for various sample orientations ϕ and different horizontal and vertical positions y and z of the pnCCD center.

In order to extract experimental structure-factor amplitudes from the collected data volume, the conventional unit cell of the HEWL crystal in the externally defined coordinate system was determined for each measured Laue pattern separately. For that purpose, based on prior fits of the individual spot positions and dominating energies between 9 keV and 25 keV, the reduction and refinement procedures of chapter 4.2 were applied. The final unit cells, used for a complete indexing of the identified Bragg peaks, could be calculated by averaging the tetragonal cells obtained from the various Laue patterns that were recorded for different detector locations at a fixed sample orientation. Quantitative analyses of the energy spectra measured at the spot positions enabled absolute intensity determination according to the algorithms for integration of single reflections and deconvolution of overlapping harmonics presented in chapters 4.5.3-4.5.6. In this way, an effective number of 3554 collected Bragg peaks of the crystal, which showed a sufficiently intense diffraction signal, could be indexed and assigned with a set $\{|F_{hkl}|^2\}$ of observed structure-factor amplitudes.
In general, structure determination of macromolecular assemblies with high spatial resolution is achieved by recording a very large number of Bragg peak intensities (> 100000) measured up to as large as possible scattering angles. Additionally, conventional diffraction experiments are performed at cryogenic temperatures in order to protect the sample from radiation damage and to reduce thermal smearing. Compared to these general conditions, the data set $\{|F_{hkl}|^2\}$ extracted from the present energy-dispersive experiment is incomplete and does not allow high resolution. Therefore, the real quality of this data set was evaluated using a simplified model of tetragonal HEWL for refinement based on three fundamental constraints which are explained in detail below: Firstly, the known space group of the HEWL structure is taken as the basis for further analyses. Secondly, temperature effects, that become manifest in thermal atomic motions within the sample, are restricted to one global parameter B quantifying the oscillation of each individual atom. Thirdly, a rigid-body model of the crystal is introduced which represents the most basic approach for structure analyses. With these simplifications, the effective number of refined parameters can be significantly reduced.
The result of a structure analysis depends on the space group being used for a refinement of the modeled crystal structure against the recorded data. In the above-described form, the data volume is present in the most general triclinic space group P1 with the lowest symmetry. However, previous investigations have shown that the quality of the refinement improves if the set of experimental structure-factor amplitudes is available in the correct tetragonal space group $P4_32_12$ in which the investigated HEWL samples crystallize [85]. Hence, with regard to the Laue symmetry 4/mmm of the related point group 422, the measured set $\{|F_{hkl}|^2\}$ was averaged over the 16 equivalent reflections [86]

$$\begin{aligned} &h\,k\,l\ ,\ \overline{h}\,\overline{k}\,\overline{l}\ ,\ k\,h\,l\ ,\ \overline{k}\,\overline{h}\,\overline{l}\ ,\ h\,k\,\overline{l}\ ,\ \overline{h}\,\overline{k}\,l\ ,\ k\,h\,\overline{l}\ ,\ \overline{k}\,\overline{h}\,l\ ,\\ &\overline{k}\,h\,l\ ,\ k\,\overline{h}\,l\ ,\ k\,\overline{h}\,\overline{l}\ ,\ \overline{k}\,h\,\overline{l}\ ,\ \overline{h}\,k\,l\ ,\ h\,\overline{k}\,l\ ,\ h\,\overline{k}\,\overline{l}\ ,\ \overline{h}\,k\,\overline{l} \end{aligned}$$

yielding the same interplanar spacing distances (4.11) of the associated equivalent lattice planes. The remaining reduced data set comprised 2293 independent reflections which served to refine the HEWL structure against the collected data in the final step.

Conventional analyses of macromolecular structures in terms of observed spot intensities are based on the theory of Wilson [87] including thermal effects within the investigated crystal. This approach relies on temperature-corrected atomic scattering factors $(f_j)_T$ of the form [88]

$$(f_j)_T = f_j e^{-B_j \sin^2\theta/\lambda^2} \quad , \tag{4.84}$$

where f_j corresponds to the atomic form factor (4.19) of a stationary atom j in the unit cell. The so-called temperature factor B_j is given by

$$B_j = 8\pi^2 \overline{u_j^2} \tag{4.85}$$

with $\overline{u_j^2}$ denoting the mean-square displacement of the atom j due to atomic vibrations. If the atoms are considered as independent three-dimensional harmonic oscillators (Einstein model), $\overline{u_j^2}$ is directly proportional to the sample temperature T [56]. Under the assumption that the temperature factors B_j are equal for all the atoms in the crystal, expressed by the simplified notation $B_j \approx B$, the structure factor (4.18) is accordingly modified to

$$(F_{hkl})_T \approx F_{hkl} e^{-B \sin^2\theta/\lambda^2}. \tag{4.86}$$

Thus, the real observable intensity I_{hkl} of a Bragg peak hkl amounts to

$$I_{hkl} \approx c|F_{hkl}|^2 e^{-2B \sin^2\theta/\lambda^2} \quad , \tag{4.87}$$

where $c = \varepsilon I_0 LP$ comprises the relevant correction factors discussed in detail in chapter 4.1.3. The exponential term in (4.87) is also referred to as the Debye-Waller factor.
In the course of data processing, the recorded set of integrated intensities is analyzed within a series of resolution shells extending over the complete range of measured d-values down to the nominal resolution (4.24). To this end, the experimental structure-factor amplitudes are averaged over those reflections with comparable d-values that belong to the same resolution shell. In order to deduce the temperature factor B from the data, the quantity $|F_{hkl}|^2$ in (4.87), which cannot be measured directly, is usually estimated by assuming a random distribution of the atoms in the crystal yielding [88]

$$\overline{|F_{hkl}|^2} \approx \overline{\sum_j f_j^2} \quad . \tag{4.88}$$

Here, $\overline{|F_{hkl}|^2}$ and $\overline{\sum_j f_j^2}$ have to be understood as the respective average values evaluated at the mean of the upper and lower limits of the considered resolution shell. Therefore, inserting (4.88) into (4.87) and taking the natural logarithm leads to

$$\ln\Big(\frac{\overline{I}_{hkl}}{\overline{\sum_j f_j^2}}\Big) \approx \ln c - 2B\,\frac{\sin^2\theta}{\lambda^2} \tag{4.89}$$

with $\overline{I}_{hkl}$ denoting the mean (normalized) intensity of all measured reflections in this shell with the midpoint $\sin^2\theta/\lambda^2$. The resulting graph of $\ln(\overline{I}_{hkl}/\overline{\sum_j f_j^2})$ against $\sin^2\theta/\lambda^2$, known as a Wilson plot, is characterized by a linear part with the slope $-2B$ that can be obtained from a least-squares fit of a straight line to the data. Typical B-factors of macromolecules are in the range between $10\,\text{Å}^2$ and $30\,\text{Å}^2$ depending on the temperature and the quality of the crystal. At low values of $\sin^2\theta/\lambda^2$, the Wilson plot shows non-linearities, which is why data points of low resolution (usually $d \geq 4.5\,\text{Å}$) are excluded from the fit [72].
The reduced data set containing 2293 independent reflections referred to the space group $P4_32_12$ was further processed by means of the programs F2MTZ [89] and TRUNCATE [90, 91] supported by CCP4 [92]. In this way, the data set could be analyzed up to an effective resolution of 2.3 Å with the completeness $C = 36\%$, where C is defined as the ratio between the number of detected unique reflections and the number of observable reflections. Using the known atomic structure of HEWL, whose asymmetric unit consists of 129 amino acids per HEWL molecule, in the program TRUNCATE, the sum (4.88) of squared atomic form factors was calculated as a function of $\sin^2\theta/\lambda^2$. The so-obtained Wilson plot for this measurement is depicted in figure 4.25 together with the least-squares fit through the linear part of the curve applied in the resolution range between $d = 4.6\,\text{Å}$ and $d = 2.6\,\text{Å}$.

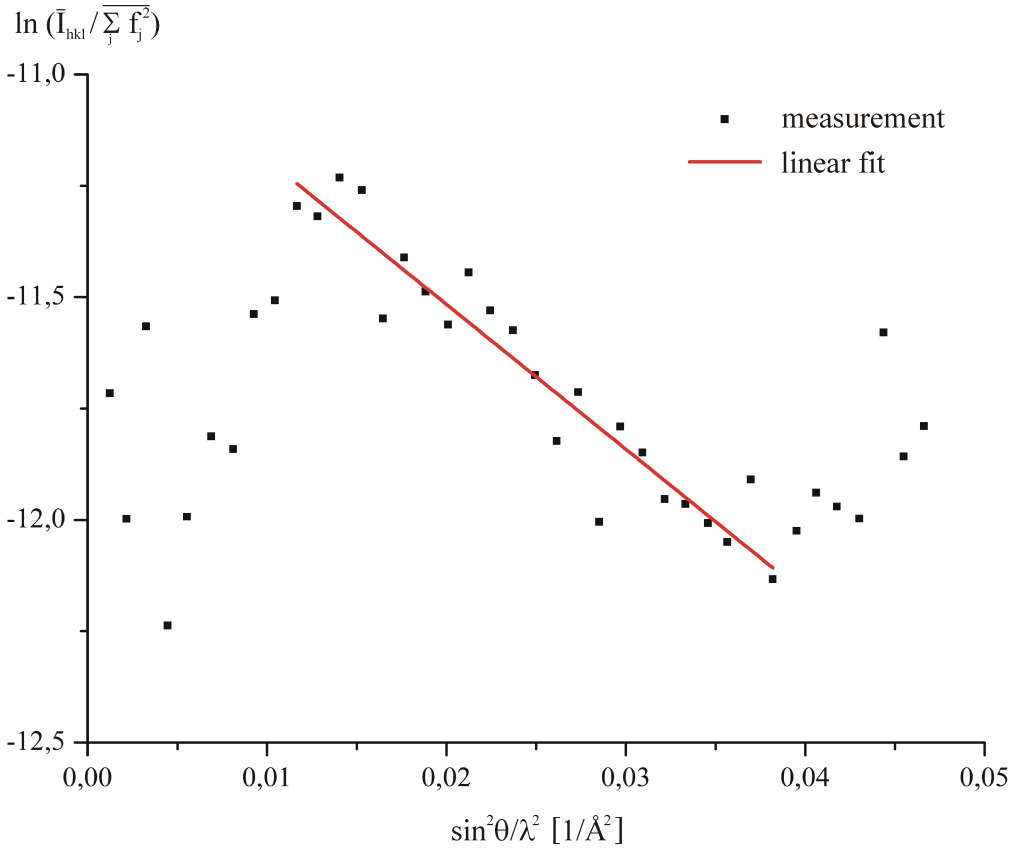

Figure 4.25: Wilson plot resulting from the recorded diffraction data of a HEWL single crystal. The linear fit of the data points is indicated by the red straight line.

The slope of the fitted line yields the temperature factor

$$B = (16.3 \pm 1.2)\,\text{Å}^2 \tag{4.90}$$

which is in agreement with results of standard techniques performed in the monochromatic mode at room temperature [85]. The non-linearity of the measured curve at values of $\sin^2\theta/\lambda^2$ below $0.01\,\text{Å}^{-2}$ ($d \geq 5\,\text{Å}$) is a consequence of scattering from solvent regions which are less well-ordered than the protein, thereby reducing the integrated intensity diffracted by the crystal. The rising tendency of the Wilson plot in the shells with the highest resolution $d \leq 2.5\,\text{Å}$ ($\sin^2\theta/\lambda^2 \geq 0.04\,\text{Å}^{-2}$) represents an anomaly in the recorded data set whose origin could not be uniquely clarified. In general, this behavior suggests that individual Bragg peaks exhibiting low d-values were assigned with too large experimental structure-factor amplitudes. Since low d-values are mainly associated with higher-order reflections, the observed effect might have been caused by weak diffraction signals of high-energetic Bragg peaks that were detected with an insufficient accuracy and not omitted for further data treatment. Additionally, the recorded data set is characterized by low statistics within the high-resolution shells which can be responsible for this anomaly.
The final step of data analysis consisted in a refinement of the crystal structure against the collected data. For that purpose, the atomic coordinates of the HEWL structure at room temperature were taken from the protein data bank PDB (ID 193L) [93]. In order to judge the quality of the data set in a basic approach, these coordinates served as the basis of a rigid-body refinement which was carried out by means of the program REFMAC5 [94, 95]. In the course of this refinement, the atoms building the HEWL structure were considered as a rigid body and assigned with a common set of six parameters, three of which representing translation and rotation coordinates, respectively. Under the described conditions, the obtained crystallographic R-factor (4.25) amounts to approximately 25%. This result is promising in so far as a relatively small set of six parameters was refined against more than 2000 collected reflections up to a resolution of 2.3 Å. From a conceptual point of view, the quality of pnCCD-generated data with regard to structure refinement of macromolecules can be markedly improved if a larger number of Bragg peaks is collected with preferably lower d-values. Particularly for analyses of electron densities, the availability of a complete data set recorded with a high resolution is essential. Moreover, optimized experimental conditions can be created by mounting the HEWL crystals on a fully automated goniometer ensuring a faster data collection and keeping them at cryogenic temperatures in order to reduce the probability of radiation damage.

5 Summary and Conclusions

In this thesis, the potential of frame store pnCCD systems for structure analyses using white synchrotron radiation was investigated. From a conceptual point of view, the pnCCD enables a four-dimensional X-ray detection reflected by the capability of simultaneous energy, time, and two-dimensional position resolution. In particular applications with a stationary sample, for which the time coordinates of detected photons are not of interest, the accessible data volume becomes effectively three-dimensional. In this case, the scattering signal of the sample can be interpreted in terms of integrated intensity distributions for each energy provided by the primary beam as well as complete X-ray spectra recorded in individual pixels.
The eROSITA pnCCD system with 384×384 pixels allows a detection of hard X-rays up to energies of about 30 keV with the highest sensitivity in the range of 10 keV at normal incidence. The performance of eROSITA type systems was analyzed under real experimental conditions by means of XRF spectroscopy with white synchrotron radiation and monochromatic X-ray exposures of single pixels at high count rates. In general, two operation modes of the pnCCD need to be distinguished:

- **Single-photon counting mode**: Individual photons are resolved within a 3D data volume spanned by two pixel directions and an energy coordinate. The safe spatial separation of different X-ray signals relies on a negligible pile-up probability ensured by a sufficiently low count rate. In concrete experiments, the pnCCD can be operated in a high gain mode providing the best possible energy resolution.

- **X-ray integration mode**: The 3D information about individual photons cannot be maintained as a result of enhanced pile-up contributions at high count rates. In order to measure intense diffraction signals with good statistics, a low gain selection is required.

It could be shown that in the SPC mode, the achievable relative energy resolution is in the range of 1% limited by accompanying continuous background signals in addition to the dark noise of the detector. In contrast, the X-ray integration mode is characterized by a degraded but sufficient energy resolution to separate pile-up peaks in the hard X-ray regime.
In the case of high local count rates, the dynamic range of the pnCCD depends on the number of electrons that can be stored in the potential wells at the detector front side. Under standard operation conditions (X-ray spectroscopy mode), the saturation limit of a single pixel, above which surplus charges spill over to neighboring pixels perpendicular to the transfer direction, amounts to about 300000 electrons. The maximum integral count rate per pixel in the full image mode is typically in the order of 10^4 cps depending on the X-ray energy and the frame rate. For high count rate experiments, the single-pixel CHC can be enhanced by means of

a more negative back contact voltage (X-ray imaging mode). A further extension of the dynamic range is possible using on-chip pixel binning which allows a substantial reduction of the readout time at the expense of position resolution in transfer direction.
The routine use of pnCCD detector systems for X-ray diffraction experiments with white synchrotron radiation requires a quantitative interpretability of the accumulated data sets. In the course of this work, various methods for analyzing pnCCD-generated data were developed in order to obtain the desired structural information about the sample. The potential of the pnCCD for applications in macromolecular crystallography could be demonstrated by the example of EDLD experiments on HEWL crystals:

- The conventional unit cell of a single crystal results from a sufficient number of measured Laue spot positions and energies. Converting the 3D information into reciprocal-space coordinates, the shortest three non-coplanar translations of the real lattice are obtained by means of suitable crystallographic reduction and refinement procedures. The lattice parameters of a tetragonal HEWL crystal could be reproduced with relative accuracies of nearly 2% for the lattice constants and 4% for the cell angles. This result is independent of the sample orientation and accessible without *a priori* information on the basis of a single-shot exposure of the crystal to white synchrotron radiation.

- The developed algorithms are applicable to diffraction patterns of higher complexity generated by polycrystalline materials without restriction. Therefore, also in the case of a double-crystalline HEWL structure, the determination of the present unit cells could be achieved within one single white X-ray exposure of the sample. In this sense, pnCCD systems enable a quantitative characterization of crystalline quality and can thus be used for fast screening experiments prior to X-ray structure analysis on an atomic level.

- As soon as the unit cell of the crystal is determined, the 3D resolution of the pnCCD provides a complete indexing of the recorded Laue pattern. Detailed investigations of the energy spectra occurring at the Bragg peak positions revealed that single reflections as well as overlapping diffraction orders contribute to the collected data volume.

- Absolute Laue spot intensities can be extracted from the pnCCD data sets with an accuracy in the range of 1% translating into a relative error of experimental structure-factor amplitudes of about 5%. To this end, a statistical analysis of multi-photon hits, which become manifest in event pile-up and pattern pile-up, is essential. The integration of single reflections relies on an appropriate background correction and the property that independently detected photon numbers follow Poisson distributions. This behavior also serves to deconvolute spatially overlapping harmonics as long as the pile-up probability of the accompanying background signal is sufficiently low.

- The structure of a HEWL single crystal could be refined against the collected data by means of a rigid-body method with a crystallographic R-factor of about 25%. This result confirms the correctness of the applied algorithms for absolute intensity determination and can be improved by recording a complete data set of HEWL at high resolution.

Bibliography

[1] P. Kraft, A. Bergamaschi, C. Broennimann, R. Dinapoli, E. F. Eikenberry, B. Henrich, I. Johnson, A. Mozzanica, C. M. Schlepütz, P. R. Willmott, and B. Schmitt, *Performance of single-photon-counting PILATUS detector modules*, Journal of Synchrotron Radiation **16** (2009), 368-375

[2] L. Strüder, U. Briel, K. Dennerl, R. Hartmann, E. Kendziorra, N. Meidinger, E. Pfeffermann, C. Reppin, B. Aschenbach, W. Bornemann, H. Bräuninger, W. Burkert, M. Elender, M. Freyberg, F. Haberl, G. Hartner, F. Heuschmann, H. Hippmann, E. Kastelic, S. Kemmer, G. Kettenring, W. Kink, N. Krause, S. Müller, A. Oppitz, W. Pietsch, M. Popp, P. Predehl, A. Read, K. H. Stephan, D. Stötter, J. Trümper, P. Holl, J. Kemmer, H. Soltau, R. Stötter, U. Weber, U. Weichert, C. von Zanthier, D. Carathanassis, G. Lutz, R. H. Richter, P. Solc, H. Böttcher, M. Kuster, R. Staubert, A. Abbey, A. Holland, M. Turner, M. Balasini, G. F. Bignami, N. La Palombara, G. Villa, W. Buttler, F. Gianini, R. Lainé, D. Lumb, and P. Dhez, *The European Photon Imaging Camera on XMM-Newton: The pn-CCD camera*, Astronomy & Astrophysics **365** (2001), L18-L26

[3] N. Meidinger, L. Andricek, S. Bonerz, J. Englhauser, R. Hartmann, G. Hasinger, S. Herrmann, P. Holl, R. Richter, H. Soltau, and L. Strüder, *Frame Store PN-CCD Detector for Space Applications*, Proceedings of SPIE **5165** (2004), 26-36

[4] L. Strüder, S. Epp, D. Rolles, R. Hartmann, P. Holl, G. Lutz, H. Soltau, R. Eckart, C. Reich, K. Heinzinger, C. Thamm, A. Rudenko, F. Krasniqi, K.-U. Kühnel, C. Bauer, C.-D. Schröter, R. Moshammer, S. Techert, D. Miessner, M. Porro, O. Hälker, N. Meidinger, N. Kimmel, R. Andritschke, F. Schopper, G. Weidenspointner, A. Ziegler, D. Pietschner, S. Herrmann, U. Pietsch, A. Walenta, W. Leitenberger, C. Bostedt, T. Möller, D. Rupp, M. Adolph, H. Graafsma, H. Hirsemann, K. Gärtner, R. Richter, L. Foucar, R. L. Shoeman, I. Schlichting, and J. Ullrich, *Large-format, high-speed, X-ray pnCCDs combined with electron and ion imaging spectrometers in a multipurpose chamber for experiments at 4th generation light sources*, Nuclear Instruments and Methods in Physics Research Section A **614** (2010), 483-496

[5] W. Leitenberger, R. Hartmann, U. Pietsch, R. Andritschke, I. Starke, and L. Strüder, *Application of a pnCCD in X-ray diffraction: a three-dimensional X-ray detector*, Journal of Synchrotron Radiation **15** (2008), 449-457

[6] S. Send, M. von Kozierowski, T. Panzner, S. Gorfman, K. Nurdan, A. H. Walenta, U. Pietsch, W. Leitenberger, R. Hartmann, and L. Strüder, *Energy-dispersive Laue diffraction by means of a frame-store pnCCD*, Journal of Applied Crystallography **42** (2009), 1139-1146

[7] A. Abboud, S. Send, R. Hartmann, L. Strüder, A. Savan, A. Ludwig, N. Zotov, and U. Pietsch, *Application of an energy-dispersive pnCCD for X-ray reflectivity: Investigation of interdiffusion in Fe-Pt multilayers*, Physica Status Solidi A **208** (2011), 2601-2607

[8] K. Kleinknecht, *Detectors for Particle Radiation*, 2nd edition, Cambridge University Press, Cambridge (1998), ISBN: 0521640326

[9] P. Marmier and E. Sheldon, *Physics of Nuclei and Particles*, Vol. I, Academic Press, New York (1969), ISBN: 0124731015

[10] O. Klein and Y. Nishina, *Über die Streuung von Strahlung durch freie Elektronen nach der neuen relativistischen Quantendynamik von Dirac*, Zeitschrift für Physik **52** (1929), 853-868

[11] C. Grupen and B. Shwartz, *Particle Detectors*, 2nd edition, Cambridge University Press, Cambridge, New York (2008), ISBN: 0521187958

[12] E. B. Podgoršak, *Radiation Physics for Medical Physicists*, 2nd edition, Springer-Verlag, Berlin, (2010), ISBN: 3642008747

[13] M. Sánchez del Río and R. J. Dejus, *XOP: A Multiplatform Graphical User Interface for Synchrotron Radiation Spectral and Optics Calculations*, Proceedings of SPIE **3152** (1997), 148-157

[14] XOP 2.3 software (2013), *http://ftp.esrf.eu/pub/scisoft/xop2.3/*

[15] A. Owens, M. Bazdaz, S. Kraft, A. Peacock, S. Nenonen, and H. Andersson, *The hard X-ray response of epitaxial GaAs detectors*, Nuclear Instruments and Methods in Physics Research A **442** (2000), 360-363

[16] M. C. Veale, S. J. Bell, L. L. Jones, P. Seller, M. D. Wilson, R. C. Cernik, J. Kalliopuska, H. Pohjonen, H. Andersson, S. Nenonen, and V. Kachkanov, *Characterization of Edgeless CdTe Detectors for use in Hard X-Ray Imaging Applications*, IEEE Transactions on Nuclear Science **59** (2012), 1536-1543

[17] K. P. O'Donnell and X. Chen, *Temperature dependence of semiconductor band gaps*, Applied Physics Letters **58** (1991), 2924-2926

[18] M. N. Mazziotta, *Electron-hole pair creation energy and Fano factor temperature dependence in silicon*, Nuclear Instruments and Methods in Physics Research A **584** (2008), 436-439

[19] S. Selberherr, *Analysis and Simulation of Semiconductor Devices*, Springer-Verlag, Wien, New York (1984), ISBN: 3211818006

[20] G. Lutz, *Semiconductor Radiation Detectors*, Springer-Verlag, Berlin, Heidelberg (1999), ISBN: 3540648593

[21] G. Lutz, P. Lechner, M. Porro, L. Strüder, and G. De Vita, *DEPFET sensor with intrinsic signal compression developed for use at the XFEL free electron laser radiation source*, Nuclear Instruments and Methods in Physics Research A **624** (2010), 528-532

[22] E. Gatti and P. Rehak, *Semiconductor Drift Chamber – an application of a novel charge transport scheme*, Nuclear Instruments and Methods in Physics Research A **225** (1984), 608-614

[23] P. Rehak, J. Walton, E. Gatti, A. Longoni, M. Sanpietro, J. Kemmer, H. Dietl, P. Holl, R. Klanner, G. Lutz, A. Wylie, and H. Becker, *Progress in semiconductor drift detectors*, Nuclear Instruments and Methods in Physics Research A **248** (1986), 367-378

[24] L. Strüder, *High resolution imaging X-ray spectrometers*, Nuclear Instruments and Methods in Physics Research A **454** (2000), 73-113

[25] N. Meidinger, H. W. Braeuninger, U. G. Briel, R. Hartmann, G. D. Hartner, P. Holl, J. Kemmer, E. Kendziorra, N. Krause, G. Lutz, E. Pfeffermann, M. Popp, C. Reppin, R. H. Richter, H. Soltau, D. Stötter, L. Strüder, J. E. Trümper, and C. von Zanthier, *PN-CCD detector for XMM and ABRIXAS*, Proceedings of SPIE **3765** (1999), 192-203

[26] H. Soltau, J. Kemmer, N. Meidinger, D. Stötter, L. Strüder, J. Trümper, C. von Zanthier, H. Bräuniger, U. Briel, D. Carathanassis, K. Dennerl, S. Engelhard, F. Haberl, R. Hartmann, G. Hartner, D. Hauff, H. Hippmann, P. Holl, E. Kendziorra, N. Krause, P. Lechner, E. Pfeffermann, M. Popp, C. Reppin, H. Seitz, P. Solc, T. Stadlbauer, U. Weber, and U. Weichert, *Fabrication, test and performance of very large X-ray CCDs designed for astrophysical applications*, Nuclear Instruments and Methods in Physics Research A **439** (2000), 547-559

[27] R. Hartmann, W. Buttler, H. Gorke, S. Herrmann, P. Holl, N. Meidinger, H. Soltau, and L. Strüder, *A high-speed pnCCD detector system for optical applications*, Nuclear Instruments and Methods in Physics Research A **568** (2006), 118-123

[28] S. M. Sze, *Physics of Semiconductor Devices*, 2nd edition, Wiley, New York (1981), ISBN: 0471056618

[29] N. Kimmel, *Analysis of the charge collection process in solid state X-ray detectors*, PhD thesis, Universität Siegen (2008)

[30] N. Meidinger, S. Bonerz, H. W. Braeuninger, R. Eckhardt, J. Englhauser, R. Hartmann, G. Hasinger, P. Holl, N. Krause, G. Lutz, E. Pfeffermann, R. H. Richter, H. Soltau, L. Strüder, and J. E. Trümper, *Frame store PN-CCD detector for the ROSITA mission*, Proceedings of SPIE **4851** (2002), 1040-1047

[31] N. Meidinger, R. Andritschke, R. Hartmann, S. Herrmann, P. Holl, G. Lutz, and L. Strüder, *pnCCD for photon detection from near-infrared to X-rays*, Nuclear Instruments and Methods in Physics Research A **565** (2006), 251-257

[32] N. Meidinger, R. Andritschke, O. Hälker, R. Hartmann, S. Herrmann, P. Holl, G. Lutz, N. Kimmel, G. Schaller, M. Schnecke, F. Schopper, H. Soltau, and L. Strüder, *Next generation of pnCCDs for X-ray spectroscopy and imaging*, Nuclear Instruments and Methods in Physics Research A **568** (2006), 141-148

[33] N. Meidinger, L. Strüder, P. Holl, H. Soltau, and C. von Zanthier, *Analysis of trapping effects on charge transfer in proton irradiated pn-CCDs*, Nuclear Instruments and Methods in Physics Research A **377** (1996), 298-311

[34] R. Andritschke, G. Hartner, R. Hartmann, N. Meidinger, and L. Strüder, *Data Analysis for Characterizing pnCCDs*, IEEE Nuclear Science Symposium Conference Record (2008), 2166-2172

[35] E. Pinotti, H. Bräuninger, N. Findeis, H. Gorke, D. Hauff, P. Holl, J. Kemmer, P. Lechner, G. Lutz, W. Kink, N. Meidinger, G. Metzner, P. Predehl, C. Reppin, L. Strüder, J. Trümper, C. von Zanthier, E. Kendziorra, R. Staubert, V. Radeka, P. Rehak, G. Bertuccio, E. Gatti, A. Longoni, A. Pullia, and M. Sampietro, *The pn-CCD on-chip electronics*, Nuclear Instruments and Methods in Physics Research A **326** (1993), 85-91

[36] L. Strüder, *private communication*

[37] M. Huth, *private communication*

[38] W. Buttler, G. Lutz, H. Bergmann, H. Dietl, D. Hauff, P. Holl, and P. F. Manfredi, *Low noise-low power monolithic multiplexing readout electronics for silicon strip detectors*, Nuclear Instruments and Methods in Physics Research A **273** (1988), 778-783

[39] M. Porro, S. Herrmann, and N. Hörnel, *Multi correlated double sampling with exponential reset*, IEEE Nuclear Science Symposium Conference Record (2007), 291-298

[40] N. Meidinger, R. Andritschke, K. Dennerl, O. Hälker, G. Hasinger, R. Hartmann, G. Hartner, S. Herrmann, P. Holl, N. Kimmel, H. Soltau, and L. Strüder, *First measurements with DUO/ROSITA pnCCDs*, Proceedings of SPIE **5898** (2005), 58980W

[41] S. Send, *Energiedispersive Röntgenspektroskopie und Laue-Beugung mit Hilfe eines Frame-Store-pnCCD*, Master thesis, Universität Siegen (2008)

[42] S. Send, A. Abboud, R. Hartmann, M. Huth, W. Leitenberger, N. Pashniak, J. Schmidt, L. Strüder, and U. Pietsch, *Characterization of a pnCCD for applications with synchrotron radiation*, Nuclear Instruments and Methods in Physics Research A **711** (2013), 132-142

[43] T. Eggert, *Die spektrale Antwort von Silizium-Röntgendetektoren*, PhD thesis, Technische Universität München (2004)

[44] R. Hartmann, S. Epp, S. Herrmann, P. Holl, N. Meidinger, C. Reich, D. Rolles, H. Soltau, L. Strüder, J. Ullrich, and G. Weidenspointner, *Large format pnCCDs as imaging detectors for X-ray free-electron-lasers*, IEEE Nuclear Science Symposium Conference Record (2008), 2590-2595

[45] A. Abboud, S. Send, N. Pashniak, W. Leitenberger, S. Ihle, M. Huth, R. Hartmann, L. Strüder, and U. Pietsch, *Sub-pixel resolution of a pnCCD for X-ray white beam applications*, Journal of Instrumentation **8** (2013), P05005

[46] N. Kimmel, J. S. Hiraga, R. Hartmann, N. Meidinger, and L. Strüder, *The direct measurement of the signal charge behavior in pnCCDs with subpixel resolution*, Nuclear Instruments and Methods in Physics Research A **568** (2006), 128-133

[47] H. Yousef, *Energy dependent charge spread function in a dedicated synchrotron beam pnCCD detector*, PhD thesis, Universität Siegen (2011)

[48] N. Meidinger, S. Bonerz, R. Eckhardt, J. Englhauser, R. Hartmann, G. Hasinger, S. Herrmann, P. Holl, N. Krause, G. Lutz, R. Richter, H. Soltau, and L. Strüder, *First measurements with a frame store PN-CCD X-ray detector*, Nuclear Instruments and Methods in Physics Research A **512** (2003), 341-349

[49] I. Ordavo, S. Ihle, V. Arkadiev, O. Scharf, H. Soltau, A. Bjeoumikhov, S. Bjeoumikhova, G. Buzanich, R. Gubzhokov, A. Günther, R. Hartmann, P. Holl, N. Kimmel, M. Kühbacher, M. Lang, N. Langhoff, A. Liebel, M. Radtke, U. Reinholz, H. Riesemeier, G. Schaller, F. Schopper, L. Strüder, C. Thamm, and R. Wedell, *A new pnCCD-based color X-ray camera for fast spatial and energy-resolved measurements*, Nuclear Instruments and Methods in Physics Research A **654** (2011), 250-257

[50] R. J. Barlow, *Statistics: A Guide to the Use of Statistical Methods in the Physical Sciences*, Wiley, Chichester (1989), ISBN: 0471922943

[51] X-ray Data Booklet (October 2009), *http://xdb.lbl.gov/*

[52] U. Pietsch, J. Grenzer, T. Geue, F. Neissendorfer, G. Brezsesinski, C. Symietz, H. Möhwald, and W. Gudat, *The energy-dispersive reflectometer at BESSY II: a challenge for thin film analysis*, Nuclear Instruments and Methods in Physics Research A **467-468** (2001), 1077-1080

[53] N. Kimmel and P. Holl, *Xonline, Driver and Analysis Software for pnCCDs*, Max-Planck-Institute Halbleiterlabor

[54] R. Andritschke, *Offline Analysis Description* (2009), Max-Planck-Institute Halbleiterlabor

[55] N. Meidinger, *Strahlenhärte von Röntgen-Sperrschicht-CCD-Detektoren*, PhD thesis, Technische Universität München (2003)

[56] C. Kittel, *Einführung in die Festkörperphysik*, 14. Auflage, Oldenbourg, München (2006), ISBN: 3486577239

[57] X.-R. Huang, StructFactor 1.0 software (2002), *http://www.ccp14.ac.uk/ccp/web-mirrors/xianrong-huang/*

[58] J. B. Roberto and B. W. Batterman, *Anharmonicity and the Temperature Dependence of the Forbidden (222) Reflection in Silicon*, Physical Review B **2** (1970), 3220-3226

[59] R. Colella, *Experimental Investigations of Bonding Charges in Diamond and Zinc Blende Structures*, Physica Scripta **15** (1977), 143-146

[60] I. R. Entin and I. A. Smirnova, *Double-Crystal Rocking Curve of the Forbidden Si 222 Reflection*, Acta Crystallographica A **45** (1989), 577-580

[61] A. Abboud, *pn-CCD Detector Utilized for Synchrotron Radiation Sources*, Master thesis, Universität Siegen (2009)

[62] Incoatec GmbH, *User Manual IμS*, 2009

[63] N. Kimmel, R. Andritschke, L. Englert, S. Epp, A. Hartmann, R. Hartmann, G. Hauser, P. Holl, I. Ordavo, L. Strüder, and J. Ullrich, *Calibration methods and performance evaluation for pnCCDs in experiments with FEL radiation*, Proceedings of SPIE **8078** (2011), 80780V

[64] *http://www.marresearch.com/products.html*

[65] R. Strzodka, M. Doggett, and A. Kolb, *Scientific Computation for Simulations on Programmable Graphics Hardware*, Simulation Modelling Practice and Theory **13**(8) (2005), 667-681

[66] F. Alghabi, U. Schipper, S. Send, A. Abboud, N. Pashniak, U. Pietsch, and A. Kolb, *Real-time Processing of pnCCD Images using GPUs*, Journal of Instrumentation (2013), in preparation

[67] International Tables for Crystallography, Volume A, *Space-Group Symmetry*, editied by T. Hahn, 5th edition, Kluwer Academic Publishers, Dordrecht (2002), ISBN: 0792365909

[68] C. C. F. Blake, D. F. Koenig, G. A. Mair, A. C. T. North, D. C. Phillips, and V. R. Sarma, *Structure of Hen Egg-White Lysozyme: A Three-dimensional Fourier Synthesis at 2Å Resolution*, Nature **206** (1965), 757-761

[69] Z. H. Kalman, *On the derivation of integrated reflected energy formulae*, Acta Crystallographica A **35** (1979), 634-641

[70] R. Kahn, R. Fourme, A. Gadet, J. Janin, C. Dumas, and D. André, *Macromolecular crystallography with synchrotron radiation: photographic data collection and polarization correction*, Journal of Applied Crystallography **15** (1982), 330-337

[71] R. Klein, R. Thornagel, and G. Ulm, *Der Speicherring BESSY II als primäres Strahlernormal*, PTB-Mitteilungen **115** (2005), 172-179

[72] H. M. Einspahr and M. S. Weiss, *Quality indicators in macromolecular crystallography: definitions and applications*, International Tables for Crystallography, Volume F, *Crystallography of Biological Macromolecules*, 64-74, edited by E. Arnold, D. M. Himmel, and M. G. Rossmann, 2nd edition, Wiley, New York (2012), ISBN: 0470660783

[73] B. N. Delaunay, *Neuere Darstellung der geometrischen Kristallographie*, Zeitschrift für Kristallographie (1933), **84**, 109-149

[74] A. L. Patterson and W. E. Love, *Remarks on the Delaunay Reduction*, Acta Crystallographica **10** (1957), 111-116

[75] H. Minkowski, *Über die positiven quadratischen Formen und über kettenbruchähnliche Algorithmen*, Journal für die reine und angewandte Mathematik, **107** (1891), 278-297

[76] C. F. Gauss, *Disquisitiones arithmeticae*, article 171, English edition, Springer-Verlag, New York (1986), English translation by A. A. Clarke, ISBN: 0387962549

[77] S. Brandt, *Datenanalyse*, 4. Auflage, Spektrum Akademischer Verlag, Heidelberg, Berlin (1999), ISBN: 3827401585

[78] W. Leitenberger, *private communication*

[79] A. F. Holleman and E. Wiberg, *Lehrbuch der Anorganischen Chemie*, 101. Auflage, De Gruyter, Berlin, New York (1995), ISBN: 3110126419

[80] M. S. Weiss, G. J. Palm, and R. Hilgenfeld, *Crystallization, structure solution and refinement of hen egg-white lysozyme at pH 8.0 in the presence of MPD*, Acta Crystallographica D **56** (2000), 952-958

[81] R. Cudney, S. Patel, K. Weisgraber, Y. Newhouse, and A. McPherson, *Screening and optimization strategies for macromolecular crystal growth*, Acta Crystallographica D **50** (1994), 414-423

[82] S. Send, A. Abboud, W. Leitenberger, M. S. Weiss, R. Hartmann, L. Strüder, and U. Pietsch, *Analysis of polycrystallinity in hen egg-white lysozyme using a pnCCD*, Journal of Applied Crystallography **45** (2012), 517-522

[83] U. Müller, N. Darowski, M. R. Fuchs, R. Förster, M. Hellmig, K. S. Paithankar, S. Pühringer, M. Steffien, G. Zocher, and M. S. Weiss, *Facilities for macromolecular crystallography at the Helmholtz-Zentrum Berlin*, Journal of Synchrotron Radiation **19**

(2012), 442-449

[84] U. Müller, *private communication*

[85] M. S. Weiss, *private communication*

[86] R. E. Dinnebier and S. J. L. Billinge, *Powder Diffraction: Theory and Practice*, 101. Auflage, The Royal Society of Chemistry, Cambridge (2008), ISBN: 0854042318

[87] A. J. C. Wilson, *The probability distribution of X-ray intensities*, Acta Crystallographica **2** (1949), 318-321

[88] D. Sherwood and J. Cooper, *Crystals, X-rays and Proteins: Comprehensive Protein Crystallography*, Oxford University Press, Oxford (2010), ISBN: 019955904X

[89] M. Kjeldgaard, F2MTZ software, *http://www.ccp4.ac.uk/dist/html/f2mtz.html*

[90] K. S. Wilson and G. S. French, TRUNCATE software
http://www.ccp4.ac.uk/dist/html/truncate.html

[91] G. S. French and K. S. Wilson, *On the treatment of negative intensity observations*, Acta Crystallographica A **34** (1978), 517-525

[92] CCP4: Collaborative Computational Project, Number 4, *The CCP4 suite: programs for protein crystallography*, Acta Crystallographica D **50** (1994), 760-763

[93] Protein Data Bank PDB, *http://www.rcsb.org/pdb/*

[94] G. N. Murshudov , REFMAC5 software
http://www.ccp4.ac.uk/dist/html/refmac5.html

[95] G. N. Murshudov, A. A. Vagin, and E. J. Dodson, *Refinement of Macromolecular Structures by the Maximum-Likelihood Method*, Acta Crystallographica D **53** (1997), 240-255

Acknowledgements

Finally, I would like to thank all my colleagues who contributed to the success of this thesis and all the people who supported me during this time:

- I am grateful to Prof. Dr. Ullrich Pietsch for the guidance through the last years and the permanent encouragement and support of the related research projects.
- I am very thankful to Prof. Dr. Lothar Strüder for the assessment of this thesis, many helpful comments to it, and fruitful discussions concerning pnCCD-specific topics.
- I would like to acknowledge PNSensor GmbH and in particular Robert Hartmann and Dr. Martin Huth for the establishment of the pnCCD systems and for the support in all kinds of technical questions.
- I give thanks to Ali Abboud and Nadija Pashniak who spent a lot of long days with me during the beamtimes at BESSY II.
- I am grateful to Dr. Wolfram Leitenberger for the experimental assistance at the EDR beamline and many helpful ideas and discussions.
- I thank Dr. Manfred Weiss for the preparation of the HEWL samples and the help with the final step of data analysis.
- I would like to express my deepest appreciation to my family and my parents for the never-ending support.
- And I thank Sandra, for her love and patience.

This work was supported by the Bundesministerium für Bildung und Forschung (BMBF) under grant 05KS7PSA and 05K10PSB.